Efficient uncertainty propagation approaches to solve a large class of fatigue crack-growth problems

Stéphanie Chahine

COLLEGE SCIENCES DOCTORAL DE L'INGENIERIE PAYS DE LA LOIRE ET DES SYSTEMES

université angers

THESE DE DOCTORAT DE

L'UNIVERSITE D'ANGERS

ECOLE DOCTORALE N° 602
Sciences pour l'Ingénieur
Spécialité : « *Mécanique des Solides, des Matériaux, des structures et des surfaces* »

Par
Stéphanie CHAHINE

Efficient uncertainty propagation approaches to solve a large class of fatigue crack-growth problems

Thèse présentée et soutenue à l'Université d'Angers, le 30/01/2023
Unité de recherche : Laboratoire Angevin de Recherche en Ingénierie des Systèmes
Thèse N° : 212076

Rapporteurs avant soutenance :

Abdelkhalak El Hami	Professeur, Université de Rouen Normandie
Rostand Moutou Pitti	Maître de conférences, HDR, Université Clermont Auvergne

Composition du Jury :

Président :	Emilio Bastidas – Arteaga	Professeur, Université de la Rochelle
Examinateurs :	Mihaela Barreau	Maître de conférences, HDR, University of Angers
	Emilio Bastidas – Arteaga	Professeur, Université de la Rochelle
Dir. de thèse :	David Bigaud	Professeur, University of Angers
Co-dir. de thèse :	Hassen Riahi	Maître de conférences, University of Angers

Invité(s)

Etienne Pessard	Maître de conférences, HDR, Arts et Métiers Paris Tech

ACKNOWLEDGMENTS

This manuscript is the result of a thesis work carried out at the Angevin Systems Engineering Research Laboratory (LARIS), Research Unit of the University of Angers. It is the fruit of a teamwork.

My first gratitude thought goes to my thesis supervisor, Mr. David BIGAUD. I warmly thank him for the trust he has placed in me, for the support, guidance and inspiration he gave me through his commitment to this work. I learnt a lot working with him.

This thesis wouldn't have been the same without my co-supervisor, Mr. Hassen RIAHI who contributed enormously to this work. His involvement, patience, perseverance, availability and thoroughness greatly helped me to finish my thesis. He followed me closely throughout the whole process and was always present and willing to meet up, answer any questions encountered along the way and constructively criticizing my work. Without his input this thesis wouldn’t have been possible.

I express my sincere thanks to Mr. Alaa CHATEAUNEUF and Mr. Etienne PESSARD for having accepted to be a part of this thesis as members of the CSI. I am grateful for their prodigious advice which has contributed to the success of this work.

I also address my gratitude to all the members of the jury for having participated in my thesis defense and for having shown interests in my work.

Also a big thank you goes to all the members of the SFD team which I was part of it. I am grateful for their welcome.

I would also like to sincerely thank all the staff of LARIS, especially Marie-Françoise Gerard, for having made all these years spent within LARIS very pleasant despite the sanitary situation.

I give special thanks to my doctoral colleagues for all the good time shared and for all their support.

I now thank and extend my affection to my family and friends for their encouragement throughout these years.

I would like to thank my parents who despite the distance were always present in difficult times and have always trusted and supported me throughout my academic career. I thank them for believing in me and continuously supporting me whatever my plans are.

Finally, I would like to thank everyone around me, who have contributed, directly or indirectly, in the success of this work and helped me eliminate doubts encountered during this long and difficult journey.

Table of content

List of figures

List of tables

Nomenclature

$\Delta\sigma$	*Variation of the nominal stress (amplitude of the loading)*
N	*Number of loading cycles*
C_{SN}	*Constant of the Wöhler curve*
m_{SN}	*Slope of the Wöhler curve*
$\Delta\sigma_D$	*Endurance limit of the material*
$\Delta\varepsilon$	*Total strain amplitude*
$\Delta\varepsilon_{el}$	*Elastic strain amplitude*
$\Delta\varepsilon_{pl}$	*Plastic strain amplitude*
ε_f'	*Fatigue ductility coefficient*
σ_f'	*Fatigue strength coefficient*
E	*Young modulus of the material*
a	*Crack length*
ΔK	*Variation of the stress intensity factor*
a_0	*Initial crack length*
a_c	*Critical crack length*
K_I	*Stress intensity factor mode I*
K_{II}	*Stress intensity factor mode II*
K_{III}	*Stress intensity factor mode III*
E_p	*Potential energy*
G	*Strain energy release rate*
μ	*Shear modulus of the material*
w_e	*Strain energy density*
δ_{xj}	*Crack opening displacement*
σ_{ij}	*Stress field*
u_i	*Displacement field*
ΔP	*Tension loading*
σ_θ	*Circumferential stress*
θ	*Bifurcation angle*
$\sigma_{r\theta}$	*Shear stress*
W^{tot}	*Total energy*
δ	*Small crack*
$\frac{da}{dN}$	*Fatigue Crack Growth Rate*
C	*Material parameters*
m	*Material parameters*
R	*Load ratio*

ΔK_{th}	*Threshold of the stress intensity factor*
K_{Ic}	*Facture toughness*
ΔK_{eq}	*Equivalent stress intensity factor*
N_f	*Number of loading cycles to failure*
r	*Distance from the crack tip to a given point*
ΔK_{eff}	*Effective stress intensity factor range*
Δa	*Crack growth increment*
D_0	*Random variable*
$\boldsymbol{p_0}$	*Vector of the initial distribution of the different level of damage*
$\boldsymbol{p_t}$	*Vector of the distribution of each level of damage*
$F_W(t;b)$	*Cumulative distribution function*
$A(t,\gamma)$	*Probabilistic process*
$f(a)$	*Probability density function*
σ_m	*Minimum stress amplitude*
σ_M	*Maximum stress amplitude*
Φ	*Arbitrary invertible function*
$Y(a)$	*Geometric correction function*
$\Psi(a)$	*Increasing function of the evolution of the crack length*
X	*Random vector of variables*
x	*Vector of real values associated to the randomness*
y	*Mechanical model response*
Y	*Probabilistic model*
Ω	*Space of random events*
T	*Iso-probabilistic transformation*
U	*Standard Gaussian random variable*
$h \equiv f \circ T$	*Function representing the physical model in standard random space*
$p_y(y)$	*Probability density*
m_Y^l	*Statistical moment*
$p_x(x)$	*Joint probability density of the random variable X*
$\varphi_u(u)$	*Joint probability density of an N-dimensional standard Gaussian random variable*
μ_Y	*Mean*
σ_Y	*Standard deviation*
P_f	*Probability of failure*
1_{Ω_F}	*Indicator function in Ω_F*
$\hat{P}_f$	*Estimation of the probability of failure*
n_p	*Quadrature order*
$I[.]$	*Integration designing a linear function*
u_n	*Random variable in the $\mathbb{R}$ space*

φ_{u_n}	*Probability density of* u_n
w_{k_n}	*Gauss-Hermite weights*
u_{k_n}	*Gauss-Hermite integration points*
$H_n(x)$	*Hermite polynomials*
$\boldsymbol{u}_i$	*Integration points*
w_i	*Integration weights*
d_T	*Highest order of the function: smallest integer*
σ_u^2	*Partial variance*
σ^2	*Total variance*
$\mathcal{F}$	*Random set*
$H(x,\theta)$	*Random field*
$\rho(x,x')$	*Correlation function*
$C_{HH}(x,x')$	*Autocovariance function*
$\hat{H}(x,\theta)$	*Approximation field*
$\Psi_{\boldsymbol{\alpha}}$	*Multivariate Hermite polynomials*
$a_{\boldsymbol{\alpha}}$	*Deterministic unknown coefficients*
$\boldsymbol{\alpha}$	*Multi-index*
$\hat{M}$	*Polynomial approximation*
$\mathbb{E}[.]$	*Mathematical expectation*
φ_N	*Probability density*
q	*Quadrature order*
p	*Degree of polynomial chaos expansion*
$\mathcal{I}_n^p$	*Set of index associated with a polynomial chaos expansion of degree* p
Y	*Mechanical response*
l_x	*Correlation lengths in the* x *direction*
l_y	*Correlation lengths in the* y *direction*
$E(\boldsymbol{x},\theta)$	*Random field*
λ_i	*Values of the correlation matrix*
ϕ_i	*Eigenvectors of the correlation matrix*
μ_E^0	*Mean of the normal random field*
σ_E^0	*Standard deviation of the normal random field*
$G(\boldsymbol{X})$	*Limit state function representing a failure scenario*
K_{eq}	*Equivalent stress intensity factor*
$f_k(x_k)$	*One-dimensional function of the individual contribution of the parameter* x_k
$\tilde{y}_s$	*Approximation of the mechanical response*
r_y	*Size of the cyclic plastic zone*
ϕ_R	*Retardation parameter*
a_{OL}	*Crack length at which the overload is applied*

a_i	*Current crack length*
$r_{p,OL}$	*Size of the plastic zone produced by the overload at* a_{OL}
$r_{p,i}$	*Size the plastic zone produced at the current crack length* a_i
$m_{wheeler}$	*Shaping exponent*
σ_{yld}	*Yielding strength of the material*
K_{red}	*Residual stress intensity factor*
$K_{max,eff,i}$	*Maximum effective stress intensity factor*
$K_{max,i}$	*Maximum apparent stress intensity factor (under constant amplitude)*
$K_{min,eff,i}$	*Minimum effective stress intensity factor*
$K_{min,i}$	*Minimum apparent stress intensity factor*
$\Delta K_{eff,i}$	*Effective stress intensity factor range*
$K_{max,OL}$	*Stress intensity factor of the overload cycle*
Δa	*Crack growth length since the overload cycle*
β	*Plastic zone size factor*
R_{eff}	*Effective stress ratio*
ϕ_a	*Acceleration factor*
K_{op}	*SIF of crack closure level*
ΔK_{th}	*Threshold stress intensity factor range*
ΔK_0	*Threshold value of the SIF range for* $R = 0$
N_f^{RAL}	*Fatigue lifetime associated to the true random amplitude loading*
N_f^{ECAL}	*Fatigue lifetime associated to the equivalent constant amplitude loading*
$\Delta\sigma_{eq}$	*Equivalent stress amplitude*
$\Delta\sigma_i$	*Random loading amplitude*
θ	*Crack tip opening angle (CTOA)*
δ	*Crack Tip Opening Displacement (CTOD)*
$d\delta$	*Variation of the CTOD*

Introduction

Fatigue of materials, considered as the cumulative damage under cyclic loads, even below their elastic limits, is identified as a major engineering problem and the most common source of failure of mechanical structures and components. 80-90% of total identified structural failures have been attributed to fatigue, which has been the cause of several catastrophic accidents such as bridge collapses and aircraft failures.

A first level of complexity that engineers will have to deal with lies in the difficulty of understanding fatigue phenomena that occur without any visible warning signs. Prediction is thus almost impossible and, consequently, the material and human damages are important.

Many researchers have been interested in understanding the physics of the fatigue phenomenon to be able to predict the service life of materials and structures subjected to cyclic loads. Their studies are mainly devoted to the modeling and monitoring of the evolution of stresses in the vicinity of micro or macroscopic cracks. The fatigue damage process is decomposed into two phases. The embrittlement of the material, in particular in the vicinity of stress concentration zones, leads, in a first phase, to the appearance of cracks which propagate, in a second phase, under the effect of the load until the sudden failure of the material. The embrittlement of the material, particularly in the vicinity of stress concentration zones, leads, first, to the initiation of cracks which propagate under the effect of the loading until the sudden failure of the material. Fatigue life, measured in number of loading cycles, is generally taken as the sum of the time taken for a crack to initiate and the time taken for it to propagate to a critical length, or to failure. The duration of each of these two phases depends mainly on the type of material and its initial defects. For most structures subjected to fatigue, the contribution of the crack initiation phase on the service life is generally low relative to that of the propagation phase (about 10% of the total service life). The fatigue life is therefore mainly represented by the duration of the propagation phase, which is estimated by integrating models representing the evolution of the crack size and the number of load cycles such as the well-known Paris-Erdogan law.

In engineering, the design of structures subject to fatigue is performed with respect to a safe fatigue lifetime that depends on the consequence of the failure. The definition of this target fatigue lifetime is not a trivial task. The concepts of fracture mechanics allow to study the behavior of structures with respect to fatigue of materials. Within this framework and under simplifying assumptions, such as a linear elastic mechanics of fracture, the service life can be adequately calculated using stress intensity factors and comparing them to the material toughness. These parameters, which define the driving forces that govern the crack during its propagation, depend on the geometry of the structure and the applied loading. In the case of simple structures, analytical expressions are available but for more complex structures, with complex geometries and/or for a mixed mode of crack propagation, following a curvilinear path, these expressions do not exist and numerical simulations, with heavy computational efforts, are necessary.

A second level of complexity, to be dealt with mainly by researchers this time, lies in the very random nature of the fatigue phenomenon. Deterministic approaches, based exclusively on the principles of fracture mechanics, provide conservative predictions and numerous studies have shown the high dispersion of the crack propagation rate recorded during experimental tests. Accurate predictions are thus only possible through the coupling between fracture mechanics and probability theory.

Different approaches can be considered to integrate the stochastic character of the crack growth process in the fatigue life estimation. Approaches based either on Markov theory or on the weighting of the equation managing the crack growth rate by a random process are very often purely statistical. In addition to the need for costly experimental work to determine the different parameters and a consequent analytical development, these models are only applicable for simple academic cases dealing with cases where the crack propagation takes place in an opening mode. However, in real engineering problems, in practice, failure occurs in mixed mode and the use of these models is largely questionable. The problem is therefore to propose an approach that allows to guarantee the best compromise between the representation of the real behavior of the fatigue crack and the consideration of the different sources of uncertainty. From the point of view of the reliability specialist, uncertainty propagation through a mechanical model is the best alternative. Different sources of uncertainties exist, mainly associated with material properties, structure geometry and loading conditions. Uncertainties in these input parameters must be incorporated into the modeling of the crack propagation process in order to characterize their effects on the mechanical response and to provide a robust prediction of the service life.

To this end, the effect of uncertainties on the mechanical response is quantified using a mechano-probabilistic coupling strategy. This quantification can have three distinct objectives and purposes: (1) Evaluate the variability of the mechanical response by computing statistical moments and constructing the probability density; (2) Measure the contribution of the variability of each uncertain parameter on the variability of the mechanical response by a sensitivity analysis based on a variance decomposition; (3) Evaluate the probability of failure with respect to one or more failure scenarios by a reliability analysis.

Mathematically speaking, for the three purposes above, the treatment of the problem relies, possibly, on several multidimensional integral calculations. In fatigue cracking problems, where mechanical models are often available in an implicit and computationally expensive form, the evaluation of integrals is not trivial. With the exception of Monte-Carlo simulations (MCS), whose application is restricted to simple problems for which an explicit formulation of the mechanical model is available, few probabilistic methods are able to address all three purposes and, moreover, most of these methods are inefficient as the stochastic dimension increases. Thus, the proposal of an uncertainty propagation approach, covering the three purposes above, and using efficient multidimensional integral schemes and robust approximation of complex mechanical problems is at least relevant.

On this last aspect, which ultimately concerns the precise approximation of the response of an implicit model, promising methods of probabilistic calculation, based on response surfaces, substitution models or

meta-models, have been developed. Their common principle is simple; it consists in building an explicit representation of the original implicit mechanical model, by simulating the latter in a set of points called design of experiments. Once this explicit representation is obtained, the three purposes of the probabilistic calculation can be easily approximated by performing an MCS on it.

Considering the previous statement and arguments, computational approaches for addressing uncertainty propagation analysis through engineering problems are developed to satisfy the following objectives:

- To achieve methodological advances in the field of uncertainty propagation through mechanical models representing complex physical phenomena and with high probabilistic dimensionality. The combination of efficient cubature formulae and metamodeling techniques will be investigated.

- The computational approaches must be sufficiently generic, on the one hand, to solve a large class of engineering problems, particularly those dealing with fatigue crack growth, and on the other hand, to be able to handle all three kinds of uncertainty propagation analysis, namely statistical moments and distributions, sensitivity, and reliability analysis.

- The computational approaches must be efficient, even for problems with a high probabilistic dimension. Less than a few hundred evaluations of the primary mechanical model would be appreciated.

- To avoid additional computational cost when switching from one kind of uncertainty propagation analysis to another.

- The quantities of interest, i.e., statistical moments, probability distributions, sensitivity indices and probability of failure, can be straightforwardly derived.

To reach our objectives, step by step, we propose a manuscript structured in three chapters whose respective contents are detailed in what follows.

Chapter I is a bibliographic summary presenting the general notions of the fatigue phenomenon. In this chapter, a state of the art of the fatigue phenomenon, deterministic and probabilistic approaches to deal with uncertainties will be presented. We will first present the basics of fracture mechanics which are the basis of all the laws used for the phenomenon of fatigue, and then we will focus on understanding the fatigue crack growth phenomenon. In addition, fatigue crack growth models will be studied, and the predictions will be compared to experimental data from the literature. Stochastic models for fatigue crack propagation will also be presented, as deterministic approaches cannot be used especially due to the random nature of the fatigue phenomenon.

Chapter II will first introduce the general principles of uncertainty propagation analysis through physical models, to make the reader aware of the related mathematical framework. The focus will be on the mathematical formulations of the quantities of interest related to the three possible types of uncertainty

propagation analysis, namely statistical moments and distributions, sensitivity, and reliability analysis. After a presentation of classical methods of computing multidimensional integrals involved in uncertainty propagation analysis, and a critical review of their advantages and limitations, six efficient cubature formulae taken from the literature will be introduced. The ability of these to conduct uncertainty propagation analysis will be evaluated on the basis of various academic and engineering problems ranging from a simple mathematical explicit model to a computationally demanding implicit model with high probabilistic dimensionality. The analysis of the advantages and disadvantages of each of these cubature formulae will allow us to orient our choice towards a class of method based on the concept of polynomial chaos.

Chapter III will introduce the well-established metamodeling technique named Polynomial Chaos Expansion (PCE) that emerged in the earlier 90's to conducted uncertainty propagation analysis through mechanical models. It consists in representing the random responses due to uncertainty on the input parameters of a mechanical model, as a series expansion on a multivariate polynomial basis, called metamodel. The mathematical formalism related to the construction of PCE-based metamodels will be recalled. Special emphasis will be put on the computation of the unknown PCE coefficients, using projection and regression techniques. The number of the PCE coefficients increases with the probabilistic dimensionality of the mechanical model and the degree of the PCE used to ensure the accuracy of the metamodels, resulting in a computational effort that is impossible to achieve using conventional approaches such as Monte-Carlo Simulation and full tensor-product integration schemes for the estimation of the PCE coefficients. To circumvent this problem, two strategies of constructing PCE-based metamodels will be introduced. The first one, which is a part of the projection techniques, aims to reduce the number of evaluations of the mechanical model involved in the computation of the multidimensional integrals defining the PCE coefficient. The second one, which is a part of the regression techniques, aims to use smart truncation schemes favoring the PCE components with the largest contributions on the variability of the model responses of interest, thus reducing the number of PCE coefficients and the computational cost required to their estimates. Then, the derivation of the quantities of interest, corresponding to moments and distribution, sensitivity reliability analysis, based on post-processing the PCE coefficients will be presented. Lastly Chapter III will address a panel of fatigue crack growth problems with different levels of complexity to show the potential of the proposed approaches to efficiently conduct the three kinds of uncertainty propagation analysis. An example application with correlated uncertain parameters will be studied. A second example will deal with fracture in ductile material, where the crack driving forces of interest are obtained from a computational cost demanding incremental finite element analysis. The third application example will deal with a large number of uncertain parameters resulting from the representation of random field of spatially varying material properties.

Chapter I: State of art on probabilistic modelling of fatigue crack propagation

1. Introduction

Fatigue of material, defined as the alteration of the mechanical properties under the effect of a cyclic load, has been identified as a major technical problem, leading to the failure of structures and mechanical components. The embrittlement of the material, particularly in the vicinity of the stress concentration zones, leads to the initiation of cracks which propagate under the effect of the loading until the sudden rupture of the material or the failure. The fatigue life, measured in terms of number of cycles loading, is the sum of the time necessary for the appearance of a macroscopic crack in the material, and of the time taken to propagate the crack until it reaches a critical size for which the component can no longer perform its service function. In most cases, the fatigue life is represented only by the duration of the propagation phase, which is estimated by integrating empirical models representing the evolution of the size of the crack to the number of cycles. These models are mainly deterministic and therefore unable to describe the stochastic character of the crack growth, which is induced by the uncertainties such as the mechanical properties of the materials, the loading, and the geometry of the structure. Indeed, different sources of dispersion must be taken into consideration in each situation to describe the real situation of the structures. If these uncertainties are not taken into account, this leads to an under dimensioning of the structure thus a higher risk of failure and therefore a much higher repair cost. To overcome this problem, stochastic models have been developed; these models have been the target of several criticisms because they are purely statistical and thus unable to describe complex phenomena such as mixed-mode propagation or crack growth retardation under the effect of overloads. Thus, the main objective of this thesis is to develop a probabilistic approach capable both of modeling the physical phenomena associated with the fatigue crack propagation process while considering its stochastic character. More precisely, the main objective is to solve problems with high stochastic dimensions (consider a high number of uncertainties) in application dealing with fatigue crack growth. Thus, an efficient uncertainty propagation approach will be presented, taking into account the unstable crack growth rate and enhancing the fatigue crack growth mechanical model using finite element model, to better represent the statistical dependence between uncertain parameters.

In order to highlight the various scientific obstacles related to the subject of the thesis, we start the bibliographical review by the presentation of the fatigue phenomenon, followed by a description of the approaches of fatigue life prediction, and develop the one based on the fracture mechanics. We will then present the basics of fracture mechanics which are the basis of all the laws used for the phenomenon of fatigue, then focus on understanding the fatigue crack growth phenomenon. Moreover, this chapter will present the interaction between the notion of dispersion and fatigue failure. Finally, a particular attention will be given to the crack propagation since it constitutes a major part of the structure life. Thus probabilistic model of fatigue crack propagation were presented because deterministic approaches cannot be used especially with the random nature of the fatigue phenomenon and if we take in consideration the effect of retardation induced by the application of an overload due to the randomness of loading.

2. Fatigue phenomenon

2.1. Basic concepts and physical aspects

Since the 19th century, the fatigue of materials *(Sobczyk and al, 1992)* was identified as a major technical problem leading to the failure of structures and mechanical components. Indeed, in most engineering structures, fatigue failure is widely observed *(Ahmadzadeh and al, 2019), (Mareau and al, 2019), (Kamal and al, 2018).* For instance, a classification study *(Schütz, 1996)* of the failure modes in military aircrafts has shown that failures induced by fatigue of materials are the most observed. Between 80% and 90% of total failures were attributed to the fatigue of materials. A material is subjected to fatigue loading when the loading applied to it varies with time and can modify its local properties until it reaches the failure of the structure. In general, one or more tiny cracks start in the material, and these grow until complete failure occurs. These cracks can be originally existent in the structure from manufacturing, or they can start early in the service life. Thus, the phenomenon of fatigue can be described as the progressive damage of a structure subjected to cyclic stresses.

Prevention of fatigue fracture is a vital aspect for structures subjected to cyclic loading, hence the analysis of fatigue crack growth is used to schedule inspection and repair. The multiplication of serious incidents with a significant number of victims especially in the field of rail transport led scientists in the mid-19th century to focus on the phenomenon of fatigue cracking. One of the most popular examples of a disaster due to fatigue failure and known as the origin of the studies of the fatigue phenomenon, is the Meudon rail accident in 1842 (figure I.1). The cause of the accident was the rupture of one of the axes of the damaged locomotive.

Figure I. 1. Illustration of the Meudon disaster from 1842 (Wikipedia)

Another accident was the failure of the fuselage of a passenger jet in 1988 (figure I.2). The problem started with fatigue cracks at rivet holes in the aluminum structure. These cracks progressively propagated during the use of the airplane, creating a large crack that caused the failure of the structure. These examples show the necessity to predict its service life to guarantee the reliability of a structure, considering that it may contain defects, such as fatigue cracks.

Figure I. 2. Fuselage failure in a passenger jet that occurred in 1988 (NASA TECHNOLOGY)

From a physical point of view, we can define the fatigue as the alteration of the mechanical properties of the material subjected to repeated loading. Consequently, weakness points or micro cracks appear in the material from which a macro crack propagates if cycle load continues until a brutal collapse of the structure. Figure I.3 shows fracture surfaces of fatigue failure and the final fracture observed of an automotive steel component *(Schijve, 2009)*.

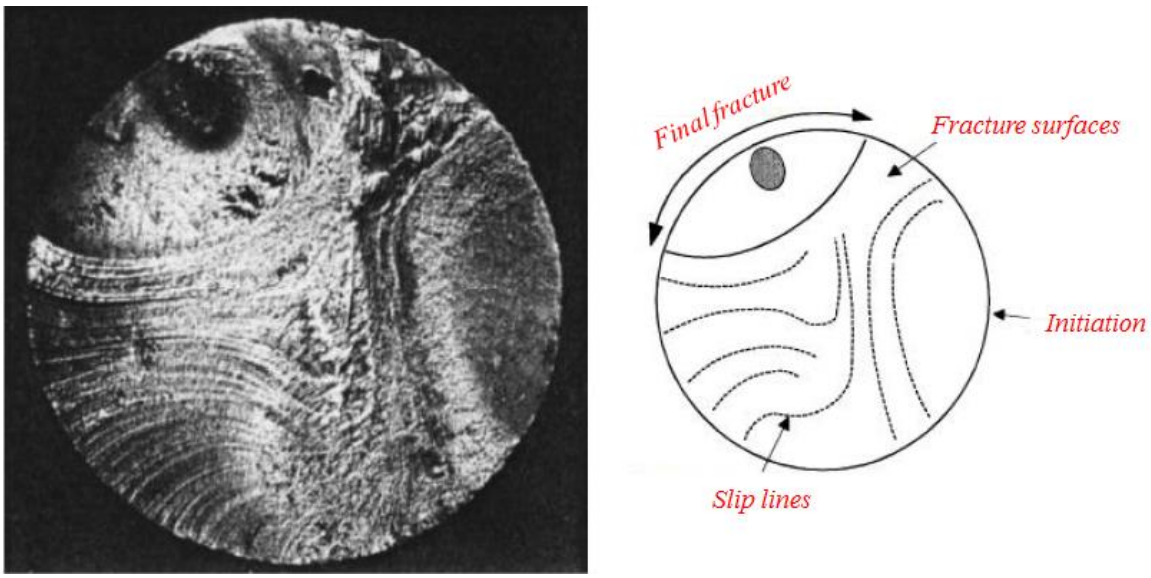

Figure I. 3. Fatigue fractography of automotive steel component (Schijve, 2009)

Experiences have shown that fatigue failures can be usually divided in three stages. First, a stage where micro-cracks start from the surface of components, which is called crack initiation stage. Then, follows a stage where these later (i.e. micro cracks) grow progressively while the cycling loading continues; this stage is called stable crack growth stage. Finally, when the remaining transversal section of the component is too small to support the applied load, a sudden breakdown is observed, which is called unstable crack growth stage. The fatigue lifetime is usually defined as the number of loading cycles leading to the failure. In every stage of the fatigue lifetime, complex physical phenomena can be observed. Furthermore, the respective fractions of these stages, towards the lifetime of the structure, can be significantly different. They mainly depend on the nature of the material and if this later contains initial defects or not *(Schijve, 2009*).

More precisely, the following factors will affect the fatigue lifetime: quality of material processing (size and distribution of inclusions, voids …), procedure of material processing (annealed, quenched, tempered…),

procedure of specimen manufactures (specimen shape, machining method), quality of specimen manufactures (scratch, surface condition), material properties (yield strength, ultimate strength, strain at failure, $\sigma - \varepsilon$ curve), geometry (length, width, thickness, transition radius,…), stress state (uniaxial, multiaxial, stress ratio), and effect of environment (temperature, corrosion, …).

Some laboratory tests conducted on smooth notched specimens have shown that when a macro-crack appears in the material, the remaining number of loading cycles to failure is very small, which means that the initiation stage is about 90% of the total fatigue lifetime. Otherwise, when the tested specimens contain sharp notch, the propagation stage is by far the most dominant and can reach 95% of the total fatigue lifetime. This later situation is usually observed in practice since engineering structures inevitably contain defects.

From an engineering point of view, the fatigue lifetime is reduced to only two stages: the crack initiation stage and the crack growth stage, since the unstable crack growth stage only takes few loading cycles, which can be neglected in the prediction of the fatigue lifetime. Figure I.4 depicts schematically the stages of the fatigue failure.

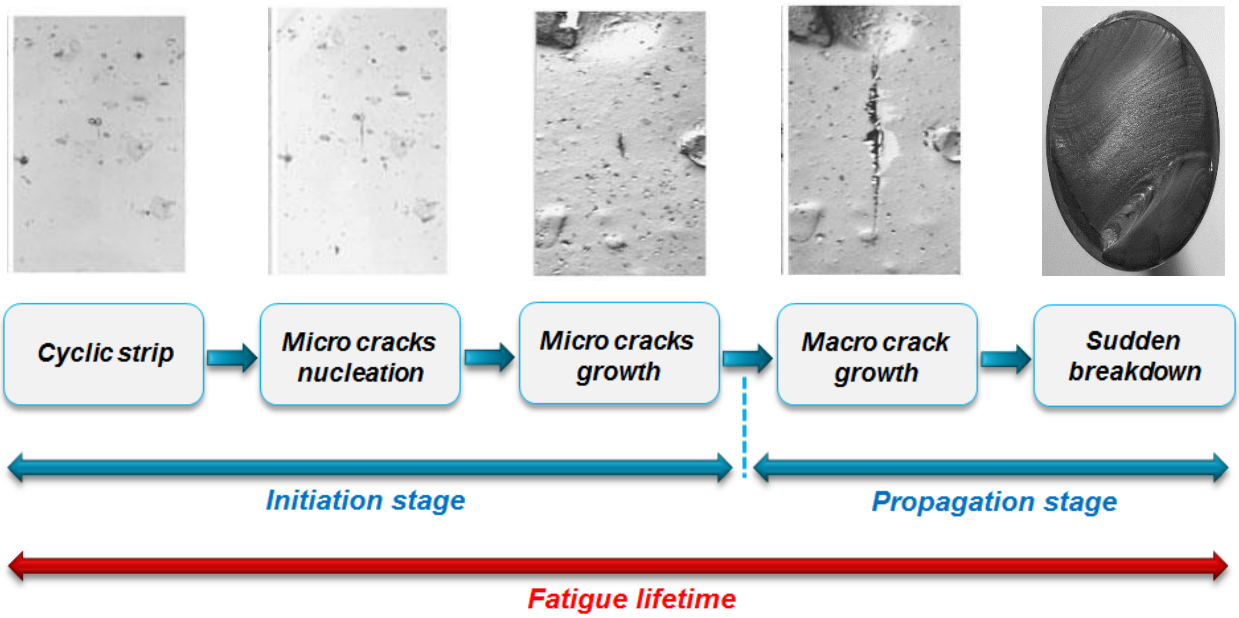

Figure I. 4. Stages of the Fatigue failure (After (Dowling, 2007))

It is worth mentioning that distinguishing the initiation and the propagation stages is of a great importance in the prediction of the fatigue lifetime, since each stage has its own influencing parameters. That is, some parameters which have significant effect on the initiation stage could have weak effects on the propagation stage, and vice versa. For instance, the material surface finishing or the material roughness affects only the initiation stage, while a corrosive environment affects proportionally the initiation and the propagation stages.

2.2. Fatigue design approaches

In engineering practices, the design of structures subjected to fatigue is performed with respect to a safe target fatigue lifetime which depends on the consequence of the failure. Many research works have been conducted from different perspectives in terms of fatigue life prediction such as (*Zhang and al, 2019), (Ai and al, 2019)* and (Liu and al, 2020) who developed fatigue life prediction methods for engineering components based on the principle of surface fatigue abrasion theory. The definition of this target fatigue lifetime is not a trivial task and,

in this context, three design concepts can be used. The first one is called Safe-Life concept, where the design is performed under limited fatigue lifetime assumption. In other words, it is supposed that the fatigue lifetime is defined as the duration of the initiation stage, which means that the structure can reach safely the retirement without observing fatigue failure. This concept is mainly used in automotive industry and the safe fatigue lifetime is defined as the weighting of a target fatigue lifetime (i.e. usually the mean fatigue lifetime) by a safety coefficient. The second one, called Fail-Safe concept, is very used in the aeronautic industry. It assumes that defects can be tolerated without affecting the structural integrity i.e. the failure does not occur before a critical crack is detected and repaired, which consequently supposes that periodic inspections are scheduled over the lifetime of the structure. The third one, called Damage Tolerance concept, has the same backbone as of the Fail-Safe, but it is based on fracture mechanics. The safe fatigue lifetime is defined as the number of loading cycles able to grow the crack until a critical length. This concept is mainly applied for high toughness materials where the crack growth is supposed to be slow. The difference between these concepts is the consequence of the different criteria required in the fatigue design. Indeed, according to each type of structure and according to its field of application, criteria are dictated by the loading applied, the types of materials. Therefore, the choice of one concept or another must take these parameters into consideration. In this thesis the Damage Tolerance concept was applied, indeed, for critical structures, in order to guarantee a high level of reliability, this concept seems best suited. However, for purely economic reasons the structures in reality are designed for a Safe-Life concept. In practical engineering, fatigue fracture of the structure may cause enormous economic losses and disastrous accidents, for that the Damage Tolerance concept and life prediction approach are important for a safe life design and reliability assessment *(Li and al, 2018), (Zheng and al, 2020), (Song and al, 2020)*.

The fatigue design methods are based on the calculation of the service life. However, each design method from the previous paragraph, takes into consideration one of the two periods (initiation period or propagation period) which constitute the fatigue damage process. Thus, there are a variety of approaches to predict the fatigue life. These approaches are based on a relationship between a load-related parameter such as stress/strain amplitude or stress intensity factors (SIF) magnitude ΔK (described later in section 3.1), and fatigue life N in terms of number of cycles. In general, three major approaches can be distinguished for the prediction of the fatigue life of the structure: the approach based on the Wöhler curve (i.e. $S-N$ curve), the approach based on local deformation and the approach based on the theory of fracture mechanics.

2.2.1. Approach based on the Wöhler curve

This approach is widely used in the design of structures likely to be subjected to fatigue damage during their lifetime. The particularity of this approach relies on its simple formulation which gives a relation between the number of cycles N and the variation of the nominal stress $\Delta\sigma$ or the stress amplitude defined as the difference between the maximum stress value and the minimum stress value divided by two ($\sigma_a = (\sigma_{min} - \sigma_{max})/2$).

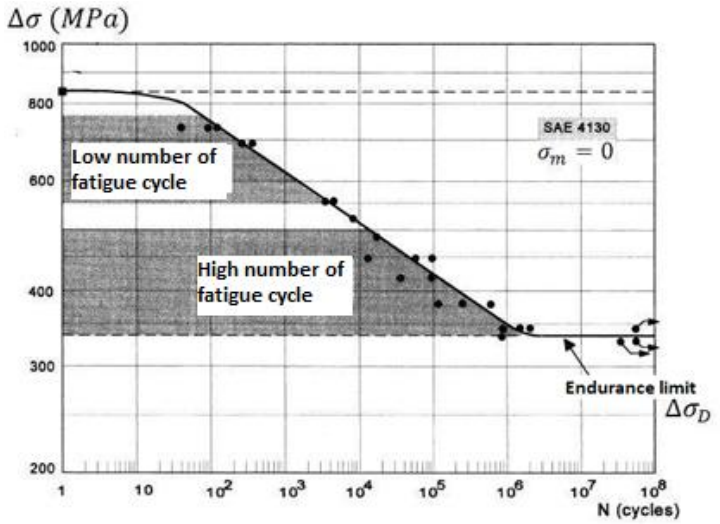

Figure I. 5. Wöhler curve for a low alloy steel SAE 4130 (Schijve, 2009)

This relationship is known as the Wöhler curve or $S-N$ curve, mathematically written (*Eurocode 3, 1996)*:

$$\Delta\sigma = max\left[\left(\frac{N}{C_{SN}}\right)^{-\frac{1}{m_{SN}}};\ \Delta\sigma_D\right] \qquad (I.1a)$$

Or in logarithmic form

$$\log\Delta\sigma = max\left[-\frac{1}{m_{SN}}\log N + \frac{C_{SN}}{m_{SN}};\log\Delta\sigma_D\right] \qquad (I.1b)$$

where C_{SN} is a constant of the Wöhler curve, $1/m_{SN}$ is the slope of the Wöhler curve and $\Delta\sigma_D$ is the endurance limit of the material which is defined as the horizontal asymptote of the Wöhler curve.

This curve distinguishes two parts:

- The first for low number of fatigue cycles, or oligo-cyclic fatigue, characterized by severe loads and which corresponds to materials with non-negligible plasticity.
- The second for high number of fatigue cycles, or polycyclic fatigue, where material behavior is characterized by zero macroscopic plasticity.

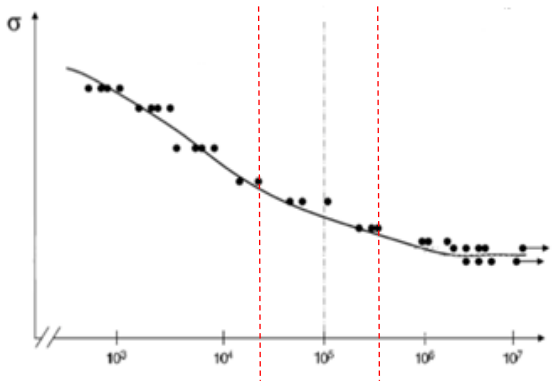

Figure I. 6. Representation of the Wöhler diagram and the domain of interest (Schijve, 2009)

If the number of repetitions (cycles) of the load is large, say, millions, then the situation is termed high-cycle fatigue. It is associated with relatively small deformations that are primarily elastic. On the contrary, low-cycle

fatigue is caused by a relatively small number of cycles, say, tens, hundreds, or thousands. Low-cycle fatigue is generally accompanied by significant amounts of plastic deformation. The transition between the two areas depends on the material under stress. It generally occurs around 10^5 cycles as shown in figure I.5 *(Schijve, 2009)*. Let us recall in our thesis that we will be interested in the intermediate zone, as shown in the figure I.6. Since we are not interested in the total lifetime but only in the propagation phase, we have to remove the number of cycles required for the initiation phase, thus we will have a moderate number of cycles.

The fatigue life expressed in term of number of cycles N to failure can be determined directly from the Wöhler curve and calculated from equations (I.1a) or (I.1b) if we have a constant amplitude loading $\Delta\sigma$. In the case of variable amplitude loading, the equations (I.1a) or (I.1b) cannot be used, thus the evaluation of the fatigue life requires the application of a whole procedure which consists first in representing the sequence of the applied loading in the form of an histogram by means of a cycle counting method such as the Rainflow method, then to calculate the damage induced by this loading history using a damage accumulation law such as Miner's law and in a last step to determine the number of histograms needed to reach the failure. Indeed, over the past decades, the fatigue damage accumulation rule and life prediction approach were investigated to prevent disastrous accidents of fatigue failure (Wang and al, 2021), (Gao and al, 2020), (Li and al, 2019). Thus, the fatigue life is deduced by converting the number of histograms into the number of loading cycles. However, the Wöhler curve approach is criticized for its conservatism in fatigue life prediction and because it does not consider the interaction effect noticed in the case of loads with variable amplitudes.

2.2.2. Approach based on local deformation

Local deformation is used to predict the fatigue life of structural components with notches. It is based on the concept of the $\varepsilon - N$ curve which relates the local deformation ε to the number of loading cycles N required to initiate a crack. This approach studies the plastic deformation that may arise in confined areas where fatigue cracks initiate. Thus, this method takes into consideration fatigue situations where local yielding is involved, which is often the case for ductile metals for short lives. The major difference with the $S - N$ curve, concerns the consideration of plasticity. This approach can only be used to predict the duration of the initiation period, similarly to the case of the $S - N$ curve where the propagation time of the fatigue tests is negligible.

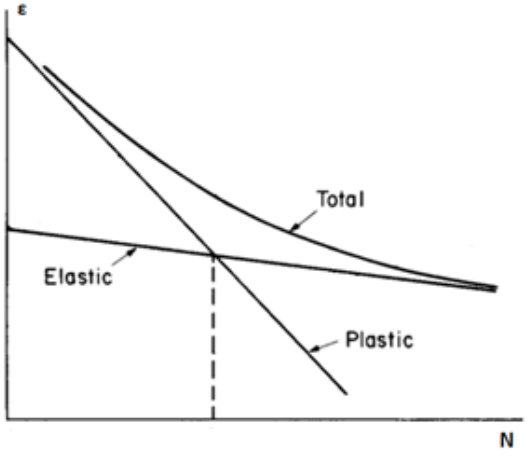

Figure I. 7. Elastic, plastic, and total strain versus life curves (Landgraf, 1970)

A wide variety of relationships between the parameters ε and N are available in the literature *(Basquin, 1910), (Coffin, 1954), (Manson, 1954)*.

The total strain amplitude can be divided into elastic and plastic parts (figure I.7):

$$\Delta\varepsilon = \Delta\varepsilon_{el} + \Delta\varepsilon_{pl} \quad (I.2)$$

where the elastic strain amplitude is related to the stress amplitude based on Hooke law:

$$\Delta\varepsilon_{el} = E\Delta\sigma \quad (I.3)$$

where *E* is the Young elastic modulus.

And the plastic strain amplitude is a measure of the half-width of the stress–strain hysteresis loop given by *(Coffin, 1954), (Manson, 1954)* as:

$$\frac{\Delta\varepsilon_{pl}}{2} = \varepsilon_f'(2N)^c \quad (I.4)$$

where ε_f' is the fatigue ductility coefficient and *c* is a constant of order -0.5.

Thus, based on Hooke law (i.e., $\Delta\varepsilon_{el} = E\Delta\sigma$), where the variation of the nominal stress $\Delta\sigma$ is derived from the Wöhler curve (i.e. $\frac{\Delta\sigma}{2} = \sigma_f'(2N)^b$), the variation of the total strain $\Delta\varepsilon$ is now given by:

$$\frac{\Delta\varepsilon}{2} = \frac{\sigma_f'}{E}(2N)^b + \varepsilon_f'(2N)^c \quad (I.5)$$

where σ_f' is the fatigue strength coefficient, *b* is a constant defining the slope on a log ε –log N plot and E is the Young modulus. Thus, fatigue with a low number of cycles and fatigue with a high number of cycles can be describes using the equation (I.5).

The application of the approach based on the local $\varepsilon - N$ curve is not feasible for the propagation stage. Indeed, when the crack propagates, the strain field at the crack tip changes constantly, which makes the calculation of the $\Delta\varepsilon$ extremely complicated. In the case of a loading at constant amplitude, the fatigue life can be obtained directly from the $\varepsilon - N$ curve or by using one of the relations of the literature. However, in the case of variable amplitude loading, a three-step procedure steps, similar to that adopted in the approach based on the Wöhler curve, should be used. The specificity of the $\varepsilon - N$ approach is that it is based on a simple formulation and provides an estimate of the initiation period, while taking into account a number of parameters considered to influence the fatigue life such as the mean stress. A similarity between the $S - N$ and $\varepsilon - N$ approaches is that none of them take in consideration the analysis of the crack growth, as in the fracture mechanics approach discussed in section 1.2.3.

2.2.3. Approach based on damage tolerance

This approach is based on the fracture mechanics. This concept is based on the idea of tolerating the presence of cracks without having a catastrophic consequences on the integrity of the structure. The approach is assumed that all material contains crack type defects which may be preexisting in the material or formed during service life. Here, the fatigue life is defined as the loading time capable of propagating these cracks, up to a critical length. Generally, this critical value is determined from the toughness of the material and the service life is calculated based on the linear elastic mechanics of fracture. This approach is applicable for the propagation period

and is founded on a relationship between the crack length and the number of loading cycles by using the stress intensity factor SIF ΔK (influenced by the loading and the geometry conditions).

The fatigue life is obtained directly by integrating:

$$N = \int_{a_0}^{a_c} f\,[\Delta K(\Delta\sigma, a)]da \qquad (I.6)$$

where a is the crack length, a_0 and a_c are respectively the initial crack length and the critical crack length, N is the number of loading cycles, ΔK is the variation of the stress intensity factor and $\Delta\sigma$ is the variation of the applied loading.

This approach is very helpful to estimate the residual life following an inspection of structures because the fatigue life is linked to a measurable parameter (i.e. the length of the crack). The parameter ΔK depends on the loading, on the crack length and on its orientation. In practical problems, its explicit formulation is not always available, and the use of a finite element model is suggested. However, the evaluation of the integral defined by equation (I.6) is difficult and can only be done numerically. Despite this difficulty, the use of SIF provides great flexibility to the fracture mechanics approach. Its application in the case of loadings with variable amplitude does not require great efforts in the formulation. In addition, it considers the interaction effect as well as the non-linear aspect of the fatigue cracks propagation.

The use of either of these approaches described previously for fatigue life prediction depends on the design strategy adopted, which depends on the type of the domain of application. The approach based on fracture mechanics concepts is very useful in practical cases where the propagation period constitutes a major part of the fatigue life. For this reason, in this work we are interested in the study of the propagation period and thus in the fracture mechanics approach to fatigue life prediction.

3. Deterministic fatigue crack growth

As already mentioned, fracture is the propagation of a macro crack as a consequence of damage. It is characterized by the irreversible separation of a continuous medium into two parts on either side of an interface. This separation is called crack and changes the fields of the displacement, deformation and stress (figure I.8).

Figure I. 8. Separation of a medium on either side of an interface and the local reference frame attached to the fracture tip

Fracture mechanic is introduced because classical mechanical approaches are not able to study the mechanical behavior of cracked bodies due to their inability to consider the very high and plastic strains at the vicinity of the crack tip.

To describe the fracture of the material new stress measurements are introduced, which are called fracture driving forces. When plastic strains are confined in the vicinity of the crack tip, these fracture driving forces are called Stress Intensity Factors (SIF) as proposed by *(Irwin, 1957)*. These factors aim to quantify the intensity of the stress singularity. For static loading, they are used to determine the intensity of the singularity in terms of both stress and displacement.

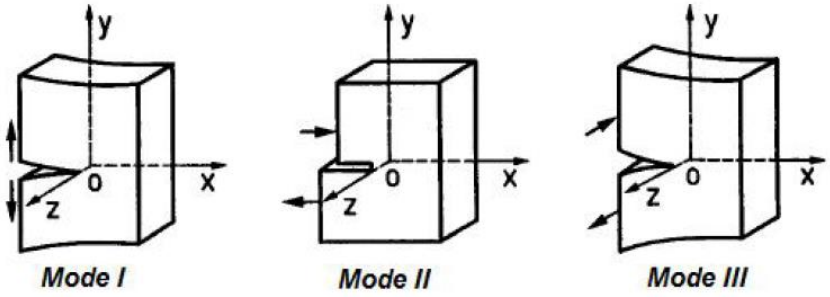

Figure I. 9. Fracture modes

As depicted in figure I.9, three fracture modes can be distinguished in the case of 3D problems: the opening mode (mode I) for loadings applied following y, the in-plane shear mode (mode II) following x and the out-of-plane shear mode (mode III) following z. Consequently, three SIF K_I, K_{II} and K_{III} are to be computed. Each one of them corresponds to one fracture mode. Despite that modes II and III are generally less dangerous than mode I which is responsible for crack growth, we will study the real case on our work. In real-life problems the displacements of the crack edges are often a combination of these three fracture modes- mixed mode- and the cracks follow a curved paths during their propagation. Many methods are proposed in the literature to compute the SIF of fracture bodies. The most used are the energetic method and the kinematic method.

3.1. Computation of stress intensity factor

To measure the SIF, it is possible to use global approach based on the energy dissipated or local approach based on the kinematic method.

3.1.1. Energetic method

It is the divergence of the stress field at the crack tip that motivated *(Griffith, 1921)* to introduce an energetic approach to the fracture mechanics. His approach is based on the computation of the strain energy release rate G. It is defined as the amount of energy able to create new crack surfaces. The crack grows by a new increment da as shown in figure I.10.

From the thermodynamic equilibrium equation of the structure and its crack a, the conservation of the total energy dW_{tot} is written as following:

$$dW_{tot} = dW_{ela} + dW_{cin} + dW_{ext} + dW_{dis} \qquad (I.7)$$

where dW_{ela} is the variation of the elastic deformation energy, dW_{cin} is the variation of the kinetic energy, the dW_{ext} is the variation of the potential energy of the external forces and dW_{dis} is the energy dissipated during the separation of the two lips of the crack, with $dW_{dis} = 2\gamma da$ where γ is the surface energy of decohesion.

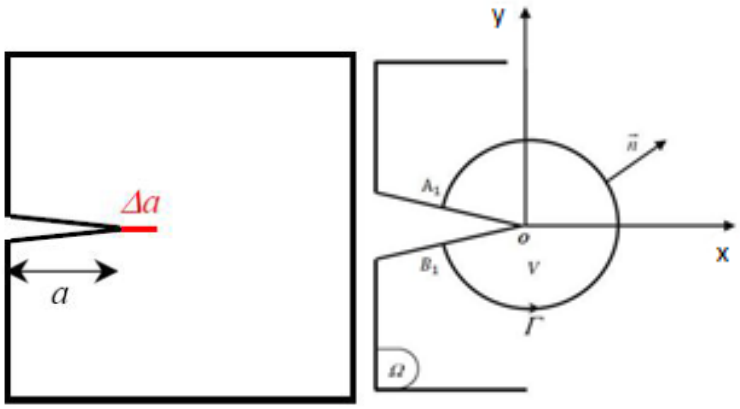

Figure I. 10. Crack growth increment (left), Integration path around the crack tip (right)

The variation of the energy which accompanies the growth of the crack of an increment da is written as follows:

$$dE_p = dW_{ela} + dW_{ext} \tag{I.8}$$

The behavior of cracks is thus characterized by the transfer of the potential energy E_p of the structure into decohesion energy in the vicinity of the tip.

$$G = -\frac{dE_p}{da} \tag{I.9}$$

If $dW_{cin} > 0$ then $G > 2\gamma$ which results in an unstable crack propagation. Indeed, the surface decohesion energy $dW_{dis} = 2\gamma da$ is used to break the molecular bonds in the material and the excess then $(G - 2\gamma)da$ is transformed into kinetic energy which induces an unstable propagation of the crack.

The strain energy release rate can also be directly linked to the stress intensity factors K_I, K_{II} andK_{III}, as follow:

$$G = \frac{K_I^2 + K_{II}^2}{E'} + \frac{K_{III}^2}{2\mu} \tag{I.10}$$

where $E' = E$ for plane stress and $E' = E/(1 - \nu^2)$ for plane strain, E and μ are the Young's and shear modulus of the material and ν is the Poisson's ratio.

The integrals of contour are tools which make it possible to characterize the singularity of the stress field in the vicinity of the point of the crack. These tools are obtained by a development based on the conservation of energy. They have the particularity of being equivalent to the strain energy release rate G and they are independent of the integration contour. Indeed, the strain energy release rate can be computed using independent integrals introduced by *(Rice, 1968).*

The J – integral (see equation I.11) is defined as the result of a path contour integral around the crack tip. The J – integral has been adapted to evaluate the strain energy release rate for nonlinear materials. The behavior of the material is considered to be non-linear elastic. In fact, Rice's idea is to consider the material not as elasto-plastic but as nonlinear elastic. He considered that the cause of the energy dissipation is not only the separation of the crack lips as in the elastic case but also in the phenomenon of plasticity. As we can see in figure I. 11, both types of behavior are identical if we do not apply a discharge.

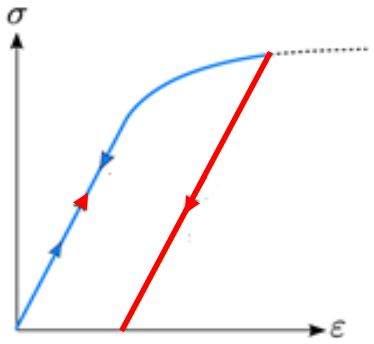

Figure I. 11. Tensile curve of a nonlinear elastic material (blue curve) and an elasto-plastic material (red curve)

Let us consider a two-dimensional cracked body Ω and Γ (shown in figure I.10) a path which surrounds the crack tip oriented by the normal $\vec{n}$ of component n_j. Based on this approach, the strain energy release rate can be expressed:

$$G = J = \int_{\Gamma} \left[w_e . \delta_{ij} - \sigma_{ij} . \frac{\partial u_i}{\partial x} \right] . n_j \, d\Gamma = \left[w_e . n_i - n_j . \sigma_{ij} . \frac{\partial u_i}{\partial x} \right] d\Gamma \qquad (I.11)$$

where $w_e = \int_{\varepsilon} \sigma_{ij} . d\varepsilon_{ij}$ is the strain energy density, δ_{ij} the crack opening displacement define as the total separation distance between the upper and lower crack surfaces at the tip due to the singularity, and, σ_{ij} and u_i are the stress and the displacement fields respectively.

Hence, the $J-$ integral expression remains valid and independent of the path Γ if there is no discharge. When the crack propagates the non-discharge hypothesis is not verified behind the tip. However, this hypothesis remains reasonable, but the path independence is not guaranteed.

The strain energy release rate alone constitutes a criterion of crack propagation but does not allow the determination of the direction of the crack propagation. To determine the direction of propagation, more information is needed, and the crack loading can provide this information through the SIF, for example.

3.1.2. Kinematic method

This approach *(Zhang, 1992)* aims to compute the SIF based on the relative displacement of the crack surfaces as depicted in figure I.12. Here, the SIF are proportional to the displacements u_x and u_y of the crack surfaces.

For a two-dimensional problem the SIF K_I and K_{II}, corresponding to the opening and the in-plane shear fracture modes respectively, can be written:

$$K_I = \frac{2\mu}{\kappa + 1} . \sqrt{\frac{2\pi}{r}} . [u_y] \qquad (I.12)$$

$$K_{II} = \frac{2\mu}{\kappa + 1} . \sqrt{\frac{2\pi}{r}} . [u_x] \qquad (I.13)$$

where $\kappa = 3 - 4\nu$ for plane strain and $\kappa = (3 - \nu)/(1 + \nu)$ for plane stress; and $\mu = E/2(1 + \nu)$ for an isotropic material.

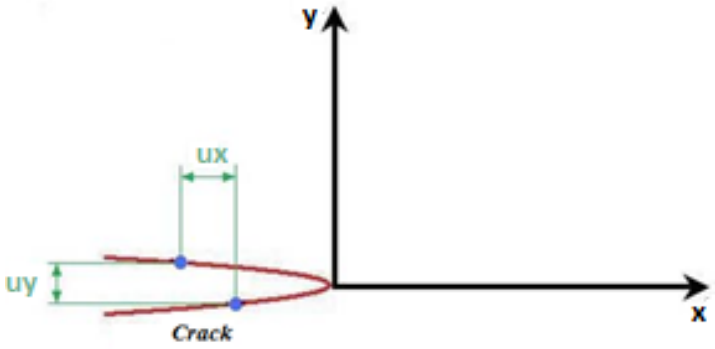

Figure I. 12. Displacements of the crack edges

This approach is very simple to be implemented in numerical solver, but its accuracy is closely related to the number of points used to interpolate the displacement field; the more interpolation points we use, the greater the precision we have. Hence, in the case of the finite elements method, this approach is not suitable since the obtained model can be time consuming.

3.1.3. Comparative study

In order to compare the two methods of computation of SIF discussed above, and to choose which one of these two calculation methods is the best and therefore the most adequate to use in the following developments, we propose to confront them on an example.

Let us consider a Compact Tension (CT) specimen which is usually used in fatigue crack growth testing. It is subjected to tension loading $\Delta P = 2.5\ kips$ in the top and the bottom pins. The required geometry parameters are given in figure I.13. For this simple geometry and loading conditions, an analytical solution *(Tada and al, 1973)* is available for the SIF K_I associated to the opening fracture mode:

$$K_I = \frac{\Delta P}{B\sqrt{w}} \frac{2+(\frac{a}{w})}{(1-(\frac{a}{w}))^{3/2}} \left[0.886 + 4.64\left(\frac{a}{w}\right) - 13.32\left(\frac{a}{w}\right)^2 + 14.72\left(\frac{a}{w}\right)^3 - 5.6\left(\frac{a}{w}\right)^4\right] \qquad (I.14)$$

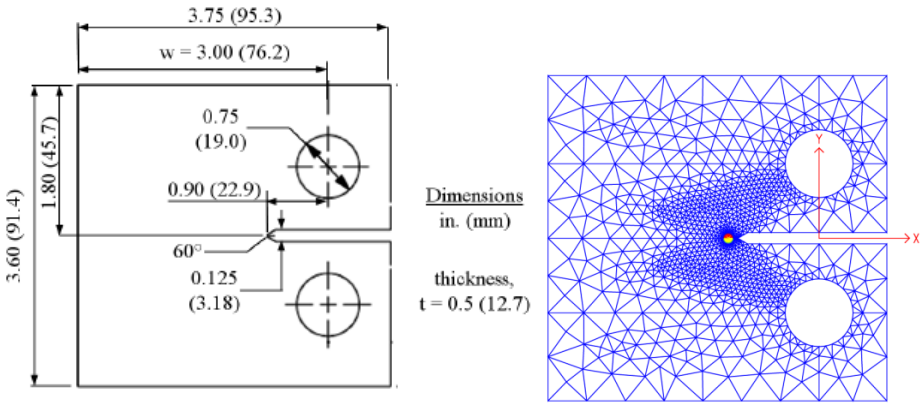

Figure I. 13. CT specimen, geometry and dimensions (left), finite elements mesh (right)

A finite elements model is developed in the software cast3m *(CASTEM, 1997)* to evaluate the accuracy of the energetic and the kinematic methods for the computation of the SIF. The analysis was performed under plane stress hypothesis and quadratic elements are used to mesh the CT specimen. In order to have good accuracy on the estimates of the fracture parameters, a refined structured mesh is adopted in the vicinity of the crack tip, as

shown in figure I.13. Figure I.14 shows the deformed mesh and the Von-Mises equivalent stress induced by the applied load to the CT specimen. As it can be seen, linear elastic fracture behavior hypothesis is verified since the yielding (i.e., plastic strain) zone is confined at the crack tip. In addition, based on the deformed shape of the crack edges, it is clear that the crack propagates in opening fracture mode.

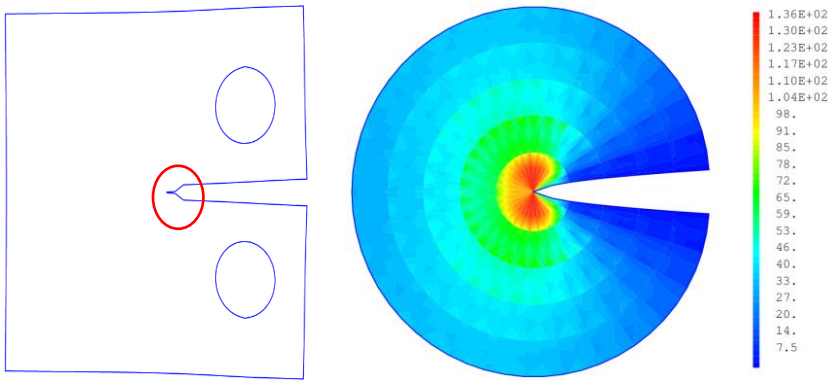

Figure I. 14. CT specimen, deformed mesh (left), Von-Mises equivalent stress (right)

Table I.1 compares the numerical estimates of the SIF K_I given by the energetic and the kinematic methods, with the analytical reference solution given by equations (I.14). As stated before, the accuracy of the energetic method is less sensitive to the integration path, defined as the number of layers of finite elements around the crack tip used in the evaluation of the integral (I.9). The accuracy of the kinematic method is dependent on mesh refinement level around the crack tip. Indeed, smaller is the mesh size, better is the accuracy on the estimates of the stress intensity factor K_I. As it can be seen, both methods give accurate results since the relative error does not exceed 0.9 % for the worst case. But the energetic method is more accurate than the kinematic method because the error is smaller. Thus, we will choose the energetic method in the following studies.

Table I. 1. Accuracy analysis of the numerical results obtained by the energetic and kinematic methods

Analytical K_I	Energetic method			Kinematic method		
	Integration path	K_I	$\|Error\|$ (%)	Mesh size	K_I	$\|Error\|$ (%)
17.755	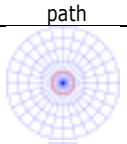	17.659	0.541	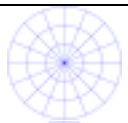	17.914	0.895
		17.682	0.415		17.875	0.677
		17.685	0.396		17.850	0.535
		17.686	0.391		17.832	0.434

3.2. Crack bifurcation criteria

In the case of crack propagation in pure mode (modes I, II or III) separately, the failure occurs when the value of the SIF reaches a critical value representing an intrinsic characteristic of the material and the direction of propagation is perpendicular to the direction of the applied load. This scenario is rarely encountered in practice,

where the cracks, influenced by the geometric conditions and by the loading, tend to propagate in mixed mode. In other words, the cracks follow curved paths during their propagation. Consequently, it is necessary to determine the condition of initiation of the failure and the direction taken by the crack within each increment during its propagation. To simulate the crack propagation based on fracture mechanics, it is necessary to select a bifurcation criteria to define the direction of the crack when propagating under mixed mode loading, depending on the loading conditions and the type of fractures.

In order to define the bifurcation angle of the crack during propagation, there exist mainly three criteria: the maximum circumferential stress, the maximum energy release rate and the maximum strain energy density.

3.2.1. Maximum circumferential stress

The crack path can be simulated based on the criterion proposed initially by *(Erdogan and al, 1963)*. They proposed a simple and intuitive criterion based on the maximum circumferential stress known also as the tangential stress σ_θ *(Chang and al, 2006).* This stress serves to resist to the applied internal pressure overflow and can be most conveniently treated by considering the equilibrium of the structure. This stress is the force exerted perpendicularly to the axis and radius of the structure in both directions. This criterion postulates that the crack tends to propagate in the direction that maximizes the mode I; thus, a crack propagates in the direction where the tangential stress ahead of the crack tip is maximum, as shown in figure I.15.

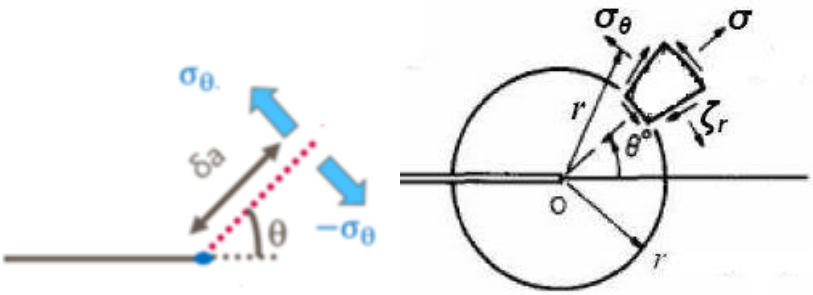

Figure I. 15. Principle of the maximum tangential stress and description of the region near the crack tip.

It is established on the idea that crack propagation occurs in the plane of maximum normal stress. Thus, in the polar system (r,θ), the propagation is in the direction θ_0 for which σ_θ is maximum at fixed radius.

The components of the stress field can be expressed in the polar system (r,θ) by:

$$\sigma_{rr} = \frac{2}{\sqrt{2\pi r}}\left[K_I(3-cos\theta)cos\frac{\theta}{2} + K_{II}(3cos\theta - 1)sin\frac{\theta}{2}\right] \qquad (I.15a)$$

$$\sigma_{\theta\theta} = \frac{2}{\sqrt{2\pi r}}\left[K_I(1+cos\theta)cos\frac{\theta}{2} - 3K_{II}sin\theta\, cos\frac{\theta}{2}\right] \qquad (I.15b)$$

$$\tau_{r\theta} = \frac{2}{\sqrt{2\pi r}}\left[K_I sin\theta\, cos\frac{\theta}{2} + K_{II}(3cos\theta - 1)\, cos\frac{\theta}{2}\right] \qquad (I.15c)$$

Thus, in mode I and II, to obtain θ_0 the location of the maximum stress, we should resolve:

$$\frac{\partial\sigma_\theta}{\partial\theta} = 0\ and\ \frac{\partial^2\sigma_\theta}{\partial\theta^2} < 0 \qquad (I.16)$$

Based on the maximization of σ_θ with respect to the crack orientation angle θ, the bifurcation angle θ_0 is solution of the following equation:

$$tan\left(\frac{\theta_0}{2}\right) = \frac{1}{4}\left(\frac{K_I}{K_{II}}\right) \pm \frac{1}{4}\sqrt{\left(\frac{K_I}{K_{II}}\right)^2 + 8} \qquad (I.17)$$

If the maximum circumferential stress is a principal stress, the shear stress $\sigma_{r\theta}$ will be zero. Therefore, θ_0 can also be considered as the solution of the equation $\sigma_{r\theta}(\theta_0) = 0$.

Some authors have shown a good consistence with this criterion *(Gdoutos, 1984), (Chambers and al, 1991),* however, some others have found this criterion to be insufficient *(Smith and al, 1985), (Royer, 1986), (Hourlier and al, 1978)*. However, this later, known since 1978, is the most efficient and used in the literature *(Bathias and al, 1997).*

3.2.2. Maximum energy release rate

The maximum energy release rate criterion proposed by *(Erdogan and al, 1963)* is based on the theory introduced by Griffith, which they assume is valid in the case of crack growth. This criterion studied the possibility of propagation in the direction that maximizes the strain energy release rate G.

$$\frac{\partial G}{\partial \theta} = 0 \; and \; \frac{\partial^2 G}{\partial \theta^2} < 0 \qquad (I.18)$$

The calculation of G for a small crack δ advance oriented at θ angle, as we can see in figure I.16, is given by the following relation with the respect of the existing crack *(Hussain and al, 1974)*:

$$G(\theta) = \frac{4}{E^*}\left(\frac{1}{3+cos^2\theta}\right)^2 \left(\frac{1-\frac{\theta}{\pi}}{1+\frac{\theta}{\pi}}\right)^{\frac{\theta}{\pi}} \times \left[(1+cos^2\theta){K_I}^2 + 8sin\theta cos\theta K_I K_{II} + (9-cos^2\theta){K_{II}}^2\right] \qquad (I.19)$$

where $E^* = \begin{cases} \frac{E}{1-\nu^2} & \text{for plane strain} \\ E & \text{for plane stress} \end{cases}$

Finally, we have to integrate and solve $\frac{\partial G}{\partial \theta} = 0$ to obtain the θ_0 angle.

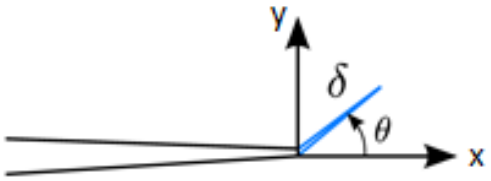

Figure I. 16. Calculation of G for an advance of δ and an angle θ

3.2.3. Maximum strain energy density

A criterion based on the solution using the maximum local density *(Westergaard, 1939)* of the total energy S at the crack tip is proposed by *(Sih, 1974), (Sih, 1991)*:

$$S = a_{11}k_I^2 + 2a_{12}k_I k_{II} + a_{22}k_{II}^2 \qquad (I.20)$$

where $k_i = \frac{K_i}{\sqrt{\pi}}$ with$i \in \{I, II, III\}$

The crack propagates in the direction that minimizes the total energy density *(Sih, 1974), (Sih, 1991)*, or in the direction where the dilatation energy density is maximum. Crack propagation begins when $S = S_c$:

$$\frac{\partial S}{\partial \theta} = 0 \quad and \quad S = a_{11}k_I^2 + 2a_{12}k_I k_{II} + a_{22}k_{II}^2 = S_c \qquad (I.21)$$

As shown in figure 1.17, for a crack making β angle with the axis of the load and then propagating with θ angle, the solution is proposed by *(Tanaka, 1974)*:

$$2(1-2\nu)\,sin(\theta_0 - 2\beta) - 2\,sin\big(2(\theta_0 - \beta)\big) - 2sin2\theta_0 = 0 \qquad (I.22)$$

(Bathias and al, 1997) give a comparison of the three criteria of bifurcation and conclude that the best consistence with the experimental one was obtained with the maximum circumferential stress criterion.

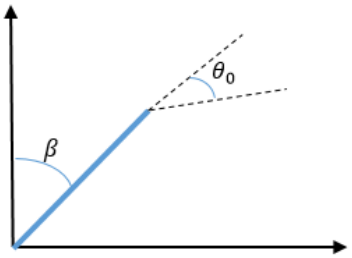

Figure I. 17. Calculation of the solution for a crack making β angle with the axis of the load and propagating with θ angle

3.3. Fatigue life computation models

In many cases, a structure could be in safe situation even if cracks are present. For this reason, the fatigue crack growth tests are important. From the experimental data given by these tests, an empirical relationship can be built between the Fatigue Crack Growth Rate (FCGR) $\frac{da}{dN}$ and the range of the SIF ΔK which mainly depends on the crack geometry and the loading conditions. From a physical point of view, the FCGR represents the crack growth speed during the loading cycles. A basic model was first proposed by Paris and Erdogan *(Paris and al, 1963)*. They assume a linear relationship between the FCGR, $\frac{da}{dN}$ and the range of the SIF ΔK as follows:

$$\frac{da}{dN} = C\,(\Delta K)^m \qquad (I.23)$$

where a is the crack length, N is the number of loading cycles, C and m are two parameters depending on the material and ΔK is the variation of the stress intensity factor.

Since this model considers only the region II of figure I.18, and do not take into consideration high toughness, modifications of this law were proposed taking into account additional parameters such as the load ratio R, the closure phenomenon *(Elber, 1971)* or the maximum stress during a cycle. The reader may refer to *(Beden and al, 2009)* for an exhaustive list of the proposed models.

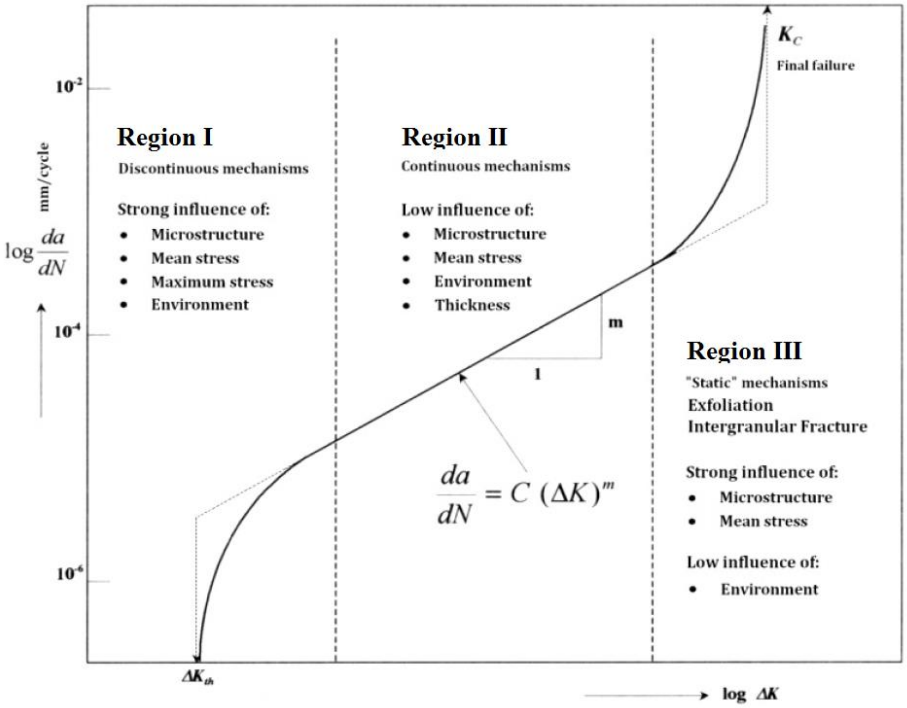

Figure I. 18. Characteristic crack growth rate curve for a ductile material

Later, after Paris and Erdogan's works, researchers have found that the FCGR does not exhibit the same behavior for all ranges of ΔK. That is to say, the FCGR is not linear for all ranges of ΔK. The general curve of the FCGR in the case of opening fracture mode and for metal-based components is shown figure I.18.

For ΔK slightly greater that a threshold ΔK_{th}, the crack will grow quickly and for medium SIF range ΔK the fatigue crack growth behavior can be described by a power law such as the Paris-Erdogan's law given in equation (I.23). In 1970, the Paris-Erdogan's model was slightly modified *(Walker, 1970)* in order to take into account the strong effect the stress ratio $R = \frac{\sigma_{min}}{\sigma_{max}}$. The modified model is:

$$\frac{da}{dN} = C_1 \frac{(\Delta K)^{m_1}}{(1-R)^{m_1(1-\gamma)}} \qquad (I.24)$$

In region III, the FCGR is faster than indicated by the Paris-Erdogan's law. Indeed, the fatigue crack growth exhibits a rapidly increasing rate towards infinity. Note that, in this region, the facture toughness K_{Ic} of the material has a significant effect on the FCGR in addition to the stress range. To take it into account, the Paris-Erdogan's model has been enhanced by *(Forman and al, 1967)* and the modified model can be written as follow:

$$\frac{da}{dN} = C_2 \frac{(\Delta K)^{m_2}}{(1-R)K_{Ic} - \Delta K} \qquad (I.25)$$

Constants $C_1, m_1, \gamma,\ C_2$ and m_2 presented in the above are empirically derived through experimental data.

Note that the previously presented fatigue crack growth models do not take into account many others parameters such as load frequency, environment factors such as the relative humidity and the temperature, and as load sequencing. Fortunately, mixed mode fatigue crack growth can be well addressed, by just substituting ΔK in equations (I.23), (I.24) or (I.25) by a mixed mode equivalent SIF ΔK_{eq}, which assumes that the crack would

propagate in opening fracture mode in the bifurcation direction defined by the bifurcation angle θ obtained by solving equation (I.19).

In the case of two-dimensional fatigue crack growth problems, ΔK_{eq} can be written as:

$$\Delta K_{eq} = cos\left(\frac{\theta}{2}\right)\left[\Delta K_I\left(1 + cos(\theta)\right) - 3\,\Delta K_{II}\, sin(\theta)\right] \qquad (I.26)$$

where ΔK_I and ΔK_{II} are the SIF ranges of the opening and the in-plane shear fracture modes respectively, and θ is the bifurcation angle calculated from equation (I.19).

To predict the fatigue life of structures subjected to fatigue crack growth, the number of loading cycles to failure N_f can be obtained by integrating the FCGR law. Using the general form of the FCGR presented by equation (I.27), this leads to the following expression:

$$N_f = \int_{a_0}^{a_c} \frac{1}{f(\Delta K, R, K_{Ic}, \dots)}\, da \qquad (I.27)$$

where $f(\Delta K, R, K_{Ic}, \dots)$ is the inverse of the second members of equations (I.23), (I.24) or (I.25), a_0 is the initial crack length, a_c is the critical crack length which can be derived from the fracture toughness of the material or can be related to a design constrains, as shown in section 2.4.3.

Indeed, studies have shown the use of linear fracture mechanics in predicting the critical crack length *(Wessel and al, 1972)*: the linear fracture mechanics defines a stress intensity factor K at the tip of a crack as a function of the applied stress σ and the dimension of the crack:

$$K = \alpha\sigma\sqrt{\pi a} \qquad (I.28)$$

α is a coefficient depending on the geometry of the structure and the crack length. The failure criterion is then a stress criterion and failure occur when the SIF reaches a critical value K_{Ic}.

The computation of the integral (I.27) is not trivial especially when the integrand is not available under an analytical form, which is often the case for real-life crack growth problems where the fracture behavior is represented by time consuming implicit models as finite elements approach-based ones. Hence, numerical schemes are usually suitable such cubature rules. *(Dowling, 2007)* has suggest using the well-known Simpson's integration rule below.

Let us consider three neighboring crack length a_j, a_{j+1} and a_{j+2}. As shown in figure I.19, the hatched area under the curve $y = \frac{1}{f(\Delta K, R, K_{Ic}, \dots)} = \frac{dN}{da}$ (i.e. the inverse of the FCGR) and between the two points of abscissa a_j and a_{j+2}, can be evaluated assuming that a second order curve (i.e. a parabola) passes through the three points (a_j, y_j), (a_{j+1}, y_{j+1}) and (a_{j+2}, y_{j+2}). If these points are assumed to be equally spaced by an increment Δa, the hatched area can be estimated as follow:

$$\int_{a_j}^{a_{j+2}} y\,da = \frac{\Delta a}{3}\left[y_j + 4\,y_{j+1} + y_{j+2}\right] \qquad (I.29)$$

The fatigue crack growth lifetime N_f is then the sum of the contributions of all areas obtained by applying equation (I.29) for each of $j = 0,2,4,\ldots,(M-2)$, where M is even. In practice, M is taken as large as possible to keep Δa reasonably small in order to obtain an accurate estimate of N_f.

Note that Simpson's rule can be also used when the integration points are not equally spaced (i.e., Δa is not constant during the whole integration process), by a little modification of equation (I.29). Consequently, the fatigue lifetime is obtained by:

$$N_f = \sum_{j=0}^{M-2} \frac{a_j(r^2-1)}{6r}\left[y_j r(2-r) + y_{j+1}(1+r)^2 + y_{j+2}(2r-1)\right] \qquad (I.30)$$

where r the distance from the crack tip to the given point P.

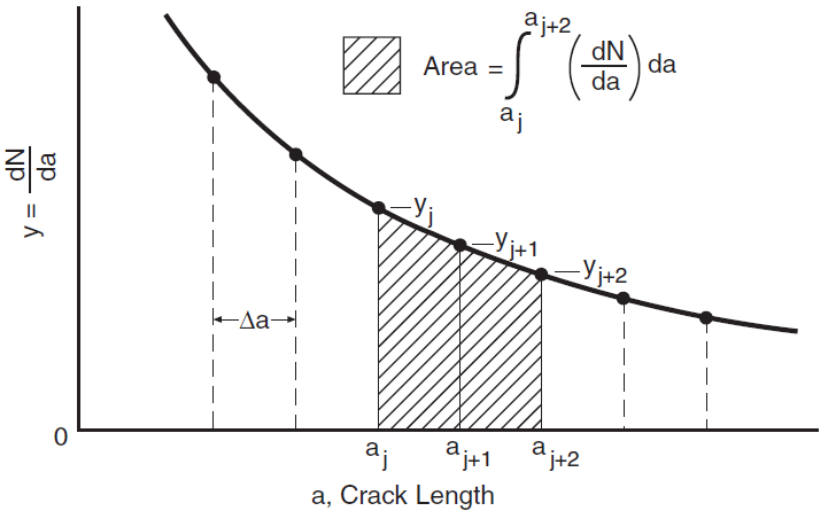

Figure I. 19. Integration principle using Simpson's rule (Dowling, 2007)

3.4. Physical description of the retardation phenomenon

3.4.1. A retardation phenomenon due to overload

The application of one or more overloads during constant amplitude loading is characterized by a retardation or even a stop of the crack propagation after returning to the initial loading conditions *(Schijve and al, 2004), (Manjunatha and al, 2004), (Daneshpour and al, 2012), (Dirik and al, 2018), (Hemnesi and al, 2022).* The retardation effect depends on several factors such as geometry, temperature, environments, and material properties. Although this phenomenon was discovered many years ago by *(Schijve, 1962),* its effects are not fully understood and described especially in term of its modelling.

It is known that the overloads induce large plastic deformation ahead of the crack tip and decreases the rates of crack propagation. This retardation is usually measured in terms of cycles and thus increases the lifetime from N_1 to N_2 as we can see in figure I.20. The retardation effect depends on the overload rate, on the value of the basic loading before the application of the overload, on the number of cycles before the overload and on the ratio of the basic loading. Indeed, it is noticed that with different load ratio the maximum crack rate recorded differs,

and this difference will have an impact on the size of the plastic zone created with the application of the overload and consequently on the number of retardation cycles *(Zhang, 2019), (Alabd Alhafez, 2018)*. However, the retardation effect was found to decrease with the increasing number of overload cycles.

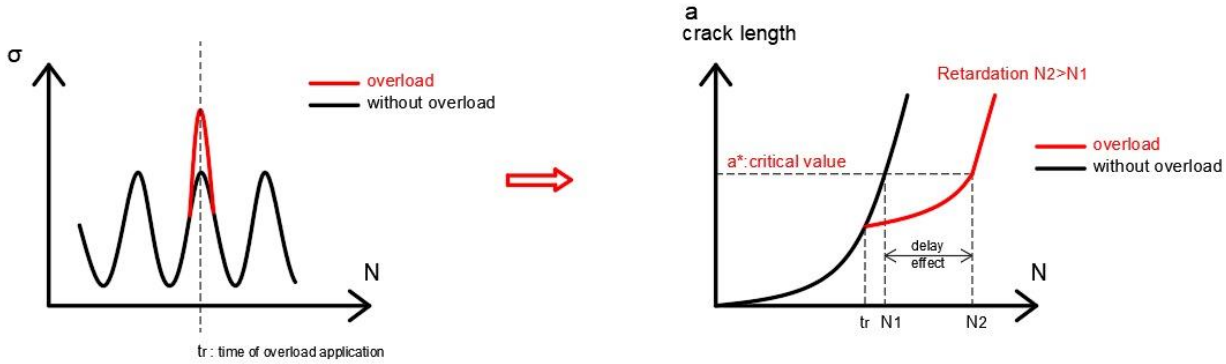

Figure I. 20. Effect of single overload on fatigue crack growth lifetime

The retardation phenomenon of a crack after the application of an overload is linked to the existence of residual stresses and to the concept of crack closure. Residual stresses are referred to stresses remaining in a structure in the absence of a mechanical loading. The experiment of *(Schijve, 1979)* has shown that the residual stresses are a cause of the retardation of the fatigue crack propagation. The plasticization at the bottom of the crack during the loading of the structure, by the singularity of the elastic stress field, gives these residual stresses in the plastic zone. In general, these stresses are compressive stresses near the crack tip (the important residual stresses in our case) and are tensile stresses away from the crack tip, thus forming an internal equilibrium for the structure.

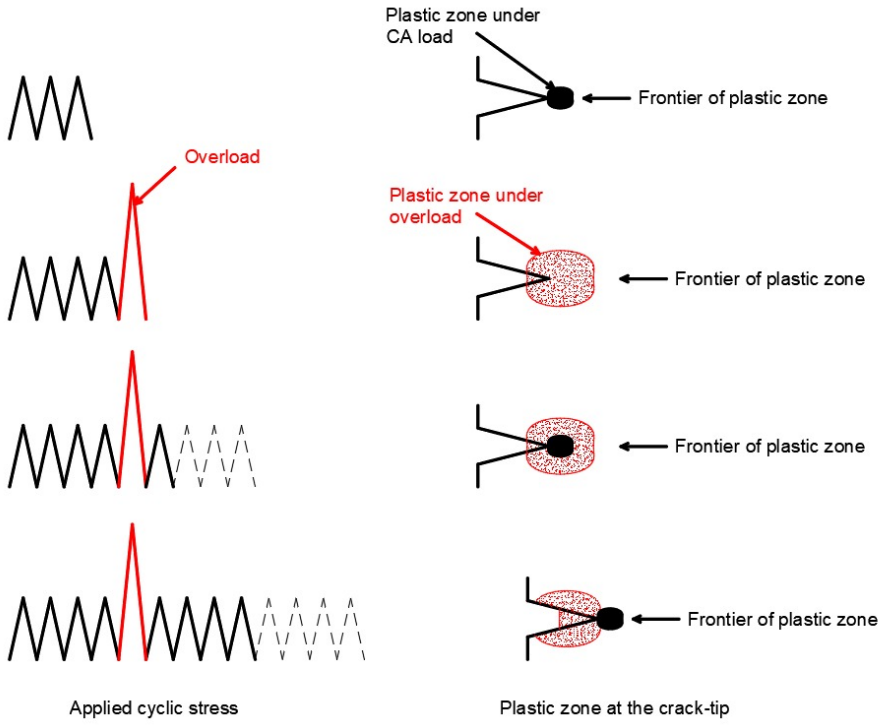

Figure I. 21. Effect of overload on the plastic zone

The determination of the residual stresses in the vicinity of the crack still presents difficulties due to the small size of the damaged plastic zone at the bottom of the crack leading to uncertainties on the evaluation of residual stresses.

Several researchers have sought to determine the residual stresses of fatigue crack tip after the application of an overload, such as (Lin and al, 2017), *(Rice, 1967), (Matsuoka and al, 1976), (Taira and al, 1979), (Fuhring and al, 1979), (Bush and al, 1988).* They concluded that as the distance from the point of application of the overload increases, the residual stresses tend to decrease gradually. Note that, most of these studies were based on the model of *(Dugdale, 1960)* which considers that the material is rigid, perfectly plastic and that the plastic zone is confined to the crack tip (see figure I.21).

The retardation effect can also be viewed as a consequence of the closure concept. This concept results from the existence of the compressive residual stresses at the crack tip. It was first shown by *(Elber, 1971)* on an aluminum alloy, by explaining that the fatigue crack can close even before that the tensile stresses are equal to zero. However, the damage occurs only when the crack tip is completely opened, thus this phenomenon can be involved in order to explain the effects of the retardation *(Lieurade, 1988)* and the influence of certain important parameters of the fatigue crack growth such as the maximum stress intensity, the load ratio, the thickness of the specimen, the overloads.... The crack closure is far more important near the edge of the specimen, thus reducing the crack growth rate *(Taleba and al, 2016).*

Also, it has been observed by many researchers that a short acceleration of the crack growth rate occurs just after the application of the overload. Thus, overloads can produce a very short acceleration of the crack growth *(Vasudevan and al, 1995)* before the significant retardation occurs (see figure I.22). However, this acceleration is observable only for a high level of overload rate and at a short distance from the application of the overload (short crack length compared to the one of the retardation effect) and thus can be neglected because it is too small to be taken into account. For instance*, (Wheatley and al, 1999)* have shown that the crack length where the acceleration is observable is 300 µm and that the crack length retardation is of the order of 10 mm.

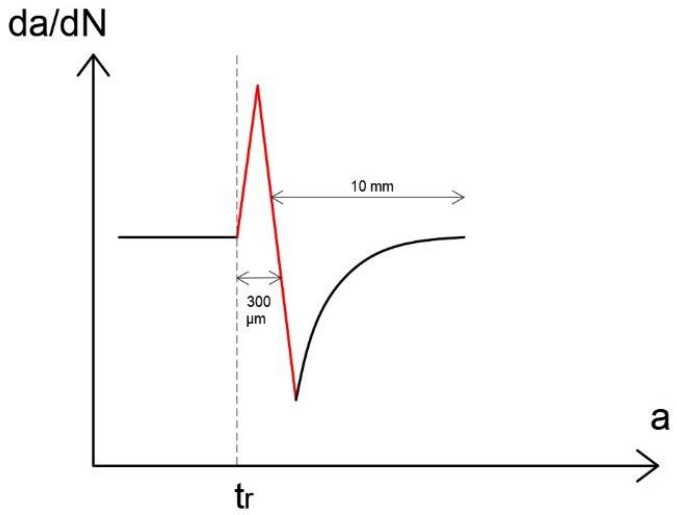

Figure I. 22. Acceleration and retardation after the application of an overload

The speed of the crack growth, after applying the overload goes through four stage: first, an increase in the crack rate, second, the rate increases very rapidly and reaches a peak, then a rapid drop in the rate is observed to reach a minimal value, and finally the rate begins to increase gradually in the plasticized zone created by the application of the overload, until it returns to almost its initial value (before the application of the overload).

In our studies, we will choose not to consider the acceleration phenomenon just occurring after the overload shown in figure I.20 because it is too negligible to be taken into account in comparison with the retardation induced by the overload.

3.4.2. Two fatigue plastic zones due to overload

The retardation keeps on until the crack has propagated out of the monotonic plastic zone of overload. Therefore, the number of retardation cycles depends on the size of this monotonic plastic overload zone (see figure I.23).

Moreover, the effect of the retardation depends on the thickness of the specimen since the size of the plastic zone differs for the in-plane stresses (used for thin specimens where we assume that out-of-plane stresses are equal to zero) and the in-plane strains (used for long specimens where we assume that the out-of-plane strains are equal to zero). The effects of the retardation are more important under plane-stress conditions *(Lang and al, 1999)* because the stress intensity factor is affected by the distance from the center of the crack. Indeed, at the center of the specimen, where the plane-strain conditions are applied, constraint is high and at the surface of the specimen where the plane-stress assumptions are used, the lack of the out-of-plane stress results with a loss of the crack tip constraint thus the stress intensity factor is lower.

In general, the fatigue crack growth can be controlled by the plastic zone. During the loading, two plastic zones are created: the cyclic plastic zone and the monotonic plastic zone related to the loading of the structure. These plastic zones are assimilated to circles characterized by their radius r_y as shown in figure I.23.
Actually, when a structure is subjected to cycling loading, a monotonic plastic zone is formed at the crack tip. Then a compressive stress is developed in the plastic zone when applying an overload leading to the creation of the cyclic plastic zone in the areas where the maximum compressive stress exceeds the yield strength *(Saxena and al, 1996)*.

The size of the plastic zone at the crack tip is one of the important parameters describing the retardation effects since it is directly related to the crack length affected by the overload. The size of this plastic zone at the crack tip is a significant characteristic of the crack behavior and can be observed directly during experiments. It depends on the mechanical properties of the material, the stress conditions: applied stress and yield stress of the material, as well as the distribution of stress and strain of the plastic zone. In fact, materials with high yield stress normally have a small cyclic plastic zone size *(Dowling, 2013), (Ralph and al, 2001)*. In real materials, the theoretically very high elastic stresses in the vicinity of a crack tip exceed the yield strength of the materials; thus, plastic yielding will occur.

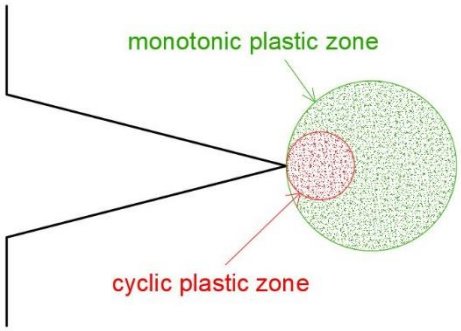

Figure I. 23. Illustration of the plastic zone at the crack tip

Irwin presented a simple method to determine the plastic zone at the crack tip assuming the materials to be elastic. He found that the creation of the cyclic plastic zone affects the geometry when it is longer than its physical size, and then, he estimated the size of the cyclic plastic zone which are approximately one quarter of the size of the monotonic plastic zone, by *(Irwin, 1960)*:

$$r_y = \frac{1}{8\pi}\left(\frac{\Delta K}{\sigma_y}\right)^2 \quad \text{For plane stress} \qquad (I.31a)$$

$$r_y = \frac{1}{24\pi}\left(\frac{\Delta K}{\sigma_y}\right)^2 \quad \text{For plane strain} \qquad (I.31b)$$

3.5. Case study

In this section a study of the effect of R as well as a comparison of the crack propagation laws through a crack growth mechanical model is conducted to study the effect of the variability of the material properties on the fatigue crack growth lifetime. The mechanical model represents a Centre Cracked Plate (CCP) specimen made of 7075-T6 aluminum alloy, subjected to tensile loads applied by five pins located at the top and the bottom. A detailed drawing of the geometry of the CCP specimen is given in figure I.24.

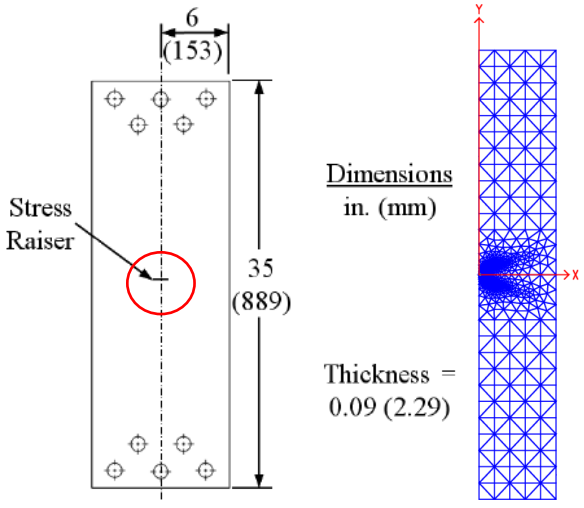

Figure I. 24. CCP specimen, geometry and dimensions (left), finite elements mesh (right)

Fortunately, since the CCP specimen is extensively used, numerous fatigue crack growth data are found in the literature. *(Hudson, 1969)* has performed fatigue crack growth characterization tests on 7075-T6 aluminum alloy CCP specimens, using multiple axial-load fatigue-testing machine which applied monotonic oscillatory loads with

a mean stress σ_m and alternating stress σ_a. The cycle count was recorded as the crack propagates through the specimen following an increment crack length ranged from $\Delta a = 0.1$ to $0.2\ inch$. It should be noted that tests are performed for several stress ratio R levels and 1 to 5 tests are performed for each stress ratio level based on different combinations of the mean stress σ_m and the alternating stress σ_a. In the following only experimental data with a $R \geq 0$ were analyzed since Hudson found that for $R < 0$, the same crack growth rate is observed as for the specimens loaded with $R = 0$.

3.5.1. Finite elements model

A finite elements model of the CCP specimen is developed using the software cast3m *(CASTEM, 1997)*, in order to use an implicit mechanical model. Due to the geometry symmetry, only one half of the CCP specimen is modeled as shown in the finite elements mesh in figure I.24. This reduces the Degree Of Freedom (DOF) of the finite elements model and consequently reduces the computation time, which becomes suitable when performing uncertainty propagation analysis.

For simplicity, the pins have been removed from the finite elements model and the true loading is replaced by an evenly distributed pressure across the top and the bottom edges of the specimen. In addition, plane stress hypothesis is assumed since the specimen thickness is small compared to the two other dimensions of the specimen. Referring to the conclusions made before, only the energetic method of paragraph 2.1.1, considering $G = J = \frac{K_I^2}{E'}$, is used herein to compute the SIF range ΔK_I.

As shown in figure I.25, based on the deformed mesh of the CCP specimen, the crack will propagate in opening fracture mode. In addition, linear elastic fracture behavior hypothesis is verified since the Von-Mises equivalent stress exceeds the yielding strength of the material $\sigma_{yld} = 75.9\ ksi$, only in the vicinity of the crack tip.

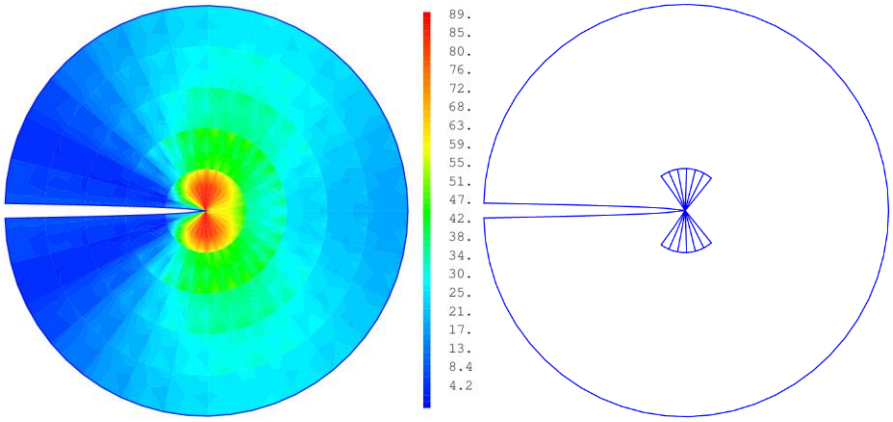

Figure I. 25. CCP specimen crack tip, deformed mesh (left), Von-Mises equivalent stress (center), yielding elements at the crack tip (right)

3.5.2. Fatigue crack growth models fitting

In this section, Hudson's experimental data *(Hudson, 1969)* are used to obtain the empirical parameters of the fatigue crack growth models. In the following, Paris-Erdogan's, Forman's and Walker's fatigue crack growth laws are investigated and compared to find the most accurate one.

a) Paris-Erdogan's law

Crack length and loading cycles incrementally recorded during experimental tests are used to compute the FCGR da/dN. The SIF range ΔK is computed using the finite elements model developed in the previous section. Then, the material parameters C and m of equation (I.23) are obtained through linear regression analysis. Constants for models fit to each stress ratio R are listed in table I.2 and a plot is provided in figure I.26 showing the data points and fitted models.

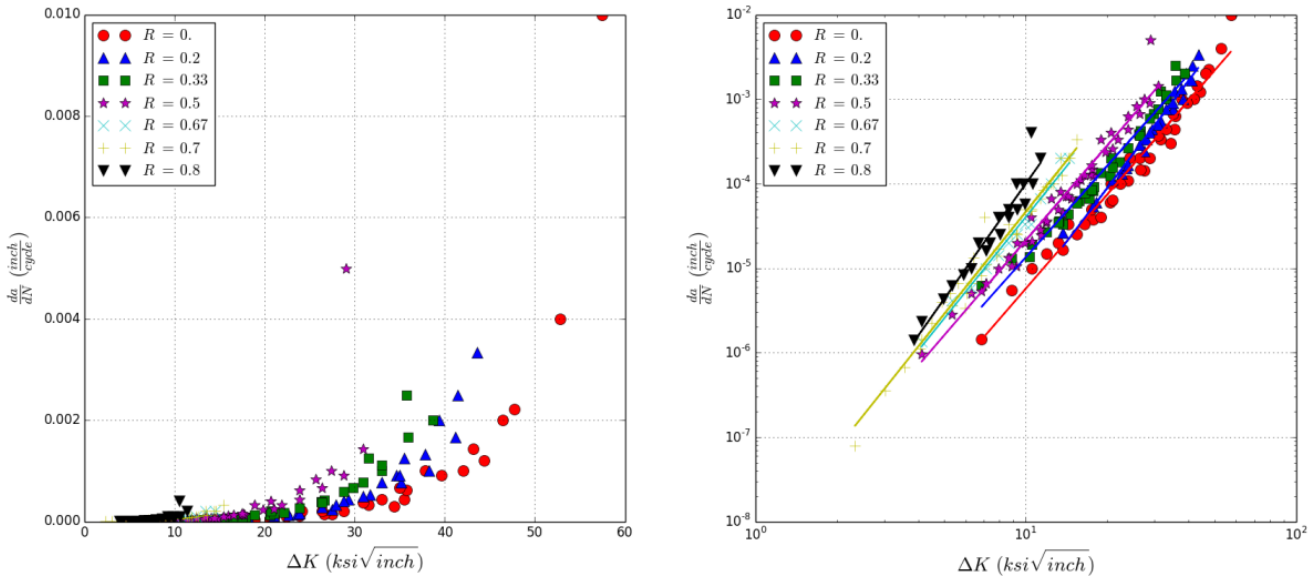

Figure I. 26. Paris-Erdogan's law fit to CCP specimen experimental data

As it can be seen, the Paris-Erdogan's law fits very well the experimental data for each stress ratio R since the goodness of fit parameter R^2_{LRGF} is close to 1 (see the right column in table I.2).

Table I. 2. Paris-Erdogan's law parameters

R	m	C	R^2_{LRGF}
0	3.70	1.14 10^{-9}	0.973
0.2	4.22	2.80 10^{-10}	0.979
0.33	3.59	3.45 10^{-9}	0.977
0.5	3.72	4.02 10^{-9}	0.969
0.67	3.98	4.22 10^{-9}	0.981
0.7	4.01	4.53 10^{-9}	0.973
0.8	4.52	3.00 10^{-9}	0.938

b) Walker's law

The Walker's law can fit all experimental data for different values of stress ratio R by a single curve when plotting the FCGR da/dN versus an effective SIF range $\Delta K_{eff} = \Delta K/(1-R)^{(1-\gamma)}$ in equation (I.24). The parameters of the Walker's law are obtained through multiple linear regression analysis applied to da/dN and ΔK is computed previously for the Paris-Erdogan's law, after transforming them to log-log space. The estimates of parameters of the Walker's law, and the fitted model are given in figure I.27 and table I.3, respectively.

Table I. 3. Walker's law parameters

m_1	γ	C_1	R^2_{LRGF}
3.82	0.56	8.19 10^{-9}	0.975

As can be seen, Walker's law fits very well the experimental data since the goodness of fit parameter R^2_{LRGF} is close to 1. It allows to consider the effect of the stress range based on linear curve compared to the Paris-Erdogan's law.

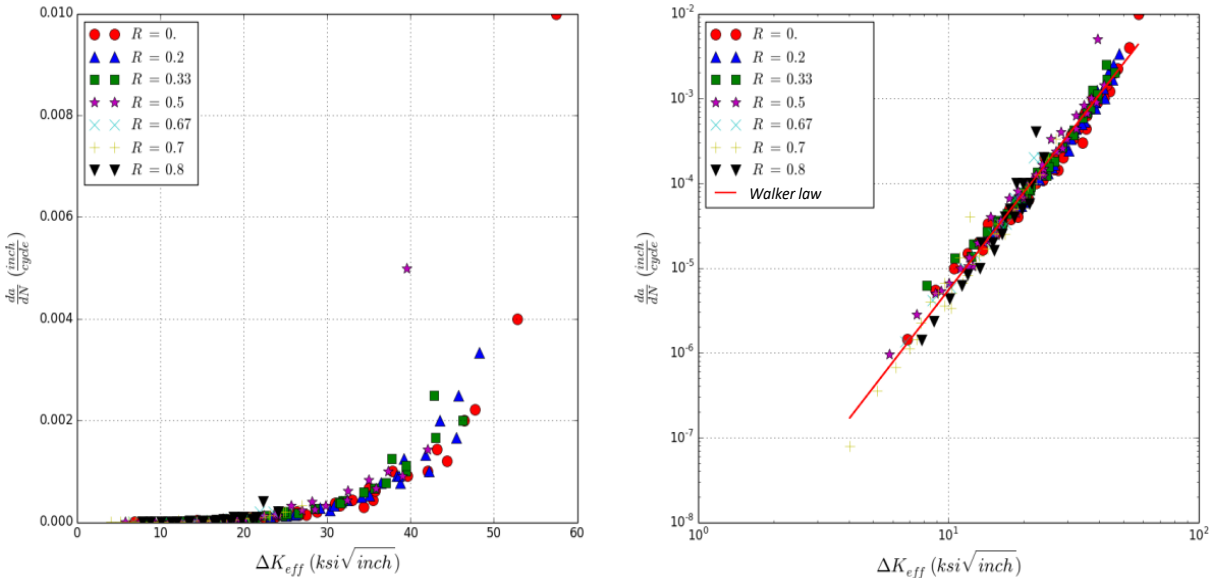

Figure I. 27. Walker's law fitted to CCP specimen experimental data

c) Forman's law

Like Walker's law, the Forman's law, represented by equation (I.25), allows also to model effect of the mean stress, thus only one model was needed to describe the entire experimental data. The parameters of the Forman's law are obtained through multiple linear regression analysis applied to da/dN and ΔK after transforming them to log-log space. The estimates of parameters m_2 and C_2 of equation (I.25) are given in table I.4. The fitted model is shown in figure I.28.

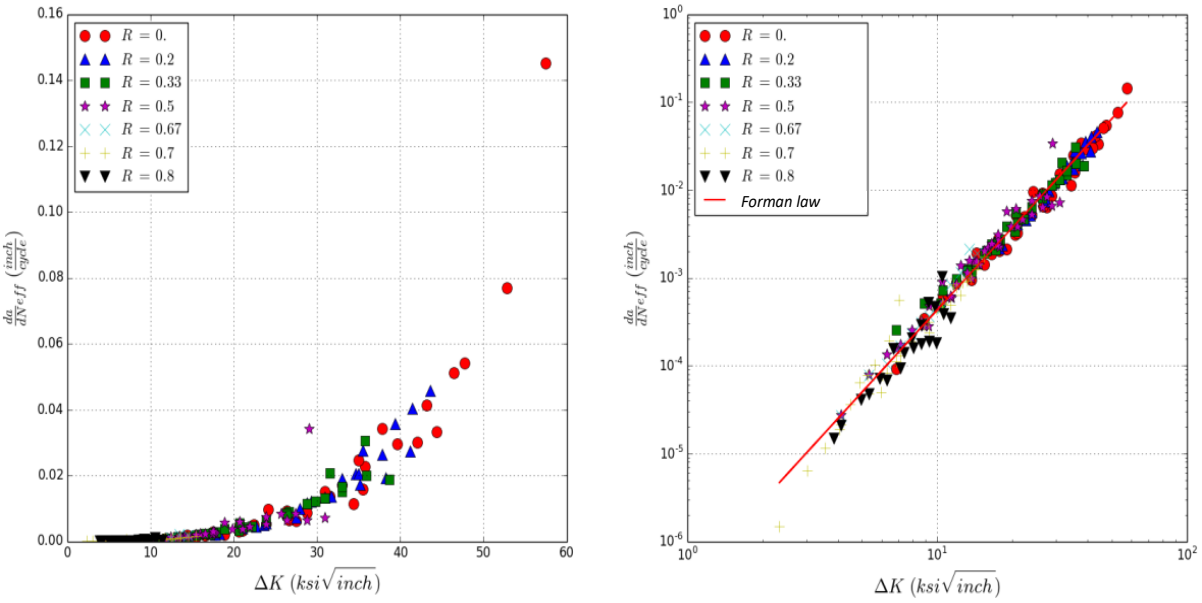

Figure I. 28. Forman's law fitted to CCP specimen experimental data

Forman's law fits very well the experimental data since the goodness of fit parameter R^2_{LRGF} is close to 1. It is to be noted that these results are obtained for fracture toughness $K_{Ic} = 72\ ksi\sqrt{inch}$ which is related to the threshold of the material. As can be seen in figure I.28, Forman's law is more suitable to fit the experimental data, than the Walker's law, especially for high SIF range values since it takes into account the unstable crack growth region (i.e., region III in the characteristic crack growth rate curve presented in figure I.18).

Table I. 4. Forman's law parameters

m_2	C_2	R^2_{LRGF}
3.11	3.32 10^{-7}	0.980

3.5.3. Deterministic analysis of fatigue crack growth

In this section fatigue crack growth lifetime analysis is performed based on Walker's and Forman's laws. The Paris-Erdogan's law is not used since it does not consider the effect of the stress level. The number of loading cycles to failure N_f is obtained through an incremental integration scheme based on the modified Simpson's formula presented in equation (I.32). Note that the integration is performed from the crack length range from a_0 to a_c, which are the initial and the critical crack lengths, respectively. This later depends on the fracture toughness of the material $K_{Ic} = 72\ ksi\sqrt{inch}$, and is computed by solving the following nonlinear equation.

$$a_c = \frac{1}{\pi}\left(\frac{K_{Ic}}{\frac{1 + 0.5\left(\frac{a_c}{w}\right) + 0.326\left(\frac{a_c}{w}\right)^2}{\sqrt{1-\left(\frac{a_c}{w}\right)}}\,\sigma_{max}}\right)^2 \qquad (I.32)$$

where σ_{max} is the maximum stress of the loading cycle and w is the CCP specimen half-width.

Table I. 5. Comparison of experimental and numerical results for N_f and a_c

R	$a_c\ (inch)$		$N_f\ (cycles)$		
	Experimental	Numerical	Experimental	Walker	Forman
0.00	0.80	1.6828 (110%)	3050	2268 (26%)	2398(21%)
0.20	1.40	2.2425 (60%)	8420	7519 (11%)	7733(8%)
0.50	1.40	2.9906 (114%)	42500	49473 (16%)	47809(12%)
0.67	1.80	3.3380 (85%)	154000	178817 (16%)	165688(8%)

Table I.5 compares experimental and numerical results of the fatigue crack growth lifetimes N_f and the critical crack lengths a_c for different loading conditions. As it can be seen, the numerical estimates of the critical crack length are twice larger than the experimental results. This discrepancy is mainly due, on the one hand, to a possible overestimated value of the crack toughness of the material K_{Ic}, and on the other hand, to the coarse crack growth increment Δa used in the experiment process which is not able to capture accurately the crack length when the fracture occurs. Indeed, according to the ASTM standard the crack increment should be around $0.05\ inch$, while the one used for the Hudson's data is ranged form $0.1\ inch$ to $0.2\ inch$.

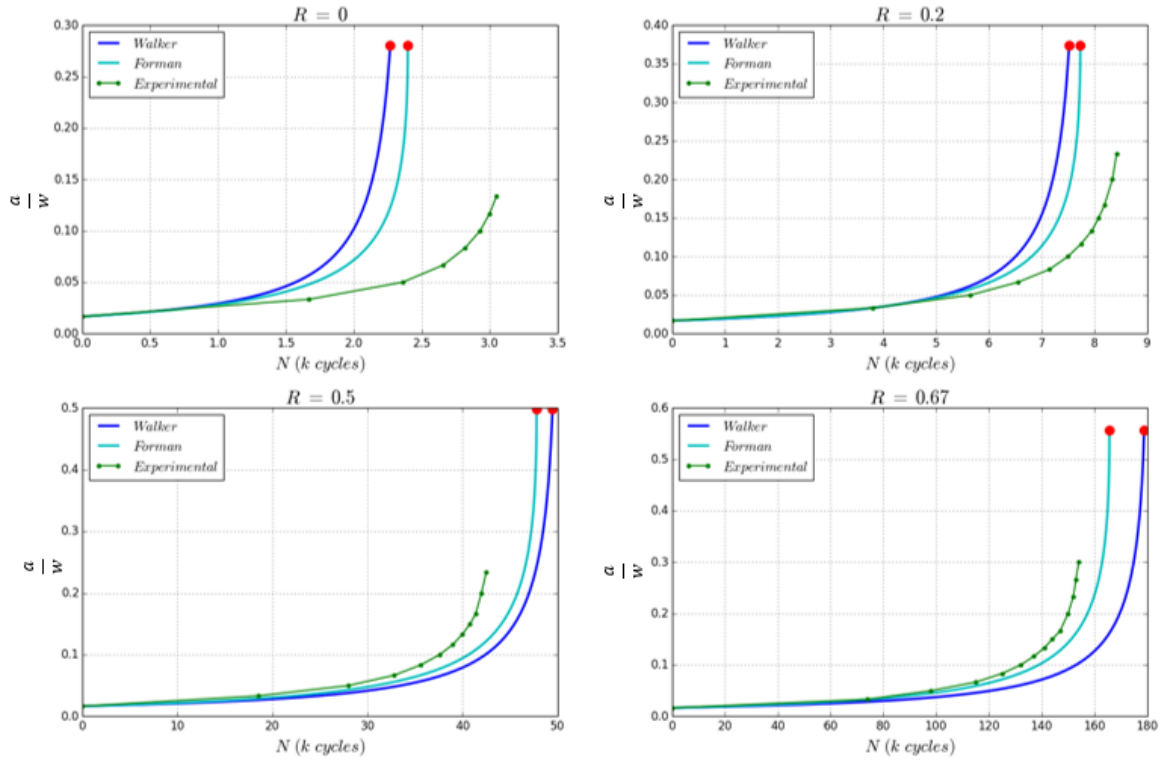

Figure I. 29. Comparison of predicted results from Walker's and Forman's FCG law with experimental data under various loading conditions

Figure I.29 shows plots of crack length versus the fatigue loading cycles, for different loading conditions. The obtained curves are compared to the experimental data. Note that to build these curves, equation (I.29) is solved following an incremental scheme where the crack length grows from a_i to a_c, based on various crack increments Δa to ensure a smooth shape.

As it can be seen a discrepancy is observed between the predictions given by Walker's and Forman's laws, and the experimental data. This discrepancy is more significant for the stress ratio $R = 0$ since it is around 26% and 21%, for Walker's and Forman's laws, respectively. More accurate predictions are obtained for the three other loading conditions since the relative error does not exceed 16% for the worst case. This discrepancy should not be fully attributed to the accuracy of the mathematical formulations of the FCG laws, but also to the limited amount of experimental data that we have, since only two tests are performed for each loading conditions and only average results were provided in Hudson's paper. Indeed, as shown first by *(Virkler and al, 1979*), and later by *(Ghonem and al, 1987)* and also by *(Wu and al, 2004)* from fatigue crack growth tests performed respectively on 68, 60 and 30 specimens, that large variability in growth rates is observed for the same material, geometry and loading condition. This issue will be deeply discussed in the following section.

4. Probabilistic fatigue crack growth

4.1. Interaction between uncertainties and fatigue failure

Despite of the huge amount of research works devoted to fatigue of materials, which certainly have contributed to a better understanding of the physics related to this failure mode, many phenomena are still misunderstood and must be studied in deep, in particular the close relationship between uncertainties and fatigue of materials

which affect the safety and reliability of the structures *(Niu and al, 2021), (Li and al, 2020), (Liao and al (1), 2020).*

Understanding the physics of the fatigue failure phenomenon and developing a predictive models with a certain level of realism remain challenging tasks despite all the amount of efforts and works that have been done so far. Unfortunately, this difficulty in developing realistic predictive models is amplified if we want to take into account the uncertainties, which are inherent characteristics of fatigue properties, observed experimentally *(Liu and al, 2022), (Ciavarella and al, 2018), (Romano and al, 2018)*. Statistical information concerning fatigue properties is most often collected from the results of tests carried out in the laboratory and not from experiments carried out under service conditions. Thus, different sources of dispersions must be taken into account in each situation, since observations made in the laboratory may not be valid in practice. For example, the dispersions observed in the laboratory are obtained from fatigue tests for which the loading is at constant amplitude whereas, in practice, the loadings which occur are rather at variable amplitude and even random.

Moreover, as we have already explained before, the fatigue life is made up of an initiation period and a propagation period. In each of these two periods, different damage mechanisms can occur. Consequently, the sources of dispersion are different, which makes their control complex. In cases where initiation takes time to appear, the dispersion observed over the fatigue life is necessarily related to uncertainties in the parameters contributing to crack initiation such as the surface condition. On the other hand, if the propagation period constitutes the major part of the fatigue life, the observed dispersion is a consequence of the uncertainties in the parameters dominating the increase of the crack length. This second situation is frequently encountered in fatigue tests carried out on notched specimens and it also seems to be the case for real structures for which the presence of defects is almost inevitable. Moreover, during their propagation, the cracks are faced with different types of metallurgical structures and imperfections due to the inhomogeneity of the materials, so that the rate as well as the direction of propagation of the crack are variable.

For many years now, some researcher's works pointed out this issue. Several studies explaining the probabilistic nature of the fatigue crack growth have discussed the necessity to consider multi sources uncertainties in fatigue reliability analyses such as *(Fei and al, 2020)* who developed a surrogate model method and an optimization model to improve the reliability based design optimization of structures*, (Lu and al (1), 2020*) who proposed an improved kriging surrogate model*, (He and al, 2020)* who proposed a probabilistic model for deducing fatigue life distribution. *(Lin and al, 2016)* took into consideration the uncertainties related to the flow behaviors and established a probabilistic model that describes these uncertainties. *(Liao and al (2), 2020)* proposed a probabilistic framework for fatigue life assessment with the consideration of the crack size and introduced an effective stress level to characterize the inhomogeneity of the stress distribution. *(Yuan and al (1), 2019) suggested an optimized model to improve the reliability and enhancing the stability of the structure*.

Experimental data obtained by *(Virkler and al, 1979)* is a well-known source of information about fatigue of engineering materials. These data, available in the literature, are probably the most famous and frequently used data sets to model crack propagation. Indeed, *(Virkler and al, 1979)* analyzed the statistical distribution of crack propagation in 2024-T3 aluminum alloy. Tests were conducted on 68 identical specimens containing a central

crack, supplied by the same company, and subjected to constant amplitude loading. Although the initial crack has the same length $a_0 = 9\,mm$ for all specimens, a variability for the fatigue lifetime was observed and, despite of this later, is recorded at the same critical crack length $a_c = 49{,}8\,mm$. As depicted in figure I.30, there is a large amount of variability in crack growth rate not only between samples but also within each sample. This variability was attributed to the heterogeneity of the material at the microscopic level.

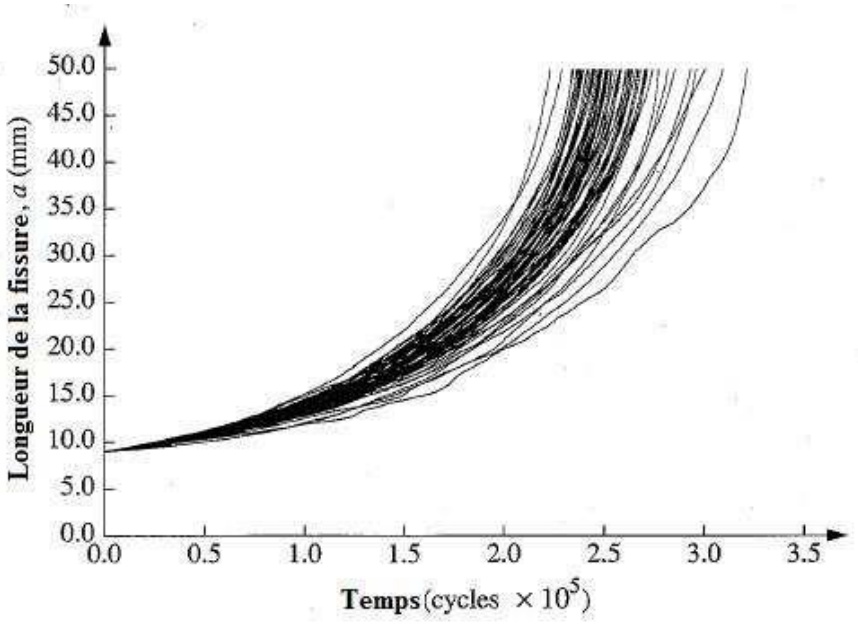

Figure I. 30. Crack length evolution curves obtained from Virkler experimental data (Virkler and *al, 1979)*

But the variability of the fatigue is not induced only by the heterogeneity of the material and can also be the result of uncertainties on the geometry parameters and the loading conditions. Thus, the uncertainties depend on the structure in terms of materials, geometry and loading, but also on the crack by its size, shape and position. It is clear that to obtain a safe design, these sources of uncertainties should be taken into account *(Oden and al, 2003)*.

In engineering problems, we are most often required to develop computationally time consuming numerical models to simulate the behavior of real structures. In addition, the sources of uncertainty are multiple, and since we do not have prior information on each of them, we are forced to take them all into account which generates a high number of uncertain parameters.

The deterministic models, presented in the above sections and used in fatigue life prediction, are unable to take into consideration these uncertainties in fatigue crack propagation phenomenon. The probabilistic approaches could address this issue, but unfortunately they suffer until now from some limitations to solve real-life engineering problems. Indeed, some of them are purely statistic *(Bogdanoff and al, 1985)* and subject of criticisms since they are not able to describe the physical phenomena related to the fatigue crack growth. Other approaches, which are mainly based on the "*probabilization"* of the fatigue crack growth rate *(Wu and al, 2004),* are time consuming, because their efficiency is affected when the probabilistic dimension (i.e. the number of random variables representing the uncertain parameters) of the problem is high, and/or the use of the mechanical model representing the fatigue crack growth is also time consuming.

The present work aims to find a response to these problems, that is to develop a robust, efficient, and accurate probabilistic approach allowing us to perform uncertainty propagation through a mechanical models dealing with fatigue crack growth problems. In addition, this approach must be able to take into account various sources of uncertainty, related the geometry, the material and the loading and evaluate their effect on the lifetime and the reliability of the structures subject to fatigue crack growth. At the same time, different types of uncertainty propagation analysis will be addressed, namely: statistical moments analysis, sensitivity analysis.

4.2. Probabilistic models of fatigue crack propagation

As already mentioned, it is well known that the crack propagation process contains various uncertainties originating from material properties, environmental conditions and mechanical loads *(Niu and al, 2020), (Yuan and al(2), 2019), (Lu and al (2), 2020)*, or from initial defects of fabrication *(Zhu and al(1), 2018), (Zhu and al(2), 2018), (He and al, 2015*). As a result, even in repeated tests, fatigue crack growth (FCG) process shows considerable uncertainty *(Zhu and al, 2020)*. Thus, probabilistic FCG modeling is vital for fatigue reliability and durability analyses of engineering components. To take into consideration scatter observed on data, many authors were interested in probabilistic models to describe the evolution of crack propagation in fatigue. The probabilistic models offer thus an appropriate framework for modelling and predicting crack propagation. *(Song and al, 2019)* proposed a probabilistic framework of low-cycle fatigue life assessment based on the wavelet neural network regression method. And to evaluate the probability distribution of fatigue life, (*Long and al, 2019)* developed an uncertainty propagation approach based on the principle of fatigue crack growth criterion. Indeed, this context enables the introduction of certain variabilities to the typical deterministic laws to describe FCG under constant or variable amplitude fatigue loading, see for instance *(Righiniotis and al, 2003), (Sankararaman and al, 2011), (Xiang and al, 2011), (Wu and al, 2003)*.

From the view of methodology, these probabilistic models may be separated into two types: one is a physical model which is derived from randomization of Paris-Erdogan's crack propagation law, and the other is the non-physical model.

4.2.1. Physical model based on Paris-Erdogan's law

One approach to probabilistic modeling of fatigue crack growth is to randomize the coefficients of a deterministic model to represent the material inhomogeneity. The model proposed by *(Tsurui and al, 1986), (Ishikawa and al, 1984)* presents a physical probabilistic modelling of fatigue crack damage in metallic materials faced in structures. In this model, it is assumed that the stress at the crack tip is described only by the SIF, and is independent of other factors such as the mean stress or the stress ratio. In addition, it is assumed that there is no retardation effect caused by overload and, even if it exists, it is negligibly small. Under these conditions, the crack growth law can be described as the Paris law in equation (I.23). The equation of damage is based on the physics of fracture mechanics and is validated by Karhunen-Loève. In the work of Fokker-Planck, a generalized equation is derived from the Paris-Erdogan's law. This equation defined the temporal variation of the crack length distribution and provided the distribution of the crack propagation life with the use of its solution. The equation is a second order differential equation and does not have a unique solution since the equation contains random variables.

Therefore this model seems to be very reasonable for the analysis of the crack propagation, however, in their work, there is not an application on the crack propagation.

Another example of the physical model is the one proposed by *(Ray and al, 1997)* to enhance the computational efficiency of the estimation of the lifetime prediction. This model proposed an algorithm for real time estimation of the crack damage based on the underlying principle of extended Kalman filtering. In this approach, the first two moments of the probabilistic damage are computed by constructing the probabilistic differential equations in the Wiener form as opposed to the Itô form. Then, the lognormal distributed crack length (LDCL) model was proposed as an improvement of the *(Ray and al, 1997)* model. The crack growth rate in this model is guaranteed to be non-negative, it is based on Karhunen-Loève expansion of the crack length process. This approach provides an additional parameter for tuning the probability distribution function. The nonlinear characteristics of the eigenfunctions in the Karhunen-Loève expansion provide better accuracy than the linear representation. This approach allows the model to capture certain nonlinear features of the crack growth statistic. Consequently, model predictions are more accurate.

4.2.2. Non-physical model

a) Model based on Markov theory

Markov processes are proposed to address probabilistic modelling of fatigue crack growth. The basic idea of this model is to define the evolution of the crack size during its propagation by a discrete Markov process over time. This model is built on several initial assumptions. It is assumed that the damage increment at the end of each damage cycle depends only on the amount of damage present at the beginning of this damage cycle regardless of the accumulated damage before the cycle. Thus, the model proposed by *(Kozin and al, 1985),* known as the B-model, is nothing else than a stationary Markov process discrete in time and having a finite number of states. This B-model can be described in the following terms.

Let us consider a random variable D_0, representing the damage present in the structure at time t = 0; and let us define the initial statistical distribution of the different levels of damage by the vector $\boldsymbol{p_0}$, as follows:
$\boldsymbol{p_0} = \{\pi_1, \pi_2, \dots, \pi_b\}$, where $\pi_j = P\{D_0 = j \geq 0, \forall\, j = 1, \dots, b\}$ verify the condition $\sum_{j=1}^{b} \pi_j = 1$.

where *b* is the number of damage levels.

Let us now consider a random variable D_0, representing the damage present in the structure at time t. The distribution of each level of damage is described by the following vector:

$$\boldsymbol{p_t} = \{p_t(1), p_t(2), \dots, p_t(b)\}, \text{where } p_t(j) = P\{D_t = j \geq 0, \qquad j = 1, \dots, b\} \tag{I.33}$$

Referring to the Markov theory, the vector $\boldsymbol{p_t}$ can be easily computed using: $\boldsymbol{p_t} = \boldsymbol{p_0}[\boldsymbol{P}]^t = \boldsymbol{p_{t-1}}[\boldsymbol{P}]$ where $\boldsymbol{p_{t-1}}$ correspond to the damage distribution at the end of the previous damage cycle and $[\boldsymbol{P}]$ is the transition probability matrix that describes the degree of severity of each damage cycle.

The cumulative distribution function of failure is defined by:

$$F_W(t;b) = p_t(b) \tag{I.34}$$

By considering j the level of damage at t=0 and $F_W(t;j,b)$ the cumulative distribution function required to reach damage level *b*, we write:

$$F_W(t;b) = \sum_{j=1}^{b-1} \pi_j F_W(t;j,b) \tag{I.35}$$

In the context of the problem of fatigue crack propagation, the damage is interpreted as the crack length and the damage cycle consists of several loading cycles.

Thus, based on Markov theory we can obtain the cumulative distribution function of the number of cycles needed to reach a given crack length. In addition, reliability and failure rate can be easily determined. The B-model has been used in different applications dealing with the problem of fatigue crack propagation *(Bea and al, 1999), (Lassen and al, 2002*).

Among the Markov processes suitable to perform crack modelling, one may also consider the class of piecewise-deterministic Markov processes (PDMP's) frequently employed in safety and reliability and can handle both discrete events and continuous evolution of physical phenomena. *(Chiquet and al, 2009)* were the first authors to use PDMP's to model fatigue crack growth as a degradation mechanism that continuously evolves in time with the growth rate changing at random times. PDMPs are able to model crack propagation in order to handle two problems: the first one is to capture the transition time between two regimes of propagation and the second one is to predict the behavior of a crack until the exit of the linear Paris regime using the first experimental points of its propagation as conditional events. PDMPs are described by two variables: an usual Euclidean state representing the physical system and a discrete variable reflecting region of propagation. PDMP's are suitable for modelling and predicting degradation processes induced by the presence of cracks in structural components.

Although the Markov chain model has been used in a wide variety of applications, it has been the target of criticisms. Indeed, the formulation of the model is based on purely statistical foundations and lacks physical consistency to describe the actual mechanism of fatigue crack propagation.

b) Yang and Manning model

The simple probabilistic model developed by Yang and Manning *(Yang and al, 1996)* aims obtaining two important probability distributions: the crack growth rate probability and probabilistic service life distribution under a specified crack length. This model was developed in order to overcome the difficulties presented in the model of Markov theory described above. In this model *(Yang and al, 1990)*, a deterministic fatigue crack growth equation is developed based on the stress intensity factors describing the failure mechanism and the orientation of the crack trajectory. The deterministic equation that was used to have a more realistic representation of the fatigue phenomenon, was randomized by assuming that the crack growth rate follows the lognormal distribution. The least square method is used to estimate the unknown parameters, and the second order approximation was used to derive the two probabilities.

To take into consideration the variability of the fatigue crack propagation process, Yang and Manning weighted the crack propagation law by a random parameter. Therefore, the crack propagation law is expressed as follows: $\frac{da\,(t)}{dt} = X(t)f(\Delta K, a, \dots)$, where f is a deterministic function defined as positive, given by the Paris law or other laws of crack propagation, consequently, the crack propagation law is transformed into a probabilistic differential equation.

After investigations of experimental data dealing with crack propagation in aircraft under random loading, Yang and Manning *(Yang and al, 1996)* suggested to write the equation in a simpler form:

$$\frac{da\,(t)}{dt} = X(t)Q[a(t)]^b \qquad (I.36)$$

where Q and b are two constants determined from the experimental data and t is an independent variable that can be interpreted as the number of loading cycles.

This model has been used especially in the aeronautics industry to conduct damage tolerance and durability analyses *(Yang and al, 1996)*. The random factor $X(t)$ is modelled by a lognormal process $Z(t) = \ln X(t)$ which should have zero mean and a standard deviation $\sigma_Z = \sqrt{\ln(1+\sigma_X^2)}$.

To quantify the statistical characteristics of fatigue crack growth dataset, *(Wu and al, 2003)* performed probabilistic crack growth modeling and verified the applicability of the Yang–Manning model. *(Li and al, 2020)* proposed a probabilistic fatigue crack growth model considering random initial crack and modified the Yang and Manning model considering a crack coalescence under multiple cracks conditions.

Although the probabilistic model of Yang and Manning offers a better compromise between physical realism and simplicity, we can see that, in the case where the propagation process is more complex such as when the loading is random, the model is unable to provide good predictions. Indeed, if the crack propagation process is complex, the deterministic law of crack growth will have a complex mathematical formulation, therefore, the complex mathematical law weighted by a random factor in the Yang and Manning model will be very difficult to solve in term of calculations. For this reason, a polynomial representation of the crack growth is proposed.

c) Polynomial model

To obtain a compromise between the realism of the physical meaning of the propagation process and the simplicity of the calculation, the polynomial model *(Ni, 2002)* has been proposed. The basic idea of the polynomial model is to replace the deterministic propagation law, which is complex if the crack growth process is complex, with a polynomial approximation.

By considering the polynomial approximation of second order, the polynomial probabilistic model is written:

$$\frac{da\,(t)}{dt} = X(t)\,[p + q\,a(t) + r\,a\,(t)^2] \qquad (I.37)$$

where p, q and r are the coefficients of the polynomial determined from the experimental data and depend on the characteristics of the material as well as on the applied load. $X(t)$ is a lognormal random process like the one used in the probabilistic model of Yang and Manning.

Following the same procedure as that of the Yang and Manning model, the quantities to be apprehended can be expressed in an analytical form.

d) Sobczyk model

This model *(Sobczyk and al, 1989), (Sobczyk and al, 1991), (Sobczyk and al, 1995)* is based on the representation of the propagation of fatigue cracks by a discontinuous probabilistic process in which the trajectories followed by the crack during its propagation are discretized into a random number of increments each having a random amplitude. *(Frondelius and al, 2022)* use the numerical solution schemes of this model and proposed an approach for high-cycle fatigue. Sobczyk's model assumes that among all the cracks that can coexist, there is one that dominates, and the growth of this crack leads to the failure of the structure. Furthermore, it is assumed that the configuration of this dominant crack is defined through a single parameter which length $A(t)$ depends on the time. In the case of mixed mode propagation, a relationship must be provided between the length of the crack $A(t)$ and the bifurcation angle $\theta(t)$ that defines the orientation of the crack.

Let $A(t,\gamma)$ be the length of the dominant crack at time t, where γ is an elementary event belonging to the space of all possible events Γ in which the probability is defined. $\gamma \in \Gamma, A(t,\gamma)$ represents a possible realization of the random crack propagation process.

The probabilistic process $A(t,\gamma)$can be represented by a random sum of increments having random amplitudes:

$$A(t,\gamma) = A_0 + \sum_{i=1}^{N(t)} Y_i(\gamma), \quad Y_i(\gamma) = \Delta A_i \tag{I.38}$$

where A_0 is the initial crack size that can be considered as a deterministic or statistic parameter, $\sum_{i=1}^{N(t)} Y_i(\gamma)$ is a serie of random variables characterizing the magnitude of the increments of crack length during its propagation and $N(t)$ is a probabilistic counting process defining the number of increments in the interval of time [0,t].

In order to simplify the implementation of the probabilistic model proposed by Sobczyk, the random variables $\sum_{i=1}^{N(t)} Y_i(\gamma)$ are assumed to be independent, identically distributed and positively defined.

The main objective of the probabilistic model of fatigue crack propagation is to construct the crack length distribution and the life distribution. The major advantage of Sobczyk's probabilistic model is that it provides an analytical formulation of the statistical characteristics of the quantities to be understood. However, the determination of parameters of this model such as the magnitude of the increment of the crack length and the critical size of the crack requires special experimental data.

e) Castillo Model

Castillo model *(Castillo and al, 2008)* is based on the same relationships as in the Wöhler curves (i.e. $S-N$ curves). Indeed, this model is constructed by establishing a relationship between the distributions of the initial crack length and the number of loading cycles at failure determined from the $S-N$ curves. The main advantage of this model is that it uses as less random expectations as possible.

Let a_0 be the random size of the dominant crack present in the structure and $f_0(a_0)$ the probability density function corresponding to it. This model considers a fatigue test conducted on a structure that is solicited by a cyclic loading with a constant amplitude varying in the interval defined by the minimum σ_m and maximum value σ_M. It determines the cumulative distribution function of the random lifetime N as a Weibull or Gumbel family of models able to reproduce not only the whole Wöhler field, but any combination of minimum and maximum stresses.

For more precision in the model formulation, the initial crack size a_0 and the number of loading cycles N are replaced respectively by normalized parameters $\frac{a_0}{a_c}$ and $\frac{N}{N_0}$, where a_c is the critical length of the crack for which the failure occurs and N_0 the number of loading cycles taken as reference.

The purpose of this model is to derive the formula $h\left(\frac{a}{a_c},\frac{N}{N_0}\right)$ giving the new crack size ratio $\frac{a}{a_c}$, and the number of cycles ratio $\frac{N}{N_0}$ and to determine the probability density function of $\frac{a_0}{a_c}$ for a given $\frac{N}{N_0}$.

The first step is to determine a function $h(\frac{a_0}{a_c},\frac{N}{N_0})$ that allows to express the crack size for a given life as a function of the initial crack length (for $N=0\,cycles$ the crack size is a_0):

$$\frac{a}{a_c}=h\left(\frac{a_0}{a_c},\frac{N}{N_0}\right) \qquad (I.39)$$

The second step is to write the distribution of the length of the current crack in terms of the distribution of the initial crack length by applying the function $h(\frac{a_0}{a_c},\frac{N}{N_0})$.

To construct the function $h(\frac{a_0}{a_c},\frac{N}{N_0})$, the theory of functional equations (Castillo and al, 2005) is used based on the following property: the expression of this function must be invariant during the life of the structure. More precisely, if a structure containing an initial crack of size $\frac{a_0}{a_c}$ is loaded during a loading time $\frac{N}{N_0}=\frac{N_1+N_2}{N_0}$ cycles, the length of the resulting final crack $\frac{a_N}{a_c}$ can be directly obtained:

$$\frac{a_N}{a_c}=h\left(\frac{a_0}{a_c},\frac{N_1+N_2}{N_0}\right) \qquad (I.40)$$

Furthermore, the crack length can also be determined in another way by decomposing the loading time *N*. It is assumed that the structure containing an initial crack is solicited during a loading time $\frac{N_1}{N_0}$ after which the crack will have a length $\frac{a_{N1}}{a_c}=h(\frac{a_0}{a_c},\frac{N_1}{N_0})$. Following this step, it is considered that the resulting structure in which there is

an initial crack of length $\frac{a_{N1}}{a_c}$ is solicited for an additional loading time $\frac{N_2}{N_0}$ after which the crack reaches the final length $\frac{a_N}{a_c}$. Thus, the value of the final crack length $\frac{a_N}{a_c}$ can be determined using:

$$\frac{a_N}{a_c} = h\left(h\left(\frac{a_0}{a_c}, \frac{N_1}{N_0}\right), \frac{N_2}{N_0}\right) \tag{I.41}$$

Thus $h\left(\frac{a_0}{a_c}, \frac{N_1+N_2}{N_0}\right) = h(h\left(\frac{a_0}{a_c}, \frac{N_1}{N_0}\right), \frac{N_2}{N_0})$ is the translation equation having as unknown the function h and its solution is:

$$\frac{a_N}{a_c} = h\left(\frac{a_0}{a_c}, \frac{N}{N_0}\right) = \phi\left(\phi^{-1}\left(\frac{a_0}{a_c}\right) + \frac{N}{N_0}\right) \tag{I.42}$$

where ϕ is an arbitrary invertible function from which the initial crack length $\frac{a_0}{a_c}$ and the lifetime $\frac{N}{N_0}$ can be expressed respectively as follows: $\frac{a_0}{a_c} = \phi\left(\phi^{-1}\left(\frac{a_N}{a_c}\right) - \frac{N}{N_0}\right)$ and $\frac{N}{N_0} = \phi^{-1}\left(\frac{a_N}{a_c}\right) - \phi^{-1}\left(\frac{a_0}{a_c}\right)$

The probability density function f_{a/a_c} of the length of the crack after a service life $\frac{N}{N_0}$ can be written in function of the probability density function f_{a_0/a_c} of the initial length of the crack (see figure I.30):

$$f_{a/a_c}\left(\frac{a}{a_c}\right) = f_{a_0/a_c}\left(\phi\left(\phi^{-1}\left(\frac{a_N}{a_c}\right) - \frac{N}{N_0}\right)\right)\frac{\phi'\left(\phi^{-1}\left(\frac{a_N}{a_c}\right) - \frac{N}{N_0}\right)}{\phi'\left(\frac{a}{a_c}\right)} \tag{I.43}$$

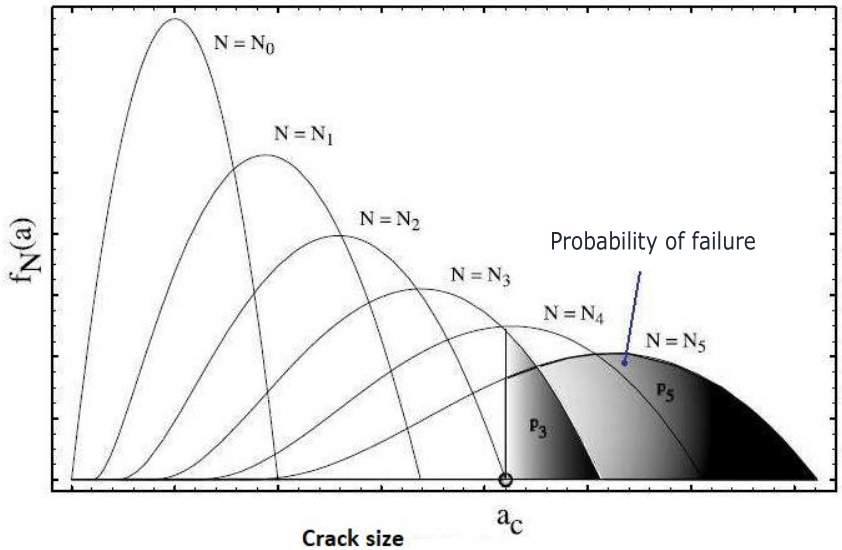

Figure I. 31. Evolution of the pdf $f_{a/a_c}\left(\frac{a}{a_c}\right)$ with the number of cycles and critical crack size

The major advantage of the model proposed by Castillo lies in the fact that it requires the knowledge of only one function, namely the distribution f_{a_0/a_c} of the initial size of the crack or the function ϕ to define the relation between the curves of Wöhler and the curves of propagation of crack under the same history of loading. This has important practical consequences since these curves can be obtained by running conventional fatigue tests and complementing them with simple crack growth data. Thus, the model allows extrapolation to any load conditions. This result justifies the simplicity of the model as well as its flexibility.

f) Madsen model

The dispersion of the fatigue life in the Castillo model is assumed to be induced only by the variability of the initial length of the crack, thus far away from the reality. Indeed, the damage function is defined as a stochastic integral. Thus the construction of the distribution of crack length is more complicated. The basic idea of the model proposed by *(Madsen and al, 1986)* is to transform the equation of the crack growth rate into a probabilistic differential equation. By the use of the Paris's law defined earlier in equation (I.23), and under a constant loading amplitude, the crack growth rate by Madsen can be written by:

$$\frac{da}{dN} = C\, Y(a)^m \Delta\sigma^m (\sqrt{\pi a})^m \qquad (I.44)$$

where C and m are parameters depending on the material, $\Delta\sigma$ is the amplitude of the loading and $Y(a)$ is a geometric correction function.

By integration of equation (I.44), and after separating of the variables, the solution of this differential equation is given by:

$$\Psi(\mathrm{a}) = C\, \Delta\sigma^m N \qquad (I.45)$$

where $\Psi(\mathrm{a})$ is an increasing function which represents the evolution of the crack length; it is defined by:

$$\Psi(\mathrm{a}) = \int_{a_0}^{a} \frac{dx}{Y(x)^m (\sqrt{\pi x})^m} \qquad (I.46)$$

Contrarily to our knowledge concerning that the parameters C and m represent the material as a random variable, in this probabilistic model, we assume that the parameter C is constant and identical for all the specimens while the parameter m is considered as a random quantity. The distribution of crack length after a given service life appears to be complicated. Thus, the construction of a sample of realizations of the crack propagation curve is easier, this by simulations of the random process and by calculating the integral.

This model is applied in several probabilistic problems dealing with fatigue crack propagation, particularly in the context of reliability analyzes. *(Casciati and al, 2007)* used this model to analyze experimental data obtained by crack propagation tests in compact tension specimens. They observed that the dispersion of experimental data is low.

4.2.3. Conclusion about the probabilistic model of fatigue crack propagation

The dispersion can have different sources such as the uncertainties that affect the parameters defining the geometry of the structure, the properties of the material and the applied loading. In this section, we have given a presentation of models dealing with the propagation of fatigue cracks in a probabilistic context. These models can be divided into two categories.

The basic idea of the first category consists in weighting the deterministic laws governing the crack growth, such as the Paris' law, by a random process which makes it possible to take into account the dispersion related to the properties of the material. The difficulty with this type of models is that they require relatively significant

experimental works to determine the various parameters involved. Besides, if the propagation process is complex, which implies a difficult deterministic mathematical model, the formulation of the probabilistic model will be also difficult to handle.

The second class of models consists in representing the probabilistic character of the crack propagation by a process of Markov chains. Even if the formulation of these models has been extended for the case of mixed mode propagation, they are very criticized because their basis is purely statistical and does not represent the real physics which accompanies the process of propagation of cracks. Even if these models have been adopted in several applications, especially in failure mode I where the crack follows the same direction during its propagation, they are far of representing a realistic case since the crack follows curvilinear and irregular paths. Also, these models do not take in consideration the effect of the retardation induced by the application of overloads. In fact, many engineering structures are frequently subjected to constant amplitude loading with occasional high peak loads, which are called overloads. For instance, due to the constant air current and occasional turbulence during the flight, aircrafts are always under the influence of this phenomenon. Curiously, as confirmed by many experimental studies *(Schijve, 1962)*, *(Schijve and al, 2004), (Manjunatha and al, 2004), (Daneshpour and al, 2012), (Dirik and al, 2018), (Hemnesi and al, 2022),* these overloads have benefit effect on the fracture behavior, since they retardation the fatigue crack growth and consequently can enhance the fatigue lifetime of the structure. This retardation effect is mainly attributed to a secondary plastic strain created around the crack tip. For this reason, it is necessary to study in deep the effect of these overloads on the crack growth behavior. In this context, the probabilistic models presented in this section do not consider the effect of the retardation.

5. Conclusion

Fatigue is the most important form of component failure due to cyclic loading. For safe and efficient design and evaluation of engineering materials that experience dynamic cyclic loading in service, it is essential to find an efficient prediction method in term of time computation reduction and which has a good precision on the computed results. For that, we have first presented the basics of fracture mechanics which are the basis of all the laws used for the phenomenon of fatigue, and then have focused on understanding the fatigue crack growth phenomenon. Methods used to compute the fracture driving forces, as the stress intensity factor in linear elastic fracture mechanics have been presented. Through a comparative study dealing with fatigue crack growth in CT specimen, we have found that the energetic method based on independent path integral is more accurate than the kinematic method. Fatigue crack growth models have also been studied, and predictions are compared to experimental data taken from the literature. We have shown that Walker's and Forman's laws are more suitable than the Paris-Erdogan's one to fit experimental data. Finally, stochastic model for fatigue crack propagation have been presented because deterministic approaches cannot be used especially with the random nature of the fatigue phenomenon.

The fatigue phenomenon can have different sources of uncertainty that can affect the parameters defining the structural geometry, material properties and applied loading. Particular attention has been paid to the presentation of models dealing with fatigue crack propagation in a probabilistic context. As mentioned earlier in this chapter, these models can be classified into two categories. In the first, the basic idea consists in weighting

the deterministic the fatigue crack growth laws, such as the law of Paris, by a random process which makes it possible to consider the uncertainty of the material properties. The difficulty with this type of model is that it requires relatively substantial experimental work to determine the statistical characteristics of parameters involved in the probabilistic modelling. Moreover, if the propagation process is complex, which implies a deterministic mathematical model that is difficult to control, the formulation of the probabilistic model will therefore be a non-trivial task. The second class of models consists in representing the stochastic character of crack propagation by a Markov chains based process. Even though the formulation of these models has been extended for the case of mixed-mode propagation, they are highly criticized because their basis is purely statistical and does not represent the true physics to the crack propagation.

Although most of these models have been adopted in several applications, most deal with failure in mode I for which the crack follows the same direction during its propagation, where in practice the cracks follow curvilinear and irregular paths. As an alternative to these probabilistic fatigue crack propagation models, we can mention other more general approaches called probabilistic finite element methods. These approaches developed during the last two decades aim to take into account the uncertainties in mechanical calculation and more precisely in finite element modeling. Unfortunately, these approaches are inefficient when the probabilistic dimension is high and the mechanical model itself is computational time demanding such is the case for problems dealing with fatigue crack growth. Thus why developing enhanced alternatives of these approaches will be the issue of this thesis.

Chapter II: Identification of efficient cubature schemes for the computation of multidimensional integrals

1. Introduction

In the previous chapter, we have highlighted that fatigue crack growth is a random process, mainly due to the uncertainties observed on the mechanical properties of the materials, on the applied loading as well as the parameters defining the geometry of the structure. As we have seen, a wide variety of models have been proposed in the literature to consider these various sources of uncertainties and to assess their effect on the fatigue crack growth life, but unfortunately, they encounter some difficulties especially when dealing with engineering problems. To overcome these limitations, uncertainties propagation methods, seems to be the best alternative. These methods have been developed over the past forty years and have been successfully applied to various problems in the fields of mechanical and civil engineering. They can be classified into two categories. The first one is intrusive methods which are represented by any scheme that adapts the governing equations of the deterministic model to propagate the effect of uncertainties on the mechanical responses. They can only be applied to a limited number of problems, where the governing equations are mathematically very simple and the variability of the uncertain parameters is low, which is unfortunately not the case of fatigue crack growth problems. The second category is the non-intrusive methods, where the probabilistic and the mechanical computations are dissociated. Indeed, the variability of the mechanical responses induced by the uncertainty of the input parameters is assessed through a series of runs of the deterministic mechanical model on some points of the random space. The main advantage of the non-intrusive methods is the fact that the mechanical model is considered as a black box. It allows us to benefit from the advanced modeling capacity of some numerical tools such as commercial finite elements codes to deal with a large number of complex mechanical problems, such as fatigue crack growth problems. However, non-intrusive methods still suffer from some limitations, mainly their inefficiency when the number of uncertain parameters is very large. This problem is often referred to as the curse of dimensionality. Despite this limitation, the intrusive methods remain a serious candidate to tackle complex mechanical problems such as the fatigue crack growth one.

In this context, this thesis aims to develop an accurate and efficient uncertainty propagation method to deal with a large class of fatigue crack growth problems. Hence, a first attempt to reach this objective will be conducted in this chapter by exploring efficient monomial cubature schemes. This chapter contains four main sections. Section 2 reviews the principle of the uncertainty propagation problem through a mechanical model. The mathematical formulation of the three finalities of the uncertainty propagation problem, such as statistical moment analysis, reliability analysis and sensitivity analysis will be also reminded. Section 3 will be devoted to the presentation of standard methods for the computation of integrals quantities derived from uncertainty propagation analysis. Section 4 reviews the mathematical formulation of some efficient

monomial cubature schemes. Finally, section 5 addresses various numerical examples to show the potential of monomial cubature schemes in the computation of multidimensional integrals involved in uncertainty propagation analysis.

2. Uncertainty propagation framework

2.1. General principle

Let us consider a mechanical model (e.g., a fatigue cracked component) having N uncertain parameters gathered in the vector $\boldsymbol{x} = \{x_1, \dots, x_N\}^T \in \mathfrak{D}_{\boldsymbol{x}}$. Mathematically speaking, this model can be represented by the following deterministic mapping f:

$$y = f(\boldsymbol{x}) \tag{II.1}$$

where $y \in \mathfrak{D}_y$ is the quantity of interest or the response of the mechanical model (e.g., a crack length, a stress intensity factor, a fatigue life, etc.) obtained either by explicit (i.e., analytical closed formula) or implicit (i.e., finite elements model) representation of the function f. In the sequel, and without a loss of generality, only models having a single mechanical response are presented, which means that y is a scalar quantity. Indeed, all the derivations hold component-wise in case of vector-valued models $\boldsymbol{y} = \{y_1, \dots, y_M\}^T \in \mathfrak{D}_{\boldsymbol{y}}$.

Due to the uncertainty embodied in the input parameters $\boldsymbol{x}$, the response y of the mechanical model becomes also uncertain by uncertainty propagation through the mapping f. Hence, we will denote by $Y = f(\boldsymbol{X})$ the probabilistic model associated to the mechanical model defined by equation (II.1), $\boldsymbol{X} = \{X_1, \dots, X_N\}^T \in \mathfrak{D}_{\boldsymbol{X}}$ an N-dimensional random variable, with a prescribed probability density function $p_{\boldsymbol{X}}(\boldsymbol{x})$, modeling the uncertainty on the input parameters $\boldsymbol{x}$ and $Y \in \mathfrak{D}_y$ a scalar random variable representing the uncertainty on the mechanical response y and following a probability density function $p_Y(y)$.

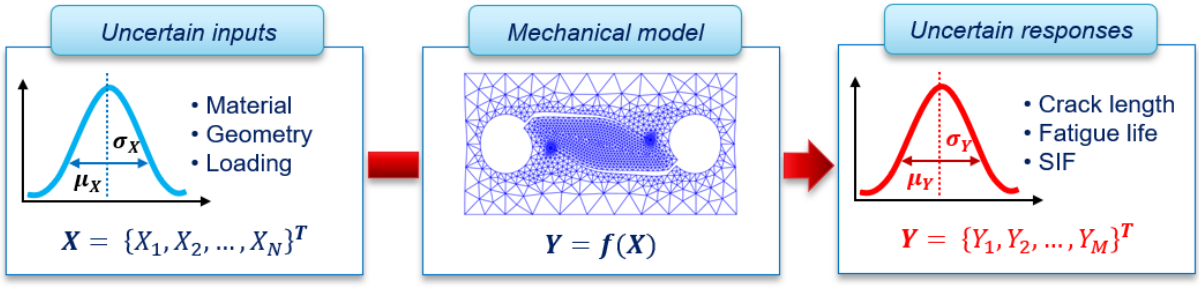

Figure II. 1. Principle of uncertainty propagation through a mechanical model

The principle of uncertainty propagation is schematically illustrated in figure II.1. As can be seen, it comprises three main steps. The first is to model the uncertainties associated with the input parameters using probabilistic models such as random variables and random fields. The choice of the suitable probabilistic model and its related parameters can be done by performing statistics if data are available or based on expert judgement. The second step is to define the mechanical model which ranges from a simple analytical formula to a complex time-consuming numerical model. The mechanical model maps the set of input parameters to the outputs of interest. In the third step, uncertainty propagation is performed through

the mechanical model using suitable coupling schemes. Then, various probabilistic analysis can be performed on the obtained results to quantify the variability of the uncertain responses.

In engineering problems, the components of the N-dimensional random variable $\boldsymbol{X}$ may have different probability distributions and may also be correlated with each other. Consequently, carrying out probabilistic computations in the physical random space couldn't be a trivial task. For this purpose, we prefer to recast the uncertainty propagation problem in the standard random space, where the N-dimensional random variable $\boldsymbol{X}$ is transformed into a N-dimensional normal variable $\boldsymbol{U} = \{U_1, \dots, U_N\}^T \in \mathbb{R}^N$ with independent components $U_i, i \in \{1, \dots, N\}$ following a standard normal distribution $\varphi_{U_i}(u_i), i \in \{1, \dots, N\}$ with zero mean and unit standard deviation. This can be easily achieved using an isoprobabilistic transform $\boldsymbol{X} = T(\boldsymbol{U})$, such as the Nataf *(Nataf, 1962)* or the Rosenblatt transformation *(Rosenblatt, 1952)*. Therefore, the deterministic mapping f representing the mechanical model, reads in the standard random space:

$$y = f \circ T(\boldsymbol{u}) \equiv h(\boldsymbol{u}) \qquad (II.2)$$

Figure II.2 illustrates the isoprobabilistic transfomation for the 2-dimensional case, where $p_{\boldsymbol{X}}(\boldsymbol{x})$ and $\varphi_{\boldsymbol{U}}(\boldsymbol{u})$ are the probability density functions of the 2-dimensional random variables $\boldsymbol{X} = \{X_1, X_2\}^T$ and $\boldsymbol{U} = \{U_1, U_2\}^T$, respectively.

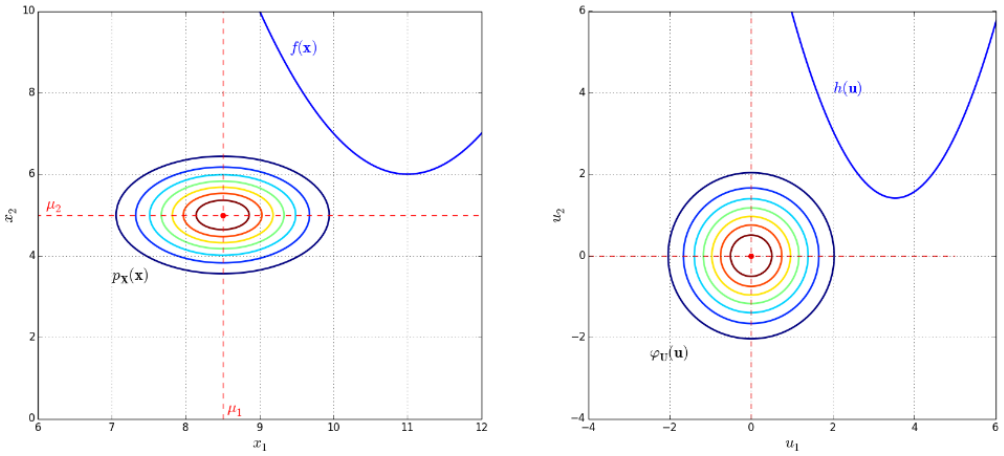

Figure II. 2. Illustration of the isoprobabilistic transformation for the 2-dimensional case

Once the uncertainty propagation through the mechanical model is carried out, three kinds of analyses can be performed, as illustrated by figure II.3.

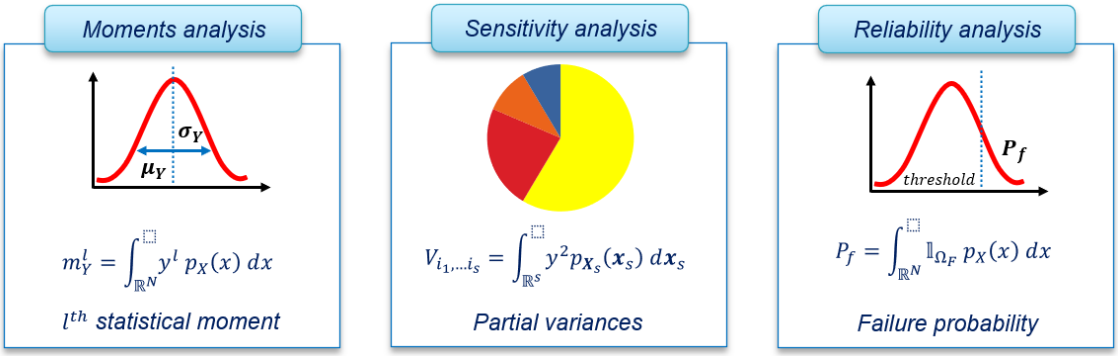

Figure II. 3. Classification of uncertainty propagation analysis

The first one, called response variability analysis, aims to compute the few first statistical moments m_Y^l and to construct the probability density function $p_Y(y)$ of the mechanical response y. Here, focus is mainly on the neighborhood of the mean value of the random variable Y. The second one, called sensitivity analysis, aims at quantifying the contribution of each uncertain input parameter on the variability of the mechanical response. Here, sensitivity indices derived from partial variances $V_{i_1,\dots i_s}$ are computed. Finally, the third one called, reliability analysis, aims at computing the probability P_f that the mechanical system under consideration fails with respect to one or more failure criteria. Here, the tails of the mechanical response distribution $p_Y(y)$ are of particular interest.

2.2. Statistical moments analysis

The uncertainty of the input parameters $\boldsymbol{x} = \{x_1, \dots, x_N\}^T$ of the mechanical model f is represented by an N-dimensional random variable $\boldsymbol{X} = \{X_1, \dots, X_N\}^T$ with prescribed $p_{\boldsymbol{X}}(\boldsymbol{x})$. Due to the uncertainty propagation, the mechanical response y becomes an uncertain quantity. As this later is considered as scalar, for the sake of simplicity as stated previously, the variability of the mechanical response y can be described by a random variable Y. To characterize the probabilistic content of Y, it is necessary to compute its statistical moments and construct its probability density function $p_Y(y)$. The l^{th} statistical moment of the random variable Y, i.e. m_Y^l, is defined as:

$$m_Y^l = \mathbb{E}[Y^l] = \int_{\mathcal{D}_Y} y^l \, p_Y(y)\, dy = \int_{\mathcal{D}_{\boldsymbol{X}}} [f(\boldsymbol{x})]^l \; p_{\boldsymbol{X}}(\boldsymbol{x})\, d\boldsymbol{x} = \int_{\mathbb{R}^N} [f \circ T(\boldsymbol{u})]^l \; \varphi_U(\boldsymbol{u}) d\boldsymbol{u} = \int_{\mathbb{R}^N} [h(\boldsymbol{u})]^l \, \varphi_U(\boldsymbol{u}) d\boldsymbol{u} \qquad (II.3)$$

where $\mathbb{E}[.]$ denotes the mathematical expectation.

It is clear from equation (II.3) that the estimation of an l^{th} order statistical moment m_Y^l requires solving a tough mathematical problem, which is the computation of N-dimensional integrals. Indeed, for engineering problems, it is difficult to obtain a closed-form solution of these integrals because the mechanical model is often given by a time-consuming implicit representation, which requires the use of numerical integration schemes, which unfortunately suffer from inefficiency when dealing with high-dimensional problems (i.e., the number N of uncertain parameters is very high.

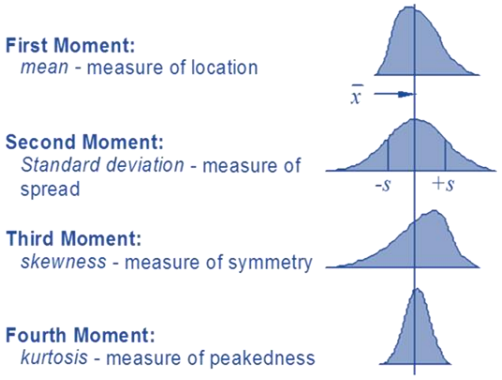

Figure II. 4. Significance of the first four statistical moments

To get a complete picture of the probabilistic content of Y you can construct its probability density function $p_Y(y)$, in addition to the estimates of the statistical moments. This can be done, by a moments-

based technique *(Pearson and Tukey, 1965)* which requires accurate estimates of the four central statistical moments namely, the mean μ_Y, the standard deviation σ_Y, the skewness δ_Y, and the kurtosis κ_Y. As depicted in figure II. 4, these statistical moments allow to measure respectively, the location, the spread, the symmetry and the peakedness of the probability density function. They can be derived easily from (II.3) and defined in standard random space as follow:

$$\mu_Y = \int_{\mathbb{R}^N} h(\boldsymbol{u})\, \varphi_U(\boldsymbol{u}) d\boldsymbol{u} \qquad (II.4)$$

$$\sigma_Y^2 = \int_{\mathbb{R}^N} [h(\boldsymbol{u}) - \mu_Y]^2\, \varphi_U(\boldsymbol{u}) d\boldsymbol{u} \qquad (II.5)$$

$$\delta_Y = \frac{1}{\sigma_Y^3} \int_{\mathbb{R}^N} [h(\boldsymbol{u}) - \mu_Y]^3\, \varphi_U(\boldsymbol{u}) d\boldsymbol{u} \qquad (II.6)$$

$$\kappa_Y = \frac{1}{\sigma_Y^4} \int_{\mathbb{R}^N} [h(\boldsymbol{u}) - \mu_Y]^4\, \varphi_U(\boldsymbol{u}) d\boldsymbol{u} \qquad (II.7)$$

Various moments-based techniques are available in the literature, among them a versatile one called shifted generalized lognormal distribution is developed *(Low, 2013)*. It has the following explicit analytical expression which is very flexible to fit a large class of probability density functions and covers a large part of the skewness-kurtosis diagram.

$$p_Y(y) \approx \frac{\alpha}{y-\gamma} \exp\left[-\frac{1}{r\beta^r}\left|\ln\left(\frac{y-\gamma}{\Delta}\right)\right|^r\right], \qquad \gamma < y < \infty \qquad (II.8)$$

where $\alpha = 1/r^{1/r}\, \beta\, \Gamma(1 + 1/r)$ with $\Gamma(.)$ is the gamma function, β and r are shape parameters, γ and Δ are for location and scale parameters, respectively.

The probability density function $p_Y(y)$ can be constructed in another way, using a kernel smoothing technique *(Wand and Jones, 1995)*, by the following approximation, which requires a sample set of the mechanical response $\{y_i\}_{i=1}^N$:

$$p_Y(y) \approx \frac{1}{N\, \Delta_K} \sum_{i=1}^{N} K\left(\frac{y - y_i}{\Delta_K}\right) \qquad (II.9)$$

where $K(.)$ is positive function named kernel and Δ_K is the bandwidth parameter.

2.3. Sensitivity analysis

Sensitivity analysis of a mechanical model provides a ranking of the uncertain input parameters with respect to their significance on the variability of the response. This information is of a great importance for the analyst, since it allows him to focus on the most significant parameters, since insignificant ones may be considered as deterministic quantities and fixed to their respective nominal values. This ranking of the uncertain input parameters can be obtained either by local or global sensitivity measurements. For that reason, sensitivity analysis methods are divided into two categories: Local Sensitivity methods (LS) and Global Sensitivity methods (GS).

The first one, that is LS methods concentrate on the measurement of the local impact of input parameters on the response of the model. In other words, it allows to study how a little change of an input parameter in the vicinity of a specific value (e.g., mean value, most probable failure point…) can influence the response of the model. The sensitivity measurements given by the most LS methods are based on the computation of the gradient of the mechanical response with respect to each of its uncertain input parameters around a given value. Many numerical techniques are available to perform such a computation efficiently, including finite-difference and adjoint differentiation schemes.

GS methods provide more complete information compared to LS methods, as they have the advantage of considering the overall impact of the input parameters and their mutual interactions on the mechanical response, not only in the vicinity of a specific point but on the whole uncertain domain, defined as the variation space of the input parameters due to their uncertainties. GS methods can be classified into two groups, the regression-based methods and the Variance-based methods, which also called in the literature ANOVA-based methods, where the term ANOVA means ANalysis Of VAriance. These later, i.e. ANOVA-based methods are very promising, and have therefore received growing attention over the last two decades compared to regression-based methods which do not provide accurate sensitivity measurements in the case of highly non-linear mechanical model *(Saltelli and Sobol 1995)*. Among ANOVA-based sensitivity measurements, we can find Fourier Amplitude Sensitivity Test (FAST) indices *(Cukier and al, 1978)* and Sobol indices *(Sobol, 1993)*. In the following, the focus will be solely on the presentation of the variance decomposition problem and the derivation of the global sensitivity measurements of Sobol. Interested readers can find in *(Saltelli and al, 2000)* an extended state-of-the-art of the available sensitivity analysis methods.

Let us suppose that the mapping f representing the mechanical model is square-integrable with respect to the probability measure associated to the probability density function $p_{\boldsymbol{X}}(\boldsymbol{x})$ of the N-dimensional random variable $\boldsymbol{X} = \{X_1, \dots, X_N\}^T$ where the components $X_{\mathrm{i}}, i \in \{1, \dots, N\}$ are independent. Under these assumptions, $p_{\boldsymbol{X}}(\boldsymbol{x})$ can be obtained as the product of the marginal probability functions $p_{X_{\mathrm{i}}}(x_{\mathrm{i}}), i \in \{1, \dots, N\}$ of each input parameter, and the mapping f can be represented by a finite hierarchical expansion known as Sobol decomposition *(Sobol, 1993)*:

$$Y = f(\boldsymbol{X}) = f_0 + \sum_{i=1}^{N} f_i(X_i) + \sum_{i_1=1}^{N-1} \sum_{i_2=i_1+1}^{N} f_{i_1,i_2}(X_{i_1}, X_{i_2}) + \cdots + f_{1,2,\dots,N}(X_1, X_2, \dots, X_N) \qquad (II.10)$$

where f_0 is a constant, $f_i(X_i)$ is a univariate component function representing the main effect of the uncertain input parameter x_{i} acting alone, $f_{i_1,i_2}(X_{i_1}, X_{i_2})$ is a bivariate component function describing the effect of interaction between the uncertain input parameters x_{i_1} and x_{i_2}, and so on. The last component in equation (II.10) represents the effect of the interaction of all uncertain input parameters on the variability of the mechanical response y.

The uniqueness of the representation given by equation (II.10) is ensured by choosing summands that satisfy the following conditions *(Sobol, 1993)*:

$$f_0 = \int_{\mathfrak{D}_{\boldsymbol{X}}} f(\boldsymbol{x})\, p_{\boldsymbol{X}}(\boldsymbol{x})\, d\boldsymbol{x} \tag{II.11}$$

$$\int_{\mathfrak{D}_{X_i}} f_{i_1,\dots,i_s}(x_{i_1},\dots,x_{i_s})\, p_{X_i}(x_i)\, dx_i = 0, \forall\, i \in \{i_1,\dots,i_s\} \tag{II.12}$$

where $\mathfrak{D}_{\boldsymbol{X}}$ is the support of the N-dimensional random variable $\boldsymbol{X} = \{X_1,\dots,X_N\}^T$, $\mathfrak{D}_{X_i}$ and $p_{X_i}(x_i)$ are the support and the marginal probability density function of the random variable X_i.

It follows from (II.11) and (II.12) that f_0 is the mean value of the function f, all summands are orthogonal, and the expectation of any summand vanish. Consequently, a recursive construction of the components functions of (II.10) can be obtained:

$$f_0 = \mathbb{E}[f(\boldsymbol{X})] \tag{II.13}$$

$$f_i(X_i) = \mathbb{E}[f(\boldsymbol{X})|X_i] - f_0 \tag{II.14}$$

$$f_{i_1,i_2}(X_{i_1},X_{i_2}) = \mathbb{E}\big[f(\boldsymbol{X})\big|X_{i_1},X_{i_2}\big] - f_{i_1}(X_{i_1}) - f_{i_2}(X_{i_2}) - f_0 \tag{II.15}$$

and so on, where $\mathbb{E}[.|.]$ denotes the mathematical conditional expectation.

Now by squaring the Sobol decomposition (II.10) and integrating over $\mathfrak{D}_{\boldsymbol{X}}$, the total variance of random variable Y representing the variability of the mechanical response y, can be obtained as follows:

$$V_Y = \mathbb{V}[Y] = \mathbb{V}[f(\boldsymbol{X})] = \sum_{i=1}^{N} V_i + \sum_{i_1=1}^{N-1}\sum_{i_2=i_1+1}^{N} V_{i_1,i_2} + \cdots + V_{1,2,\dots,N} \tag{II.16}$$

where $\mathbb{V}[.]$ denotes the mathematical variance, and the components $V_{i_1,\dots,i_s}$ appearing in the above expansion, are referred to as s^{th} order partial variances and defined by:

$$V_{i_1,\dots,i_s} = \mathbb{V}\big[f_{i_1,\dots,i_s}(x_{i_1},\dots,x_{i_s})\big], \quad s \in \{1,\dots,N\} \tag{II.17}$$

The ratio between the s^{th} order partial variances $V_{i_1,\dots,i_s}$ and the total variance V_Y, given by (II.16), provides a normalized sensitivity measurement $S_{i_1,\dots,i_s}$, called Sobol's sensitivity index *(Sobol, 1993)*, describing the sensitivity of the mechanical response Y to the interaction between the uncertainties related to the input parameters $(x_{i_1},\dots,x_{i_s})$. It is defined by:

$$S_{i_1,\dots,i_s} = \frac{V_{i_1,\dots,i_s}}{V_Y} \tag{II.18}$$

Moreover, the Sobol total sensitivity indices S_i^T, $i \in \{1,\dots,N\}$ can be easily derived in the same way. They are introduced to evaluate the total effect of uncertain input parameters:

$$S_i^T = \frac{V_i^T}{V_Y} \tag{II.19}$$

where V_i^T is the total variance accounting the main effect of the uncertain input parameter x_i (i.e., when the uncertainty related to x_i acting solely on the mechanical response) and higher order effect resulting from the interaction with the uncertainties of the other input parameters.

The total variance can be defined by:

$$V_i^T = \mathbb{E}_{\sim X_i}[\mathbb{V}_{X_i}[Y]] = \mathbb{E}_{\sim X_i}[\mathbb{V}_{X_i}[f(\boldsymbol{X})]] \qquad (II.20)$$

where the inner term $\mathbb{V}_{X_i}[.]$ is the variance of Y only due to the uncertainty of the input parameter x_i and the outer term $\mathbb{E}_{\sim X_i}[.]$ is the expectation value due to the uncertainties related to all input parameters $\sim x_i$ except x_i.

After performing some algebraic operations, the total variance can be rewritten as follow:

$$V_i^T = \mathbb{E}_{\sim X_i}\left[\mathbb{E}_{X_i}[f(\boldsymbol{X})^2] - \left(\mathbb{E}_{X_i}[f(\boldsymbol{X})]\right)^2\right] = \mathbb{E}[f(\boldsymbol{X})^2] - \mathbb{E}_{\sim X_i}[\left(\mathbb{E}_{X_i}[f(\boldsymbol{X})]\right)^2] = \mathbb{E}[f(\boldsymbol{X})^2] - \mathbb{E}_{\sim X_i}[\left(\mathbb{E}_{X_i}[f(\boldsymbol{X})]\right)^2] \qquad (II.21)$$

The first term in (II.21) is the second order statistical moment m_Y^2 which can be derived from (II.3) by setting l equal to 2. However, the computation of the second term is more complex since it involves the evaluation of two integrals:

$$\mathbb{E}_{\sim X_i}[\left(\mathbb{E}_{X_i}[f(\boldsymbol{X})]\right)^2] = \int_{\sim X_i}\left(\int_{X_i} f(\boldsymbol{x})\ p_{X_i}(x_i)\, dx_i\right)^2 p_{\sim \boldsymbol{X_i}}(\sim \boldsymbol{x_i}) d\sim \boldsymbol{x_i} \qquad (II.22)$$

The inner integral is one-dimensional and can be easily computed by numerical integration schemes or analytically if the integrand is available under closed form explicit solution. However, the outer integral is multidimensional, and its evaluation is not trivial by conventional integration schemes, especially when the integrand is only available under a time-consuming implicit form and the integration dimension is very high. As shown in subsection 2.2, sensitivity analysis presents the same difficulties as of statistical moments analysis, since, mathematically speaking, the problem in both cases is to compute multidimensional integrals.

For the consistency throughout the manuscript of this thesis, equation (II.22) is rewritten in the standard random space. It now reads:

$$\mathbb{E}_{\sim X_i}\left[\left(\mathbb{E}_{X_i}[f(\boldsymbol{X})]\right)^2\right] = \mathbb{E}_{\sim U_i}[\left(\mathbb{E}_{U_i}[f(\boldsymbol{U})]\right)^2] = \int_{\sim U_i}\left(\int_{U_i} h(\boldsymbol{u})\ \varphi_{U_i}(u_i)\, du_i\right)^2 \varphi_{\sim \boldsymbol{U_i}}(\sim \boldsymbol{u_i}) d\sim \boldsymbol{u_i} \qquad (II.23)$$

2.4. Reliability analysis

Reliability analysis aims to assess the safety level of an engineering system or structure against a prescribed failure criterion. Commonly, the failure criterion concept can be defined as the gap between two fundamental quantities named the *Demand* and the *Capacity*, respectively. In mechanical engineering, as well as in civil engineering, the *Demand* can be defined as the system response, such as a stress intensity factor or a crack length, induced by the loading conditions. The *Capacity*, on the other hand, represents a

threshold level, such as an ultimate stress intensity factor (i.e., fracture toughness) or crack length, beyond which the system collapses. Mathematically speaking, the failure criterion is characterized by the limit state function, or the performance function, denoted G. It is defined as a mapping of the uncertain parameters $\boldsymbol{x} = \{x_1, \dots, x_N\}^T$. The random space can be split up into two regions: the failure domain $\Omega_F = \{\boldsymbol{x} \in \mathfrak{D}_X | \, G(\boldsymbol{x}) < 0\}$ and the safety domain $\Omega_S = \{\boldsymbol{x} \in \mathfrak{D}_X | \, G(\boldsymbol{x}) > 0\}$. The set of points $\Gamma = \{\boldsymbol{x} \in \mathfrak{D}_X | \, G(\boldsymbol{x}) = 0\}$ represents the limit state surface which is the frontier between the failure and the safety domains. Figure II. 5 schematically illustrates these concepts in the case of a two-dimensional random space.

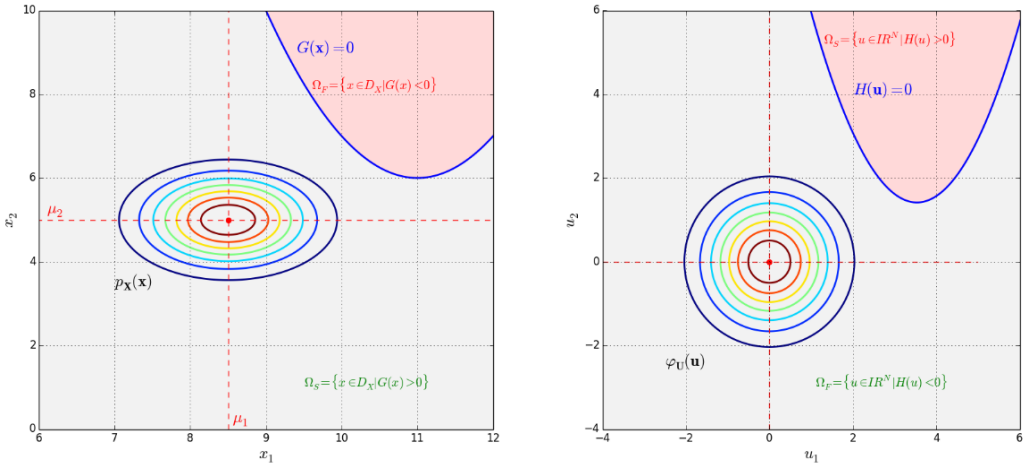

Figure II. 5. Reliability concepts in the physical random space (left) and the standard random space (right)

According to the above concepts, the probability of failure, denoted P_f, and defined as the complementary event of the reliability R, that is $P_f = 1 - R$, reads:

$$P_f = \text{Prob}[G(\boldsymbol{x}) \leq 0] = \int_{G(\boldsymbol{x})\leq 0} p_{\boldsymbol{X}}(\boldsymbol{x}) \, d\boldsymbol{x} = \int_{\mathbb{R}^N} \mathbb{I}_{\Omega_F}(\boldsymbol{x}) \, p_{\boldsymbol{X}}(\boldsymbol{x}) d\boldsymbol{x} \qquad (II.24)$$

where $p_{\boldsymbol{X}}$ is the joint probability density of the random vector $\boldsymbol{X}$, and $\mathbb{I}_{\Omega_F}$ is the indicator function on Ω_F, which is equal to 1 if $G(\boldsymbol{x}) \leq 0$ and 0 otherwise.

As can be seen, the estimation of the probability of failure P_f is nothing other than the computation of a multidimensional integral, which reminds us of the same computational problem encountered in subsections 2.2 and 2.3 presenting statistical moments and sensitivity analysis. As the limit state function G is often not available in explicit form, especially when dealing with engineering problems, the integral in above equation cannot be analytically computed. Instead, numerical methods are often employed. The efficiency of the numerical scheme mainly depends on the complexity of the limit state function and the problem dimensionality N. To avoid multidimensional integrals computation in the estimation of the probability of failure, an approximation technique called First Order Reliability Method (FORM) has been developed in the early seventies *(Hasofer and Lind, 1974)*. To apply FORM, the first step is to rewrite the reliability problem in the standard random space, using probabilistic transformation as shown in subsection 2.1. Consequently, the probability of failure defined earlier by equation (II.24), is now given by the following expression:

$$P_f = \int_{G(x)\leq 0} p_X(x)\, dx = \int_{H(u)\leq 0} \varphi_U(u) du = \int_{\mathbb{R}^N} \mathbb{I}_{\Omega_F}(u)\, \varphi_U(u) du \qquad (II.25)$$

where $H(\boldsymbol{U}) \equiv G \circ T(\boldsymbol{U}) = G(\boldsymbol{X})$ is the limit state function in the standard random space, φ_U is the standard multinormal probability density function and $\mathbb{I}_{\Omega_F}$ is the indicator function on Ω_F, which is equal to 1 if $H(\boldsymbol{u}) \leq 0$ and 0 otherwise.

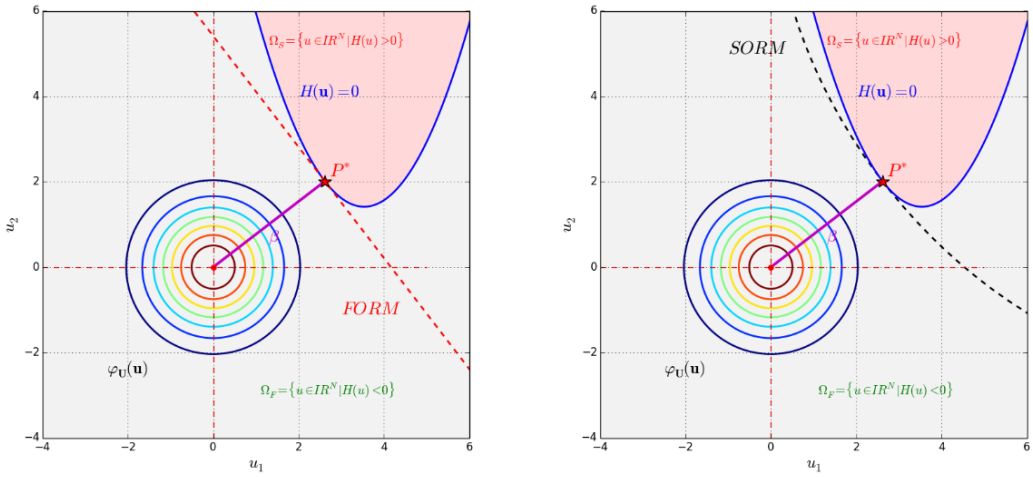

Figure II. 6. Approximation of the probability of failure using FORM (left) and SORM (right).

Then, the FORM approximation substitutes the limit state function H by a hyperplane tangent to the true failure domain at the Most Probable Failure Point (MPFP) denoted P^*, also called the design point, which is defined as the nearest point of the limit state surface to the origin of the standard random space as depicted in figure II.6. The MPFP is obtained by solving the following constrained optimization problem:

$$\begin{cases} \|\boldsymbol{u}^*\| = \min_{\boldsymbol{u}\in\mathbb{R}^N} \|\boldsymbol{u}\| \\ subject\ to\ H(\boldsymbol{u}) = 0 \end{cases} \qquad (II.26)$$

Once the coordinates $\boldsymbol{u}^* = \{u_1, u_2, \dots, u_n\}^T$ of P^* are found, the Hasofer-Lind reliability index $\beta_{HL} = \|\boldsymbol{u}^*\|$ is computed, and the first order approximation of the probability of failure reads:

$$P_f \approx P_{f,FORM} = \Phi(-\beta_{HL}) \qquad (II.27)$$

where Φ is the cumulative distribution function of a standard normal variable.

The FORM approximation of the probability of failure is often satisfactory, especially for high values of the reliability index, provided that the MPFP is well identified. It is clear from figure II.5 that FORM approximation is exact only when the true limit state function is linear. Unfortunately, this situation is rarely encountered in real life problems where the corresponding limit state function can be highly nonlinear. For this reason, the Second Order Reliability Method (SORM) has been developed. As depicted in figure II.5, it uses a quadratic surface to better fit the true failure domain. Based on Breitung's approximation *(Breitung, 1984)* the SORM estimation of the probability of failure writes:

$$P_f \approx P_{f,SORM} = \Phi(-\beta_{HL}).\prod_{i=1}^{N-1} \frac{1}{\sqrt{1-\beta_{HL}.\kappa_i}} = P_{f,FORM}.\prod_{i=1}^{N-1} \frac{1}{\sqrt{1-\beta_{HL}.\kappa_i}} \qquad (II.28)$$

where κ_i, $i \in \{1, \dots, (N-1)\}$ are the main curvatures of the limit state function at the MPFP.

As can be seen from (II.28), SORM simply improves the estimation of the failure probability given by FORM through a ponderation by a correction factor $\prod_{i=1}^{N-1}\frac{1}{\sqrt{1-\beta_{HL}\cdot\kappa_i}}$ including information about the curvature of the limit state function. Note that, these curvatures are taken as positive quantities for a convex limit state function. Breitung *(Breitung, 1984)* has shown that the approximation given by SORM is accurate for high values of the reliability index, since it tends toward the exact value of the failure probability when the reliability index is infinite. However, SORM becomes inefficient when the dimensionality N of the reliability problem is high. This is due to the computation of the $(N-1)$ curvatures, which requires the evaluation of the second order derivatives of the limit state function with respect to the uncertain input parameters. This could lead to an unaffordable computation cost, especially for time-consuming implicit limit state functions, where the second order derivatives are computed using a finite difference scheme.

3. Classical methods for multidimensional integration

3.1. Mathematical problem statement

Performing uncertainty propagation analysis involves computation of multidimensional integrals, as shown in the previous section if we refer to equations (II.3), (II.23) and (II.25), respectively, for the evaluation of the statistical moments, the partial variances, and the probability of failure. This question is rather difficult to solve, especially when the integrand is only available in an implicit form and the integrals have a high dimensionality. In the following, we will focus on classical methods commonly used to compute multidimensional integrals. But let us first recalls the mathematical problem to be addressed. The aforementioned integrals can be represented by the following Gaussian-weighted integral, since they are defined in the standard random space:

$$I[\mathfrak{f}] = \int_{\mathbb{R}^N} \mathfrak{f}(\boldsymbol{u})\,\varphi_{\boldsymbol{U}}(\boldsymbol{u})d\boldsymbol{u} = \frac{1}{\left(\sqrt{2\pi}\right)^N}\int_{\mathbb{R}^N} \mathfrak{f}(\boldsymbol{u})\exp\left[\frac{\boldsymbol{u}^T\boldsymbol{u}}{2}\right]d\boldsymbol{u} \qquad (II.29)$$

where $I[\mathfrak{f}]$ denotes the integration for short, $\mathfrak{f}(\boldsymbol{u})$ denotes an arbitrary integrand. For instance, if the second order statistical moment σ_Y^2 is concerned, $\mathfrak{f}(\boldsymbol{u}) = [h(\boldsymbol{u}) - \mu_Y]^2$ (see equation (II.5)), else if sensitivity analysis is addressed $\mathfrak{f}(\boldsymbol{u}) = h(\boldsymbol{u})$ (see equation (II.23)), or $\mathfrak{f}(\boldsymbol{u}) = \mathbb{I}_{\Omega_F}(\boldsymbol{u})$ (see equation (II.25)) if reliability analysis is to be performed.

3.2. Monte-Carlo Simulation

One of the simplest ways to compute the above integral $I[\mathfrak{f}]$ is to use Monte-Carlo Simulations (MCS) *(Metropolis and Ulam, 1949)*. The basic idea behind this technique relies on drawing a random sample $\{\boldsymbol{u}^1, \dots, \boldsymbol{u}^M\}$ according to the standard multinormal distribution $\varphi_{\boldsymbol{U}}(\boldsymbol{u})$ of the random vector $\boldsymbol{U} = \{U_1, \dots, U_N\}^T$, representing the uncertain input parameters $\boldsymbol{x} = \{x_1, \dots, x_N\}^T$ in the standard random space. Then, the mechanical model is evaluated for each sample to obtain a set of values $\{\mathfrak{f}(\boldsymbol{u}^1), \dots, \mathfrak{f}(\boldsymbol{u}^M)\}$ of the integrand $\mathfrak{f}(\boldsymbol{u})$. Finally, the integral $I[\mathfrak{f}]$ could be approximated by the following weighted summation:

$$I[\mathcal{f}] = \int_{\mathbb{R}^N} \mathcal{f}(\boldsymbol{u})\, \varphi_U(\boldsymbol{u}) d\boldsymbol{u} \approx \frac{1}{M} \sum_{k=1}^{M} \mathcal{f}(\boldsymbol{u}^k) \qquad (II.30)$$

It is clear from equation (II.30) that the approximation given by the MCS for the integral $I[\mathcal{f}]$ appears as an estimate $\tilde{\mu}_{\mathcal{f}(\boldsymbol{u})}$ of the mean of the integrand $\mathcal{f}(\boldsymbol{u})$, with a standard error ϵ_{MCS}:

$$\epsilon_{MCS} \equiv \sqrt{\mathbb{V}[\mathcal{f}(\boldsymbol{u})]} = \frac{\tilde{\sigma}_{\mathcal{f}(\boldsymbol{u})}}{\sqrt{M}} \qquad (II.31)$$

where $\tilde{\sigma}_{\mathcal{f}(\boldsymbol{u})}$ is the standard deviation of the sample $\{\mathcal{f}(\boldsymbol{u}^1), \dots, \mathcal{f}(\boldsymbol{u}^M)\}$.

The main advantage of MCS is that it is very straightforward to implement. In addition, it has a high robustness since it can deal with integrand with a high level of complexity such that in the cases where this later represents a mechanical model exhibiting nonlinear behavior. Also, its efficiency is weakly affected by the dimensionality of the integral and can be applied to mechanical models having high number of uncertain input parameters. As can be seen in equation (II.31), the error ϵ_{MCS} decreases in $1/\sqrt{M}$, which explains the main drawback of MCS, namely its low convergence rate. Convergence is even slower when small probabilities of failure have to be computed for the purpose of reliability analysis. For instance, to estimate probabilities of failure of magnitude 10^{-6}, with an error ϵ_{MCS} of 5%, more than 4.10^8 evaluations of the integrand should be performed. Furthermore, it should be noticed that if the statistical moments analysis is addressed, the convergence of the MCS is also affected when high order statistical moments, such as the skewness and the kurtosis have to be evaluated. The poor convergence rate of MCS is mainly due to the use of pseudo-random numbers generator where the obtained sample points $\{\boldsymbol{u}^1, \dots, \boldsymbol{u}^M\}$ are not uniformly distributed in the random space. To overcome this problem other sampling schemes can be used, such as Latin hypercube sampling *(Mckay and al, 1979)* and quasi-random numbers *(Niederreiter, 1992)*. It has been shown in the literature *(Owen, 1992)*, that Latin hypercube sampling gives more accurate results compared to pseudo-random numbers since the associated error is lower than $\sqrt{M/M-1}\,\epsilon_{MCS}$. Various integration schemes based on quasi-random numbers are available. Indeed, such samples can be built from different quasi-random sequences such as those developed by Faure *(Faure, 1982)*, Halton *(Halton, 1960)*, Hammersley *(Hammersley and Handscomb, 1964)* and Sobol *(Sobol, 1998)*. Quasi-random numbers are more efficient in performing high-dimensional integration *(Schlier, 2004*), especially when derived from the Sobol sequence, since the convergence rate is in $\ln^N(M)$ which is much faster than the convergence rate $1/\sqrt{M}$ obtained by pseudo-random numbers. It is also known *(Wang and al, 2004)* that quasi-random numbers built from Hammersley sequence give a good balance between efficiency and accuracy. It is also worth mentioning that quasi-random numbers ensure a good performance when the integrand is very sharp or even discontinuous *(Schürer, 2003)*. Figure II.7 compares the distributions of 500 sample points obtained by pseudo-random numbers generator, Latin hypercube sampling, and Halton quasi-random sequence *(Halton, 1960)*.

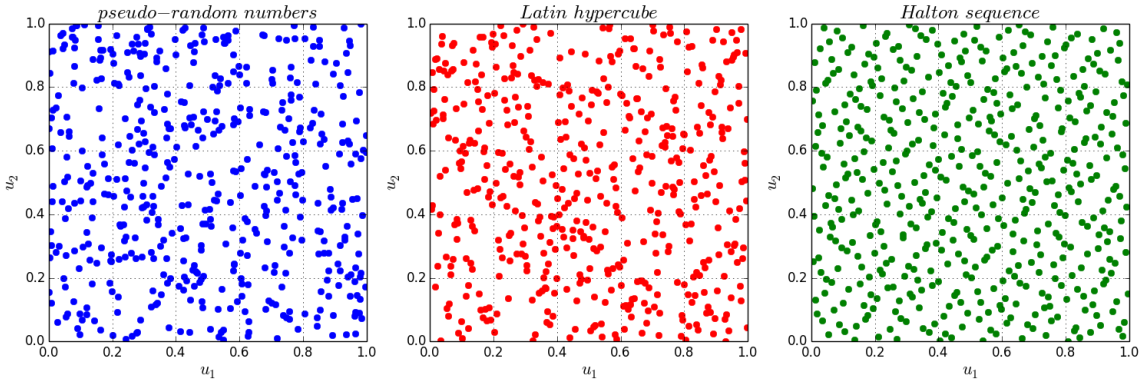

Figure II. 7. Distribution in the two-dimensional random space $[0,1]^2$ of sample points given by pseudo-random numbers generator (left), Latin hypercube sampling (center) and Halton quasi-random sequences (right).

3.3. Tensor-product cubature methods

Cubature methods *(Stroud, 1971; Cools and Rabinowitz, 1993; Cools, 2002; Lu and Darmofal, 2004)* are an alternative tool to MCS for the computation of multidimensional integrals. In this section we focus on full tensor-product method *(Brezin and Zhidkov, 1965)* and sparse grid method *(Smolyak, 1963; Gerstner and Griebel, 1998),* which are efficient to deal, respectively, with low and moderate dimensionality integration problems.

3.3.1. Full tensor-product cubature method

Full tensor-product cubature schemes are probably among the most used techniques to perform numerical integration. They have been extensively used in the field of uncertainty propagation for engineering problems, such as in *(Baldeweck, 1999)* to compute the first four statistical moments of mechanical responses, and in *(Ghanem, 1999)* for stochastic finite elements computations. For the sake of simplicity, let us first present the one-dimensional case, i.e. when the mechanical model has only one uncertain input parameter. Thus, the dimensionality N is now equal to 1, and the random vector $\boldsymbol{U}$ representing the uncertain input parameters in the standard random space, becomes a scalar quantity denoted U, which is nothing other than a standard normal variable with probability density function $\varphi_U(u)$. Under these conditions, the integral (II.29) reads:

$$I[\mathcal{f}] = \int_{\mathbb{R}} \mathcal{f}(u)\, \varphi_U(u) du = \frac{1}{\sqrt{2\pi}} \int_{\mathbb{R}} \mathcal{f}(u) \exp\left[\frac{u^2}{2}\right] du \qquad (II.32)$$

According to the cubature method, and after considering that the integrand $\mathcal{f}(u)$ is square integrable, the integral (II.32) can be approximated, as in the case of MCS, by a weighted summation of the integrand as follows:

$$I[\mathcal{f}] = \int_{\mathbb{R}} \mathcal{f}(u)\, \varphi_U(u) du \approx \sum_{k=1}^{M} w^k\, \mathcal{f}(u^k) \qquad (II.33)$$

where $\{u^1, \dots, u^M\}$ and $\{w^1, \dots, w^M\}$ are integration points and weights and M is the level of the quadrature scheme.

The integration points and weights depend on the integration domain and on the weight function $\varphi_U(u)$, but not on the integrand $f(u)$. As we work in the standard random space, and consequently the weight function in the integral (II.33) is $\exp\left[\frac{u^2}{2}\right]$, the cubature scheme is called Gauss-Hermite integration scheme, and the integration points are the roots of the M^{th} order Hermite polynomial. In the literature, for the one-dimensional Gauss-Hermite integration scheme, the term quadrature is used instead of cubature.

Now, let us come back to the multidimensional case. Since the uncertainty propagation problem is written in the standard random space, the random vector $\boldsymbol{U} = \{U_1, \dots, U_N\}^T$ is represented by N independent standard normal variables and the corresponding joint probability density function $\varphi_U(\boldsymbol{u})$ can be obtained simply as the product of the probability density functions $\varphi_{U_i}(u_i), i \in \{1, \dots, N\}$ of the set of random variables $U_i, i \in \{1, \dots, N\}$. Accordingly, one-dimensional cubature formulae $I_i^{M_i}, i \in \{1, \dots, N\}$ of level $M_i, i \in \{1, \dots, N\}$, as the one used in equation (II.33), can be derived from each probability density function $\varphi_{U_i}(u_i)$, and the multidimensional integral (II.29) can be approximated using the so-called full tensor-product cubature scheme given below:

$$I[f] = \int_{\mathbb{R}^N} f(\boldsymbol{u})\, \varphi_U(\boldsymbol{u}) d\boldsymbol{u} \approx I_1^{M_1} \otimes \cdots \otimes I_N^{M_N}[f] \approx \sum_{k_1=1}^{M_1} \dots \sum_{k_N=1}^{M_N} w^{k_1} \dots w^{k_N} f(u^{k_1} \dots u^{k_N}) \qquad (II.34)$$

The accuracy of the approximation given by equation (II.34) could be measured by the degree of the polynomial below which the cubature will gives the exact value. In the case of isotropic cubature scheme, which means that the same numbers of integration points $M_1 = \cdots M_N = M$ are used in each direction of the integration domain, equation (II.34) allows to exactly integrate a multidimensional polynomial with degree not greater than $2M - 1$. Consequently, the required number of evaluations of the integrand is M^N, which clearly grows exponentially with the dimensionality N of the integral and leads to intractable computations when the mechanical model is time-consuming itself. This is the main drawback of full tensor-product cubature schemes.

3.3.2. Sparse grid method

An alternative to avoids the curse of dimensionality of full tensor-product cubature schemes, is the use of sparse grid integration also called Smolyak's cubature scheme *(Smolyak, 1963; Gerstner and Griebel, 2003, Nobile and al, 2006; Ganapathysubramanian and Zabaras, 2007)*. The key idea is to use linear combinations of tensor-products of one-dimensional cubature formulae $I_i^{M_i}, i \in \{1, \dots, N\}$ of level $M_i, i \in \{1, \dots, N\}$, each one is able to integrate exactly any one-dimensional polynomial of degree up to $2M_i - 1, i \in \{1, \dots, N\}$. To enhance its efficiency, only tensor-products combinations with relatively small number of integration points are used and higher degree combinations are excluded. The linear combination is performed in such a way that suitable interpolation property for the one-dimensional case is preserved for higher order dimensionality *(Novak and Ritter, 1999)*. Accordingly, the Smolyak formula of level M is given by:

$$I[\mathcal{f}] = \int_{\mathbb{R}^N} \mathcal{f}(\boldsymbol{u})\, \varphi_U(\boldsymbol{u}) d\boldsymbol{u} \approx \sum_{|\boldsymbol{i}|=M}^{M+N-1} (-1)^{M+N-1-|\boldsymbol{i}|}\ C_{N-1}^{|\boldsymbol{i}|-M}\ Q_{|\boldsymbol{i}|}^N \qquad (II.35)$$

where $\boldsymbol{i} = \{i_1, \dots, i_N\} \in \mathbb{N}^N$ is a multi-index with $|\boldsymbol{i}| = \sum_{k=1}^N i_k$, C denotes the combination operator and $Q_{|\boldsymbol{i}|}^N$ is a suitable multidimensional cubature, which is built through integration points $\left\{u_1^{k_i}, u_2^{k_i}, \dots, u_{M_i}^{k_i}\right\}, i \in \{1, \dots, N\}$ and weights $\left\{w_1^{k_i}, w_2^{k_i}, \dots, w_{M_i}^{k_i}\right\}, i \in \{1, \dots, N\}$ associated to one-dimensional cubature formulae $I_i^{M_i}, i \in \{1, \dots, N\}$ of level $M_i, i \in \{1, \dots, N\}$. It reads:

$$Q_{|\boldsymbol{i}|}^N = \sum_{|\boldsymbol{i}|} \sum_{k_1=1}^{M_1} \dots \sum_{k_N=1}^{M_N} w_{M_1}^{k_1} \dots w_{M_N}^{k_N}\, \mathcal{f}\left(u_{M_1}^{k_1} \dots u_{M_N}^{k_N}\right) \qquad (II.36)$$

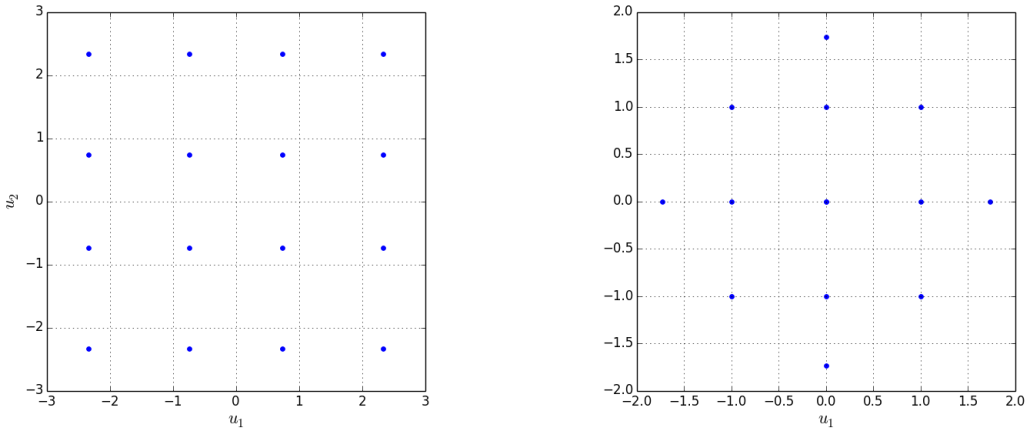

Figure II. 8. Two-dimension full (left) and sparse (right) grids built from Gauss-Hermite integration points

Figure II. 8 compares, for the two-dimensional case, Smolyak's grid of level $l = 3$ and full tensor-product grid of level $M = l + N - 1 = 3 + 2 - 1 = 4$. It is clearly shown that for the same given level of accuracy, Smolyak's cubature formula is more efficient since the corresponding grid uses less integration points than the grid obtained by full tensor-product. Indeed, in *(Novak and Ritter, 1999)* it is proven that the number of evaluations of the integrand in Smolyak's cubature formula (2.35) of degree M is $2^{M-1} N^{M-1}/(M-1)!$, which increases polynomially with the dimensionality N of the integral to be computed. According to *(Fichtl and Prinja, 2011)*, the use of Smolyak's cubature formula of degree $d+1$ or $d+2$ requires less integrand evaluations than full tensor-product cubature formula of degree d, especially for higher values of N. The efficiency of Smolyak cubature formula can be further enhanced by using nested sparse grids which allows to prevent extra computations.

Let us consider two sparse grids $G^l(\boldsymbol{u})$ and $G^{l+1}(\boldsymbol{u})$ of level l and $l+1$, respectively. These are nested if the points of the grid $G^l(\boldsymbol{u})$ align with those of grids of a higher degree $G^{l+1}(\boldsymbol{u})$. Unfortunately, Gauss-Hermite integration points have poor nesting, since only the center point belongs to all possible grids. Other types of integration points with bounded support, such as Gauss-Legendre, Gauss-Patterson and Clenshaw-Curtis *(Liu and al, 2011)* have a better nesting and can be used to avoid this problem. This only needs to perform the integration in an appropriate standard random space defined by standard uniform random variables rather than standard normal random variables.

Despite, the various improvements of Smolyak's cubature formula it remains inefficient for higher dimensionality integration problems. In addition, it has another critical drawback, since large negative weights can be produced during combinations of tensor-products, which means ill-conditioning in the computation of integral involving non-polynomial integrand. Indeed, the results obtained by *(Bernardo, 2015)* from a benchmark study conducted on a large family of integrand functions with dimensionality up to 24 have shown that Smolyak's cubature formula is not reliable as it reproduces large errors, mainly due to large negative weights.

4. Efficient cubature methods

In section 3 we focused on the classical methods used to perform multidimensional integration. The main objective was to introduce the mathematical issue behind multidimensional integration and to present the general principle of cubature integration in a soft manner. In this new section, we focus on the most efficient cubature formulae available in the literature of integration methods *(Stroud, 1971; Cools, 2003)*. These formulae are said to be efficient here because they use few integration points (i.e., only a few tens of points are needed for moderate dimensionality and a few hundreds of points are required for high dimensionality); therefore, a limited number of integrand evaluations is needed to achieve a good accuracy. They are similar to MCS, in that only one weighted summation is needed to approximate a multidimensional integral, unlike on the tensor product-based formulae where a weighted summation is performed in each direction of the integration domain, since the integration points are smartly selected to reduce computational efforts. The main difference between these efficient cubature formulae is the way in which the integration points are selected. Indeed, to further improve the efficiency of the cubature scheme, the idea is to use symmetric integration points, such those developed first by *(Genz, 1986)* to perform integration on hypercube and extended later by *(Genz and Keister, 1996)* for infinite integration domains. The obtained formulae are called complete-symmetric cubature formulae. Based on the invariant theory and orthogonal arrays, *(Victoir, 2004)* has developed quasi-symmetric cubature formulae, also called thinned cubature formulae *(Bernardo, 2015),* which use only parts of the integration points in the same symmetric set, in contrast to the full-symmetric cubature formulae which use all integration points in a symmetric set. These efficient cubature formulae have been extensively studied, but only applied to solve purely mathematical problems. Indeed, until the works conducted by *(Lu and al, 2004; Victoir, 2004)*, they were unknown in the engineering fields, in particular thinned cubature formulae. In the last decade, they received a growing attention and some applications to solve engineering problems were noticed *(Wei and al, 2008; Xu and al, 2012; Xu and Lu, 2017; Xiao and Lu, 2018; Xu and Dang, 2019; Ding and Xu, 2021)*.

As part of this thesis work, a first attempt will be conducted in this chapter to extend the application of these efficient cubature to more complex mechanical problems involving a high number of uncertain parameters. But firstly, let us identify to the main efficient cubature schemes available in the literature and their mathematical formulation. These formulae, all of them of fifth degree, are useful to compute Gaussian weighted integral particularly the first four statistical moments *(Xu and Lu, 2017)*, as they allow a good

accuracy while the number of evaluations of the integrand grows quadratically with the dimension of the integral.

4.1. Formula I

This formula of degree 5 given by *(Stroud, 1971)*, is only valid for a moderate range of dimensions $2 \leq N \leq 7$ and requires $N^2 + N + 2$ integration points as depicted in figure II.9 for the two-dimensional case. According to this formula, the integral (II.29) can be approximated by the following weighted sum:

$$I[f] \approx A\left[f\left(\sqrt{2}\eta, \sqrt{2}\eta, \dots, \sqrt{2}\eta\right) + f\left(-\sqrt{2}\eta, -\sqrt{2}\eta, \dots, -\sqrt{2}\eta\right)\right]$$

$$+B\left[\sum_{permutation} f\left(\sqrt{2}\lambda, \sqrt{2}\xi, \dots, \sqrt{2}\xi\right) + f\left(-\sqrt{2}\lambda, -\sqrt{2}\xi, \dots, -\sqrt{2}\xi\right)\right]$$

$$+C\left[\sum_{permutation} f\left(\sqrt{2}\mu, \sqrt{2}\mu, \sqrt{2}\gamma, \dots, \sqrt{2}\gamma\right) + f\left(-\sqrt{2}\mu, -\sqrt{2}\mu, -\sqrt{2}\gamma, \dots, -\sqrt{2}\gamma\right)\right] \quad (II.37)$$

where the terms appearing in the summations are built from all possible distinct permutations of the input variables (see figure II.9 left).

The constants A, B, C, μ, γ, η and ξ are given by *(Stroud, 1967; Stroud, 1971)*. They can have multiple real solutions and some of the derived integration points could take on complex values. For instance, the constants μ, γ and η can be obtained by solving the following equations, and as can be seen complex solutions happen for $N > 7$:

$$\mu = -3 \pm \sqrt{16 - 2N}$$

$$\gamma^2 = \frac{3 \pm \sqrt{7 - N}}{2(16 - N \pm 4\sqrt{16 - 2N})}$$

$$\eta^2 = \frac{N(N-7) \pm (N^2 - 3N - 16)\sqrt{7 - N}}{2(2N^3 - 7N^2 - 16N + 128)} \quad (II.38)$$

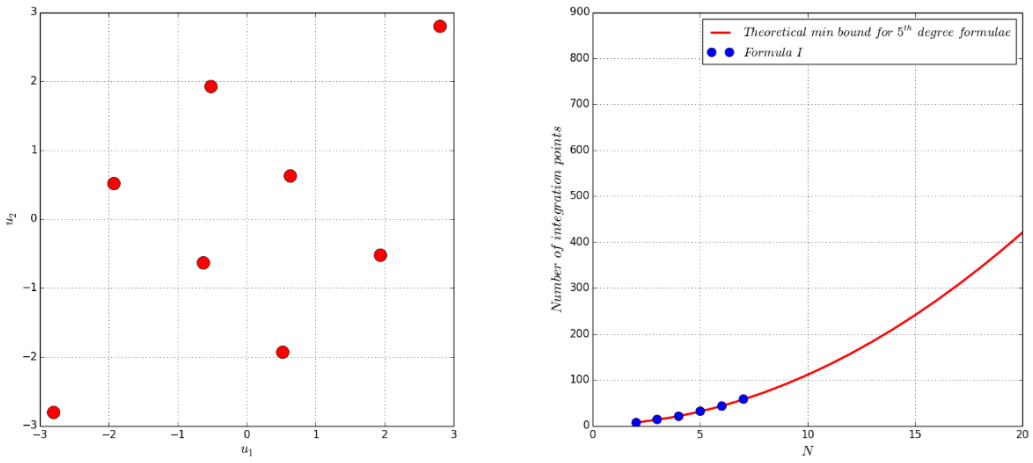

Figure II. 9. Integration points given by formula I (left) and comparison of the number of integration points with the theoretical min bound of formulae of degree 5 (right)

Formula I is the most efficient among the known integration formulae of degree 5 for $N \geq 4$, since it requires just one more point than the number of integration points given theoretically, which is $N^2 + N + 1$, as can be seen from the plot (red line) of figure II.9.

4.2. Formula II

We give here another fifth-degree formula derived by *(Mysovskikh, 1980)* which requires $N^2 + 3N + 2$ integration points as shown in figure II.10 for the two-dimensional case. Based on this formula, the approximation given for the integral (II.29) reads:

$$I[f] \approx \frac{2}{N+2} f(\mathbf{0}) + \frac{N^2(7-N)}{2(N+1)^2(N+2)^2} \sum_{j=1}^{N+1} \left[f\left(\sqrt{N+2} \times \boldsymbol{a}^j\right) + f\left(-\sqrt{N+2} \times \boldsymbol{a}^j\right) \right]$$

$$+ \frac{2(N-1)^2}{(N+1)^2(N+2)^2} \sum_{j=1}^{N(N+1)/2} \left[f\left(\sqrt{N+2} \times \boldsymbol{b}^j\right) + f\left(-\sqrt{N+2} \times \boldsymbol{b}^j\right) \right] \qquad (II.39)$$

where $\mathbf{0}$, $\boldsymbol{a}^j$ and $\boldsymbol{b}^j$ are the integration points representing respectively the center point of the integration domain, the vertices of a regular simplex and the midpoints of the vertices of a regular simplex projected onto the surface of the sphere $S_N \equiv \{\boldsymbol{x} \in \mathbb{R}^N : x_1^2 + x_2^2 + \cdots x_N^2 = 1\}$.

The points set $\boldsymbol{a}^j$ and $\boldsymbol{b}^j$ allowing to compute Gaussian weighted integral, are given by the following expressions:

$$\boldsymbol{a}^j = \left(a_1^j, a_2^j, \dots, a_N^j\right), \qquad j = 1,2,\dots,N+1 \qquad (II.40)$$

$$a_i^j = \begin{cases} -\sqrt{\dfrac{N+1}{N(N-i+2)(N-i+1)}}, & for\ i < j \\ \sqrt{\dfrac{(N+1)(N-j+1)}{N(N-j+2)}}, & for\ i = j \\ 0, & for\ i > j \end{cases} \qquad (II.41)$$

$$\boldsymbol{b}^j = \sqrt{\frac{N}{2(N-1)}} (\boldsymbol{a}^k + \boldsymbol{a}^l), \quad k < l, \quad l = 1,2,\dots,N+1 \qquad (II.42)$$

Formula II is somewhat less efficient than formula I, but it is valid for a wide range of dimensions $N > 3$. Note that when $N < 7$, the integration weights are all positive, but for $N > 7$, negative integration weights appear, which is mathematically reasonable, but may lead to unacceptable large errors or even physically meaningless results. Therefore, higher dimensional integration should be handled with more care.

As depicted in figure II.10, the number of required integration points grows quadratically with the dimension of the integral to be computed. Note that for higher dimensions, formula II remains efficient since the number of evaluations of the integrand is close the one given by the theoretical lower bound.

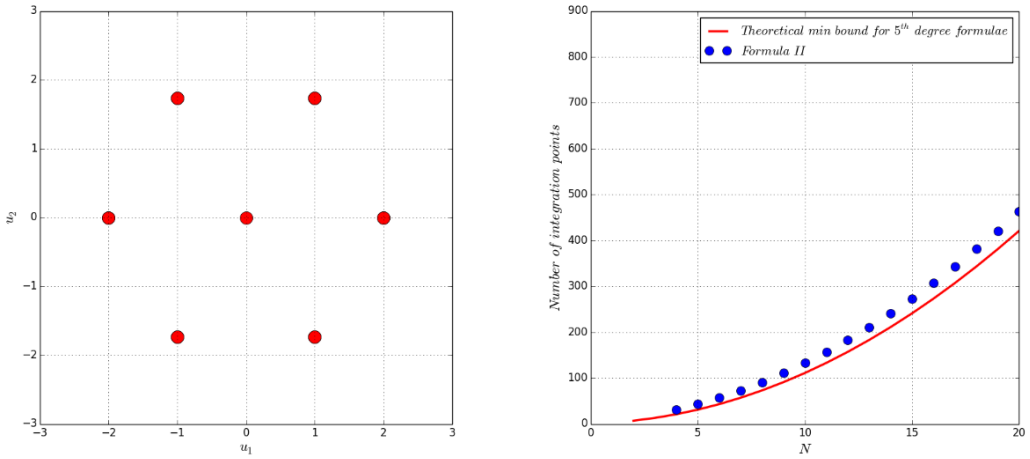

Figure II. 10. Integration points given by formula II (left) and comparison of the number of integration points with the theoretical min bound of formulae of degree 5 (right)

4.3. Formula III

This formula firstly given in *(Stroud and Secrest, 1963)* and later found in *(Stroud, 1971)* is very similar to formula II. Indeed, formula III is derived from a formula for an integration formula on the surface of the unit *N*-sphere. Moreover, for radially symmetric functions $f(|\boldsymbol{x}|)$, formulae II and III leads to exactly the same results. The main difference between them lies in choice of the integration weights and points: the integration points used in formula III are built on all distinct reflections and permutations of the input variables. Referring to formula III, the integral (II.29) can be approximated by the following series of summations:

$$I[f] \approx \frac{2}{N+2} f(\mathbf{0}) + \frac{4-N}{2(N+2)^2} \sum_{full\ sym} f(\sqrt{N+2}, 0, \dots, 0)$$

$$+ \frac{1}{(N+2)^2} \sum_{full\ sym} f\left(\sqrt{\frac{N}{2}+1}, \sqrt{\frac{N}{2}+1}, \dots, 0\right) \qquad (II.43)$$

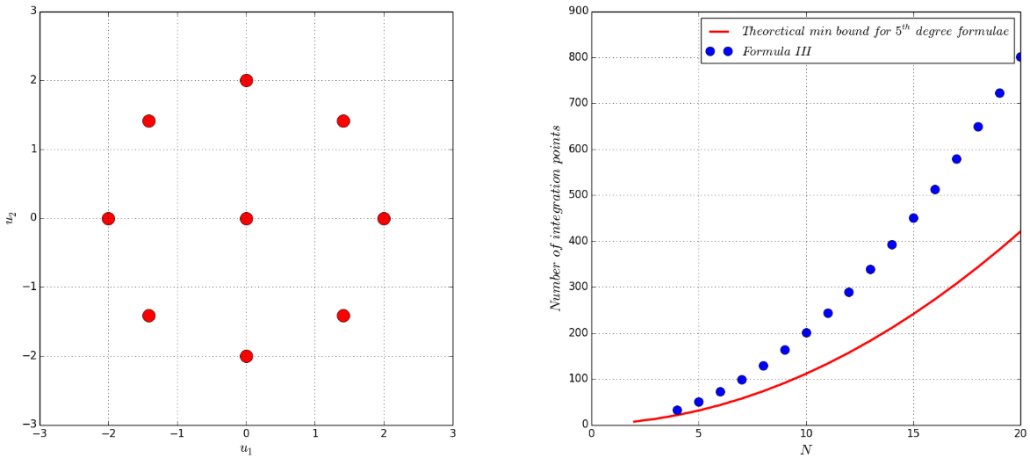

Figure II. 111. Integration points given by formula III (left) and comparison of the number of integration points with the theoretical min bound of formulae of degree 5 (right)

This formula is also of algebraic degree 5 and requires $2N^2 + 1$ integration points. Although, the number of integration points grows quadratically with the dimension of integration, formula III is less efficient than

the two previous formulae, especially for higher dimensions as depicted in figure II. 11. In addition, the space-filling of the integration points of formula III is different from the one of formula II, while the two formulae have some similarities.

4.4. Formula IV

This formula developed for the first time by *(McNamee and Stenger, 1967),* based on the theory of invariants. Using the same procedure *(Phillips, 1980)* has constructed the following fifth degree cubature formula to compute the weighed Gaussian integral in equation (II.29):

$$I[f] \approx \frac{N^2 - 7N + 18}{18} f(\mathbf{0}) + \frac{4 - N}{18} \sum_{full\ sym} f(\sqrt{3}, 0, \dots, 0)$$

$$+ \frac{1}{36} \sum_{full\ sym} f(\sqrt{3}, \sqrt{3}, \dots, 0) \qquad (II.44)$$

Formula IV has the same efficiency as formula III since $2N^2 + 1$ integration points are also required to approximate a multidimensional integral. The main difference between them is that, for formula IV, the position of the integration points is independent of the dimension N, as shown in equation (II.44). Indeed, from a geometrical point of view, the integration points of formula IV lie on the surface of a sphere of constant radius, whereas for formula III, the integration points fill the surface of a sphere whose radius increases with the dimension N. This fact could lead to a significant gap in the accuracy of the estimate given by formulae III and IV, and it will be interesting to investigate it in the following. It is important to note that for the two-dimensional case, formula IV is identical to the one constructed by full tensor-product scheme. As can be seen in figure II.12, the integration points of formula IV have the same locations as in Gauss-Hermite grid of level 3.

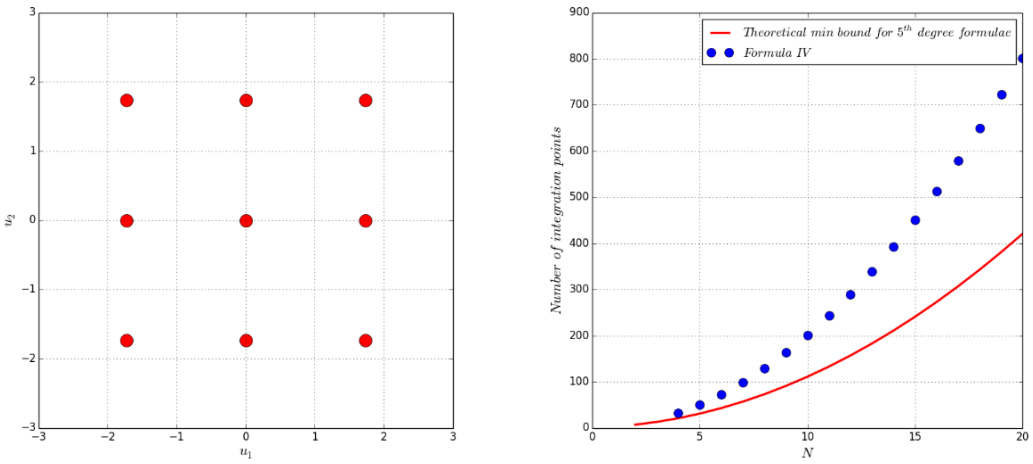

Figure II. 122. Integration points given by formula IV (left) and comparison of the number of integration points with the theoretical min bound of formulae of degree 5 (right)

4.5. Formula V

This formula has been developed by *(Victoir, 2004)* and later by *(Kuperberg, 2006)* based on the theory of invariant and orthogonal arrays. Referring to the construction proposed by *(Kuperberg, 2006)*, the

integration points are built by starting with an equal weight cubature formula of degree d, having a convolutional structure such as in a tensor-product formula, and then a large portion of this integration points are removed using an orthogonal array that preserves the degree d of accuracy. This procedure of integration points removal is called thinning, and, for this reason, formula V is also known as thinned cubature formula. It produces all positive integration weights and interior integration points, which is appropriate from a physical point of view and provides good robustness when dealing with higher dimension.

For Gaussian integration domain, two classes of fifth degree formula V are available. The first is of the following form and valid when the dimension N is of the form $N = 3k - 2$:

$$I[f] \approx \frac{2}{N+2} f(\mathbf{0}) + \frac{N}{N+2} \sum_{permutation} f(h\sqrt{3}, \dots, h\sqrt{3}, 0, \dots, 0) \qquad (II.45)$$

where h is the permutation of ± 1 and k is the number of $h\sqrt{3}$ in the integration point $(h\sqrt{3}, \dots, h\sqrt{3}, 0, \dots, 0)$.

The second class of formula V is valid for $N \geq 3$ and can approximate the integral (II.29) by the following expression:

$$I[f] \approx \frac{8N}{(N+2)^2} \sum_{permutation} f\left(h\sqrt{\frac{N+2}{2}}, 0, \dots, 0\right)$$

$$+ \frac{(N-2)^2}{(N+2)^2} \sum_{permutation} f\left(h\sqrt{\frac{N+2}{N-2}}, \dots, h\sqrt{\frac{N+2}{N-2}}\right) \qquad (II.46)$$

where h is also the permutation of ± 1.

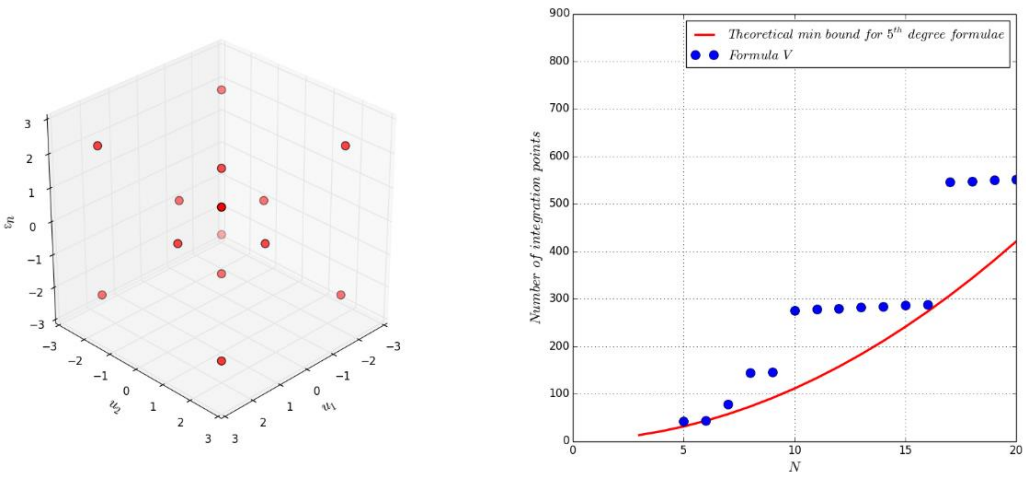

Figure II. 133. Integration points given by formula V (left) and comparison of the number of integration points with the theoretical min bound of formulae of degree 5 (right)

Integration points, given by formula V of the second class, in the case of three-dimensional Gaussian integration domain are plotted in figure II.13. The efficiency of formula V is remarkable for higher dimension, especially when the degree of accuracy of the cubature formula is relatively low. Indeed, the

number of integration points required is less than 40 for formula V of degree 3 and 1000 for formula V of degree 5. This formula is efficient to compute accurately integrals with dimension up to 24. Despite this, the use of formula V in engineering is limited to a few applications. The main drawback of the formula V is that the construction of orthogonal arrays, especially for higher dimensions, is not a trivial task. In this work, the proposed formula V allows us to investigate the computation of multidimensional integrals with dimension up to 16.

4.6. Formula VI

The mathematical formulation of this formula is very similar to that of formula II. Based on a high-order unscented transformation *(Zhang and al, 2014)*, it was first developed for the purpose of non-linear estimation of Kalman filter. After that, it was used by *(Xiao and Lu, 2018)* to perform reliability analysis on some academic engineering problems. The results obtained show that formula VI can accurately estimate the high-order statistical moments of limit-state functions.

The integration points of this formula can be divided into three types. The first type is represented by one integration point $\boldsymbol{u_0}$ located on the origin $(0,\dots,0)$ of the standard random space with weight w_0:

$$\begin{cases} \boldsymbol{u_0} = (0,\dots,0) \\ w_0 = \dfrac{-2N^2 + (4-2N)\Delta^2 + 4(\Delta+1)N}{(N+\Delta)^2(4-N)} \end{cases} \qquad (II.47)$$

The second type is represented by $2N$, equidistant points from the origin, located on the axis of the integration domain, and with the same weight w_1:

$$\begin{cases} \boldsymbol{u}_{j_1} = \sqrt{\dfrac{(4-N)(N+\Delta)}{\Delta+2-N}}\,\vec{\boldsymbol{e}}_{j_1} \\ \boldsymbol{u}_{j_1+N} = -\sqrt{\dfrac{(4-N)(N+\Delta)}{\Delta+2-N}}\,\vec{\boldsymbol{e}}_{j_1}, j_1 = 1,2,\dots,N \\ w_1 = \dfrac{(\Delta+2-N)^2}{2(N+\Delta)^2(4-N)} \end{cases} \qquad (II.48)$$

where $\boldsymbol{e}_{j_1} = [0,\dots,0,1,0,\dots,0]^T$.

The third type contains $2N(N-1)$ integration points lying on the diagonal of a plan defined by two coordinate axes and having the same weight w_2:

$$\begin{cases} \boldsymbol{u}_{j_2} = +\sqrt{N+\Delta}\,\vec{\boldsymbol{e}}^{+}_{j_2} \\ \boldsymbol{u}_{j_2+\frac{N(N-1)}{2}} = -\sqrt{N+\Delta}\,\vec{\boldsymbol{e}}^{+}_{j_2} \\ \boldsymbol{u}_{j_2+N(N-1)} = +\sqrt{N+\Delta}\,\vec{\boldsymbol{e}}^{-}_{j_2} \\ \boldsymbol{u}_{j_2+\frac{3N(N-1)}{2}} = -\sqrt{N+\Delta}\,\vec{\boldsymbol{e}}^{-}_{j_2},\ j_2 = 1,2,\dots,\dfrac{N(N-1)}{2} \\ w_2 = \dfrac{1}{(N+\Delta)^2} \end{cases} \qquad (II.49)$$

where $\vec{e}_{j_2}^{+} = \{\sqrt{\frac{1}{2}}(\vec{e}_k + \vec{e}_l); k < l, k, l = 1,2, \dots, n\}$ and $\vec{e}_{j_2}^{-} = \{\sqrt{\frac{1}{2}}(\vec{e}_k - \vec{e}_l); k < l, k, l = 1,2, \dots, n\}$.

Formula VI has the same efficiency as formulae III and IV since it requires $2N^2 + 1$ integration points. But, as can be seen in the above equations, it has a small particularity, i.e. a free parameter Δ intervenes for the computation of the integration weights and points, which gives flexibility to formula VI and some values can contribute to enhance its accuracy. Indeed, as shown in *(Zhang and al, 2014) for the two-dimensional case,* formula VI can theoretically capture the first six statistical moments of the input random variables when $\Delta = 0.835$ *or* $\Delta = 19.165$. Note that, when $\Delta = 4$, formula VI is nothing else then a third-degree Gauss-Hermite integration scheme.

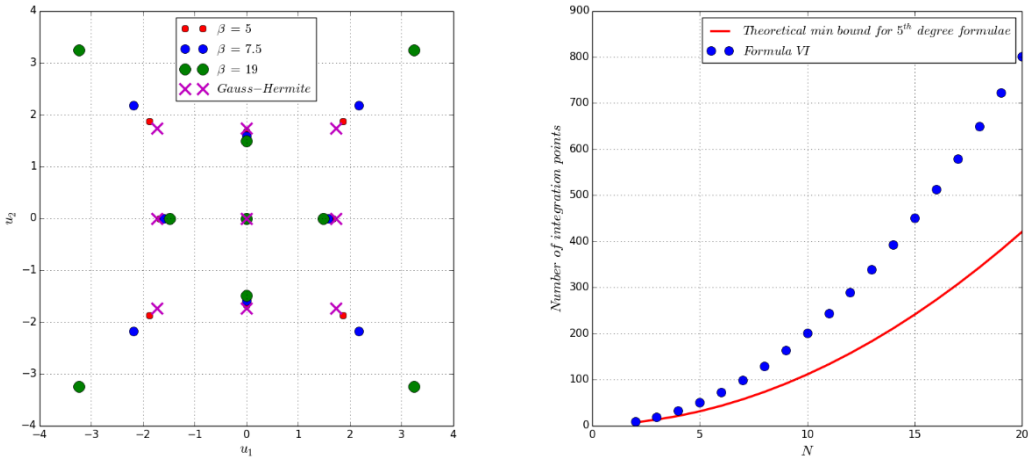

Figure II. 14. Integration points given by formula VI (left) and comparison of the number of integration points with the theoretical min bound of formulae of degree 5 (right)

In figure II.14, we can clearly see the impact that the parameter Δ can have on the location of the integration points in the integration domain. When $\Delta > 4$, the distance to the origin of some integration points of formula VI is much larger than those of the corresponding integration points of the Gauss-Hermite scheme. As depicted in figure II.14, for $\Delta = 19$ some of the integration points are located around ± 3 standard deviation of the mean of the input random variables. This can be very useful in the reliability analysis, as it can help to capture the probabilistic content of the tails of the distributions of the input random variables. Note that there is no optimal value of the parameter Δ, except for the two-dimensional and three-dimensional cases, where Δ is set to as 0.835 and 1.417, respectively, to capture the first four statistical moments of the input random variables. For the other cases *(Zhang and al, 2014)* have demonstrated that when Δ is set to 2, formula VI provides a good stabilization of the numerical computation.

5. Numerical examples

In this section, two sets of numerical problems encountered when propagating uncertainty through models are addressed to conduct a comparative study between the cubature formulae presented in the previous section. The main objective is to illustrate their ability to provide probabilistic characteristics of model response, including tail distribution, reliability, and sensitivity indices. The first set of problems, related to

explicit models, concerns elementary analytical models that represent either a purely mathematical function or a problem related to mechanical analysis. The second set, related to implicit models, includes computationally intensive mechanical models whose responses are available through numerical calculations. Where the exact solution does not exist, estimates of the quantities of interest given either by direct Monte-Carlo Simulations (MCS) or by a full tensor-product Gauss-Hermite Integration (GHI) scheme have been used to assess the accuracy and efficiency of cubature formulae I, II, III, IV, V and VI.

5.1. Explicit models

5.1.1. Purely mathematical integration problem

Let us consider a simple integrand function that is widely used in the literature to conduct benchmark studies *(Xu and Rahman, 2004)* on integration methods.

$$f(\boldsymbol{x}) = \sqrt{1 + \boldsymbol{x}^T \boldsymbol{x}/2} \qquad (II.50)$$

where $x_i, i = 1, \dots, N$ are uncertain parameters represented by identically normal distributed random variables $X_i, i = 1, \dots, N$ with mean 0 and standard deviation σ.

This function has a bell shape around the origin which becomes more pronounced as the dimension N increases, making it more difficult to integrate for higher dimensions. Thus, we first want to study the effect of dimension N on the accuracy of the results given by the six cubature formulae presented previously. The expected value, that is the first order statistical moment of the function (II.50), is computed for increasing dimension N, and by assigning the standard deviation σ of the input random variable the value $\sqrt{2}/2$. The obtained estimates given by 10^5 MCS and Gauss-Hermite (GH3) cubature scheme of level 3, taken here as the reference solutions, are reported in Table II.1. As can be seen, both methods give accurate results and as expected, the convergence of MCS is slow but less impacted by the dimension of integration. Conversely, the efficiency of Gauss-Hermite cubature scheme is closely related to the dimension of integration. Indeed, the number of required evaluations of the integrand grows exponentially with the dimension of integration. For instance, to compute an integral of dimension 10 with a good level of accuracy, 59049 evaluations of the integrand are required.

Table II. 1. Expectation value of the integrand (II.50) given by 10^5 MCS and GH3 for various values of the dimension of integration

	N							
	3	4	5	6	7	8	9	10
MCS	1.3044	1.3934	1.4778	1.5585	1.6349	1.7088	1.7793	1.8477
GH3	1.3023 (27,0.16%)	1.3913 (81,0.14%)	1.4757 (243,0.14%)	1.5561 (729,0.15%)	1.6328 (2187,0.12%)	1.7064 (6561,0.13%)	1.7772 (19683,0.11%)	1.8454 (59049,0.12%)

The relative error, taken as an indicator of accuracy and defined as the difference between the estimates obtained by the six cubature formulae presented in the previous section and those given by MCS, are plotted in figure II.15. As can be seen, all formulae give accurate estimates of the expected value of the function (II.50) for the integration dimension up to 10, since the relative error does not exceed 6% in the worst case, which is recorded for formula IV and $N = 10$. Except for formula IV, where the relative error

grows exponentially, the accuracy of the other formulae seems to be less affected by the integration dimension N, especially for formula V which gives the lower relative error.

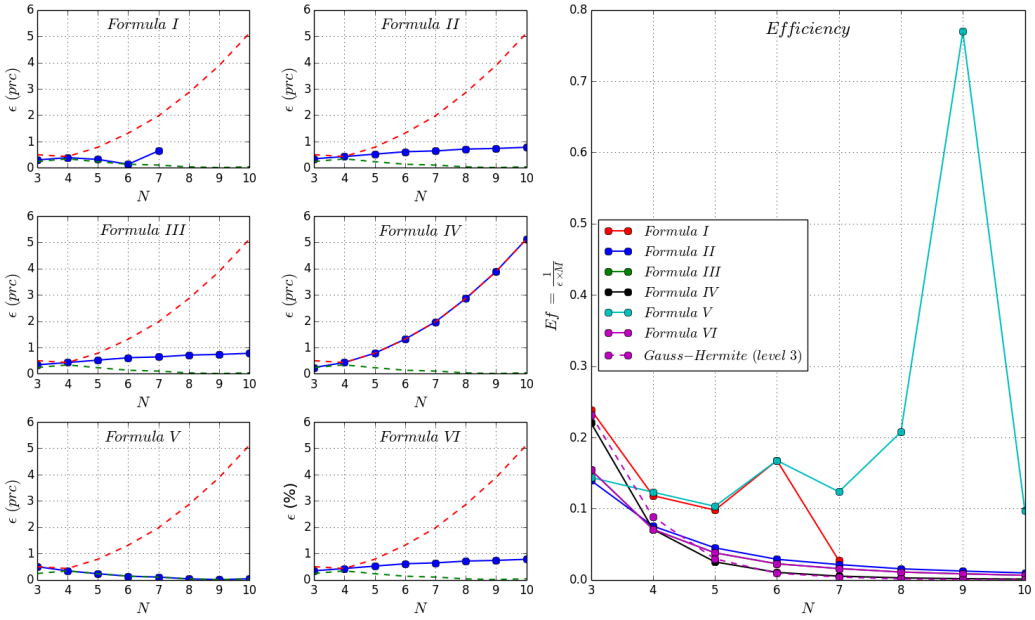

Figure II. 15. Evaluation of the accuracy and the efficiency of cubature formulae I to VI

In order to push our comparative analysis a little further, an efficiency index, noted Ef, is introduced. It is defined as a function of the number of evaluations of the integrand M and the relative error ϵ computed previously, and reads as follows:

$$Ef = \frac{1}{M_\epsilon} = \frac{1}{M \times \epsilon} \qquad (II.51)$$

As can be seen from equation (II.51), the smaller the quantity $M \times \epsilon$, the better the efficiency of the considered integration scheme. In addition, it can be noted that the number of evaluations of the integrand M is commonly used to evaluate the accuracy of a cubature scheme. Here, a *weighted* or *effective* one, denoted M_ϵ, is used. The idea behind this is to include in the efficiency measurement the effect of a possible loss of accuracy when the dimension of integration increases. Moreover, this efficiency index can be very useful in identifying the cubature scheme that offers the best balance between accuracy and efficiency.

The efficiency index Ef is plotted in figure II.15. As can be seen, except for formulae I and V which exhibit some particular behavior, the efficiency of all the other cubature formulae cubature scheme decreases with the dimension of integration. As expected, this loss of efficiency is more significant in the case of Gauss-Hermite integration scheme.

Formula V gives the better balance between accuracy and efficiency when dealing with higher dimensions integration problems. The higher efficiency of formula V is observed for $N = 9$, followed by a significant decrease for $N = 10$. Indeed, although the level of accuracy remains relatively the same for $N = 9$ and $N = 10$, the number of evaluations of the integrand increases suddenly from 146 for $N = 9$ to 276 for $N = 10$. This significant growth of the number of integrand evaluations is explained in section 4.5 and can be clearly seen in figure II.13. Compared to the Gauss-Hermite integration scheme, the formula V is 1666 and 690

times more efficient for $N = 9$ and $N = 10$, respectively. Unfortunately, the formula V is only able to deal with integration problems with moderate dimension. As explained in section 4.5, this is mainly due to the fact that the construction of orthogonal arrays, used to drive the integration points, is not a trivial task.

The formula I also gives a good balance between accuracy and efficiency, even for lower dimensions where the others cubature formulae fail to give better results than the Gauss-Hermite integration scheme. Unfortunately, the formula I is only able to compute integrals with dimension up to 7.

As a conclusion for this first example, dealing with purely mathematical integration problem, we have shown that cubature formulae I-VI are by far more efficient than traditional integration methods such as MCS and full tensor-product GHI. In addition, their efficiency is less affected by the dimension of integration. Hence, these cubature formulae could be serious candidates for computing high-dimensional integrals such as those encountered in uncertainty propagation problems.

5.1.2. Analytical mechanical models with mixed random variables

In the first example the uncertain parameters were represented by identical normal distributed random variables having the same statistical characteristics. This situation is rarely encountered in real-life problems since the uncertain parameters often follow different kinds of distributions. In addition, the use of the normal distribution in uncertainty modeling could be viewed as a special case due to its mathematical properties which could simplify the probabilistic computations, and consequently may give a truncated picture of the ability of the uncertainty propagation method. In this section, an analysis will be conducted, through uncertainty propagation problems involving uncertain parameters whose variability is modeled with a mixture of normal and non-normal random variables, to evaluate the accuracy and the efficiency of the cubature formulae I-VI when dealing with such problems.

Three analytical models taken from the literature are considered. The first one $G_1(\boldsymbol{x})$, obtained from *(Melchers and Ahammad, 2004)*, represents a purely mathematical function. The second $G_2(\boldsymbol{x})$ and the third $G_3(\boldsymbol{x})$ ones are obtained from *(Hong and Lind, 1996)* and *(Panmetsa and Grandhi, 2003),* respectively, and both represent performance functions related to structural reliability problems. The mathematical formulations of these models are given in the following equations:

$$G_1(\boldsymbol{x}) = x_1\, x_2\, x_3\, x_4 - \frac{x_5\, x_6^2}{8} \qquad (II.52)$$

$$G_2(\boldsymbol{x}) = 7.645 \times 10^{-4} x_1 x_2 \left(1 - 7.217 \times 10^{-3} \frac{x_2}{x_3}\right) - x_4 - x_5 \qquad (II.53)$$

$$G_3(\boldsymbol{x}) = \sqrt{\frac{3x_1\, x_2\, (x_5 - x_6)}{\left(\frac{\pi x_3}{30}\right)^2\, (x_5^3 - x_6^3)}} - 0.37473 \qquad (II.54)$$

The probability distributions and the statistical characteristics (i.e., mean, and standard deviation) of the random variables $\boldsymbol{X}$ used to represent the variability of the uncertain parameters $\boldsymbol{x}$ related to the above models are given in table II. 2.

Table II. 2. Probability distributions and statistical characteristics of the random variables related to the performance functions $G_1(\boldsymbol{x})$, $G_2(\boldsymbol{x})$ and $G_3(\boldsymbol{x})$

Performance function	Random variable	Distribution	μ	σ
$G_1(\boldsymbol{x})$	X_1	Weibull	4	0.1
	X_2	Lognormal	25000	2000
	X_3	Gumbel	0.875	0.1
	X_4	Uniform	20	1
	X_5	Exponential	100	100
	X_6	Normal	150	10
$G_2(\boldsymbol{x})$	X_1	Normal	1.01	0.0606
	X_2	Lognormal	400	40
	X_3	Normal	20	3.6
	X_4	Normal	$95.87\ 10^{-3}$	$9.587\ 10^{-3}$
	X_5	Gumbel	$67.11\ 10^{-3}$	$6.711\ 10^{-3}$
$G_3(\boldsymbol{x})$	X_1	Weibull	0.9377	0.0459
	X_2	Normal	220000	5000
	X_3	Normal	21000	1000
	X_4	Uniform	0.29/385.82	0.0058/385.82
	X_5	Normal	24	0.5
	X_6	Normal	8	0.3

For each of the performance functions $G_i(\boldsymbol{x}), i = 1,2,3$, the objective is to compute its first four statistical moments using the cubature formulae I-VI. To evaluate their accuracy, the estimates obtained are compared to those obtained by 10^5 MCS, taken here as a reference solution, since no closed-form solution is available for the three problems. The MCS results for the mean μ, the standard deviation σ, the skewness γ and the kurtosis κ of the three performance functions are listed in table II.3.

Table II. 3. Results of the first four statistical moments of the performance functions $G_1(\boldsymbol{x})$, $G_2(\boldsymbol{x})$ and $G_3(\boldsymbol{x})$

	μ	σ	γ	κ
$G_1(\boldsymbol{x})$	1466105.83	389291.79	-0.58371	5.02757
$G_2(\boldsymbol{x})$	0.09925	0.03425	0.02989	3.17895
$G_3(\boldsymbol{x})$	0.07863	0.02675	0.17250	3.14157

In figure II.16, the ratios of the estimates of the first four statistical moments obtained by cubature formulae I-VI to the reference solution given by MCS are plotted. These ratios are considered here as an indicator of accuracy. Indeed, the closer the value of this ratio is to 1, the more is accurate the prediction given by cubature formulae I-VI. As can be seen, for all three performance functions, all cubature formulae give accurate results for the mean and the standard deviation, since the corresponding ratios $\hat{\mu}/\mu_{MCS}$ and $\hat{\sigma}/\sigma_{MCS}$ respectively are very close to 1. In addition, we can clearly observe that the use of mixture of different types of random variables has a weak effect on the accuracy of the first two statistical moments of the performance functions.

For higher order statistical moments such as the kurtosis and the skewness, a divergence is observed between the estimates given by the cubature formulae I-VI and the reference solution obtained by MCS. This discrepancy is related to the order of the statistical moment to be computed and to the use of a mixture of normal and non-normal random variables to model the uncertain parameters. The mixture of

random variables used in the performance function $G_1(\boldsymbol{x})$ appears to have the most significant impact on the accuracy of the statistical moment estimates. Indeed, as can be seen in table II.2, the variability of the performance function $G_1(\boldsymbol{x})$ is induced by the most heterogeneous combination of random variables compared to the other performance functions $G_2(\boldsymbol{x})$ and $G_3(\boldsymbol{x})$. It is important to notice that the probabilistic computations are performed in the standard random space rather than the physical random space, which means that the real distributions are rewritten as a function of standard normal distributions. This may mitigate the effect that using a mixture of different kinds of random variables might have on the accuracy. Note that for formula VI, different values of the free parameter Δ are used to ensure the best possible estimates of the statistical moments of the performance functions. These values vary in the range [1.5, 2.5].

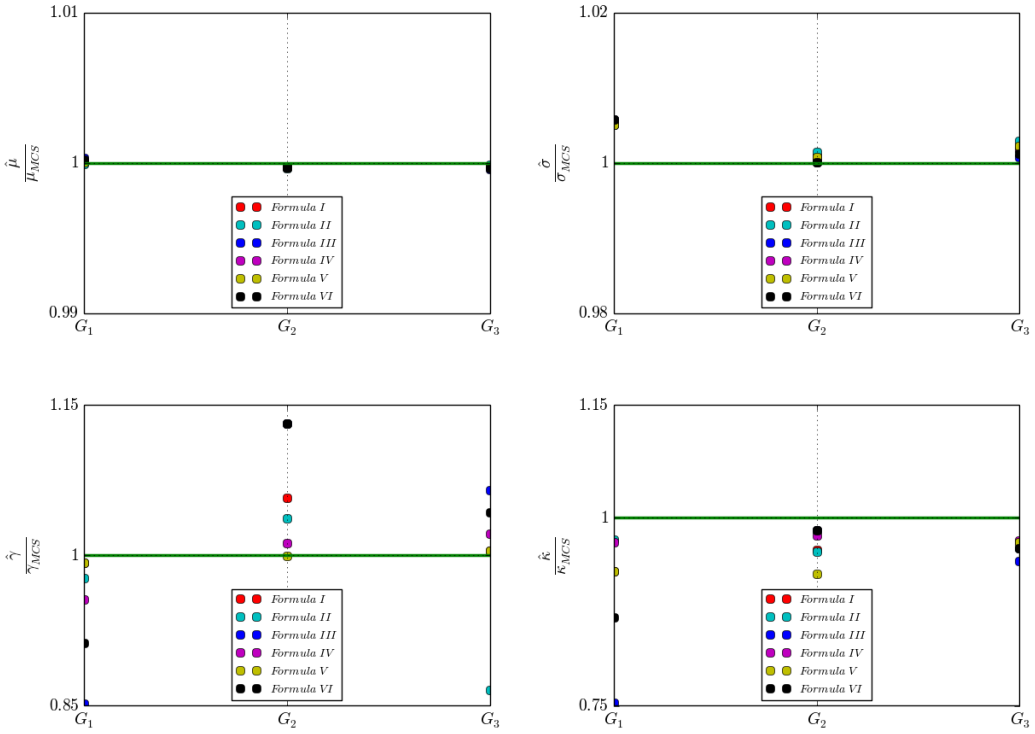

Figure II. 16. Ratios of estimates obtained by cubature formulae I-VI to the reference first four statistical moments given by MCS for the performance functions $G_1(\boldsymbol{x})$, $G_2(\boldsymbol{x})$ and $G_3(\boldsymbol{x})$

Figure II.17 compare the Probability Density Functions (PDF) $f_{G_i}, i = 1,2,3$ built from 10^5 MCS to those obtained from a moments-based technique using the previous estimates of the first four statistical moments of the performance functions $G_i(\boldsymbol{x}), i = 1,2,3$. As can be seen, the plotted results confirm our previous observation on the effect of using a mixture of different types of distributions to represent the variability of the uncertain parameters, since the PDFs are in good agreement in the cases of the performance functions $G_2(\boldsymbol{x})$ and $G_3(\boldsymbol{x})$. There is also then a discrepancy between the PDFs for the performance function $G_1(\boldsymbol{x})$ where a highly heterogonous combination of distributions is used to model the variability related to the uncertain parameters, which is due to the relative inaccuracy of the estimates of the higher order statistical moments, mainly for skewness and kurtosis. Note that the accuracy of the PDFs can be enhanced by using shifted generalized lognormal distribution technique *(Low, 2013)* or kernel

smoothing technique *(Wand and Jones, 1995)*, instead of the use of moments-based technique which requires a higher accurate estimate of the skewness and the kurtosis.

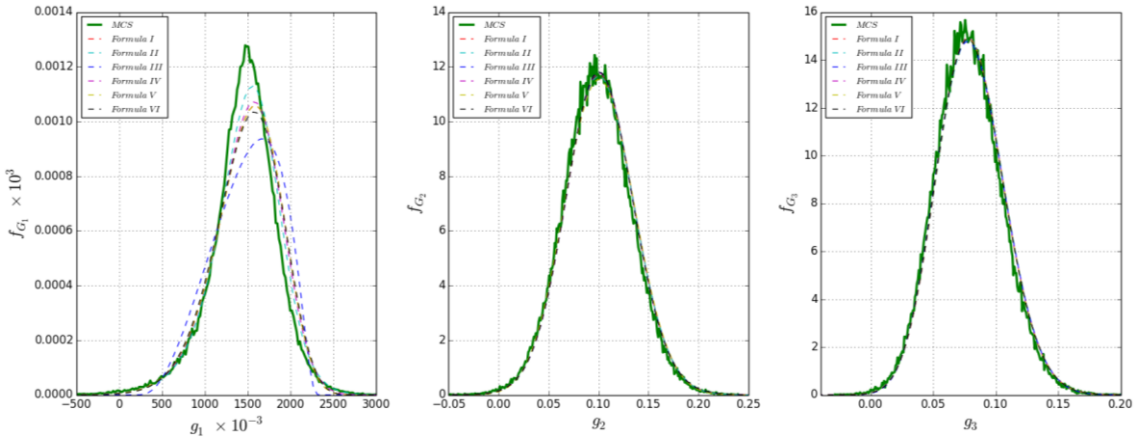

Figure II. 17. Comparison of the PDFs of the of the performance functions $G_1(\boldsymbol{x})$, $G_2(\boldsymbol{x})$ and $G_3(\boldsymbol{x})$

Next step, we assess the ability of the proposed approach to perform a reliability analysis, where the objective is to compute the probability of failure, or the reliability index related to a performance function. Usually, these quantities of interest are derived from probabilistic information provided by the tails of the distribution of the random variable representing the variability of the performance function. Hence, the PDF should be enough accurate in the vicinity of the tails to ensure reliable probabilistic information.

Figure II.18 shows the Cumulative Distribution Functions (CDFs) $F_{G_i}, i = 1,2,3$ of the performance functions $G_i(\boldsymbol{x}), i = 1,2,3$. These CDFs are nothing else than the evolutions of the failure probability noted P_f. They are plotted in a logarithmic scale on the vertical axis to emphasize the behavior around the tails. As can be seen, for the performance functions $G_2(\boldsymbol{x})$ and $G_3(\boldsymbol{x})$ the CDFs built from moments-based technique agree well with the reference CDFs obtained from 10^5 MCS, but with a small deviation around the distribution tail. In addition, the CDFs constructed from statistical moments obtained from cubature formulae I-VI are in good agreement since the gap between them is not significant. They can provide, in the cases of the performance functions $G_2(\boldsymbol{x})$ and $G_3(\boldsymbol{x})$, accurate estimates of the failure probabilities of an order of magnitude of 10^{-3}. However, for the performance function $G_1(\boldsymbol{x})$, a large deviation is observed between the CDFs built from moments-based technique and the one obtained from 10^5 MCS, almost in the entire range of the distribution. This is mainly due to the inaccurate estimates of higher order statistical moments. The discrepancy between the CDFs derived from statistical moments given by cubature formulae I-VI is also significant. We can clearly observe that formula II gives the best results, whereas formula III gives the worst ones.

In addition to the CDFs curves, figure II.18 shows the ratios of the estimates of the reliability index given by the proposed method, denoted by $\hat{\beta}$ and the reliability index given by MCS, denoted by β_{MCS}. These reliability indices are computed from the failure probability estimated from the corresponding CDFs constructed previously, using the following equations:

$$\hat{\beta} = \Phi^{-1}(\hat{P}_f), \qquad \beta_{MCS} = \Phi^{-1}(P_{f,MCS}) \tag{II.55}$$

where Φ denotes the standard normal cumulative distribution function.

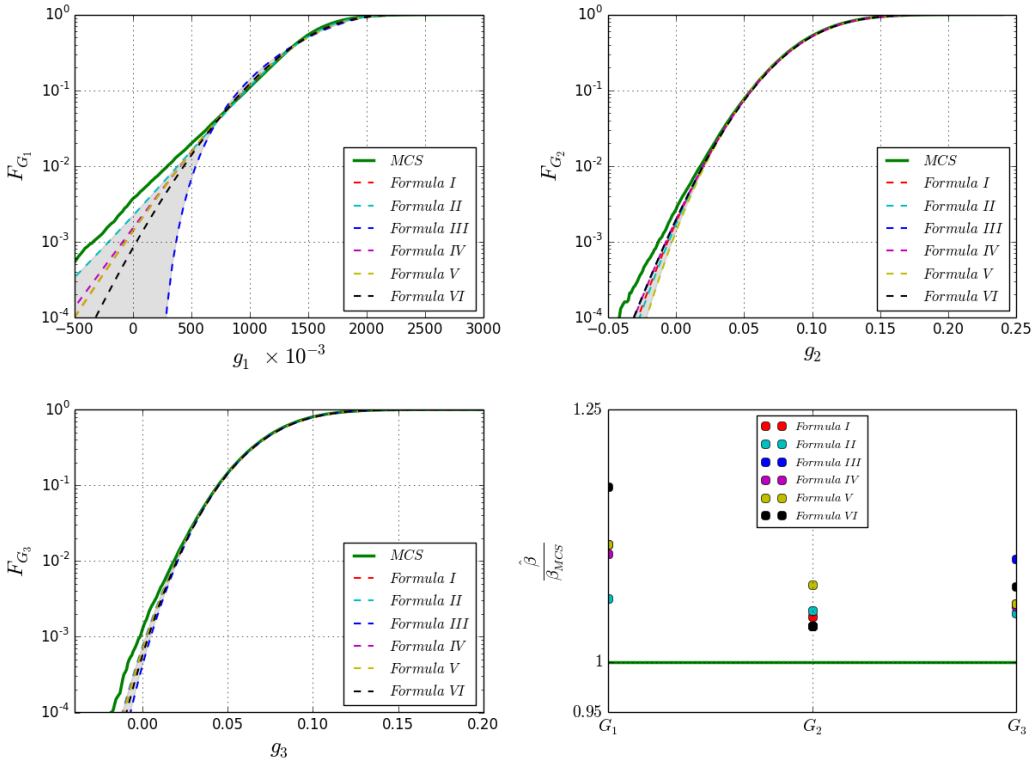

Figure II. 18. Comparison of the CDFs and the reliability indices of the performance functions $G_1(\boldsymbol{x})$, $G_2(\boldsymbol{x})$ and $G_3(\boldsymbol{x})$

As can be seen from figure II.18, the proposed method gives accurate estimate of the reliability index in the cases of the performance functions $G_2(\boldsymbol{x})$ and $G_3(\boldsymbol{x})$, since the ratio $\hat{\beta}/\beta_{MCS}$ is close to 1. Indeed, the values of the latter vary in the range [1.035, 1.102]. However, for the performance function $G_1(\boldsymbol{x})$, the results are less accurate particularly those given by cubature formula I, which largely deviate from the reference solution given by MCS, since the ratio $\hat{\beta}/\beta_{MCS}$ is around 3.73. For the other cubature formulae, the value of the ratio $\hat{\beta}/\beta_{MCS}$ varies between 1.062 and 1.173, given by cubature formulae II and VI, respectively.

This example clearly shows the ability of the proposed method to perform accurately either statistical moments or reliability analysis, on explicit physical models related to real-life engineering problems involving different kind of mixture of normal and non-normal random variables. This accuracy is reached at a very low computational effort compared to classical uncertainty propagation strategies such those based on Gauss-Hermite quadrature, MCS and FORM. It may also be retained that problems involving a higher heterogeneous mixture of random variables should be treated with care and particular attention should be paid to the choice of the cubature formula used for the computation of the integral quantities.

5.2. Implicit models

5.2.1. Deflection of truss structure

The following example deals with of a planar truss structure as shown in figure II.19. This problem was first introduced by *(Lee and Kwak, 2006)* to conduct reliability analysis based on response surface method. After that it has been widely used by other authors *(Blatman, 2009; Konakli and Sudret, 2016; Xu and Kong, 2018)* to conduct different kinds of probabilistic analysis.

The truss structure comprises 11 horizontal bars and 12 oblique bars made of the same constitutive material and subjected to six vertical loads located in its upper part. Under this loading, the mechanical response of interest is represented by the mid-span deflection, noted by v. Since the analytical solution is not available, this mechanical response is obtained by a numerical model implemented under a finite element software *(cast3m, 2021)*. In figure II.19, the finite element mesh and the deformed shape of the truss structure are depicted.

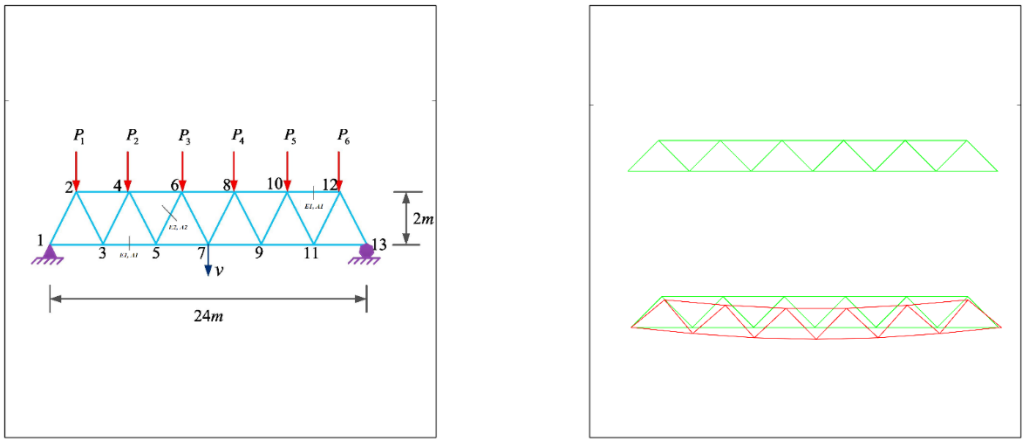

Figure II. 19. Truss structure: geometry and applied loads (left), finite element mesh and deformed shape (right)

Ten uncertain parameters are considered for this problem. They are the vertical loads denoted by $P_i, i = 1,2,\dots,6$, the Young's modulus and cross-section areas of the horizontal bars denoted by E_1 and A_1, respectively, and the Young's modulus and cross-section areas of the oblique bars denoted by E_2 and A_2, respectively. They are represented by independent random variables, gathered in the vector $\boldsymbol{X} = \{E_1, E_2, S_1, S_2, P_1, P_2, P_3, P_4, P_5, P_6\}^T$, whose distribution type, mean μ and standard deviation σ are listed in table II.4.

Table II. 4. Truss structure: probability distributions and statistical characteristics of the random variables

Parameter	Distribution	μ	σ
E_1, E_2	Lognormal	210000 MPa	21000 MPa
S_1	Lognormal	0.002 m^2	0.0002 m^2
S_2	Lognormal	0.001 m^2	0.0001 m^2
$P_1, \dots, P_6$	Gumbel	50 kN	7.5 kN

First, we conduct statistical moments analysis to assess the effect of the uncertain parameters on the variability of the mechanical response of interest. The involved multidimensional integrals for the first four statistical moments of the mid-span deflection $v(\boldsymbol{X})$ are computed using cubature formulae II-VI. The

obtained results are given in table II. 5. Note that cubature formula I is not used here since it is only valid for integration dimension up to 7.

Table II. 5. Truss structure: statistical moments of the mid-span deflection

Statistical moments	Cubature formula					MCS
	II	III	IV	V	VI	
μ	0.07940	0.07942	0.07940	0.07940	0.07942	0.07938
σ	0.01108	0.01109	0.01107	0.01107	0.01109	0.01107
γ	0.46478	0.48255	0.41967	0.45553	0.48538	0.49200
κ	3.24564	3.48523	2.67713	3.19121	3.45394	3.44554
Number of FEM runs	133	201	201	276	201	10^5

The reference values of the statistical moments are obtained by 10^5 crude MCS directly performed on the Finite Element Model (FEM) of the truss structure. Figure II.20 displays the convergence of MCS for the estimates of the first four statistical moments of the mechanical response. As can be seen, convergence is well achieved since the estimates of the quantities of interest no longer vary after 10^5 runs of the FEM. The PDF of the mid-span deflection is also plotted and compared to some standard distributions. As we can observe, the PDF of the mid-span deflection is accurately approximated by the lognormal distribution. This is a remarkable result since an analytical formulation of the PDF is now available and the probability of occurrence of each possible event (i.e., the possible value of the mid-span deflection) can be easily derived. Moreover, the CDF of the mechanical response is built by integrating the PDF previously obtained by MCS. This CDF can be directly used to perform a serviceability reliability analysis of the truss structure, defined as exceeding a maximum allowable deterministic deflection.

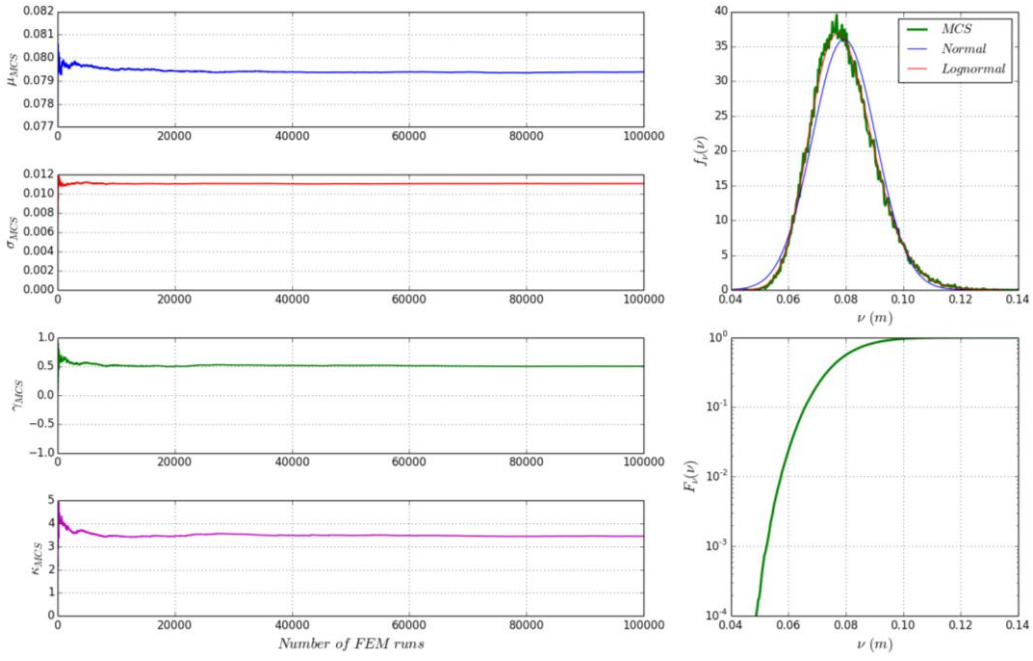

Figure II. 20. Truss structure: convergence of MCS

As can be seen in table II.5, all cubature formulae give accurate estimates of the first two statistical moments of the mechanical response, since in the worst case the relative error is about 0.05% and 0.18% for the mean and the standard deviation, respectively. Formula II provides the best balance between accuracy and efficiency since it only requires 133 runs of the FEM, instead of 201 evaluations for cubature

formulae III, IV and VI, and 273 evaluations for cubature formula V. As expected, the accuracy of the computation of the higher order statistical moments of the mechanical response decreases with the moment order. Indeed, for skewness and kurtosis only cubature formulae III and VI provide the closest estimates to the reference solution.

Figure II.21 compares the PDFs and the CDFs built using a moments-based technique and those given by MCS. As can be seen, the PDFs given by the proposed method, especially those based on cubature formulae III and VI, fit very well the PDF built from 10^5 MCS in the entire region, including the tails. The CDFs curves plotted in the logarithmic scale following the vertical axis, clearly demonstrate the good accuracy level of the proposed method when the statistical moments are derived from cubature formula VI, since the deviation from the reference solution is insignificant in the vicinity of the tails. This accuracy is achieved with higher efficiency, since it only requires 201 calls of the FEM.

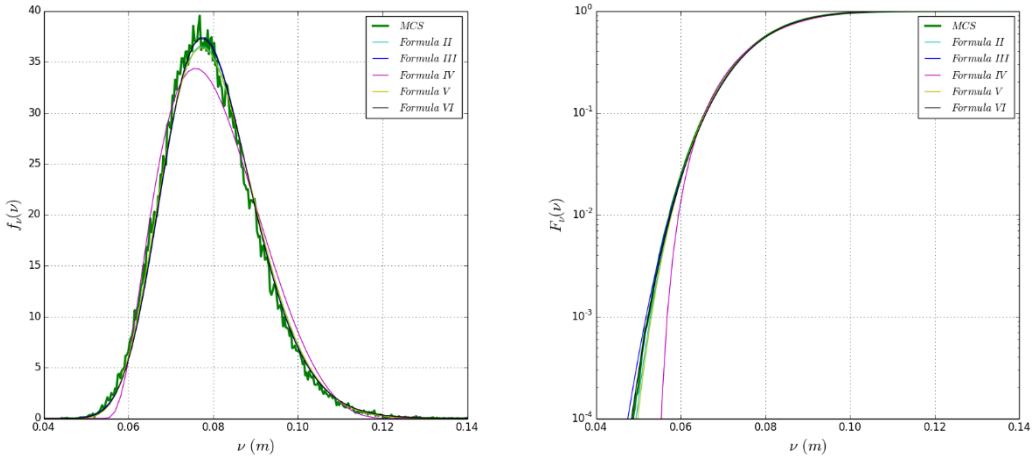

Figure II. 21. Truss structure: comparison of the PDFs and CDFs of the mechanical response

In a next step, the reliability analysis is performed to assess the accuracy of the proposed approach in estimating the probability of failure of the truss structure with respect to a threshold deflection denoted by $\nu_{threshold}$ and taken as a deterministic quantity. The associated performance function reads:

$$G(\boldsymbol{x}) = \nu_{threshold} - \nu(\boldsymbol{x}) \qquad (II.56)$$

To evaluate the effect of the order of magnitude 10^{-k} of the failure probability on the accuracy of the estimates, a parametric study is carried out, where the threshold deflection varies in the range [0.1 m, 0.14 m]. Note that, only cubature formula VI is used, since it gives the most accurate results as stated in the statistical moments analysis conducted previously. The results obtained regarding failure probabilities and associated reliability indices, are listed in table II.6 and compared to the reference solutions given by Importance Sampling (IS). For comparison purposes, the reliability analysis is also performed by FORM, where the results obtained are reported in table II.6. The relative error, denoted by ϵ_β, is defined as the difference between the reliability index estimates given by either the proposed method or FORM, and those provided by IS.

As can be seen from the results reported in table II.6, the proposed method, based on cubature formula VI, gives accurate results since the relative error on the reliability index estimation does not exceed 2.51%

in the worst case, when recorded for a threshold deflection of 0.1 m. Moreover, as we can observe, this accuracy is less affected by the magnitude of the failure probability compared to the FORM method where the relative error increases with the magnitude of the failure probability.

Table II. 6. Truss structure: comparison of the reliability analysis results given by the proposed method, IS and FORM

$v_{threshold}$	IS		FORM			Formula VI		
	$\hat{P}_f$	$\hat{\beta}$	$\hat{P}_f$	$\hat{\beta}$	$\epsilon_\beta(\%)$	$\hat{P}_f$	$\hat{\beta}$	$\epsilon_\beta(\%)$
0.10 m	4.09 10^{-2}	1.75	2.80 10^{-2}	1.91	9.14	4.40 10^{-2}	1.7060	2.51
0.11 m	9.90 10^{-3}	2.38	5.04 10^{-3}	2.57	7.98	9.22 10^{-3}	2.3565	0.98
0.12 m	1.35 10^{-3}	3.17	7.62 10^{-4}	3.17	6.73	1.66 10^{-3}	2.9368	1.12
0.13 m	2.16 10^{-4}	3.71	2.64 10^{-4}	3.71	6.00	2.64 10^{-4}	3.4662	0.96
0.14 m	3.44 10^{-5}	4.21	3.98 10^{-5}	4.21	5.78	3.98 10^{-5}	3.9453	0.87

In the following, we conduct a sensitivity analysis of the truss structure with respect to the mid-span deflection. The main purpose is to evaluate the contribution of each uncertain parameter on the variability of the mechanical response. Hence, the quantities of interest are first-order and total Sobol sensitivity indices, denoted by S_1 and S_T, respectively. The reference solution, listed in table II.7, is obtained by crude MCS based on 10^6 samples for each Sobol index. These preliminary results show that the effect of interactions between uncertain parameters is small compared to the effect of each uncertain parameter considered separately, since the values of the total and first-order Sobol indices are too close. Note that for uncertain parameters with a non-significant effect, the total Sobol indices are smaller than the corresponding first-order Sobol indices. This result is contradictory since the total indices should be larger than the first-order ones; it is a consequence of the small bias of the MCS estimator as explained in *(Owen, 2013)*.

Table II. 7. Truss structure: first-order and total Sobol sensitivity indices obtained by MCS

	E_1	E_2	S_1	S_2	P_1	P_2	P_3	P_4	P_5	P_6
$\hat{S}_1^{MCS}$	0.3662	0.0137	0.3664	0.0138	0.0060	0.0383	0.0777	0.0770	0.0380	0.0059
$\hat{S}_T^{MCS}$	0.3696	0.0126	0.3712	0.0126	0.0047	0.0374	0.0776	0.0773	0.0374	0.0048

As shown in section 2.3, the computation of the total Sobol indices involves the evaluation of a multidimensional integral composed of two parts (see equation II.22): the inner part is a one-dimensional integral which is computed by Gauss-Hermite quadrature scheme of level 3 (GH3), and the outer part corresponding to an (N-1)-dimensional integral is computed by one of the cubature formula II-VI. The first-order Sobol indices also involve the evaluation of a multidimensional integral composed of two parts. But conversely, the inner part corresponds to an (N-1)-dimensional integral that is computed by one of the cubature formula II-VI and the outer part is a one-dimensional integral computed by the Gauss-Hermite quadrature scheme of level 3. Figure II.22 compares the estimates of the first-order Sobol indices given by the proposed method with those of the reference solution; they are plotted in decreasing order of importance.

As can be seen, the proposed method, independently from the used cubature formula, allows to range in the right order of importance the uncertain parameters, as the reference method. This information is quite important since it allows us to distinguish parameters with significant effect on the mechanical response from those having a weak effect. For uncertain parameters with dominant contributions, which are the

cross-section areas S_1 and the Young's modulus E_1 of the horizontal bars, the first-order indices obtained by the proposed method are in good agreement with the reference ones. Indeed, the relative error varies in the ranges [0.1%, 1.8%] and [0.13%, 1.74%], respectively for the first-order indices corresponding to the uncertain parameters S_1 and E_1. We can also observe that the proposed method based on cubature formula V, provides the most accurate results over all the first-order indices, compared to the other cubature formulae, since the maximum relative error is around 5%, which is recorded on the estimate of the first-order index related to the uncertain parameter with the weakest main effect P_1.

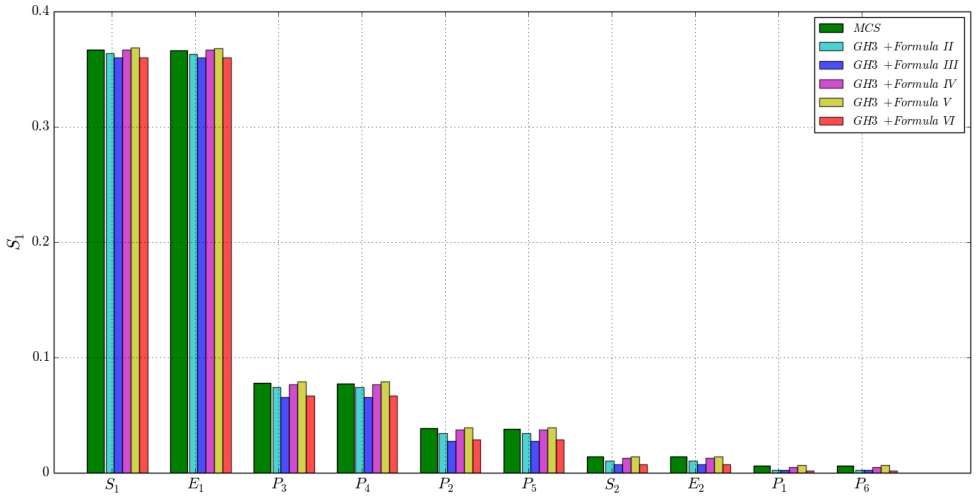

Figure II. 22. Truss structure: comparison of the estimates of the first-order Sobol indices

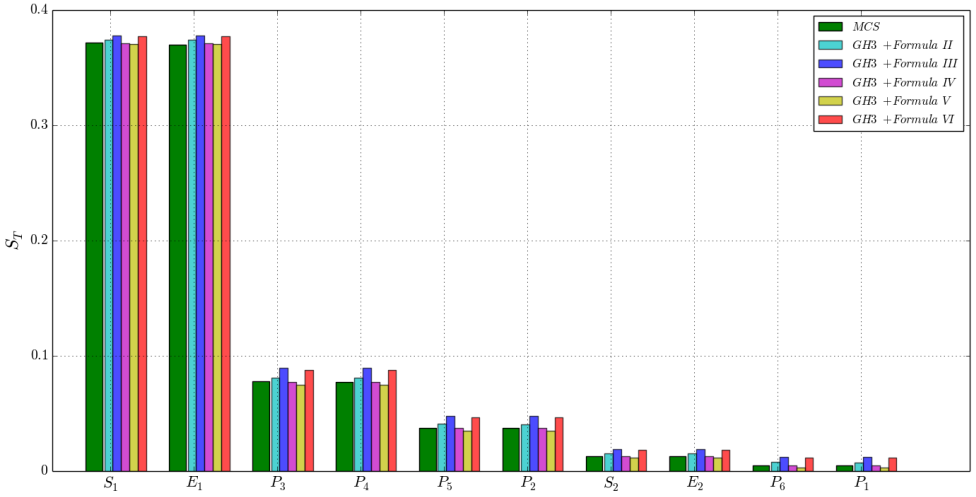

Figure II. 23. Truss structure: comparison of the estimates of the total Sobol indices

In figure II.23, we assess the accuracy of the proposed method for the computation of the total Sobol indices. As can be seen, observations quite similar to those made for the previous first-order indices, can be made. Indeed, for the uncertain parameters having a significant effect on the variability of the mechanical response, which are also the cross-section areas S_1 and the Young's modulus E_1 of the horizontal bars, the proposed method independently of the cubature formula used for the evaluation the integral quantities, gives accurate estimates of the total indices since the relative error varies in the ranges [0.1%, 1.8%] and [0.16%, 2.11%], respectively for the total indices corresponding to the uncertain parameters

S_1 and E_1. Among the proposed cubature formulae, the most accurate estimates are given by formula VI, since the corresponding relative error is in the range [0.1%, 6.25%].

Note that the computation of the first-order or the total Sobol indices requires the same number of FEM calls when the same cubature formula is used to evaluate the integrals involved in each case. In table II.8 the computation costs of the proposed method based on cubature formulae II-VI and compared to those required by Full Tensor-product Gauss-Hermite method of level 3 (FTGH3) and MCS are listed. As can be observed, the proposed method is by far the most efficient for computing the Sobol sensitivity indices. The cubature formulae IV and V, which provide the most accurate results, require 5092 and 4657 runs of the FEM, respectively.

Table II. 8. Truss structure: comparison of the computational costs of the proposed method, FTGH3 and MCS

Method	Cubature formula					FTGH3	MCS
	II	III	IV	V	VI		
Number of FEM runs	3464	5092	5092	4657	5092	10x59049	$10x10^6$

Through this example, we have demonstrated the ability of the proposed method, based on different efficient cubature formulae, to perform an uncertainty propagation analysis on an explicit mechanical model involving moderate probabilistic dimensionality (i.e., number of random variables representing the uncertain parameters). It has been shown that the three possible types of uncertainty propagation analysis, which are statistical moments and distributions analysis, reliability analysis and sensitivity analysis, can be addressed with low computational cost. It may be retained that all cubature formulae give accurate estimates of the mean and the standard deviation of the quantities of interest. However, for higher order statistical moments, cubature formulae III and VI seems to be the most accurate. This high level of accuracy on the estimates of the first four statistical moments makes it possible the use of moment-based techniques to build particularly accurate PDFs in the vicinity of the distribution tails, which are useful for reliability analysis. In the case of sensitivity analysis, cubature formulae VI and V give the closest estimates to the reference solutions, for the total and the first-order Sobol indices, respectively.

5.2.2. Heat conduction in a square plate

Let us consider a two-dimensional stationary heat-conduction in a square plate defined on the spatial domain $\Omega = (-0.5m, 0.5m) \times (-0.5m, 0.5m)$, as shown in figure II.24. This example was first introduced by *(Nouy, 2010)* and used later in the literature (*Konakli and Sudret, 2016)* of uncertainty propagation analysis as a benchmark problem. The temperature field denoted by $T(\boldsymbol{z})$, $\boldsymbol{z} = (x, y) \in \Omega$ is described by the following partial differential equation:

$$-\nabla(k(\boldsymbol{z}) \cdot \nabla T(\boldsymbol{z})) = Q \cdot \mathbb{I}_{\Omega_1} \qquad (II.57)$$

where $Q = 2000\ W/m^3$ is a heat source applied in the square area $\Omega_1 = (0.2m, 0.3m) \times (0.2m, 0.3m)$, $\mathbb{I}_{\Omega_1}$ is the indicator function equal to 1 if $\boldsymbol{z} \in \Omega_1$, and $k(\boldsymbol{z})$ is the thermal conductivity of the constitutive material of the plate which is considered as a spatially varying quantity. The boundary conditions applied to the square plate are: $T = 0$ on the top edge and $\nabla T \cdot \boldsymbol{n}$ on the left, bottom, and right edges, where $\boldsymbol{n}$ is the vector

normal to the boundary. The model response represents the average temperature $\tilde{T}_{\Omega_2}$ in the square area $\Omega_2 = (-0.2m, -0.3m) \times (-0.2m, -0.3m)$, which is defined by the following integral:

$$\tilde{T}_{\Omega_2} = \frac{1}{|\Omega_2|} \int_{\boldsymbol{z} \in \Omega_2} T(\boldsymbol{z}) d\boldsymbol{z} \qquad (II.58)$$

where $T(\boldsymbol{z})$ is the temperature field in the whole square area Ω, computed from a FEM implemented in the software *(cast3m, 2021)*. The finite element mesh (see Figure II.24) is made of 1926 3-noded triangular elements and 3690 nodes.

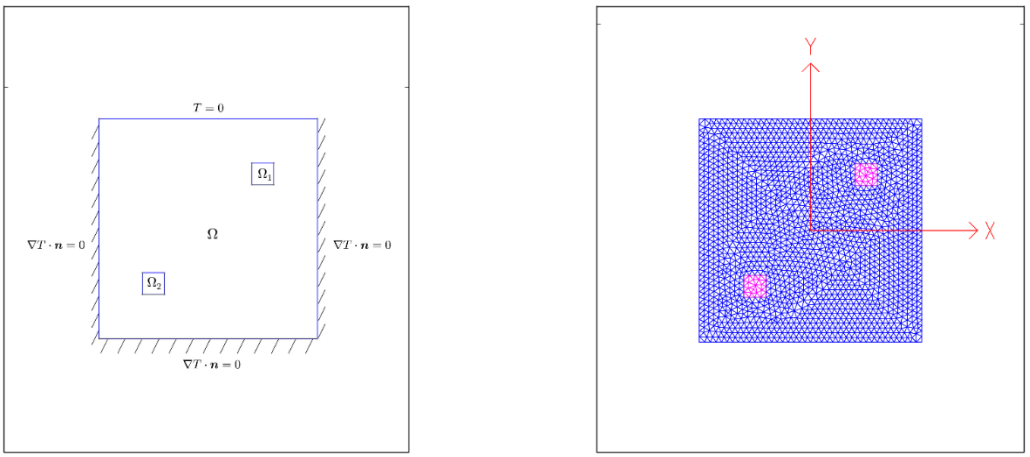

Figure II. 24. Heat conduction in square plate: geometry and boundary conditions (left),and finite element mesh (right)

The thermal conductivity $k(\boldsymbol{z}, \omega)$ of the constitutive material of the plate is considered as a spatially varying uncertain parameter, modelled by a two-dimensional lognormal field, with mean value $\mu_k = 1\ W/°C\ m$ and standard deviation $\sigma_k = 0.3\ W/°C\ m$. It is defined as the exponential of a normal random field $v(\boldsymbol{z}, \omega)$ with mean $\mu_v = \ln(\mu_k) - \frac{1}{2}\ln(1 + \sigma_k^2/\mu_k^2)$ and standard deviation $\sigma_v = \sqrt{\ln(1 + \sigma_k^2/\mu_k^2)}$:

$$k(\boldsymbol{z}, \omega) = \exp[v(\boldsymbol{z}, \omega)] = \exp[\mu_v + \sigma_v . u(\boldsymbol{z}, \omega)] \qquad (II.59)$$

where ω is a parameter which allows to emphasize the random nature of $k(\boldsymbol{z}, \omega)$, $u(\boldsymbol{z}, \omega)$ is a standard normal random field with zero mean and unit standard deviation. It is governed by the following square exponential autocorrelation function:

$$\rho(\boldsymbol{z}_1, \boldsymbol{z}_2) = \exp\left[-\frac{\|\boldsymbol{z}_1 - \boldsymbol{z}_2\|^2}{l_c^2}\right] \qquad (II.60)$$

where l_c denotes the correlation length, which is set equal to $0.2\ m$.

The standard normal field $u(\boldsymbol{z}, \omega)$ is discretized using the Expansion Optimal Linear Estimation (EOLE) method *(Li and Der Kiureghian, 1993)*, and its M^{th} order approximation denoted by $\hat{u}(\boldsymbol{z}, \omega)$, reads:

$$\hat{u}(\boldsymbol{z}, \omega) = \sum_{i=1}^{M} \frac{\boldsymbol{\phi}_i^T \boldsymbol{C}_{z,z_i}}{\sqrt{\lambda_i}} u_i(\omega) \qquad (II.61)$$

In this approximation, $u_i(\omega), i \in \{1, \dots, M\}$ are independent standard normal variables, $\boldsymbol{C}_{z,z_i}$ is a vector with components $\boldsymbol{C}_{z,z_i}^j = \rho(\boldsymbol{z}, \boldsymbol{z}^j), j \in \{1, \dots, m\}$, where $\boldsymbol{z}^j, j \in \{1, \dots, m\}$ are the nodes of an appropriate defined mesh

(i.e. this mesh is only used to discretize the random field and is different from the one used in the finite element computations), λ_i and $\boldsymbol{\phi}_i^T$ are respectively eigenvalues and eigenvectors of the correlation matrix $\boldsymbol{C}_{z,z}$ with components $\boldsymbol{C}_{z,z}^{k,l} = \rho(\boldsymbol{z}^k, \boldsymbol{z}^l), k, l \in \{1, \dots, m\}$.

According to the EOLE method, and in the case of a square exponential autocorrelation function, the element size of the mesh used to discretize the random field must be in the range $[l_c/2, l_c/3]$ *(Sudret and Der Kiureghian, 2000)*. Based on this rule, we use a square uniform mesh containing 169 elements of size 0.08 m. Furthermore, to obtain an accurate EOLE approximation of the random field $u(\boldsymbol{z}, \omega)$, the truncation order M in equation (II.61) is set to 53, which is obtained according to the following criterion:

$$\sum_{i=1}^{M} \lambda_i \geq 0.99 \sum_{i=1}^{m} \lambda_i \qquad (II.62)$$

Equation (II.62) means that only the M first largest eigenvalues, which contribute 99% of the sum of all the m available eigenvalues resulting from the decomposition of the correlation matrix, are retained. This leads to a relative variance error $\epsilon(\boldsymbol{z}) = \mathrm{Var}[u(\boldsymbol{z}, \omega) - \hat{u}(\boldsymbol{z}, \omega)]/\mathrm{Var}[u(\boldsymbol{z}, \omega)]$ less than 0.092%. Note that, the eigenvalues are first sorted in ascending order, before selecting the most important of them. Figure II.25 shows the 20 first shape functions $\boldsymbol{\phi}_i^T \boldsymbol{C}_{z,z_i}, i \in \{1, \dots, 53\}$ used in the EOLE method to build the realizations of the random field $u(\boldsymbol{z}, \omega)$.

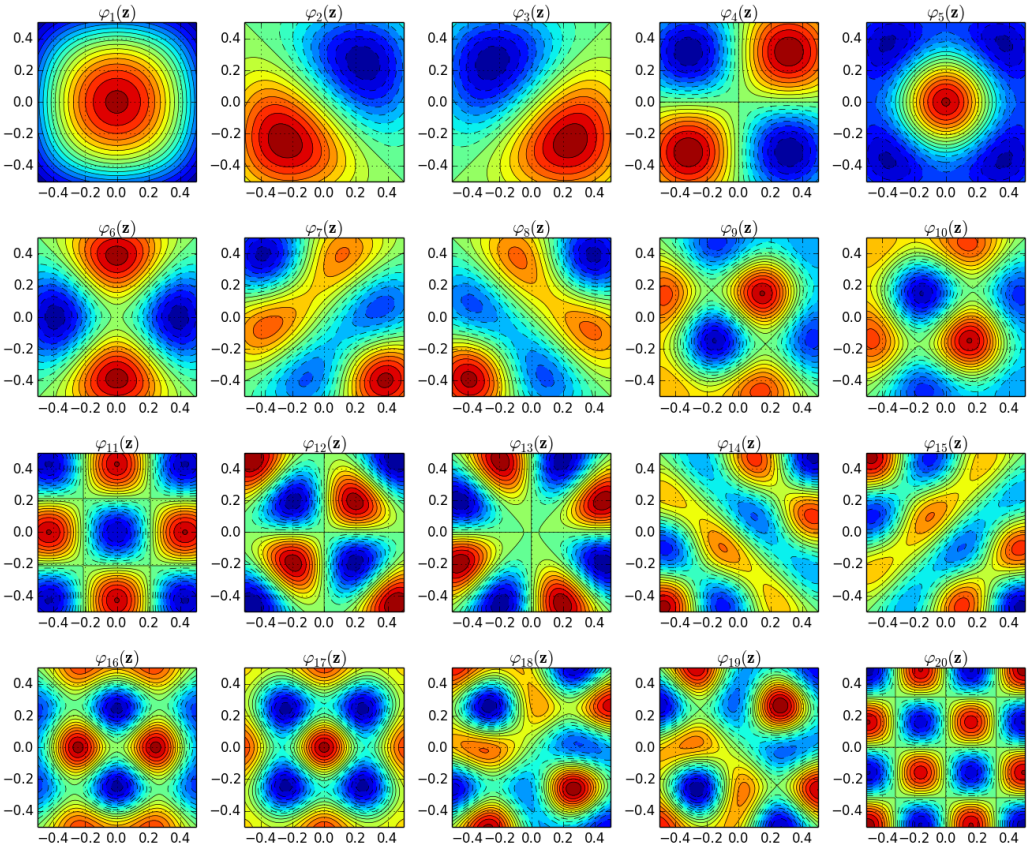

Figure II. 25. Heat conduction in square plate: 20 first shape functions $\boldsymbol{\phi}_i^T \boldsymbol{C}_{z,z_i}, i \in \{1, \dots, 53\}$ according to the EOLE method

Now, for a given realization of the random variables $u_i(\omega), i \in \{1, \ldots, 53\}$, and using equations (II.59) and (II.61), a realization $\hat{k}(\boldsymbol{z}, \omega)$ of the random field representing the thermal conductivity of the square plate is easily obtained. A sample of 10 realizations of $\hat{k}(\boldsymbol{z}, \omega)$ is depicted in figure II.26.

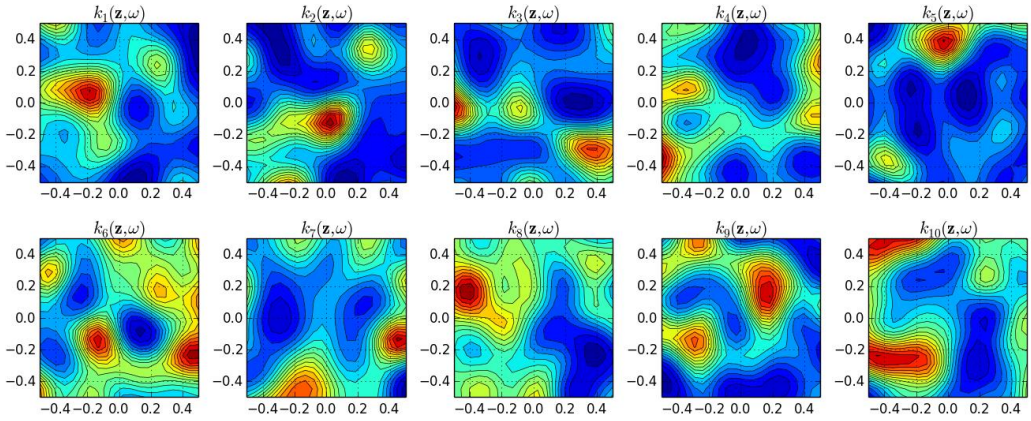

Figure II. 26. Heat conduction in square plate: example of 10 realizations of the thermal conductivity field $\hat{k}(\boldsymbol{z}, \omega)$

Because of the spatially varying uncertainty of the thermal conductivity, the temperature within the square plate is also an uncertain spatially varying parameter that can be conveniently modeled by a random field. The temperature field $T(\boldsymbol{z}, \omega)$ is computed from the FEM implemented on the cast3m software. Figure II.27 shows the realizations of $T(\boldsymbol{z}, \omega)$ associated with the previous realizations of the thermal conductivity field shown in figure II.26.

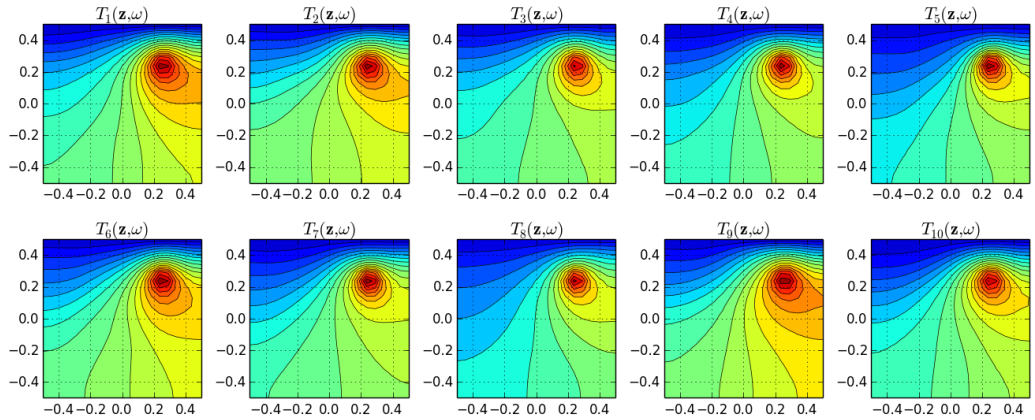

Figure II. 27. Heat conduction in square plate: example of 10 realizations of the temperature field $T(\boldsymbol{z}, \omega)$

Since the model response of interest, defined as the average temperature $\tilde{T}_{\Omega_2}$ recorded in the square area Ω_2, is a scalar parameter as we can see in equation (II.58), the associated uncertainty can be simply modeled by a random variable, whose statistical characteristics are to be determined. Thus, we are first interested in the computation of the first four statistical moments of the model response $\tilde{T}_{\Omega_2}$. The multidimensional integrals involved in these computations are evaluated by the cubature formulae II, III, IV and VI. Note that the cubature formulae I and V are not used here because they are only capable of computing integrals of maximum dimension up to 7 and 16, respectively. The results given by the proposed method based on the aforementioned cubature formulae are listed in table II.9, along with those obtained by 10^5 crude MCS applied directly to the square plate FEM. Figure II.28 shows the convergence of the estimates given by MCS, taken here as a reference solution. We can observe that the convergence of the

first four statistical moments is well achieved with 10^5 samples of model response, and as expected, the convergence of higher order statistical moments is slower than the convergence of the mean and the standard deviation. In addition, the PDF of the model response is constructed and compared to some standard distributions. The comparison show that the PDF fits a lognormal distribution. The CDF is also simply deduced from the integration of the corresponding PDF, allowing, if desired, a reliability analysis to be performed without spending additional computational effort (i.e., no additional runs of the FEM are required).

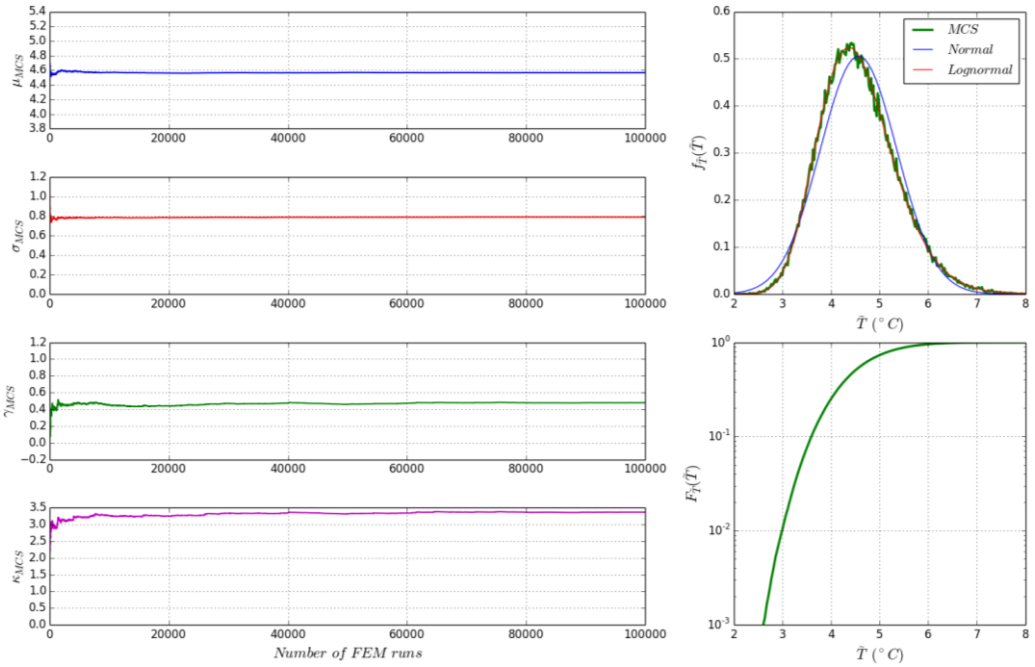

Figure II. 28. Heat conduction in square plate: convergence of MCS

The results depicted in table II.9 show that all the cubature formulae employed in this example give accurate estimates of the first two statistical moments of the model response $\tilde{T}_{\Omega_2}$ since the maximum error is around 0.032% and 0.2% for the mean and the standard deviation, respectively. The cubature formula II appears to be the most economical integration scheme since it requires only 2971 runs of the FEM to achieve the best recorded accuracy compared to the other cubature formulae. For skewness and kurtosis, cubature formulae II and VI give the closest estimates to the reference solution.

Table II. 9. Heat conduction in square plate: statistical moments of the average temperature $\tilde{T}_{\Omega_2}$

Statistical moments	Cubature formula				MCS
	II	III	IV	VI	
μ	4.5678	4.5678	4.5681	4.5678	4.5666
σ	0.7880	0.7877	0.7876	0.7878	0.7891
γ	0.5388	0.5543	0.46112	0.5530	0.4787
κ	3.7140	4.5166	3.6658	3.9075	3.3649
Number of FEM runs	2971	5619	5619	5619	10^5

Figure II.29 compares the PDFs and CDFs obtained from moments-based technique to those derived from MCS. As can be seen, the PDFs and CDFs derived from statistical moments computed by cubature formulae II, III and VI are in good agreement with those of the reference solution and allow to estimate accurately

tail probabilities of order magnitude 10^{-2}, which can be useful to conduct reliability analysis. Indeed, let us consider the following performance function:

$$G(\boldsymbol{x}) = T_{threshold} - \tilde{T}_{\Omega_2}(\boldsymbol{x}) \qquad (II.63)$$

where $T_{threshold}$ is a deterministic parameter that indicates a threshold temperature that should not be exceeded in order to ensure the integrity of the square plate with respect to the loading conditions.

A parametric study is conducted in the following, where the threshold temperature varies from 6 °C to 7.5 °C. The failure probabilities $\hat{P}_f$ and the corresponding generalized reliability indices $\hat{\beta}$ are computed and listed in table II.10. Note that the failure probabilities are directly obtained from the CDFs corresponding to cubature formulae II, IV and VI, which give the exact results as demonstrated previously.

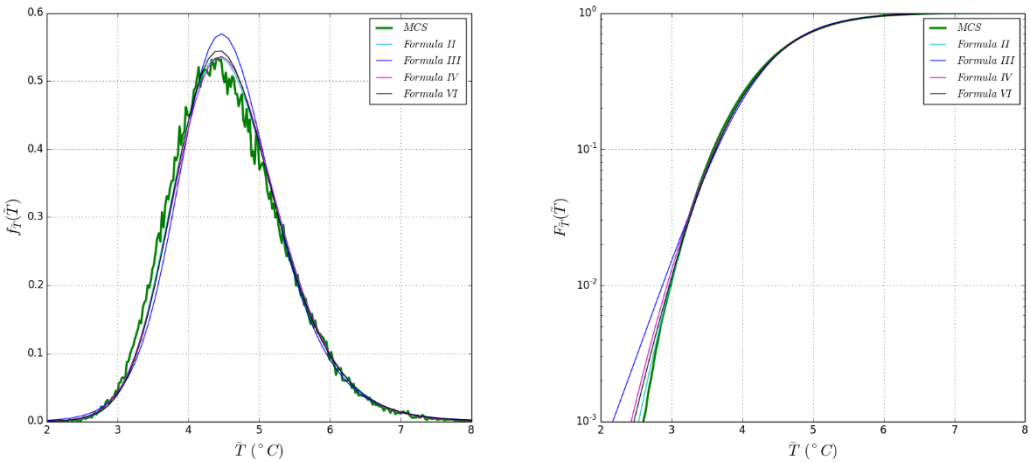

Figure II. 29. Heat conduction in square plate: comparison of the PDFs and CDFs of the model response $\tilde{T}_{\Omega_2}$

For threshold temperatures $T_{threshold} \in \{6, 6.5\}$ ℃, which lead to failure probabilities of magnitude 10^{-2}, the proposed method, regardless of the cubature formula used to compute the multidimensional integrals, gives accurate estimates of the reliability indices since the relative error varies in the range [0.2%, 1.84%] which can be explained by the higher accuracy achieved for tail probabilities of magnitude 10^{-2}. The estimates of the reliability indices corresponding to failure probabilities of magnitude 10^{-3} are also in agreement with the reference solution since the maximum relative error is less than 5%, except for a threshold temperature $T_{threshold} = 7.5$ ℃ where the relative error is about 6.32% for cubature formula VI.

For higher threshold temperatures however, a relatively significant discrepancy is observed between the estimates of the reliability indices given by the proposed method and those of MCS, since the relative error is in the range [6.06%, 9.01%]. Despite this, these results can be considered reasonable preliminary estimates of low failure probabilities since they require an affordable computational effort. Indeed, due to the high dimensionality of this problem, FORM and SORM approaches are inefficient even though they are usually able to provide inexpensive estimates of the quantities of interest required in reliability analysis.

Table II. 10. Heat conduction in square plate: comparison of the reliability analysis results given by the proposed method and MCS

$T_{threshold}$	MCS		Cubature formula					
			II		IV		VI	
	$\hat{P}_f$	$\hat{\beta}$	$\hat{P}_f$	$\hat{\beta}$	$\hat{P}_f$	$\hat{\beta}$	$\hat{P}_f$	$\hat{\beta}$
6.0 °C	$4.578\ 10^{-2}$	1.6872	$4.628\ 10^{-2}$	1.6820	$4.493\ 10^{-2}$	1.6962	$4.612\ 10^{-2}$	1.6837
6.5 °C	$1.542\ 10^{-2}$	2.1591	$1.653\ 10^{-2}$	2.1314	$1.569\ 10^{-2}$	2.1523	$1.704\ 10^{-2}$	2.1192
7.0 °C	$4.800\ 10^{-3}$	2.5899	$5.551\ 10^{-3}$	2.5395	$5.162\ 10^{-3}$	2.5648	$6.054\ 10^{-3}$	2.5090
7.5 °C	$1.130\ 10^{-3}$	3.0538	$1.792\ 10^{-3}$	2.9126	$1.640\ 10^{-3}$	2.9401	$2.114\ 10^{-3}$	2.8607
8.0 °C	$2.400\ 10^{-4}$	3.4917	$5.732\ 10^{-4}$	3.2519	$5.191\ 10^{-4}$	3.2800	$7.440\ 10^{-4}$	3.1770

The above analysis clearly demonstrates the ability of the proposed method to effectively handle the propagation of uncertainty through a complex and time-consuming model with high probabilistic dimensionality. With accurate estimates of the first four statistical moments, the PDF of the model response is also accurately built across the entire range of the distribution, including the tails, simply using a moments-based technique. This then allows us to perform reliability analysis for various *Demand* thresholds (i.e., see section 2.4) of a prescribed performance function describing the serviceability of the square plate subjected to heat conduction.

6. Conclusion

In this chapter, we have briefly recalled the general principles of the uncertainty propagation problem through models representing physical phenomena. Depending on the expected results, three types of analysis can be performed: statistical moments and distribution analysis, sensitivity analysis or reliability analysis. For these three types of analysis, the mathematical formulations of the quantities of interest have been presented. It has been shown that the main issue is always the same, namely, to handle multidimensional integrals. Unfortunately, classical integration methods may lead to intractable computations, especially when these integrals have high dimensionality and the integrand is only available under an implicit model that requires computational time, which is often the case when dealing with engineering problems.

A first attempt has been made in this chapter to overcome this difficulty, which aims at using efficient cubature schemes, where a limited number of integrand evaluations are required to obtain accurate estimates, instead of the classical greedy integration methods such as Monte-Carlo simulation and full tensor-product rules. Six cubature formulae are identified in the literature, whose efficiency and accuracy are assessed across several academic and engineering problems ranging from a simple mathematical explicit model to an implicit model that is computationally demanding and involves a large number of uncertain parameters. The analysis performed in the first example reveals that, except for cubature formula IV, for which the relative error grows exponentially but remains by far more efficient than Monte-Carlo simulation and Gauss-Hermite quadrature, the accuracy of the other formulae seems to be less affected by the integration dimension N, especially for formula V which gives the best balance between accuracy and efficiency. With the second example, which deals with uncertainty propagation through explicit mechanical models involving mixture of different types of random variables, it has been proven that the

proposed method is able to carry out accurately, either statistical moments or reliability analysis, without requiring a huge computational effort. But it has been noticed that problems involving higher heterogeneous mixture of random variables should be handled with care. The third example, which involves a time-consuming implicit mechanical model with a moderate probabilistic dimensionality (i.e., 10 scalar uncertain parameters), has revealed that the proposed method is able to tackle the three kinds of uncertainty propagation analysis with a high efficiency. Indeed, all cubature formulae give accurate estimates of the two first statistical moments of the quantities of interest. However, cubature formulae III and VI are the only best candidates for the computation of higher order statistical moments. This high level of accuracy on the estimates of the first four statistical moments makes possible the use of moment-based techniques to build PDFs especially accurate in the vicinity of the distribution tails, which makes possible to conduct reliability analysis without additional computational effort. In the case of sensitivity analysis, it has been shown that the proposed method, regardless of the cubature formula used to handle the integrals quantities, allows to range the uncertain parameters in the right order of importance as the reference method. It appears that cubature formulae VI and V gives the closest estimates to the reference solutions, respectively for the total and the first-order Sobol indices. The fourth example has a high probabilistic dimensionality, since a 53^{rd} order EOLE representation is needed to model accurately the space-depending randomness of the thermal conductivity of the square plate. It has been shown that only cubature formulae II, III, IV and VI can be used to face such a high probabilistic dimensionality and all of them give accurate estimates of the mean and the standard deviation. It appears that cubature formula II gives the best balance between accuracy and efficiency, and formula IV provides the closest estimates of the first four statistical moments to those given by MCS. Afterwards, the reliability indices corresponding to failure probabilities of magnitude up to 10^{-3} and for a given performance function were obtained without additional runs of the FEM and were able to guarantee a relative error below 5%.

The analysis performed in this chapter clearly demonstrates the strong potential of the proposed method to conduct various types of uncertainty propagation analysis with a high level of accuracy. We highlight the remarkable computational cost savings provided by the efficient cubature formulae used to handle the integral quantities required in probabilistic analysis, compared to most of classical integration schemes such as MCS and its variants, the full tensor-product quadrature and the sparse grid method. Despite these enhancements, we stress at the same time the need for further studies to establish the efficiency and the accuracy of the proposed approach to handle uncertainty propagation problems with a much higher level of complexity. Indeed, the number of evaluations of the physical model varies from a few hundred to a few thousand to handle uncertainty propagation problems with moderate and high probabilistic dimensionality respectively. This computational cost would be unaffordable for time-consuming deterministic physical models such as those encountered in fatigue fracture mechanics for instance. Naturally, the question we have to ask ourselves is: is there a way to further improve the efficiency of the proposed method?

We try to answer this question in the next chapter of the thesis.

Chapter III: Unified approaches for uncertainty propagation analysis

1. Introduction

In the previous chapter, an original approach based on efficient cubature formulae has been developed to carry out uncertainty propagation through-time consuming physical models with moderate to high probabilistic dimensionality. We have clearly demonstrated that this approach is by far more efficient than the existing methods based for instance on MCS or tensor-product cubature schemes for dealing with multidimensional integrals relative to the computation of the quantities of interest such as statistical moments, sensitivity indices and probability of failure. Unfortunately, we have also pointed out that in some situations this efficiency could be affected. Indeed, the set of physical model evaluations required to compute these multidimensional integrals depends not only on the integration points related to the cubature formula used, but also on the type of the uncertainty propagation analysis to be addressed. The comparison of equations (II.3), (II.23) and (II.25) (see Section 2 of Chapter II), which represent the multidimensional integrals to be evaluated when dealing with the computation respectively of, l^{th} order statistical moment, partial variance, and probability of failure, clearly shows that the integrand is not the same for these three cases. Obviously, for a given problem these integrands are built on the same physical model, but for each computation case the associated integrand is a function of a different set of random variables representing the uncertain parameters. Therefore, a different set of runs of the physical model is needed. Hence, evaluating the physical model, which is itself time-consuming, each time when moving from one type of uncertainty propagation analysis to another, will probably lead to an unaffordable computation cost. For problems of crack growth in mechanical components or in civil engineering structures under fatigue loading, the related physical models are, in some situations, computational time-demanding. For instance, when dealing with variable amplitude fatigue loading, the quantity of interest, which is the fatigue lifetime, is often computed using an implicit physical model and following a cycle-by-cycle integration scheme, since the amount of loading-induced damage is different in each cycle. This inevitably leads to a huge computational effort for one run of the physical model, especially when High Cycle Fatigue (HCF) region is of interest. It is clear here that if we find a way to substitute the implicit physical model with an explicit formulation, the computational effort required in the uncertainty propagation analysis could be significantly reduced. The key idea is to build an accurate mathematical approximation of the model response based on a limited set of evaluations of the primary implicit model. Such an approximation is referred to as a *response surface*, *surrogate model* or *metamodel*. Many techniques for building metamodels are available in the literature, among them we can find, the Support Vector Regression (SVR) *(Vapnik and al, 1997; Smola and Schölkopf, 2006)*, Kriging based on random processes *(Krige, 1951; Matherson, 1962; Santner and al, 2003; Rasmussen and Williams, 2006; Dubourg, 2011)*, High-Dimensional Model Representation (HDMR) *(Rabitz and Aliş, 1999; Li and al, 2002; Xu and Rahman, 2004;*

Rahman, 2008; Riahi, 2013; Tang and al, 2016; Ding and Xu, 2021) and Polynomial Chaos Expansion (PCE) *(Ghanem and Spanos, 1991; Soize and Ghanem, 2004, Berveiller, 2005; Blatman, 2009)*. The latter technique, denoted by PCE, consists in expanding the response of an implicit physical model over appropriate finite polynomial chaos bases whose components are orthonormal to each other with respect to the joint probability density representing the variability of the uncertain input parameters. Since its appearance in the early 1990's thanks to the work of *(Ghanem and Spanos, 1991)*, PCE has been extensively applied to mechanical and civil engineering problems with uncertain parameters and, at the same time, has been gradually enhanced, mainly to cope dimensionality curse problem encountered when the number of uncertain parameters is high. In the literature two ways of enhancement are distinguished. The first way aims to use efficient techniques *(Blatman and Sudret, 2011; Choi and al, 2012; Riahi, 2013; Ahlfeld, 2016; Camacho and al, 2017; Zhang and Qiu, 2020; Cao and al 2022)*, ranging from integration schemes to regression algorithms, to compute the unknown coefficients of the PCE. The second way aims to use suitable truncation schemes *(Blatman and Sudret, 2009; Blatman and Sudret, 2010; Hu and Youn, 2011; Peng and al, 2013; Hawchar and al, 2017; Abraham and al, 2017)* to discard the unknown coefficients with a weak contribution to the PCE, thus significantly reducing the computational cost.

The present chapter aims to develop a *unified* method of uncertainty propagation, (i.e., able to handle all three types of probabilistic computation analyses efficiently) by combining PCE and the cubature formulae studied in Chapter II. Two alternatives will be investigated: the first one, called *full-PCE,* uses a full polynomial expansion to build a metamodel of the model response where the unknown coefficients are computed by projection based on cubature formulae I-VI; the second alternative, called *sparse-PCE*, uses a suitable truncation algorithm based on second moments prior information, able of adaptively discarding the insignificant coefficients of the PCE in the metamodel construction process, and the remaining significant coefficients are computed by regression.

This chapter is organized into two main sections. In section 2, we first recall the mathematical framework of PCE and the key ingredients for setting up PCE metamodels to represent the responses of implicit physical models. The two alternatives, named full-PCE and sparse-PCE, developed to enhance the efficiency of PCE metamodels, are given a special attention. In section 3, four application examples dealing with fatigue fracture problems with different levels of complexity are addressed to validate the proposed approaches and to demonstrate their ability to deal with various types of uncertainty propagation analysis with an affordable computational cost.

2. Polynomial Chaos Expansion (PCE):

2.1. Construction of PCE-based metamodels

Let us consider a computational model f describing the behavior of an engineering system, whose input parameters $\boldsymbol{x} = \{x_1, \dots, x_N\}^T \in \mathfrak{D}_{\boldsymbol{x}}$ are uncertain quantities represented by an N-dimensional random variable $\boldsymbol{X} = \{X_1, \dots, X_N\}^T \in \mathfrak{D}_{\boldsymbol{X}}$ with a prescribed probability density function $p_{\boldsymbol{X}}(\boldsymbol{x})$, and $y = f(\boldsymbol{x})$ the model response

of interest taken for the sake of simplicity as a scalar. Let also assume that the random variable Y with a probability density function $p_Y(y)$, representing the variability of the model response y induced by the randomness of the input parameters, has a finite variance, and that the components of the N-dimensional random variable $\boldsymbol{X} = \{X_1, \dots, X_N\}^T$ are statistically independent. The PCE-based metamodel of $Y = f(\boldsymbol{X})$ thus reads *(Xiu and Karniadakis, 2002)*:

$$Y = f(\boldsymbol{X}) \approx f^{PCE}(\boldsymbol{X}) = \sum_{k=0}^{P-1} a_k \, \boldsymbol{\Psi}_{\boldsymbol{\alpha}_k}(\boldsymbol{X}) \qquad (III.1)$$

where P denotes the number of terms in the PCE, $\boldsymbol{\alpha}_k = (\alpha_k^1, \dots, \alpha_k^N), k = 0, \dots, P-1$ a set of multi-indices also called *N*-tuples of integers (i.e., $\boldsymbol{\alpha}_k \in \mathbb{N}^N$), $\boldsymbol{\Psi}_{\boldsymbol{\alpha}_k}, k = 0, \dots, P-1$ a set of multivariate orthonormal polynomials with respect to $p_{\boldsymbol{X}}(\boldsymbol{x})$, whose total degree $|\boldsymbol{\alpha}_k| = \alpha_k^1 + \cdots + \alpha_k^N$ and $a_k, k = 0, \dots, P-1$ a set of real valued deterministic coefficients to be determined.

The above expansion is referred to as full-PCE metamodel. It is shown *(Ghanem and Soize, 2004)* that the latter converges to the true model response, in the sense of the $\mathcal{L}^2 - norm$, when the number of terms $P \to +\infty$, that is:

$$\lim_{P \to +\infty} \left\| Y - \sum_{k=0}^{P-1} a_k \, \boldsymbol{\Psi}_{\boldsymbol{\alpha}_k}(\boldsymbol{X}) \right\|_{\mathcal{L}^2}^2 = \lim_{P \to +\infty} \mathbb{E}\left[(Y - \sum_{k=0}^{P-1} a_k \, \boldsymbol{\Psi}_{\boldsymbol{\alpha}_k}(\boldsymbol{X}))^2 \right] = 0 \qquad (III.2)$$

where $\mathbb{E}[.]$ denotes the mathematical expectation.

The size of the PCE-based metamodel given by equation (III.1), that is the number of terms P retained in the summation, can be determined by following one of the truncation schemes available in the PCE literature *(Blatman, 2009)*. The most used truncation scheme consists in retaining the terms corresponding to multivariate polynomials $\boldsymbol{\Psi}_{\boldsymbol{\alpha}_k}, k = 0, \dots, P-1$ where whose total degrees $|\boldsymbol{\alpha}_k| = \alpha_k^1 + \cdots + \alpha_k^N, k = 0, \dots, P-1$ do not exceed a prescribed degree p, chosen to ensure a better accuracy of the metamodel. Based on this rule, the number of terms P in the truncated PCE is given by:

$$P = \frac{(p+N)!}{p!\,N!} \qquad (III.3)$$

Equation (III.3) clearly shows that the number of terms in the PCE grows exponentially with N, which could induce an unaffordable computational cost in the determination of the unknown coefficients when dealing with uncertainty propagation problems with a high probabilistic dimensionality and especially when the corresponding physical model is itself computationally time-demanding.

Once the truncation degree p has been chosen, the procedure used for setting up the PCE-based metamodel requires first, an algorithm *(Sudret and Der Kiureghian, 2000)* allowing to generate the set of multi-indices $\boldsymbol{\alpha}_k, k = 0, \dots, P-1$ corresponding to P multivariate polynomials $\boldsymbol{\Psi}_{\boldsymbol{\alpha}_k}, k = 0, \dots, P-1$ of respective degrees not greater than p, and, second, sets of univariate orthonormal polynomials $\Psi_{\alpha_k^i}, i = 1, \dots, N$ are chosen with respect to each marginal distribution $p_{X_i}(x_i),\ i = 1, \dots, N$ of the random variables $X_i,\ i = 1, \dots, N$, to construct

the polynomial chaos basis $\{\boldsymbol{\Psi}_{\boldsymbol{\alpha}_k}\}_{k=0}^{k=P-1}$. When the components of the N-dimensional random variable $\boldsymbol{X} = \{X_1, \dots, X_N\}^T$ are independent, the joint probability density function $p_{\boldsymbol{X}}(\boldsymbol{x})$ can be simply obtained as the product of the marginal distributions $p_{X_i}(x_i),\ i = 1, \dots, N$ of the random variables $X_i,\ i = 1, \dots, N$, that is $p_{\boldsymbol{X}}(\boldsymbol{x}) = \sum_{i=1}^{N} p_{X_i}(x_i)$. Consequently, each multivariate polynomial $\boldsymbol{\Psi}_{\boldsymbol{\alpha}_k}(\boldsymbol{X}), k = 0, \dots, P-1$ of the polynomial chaos basis can be derived as follows by a tensorization of appropriate univariate polynomials $\Psi_{\alpha_k^i}(X_i), i = 1, \dots, N$, with respective degrees $\alpha_k^i, i = 1, \dots, N$:

$$\boldsymbol{\Psi}_{\boldsymbol{\alpha}_k}(\boldsymbol{X}) = \prod_{i=1}^{N} \Psi_{\alpha_k^i}(X_i) \qquad (III.4)$$

In the above equation, the set of univariate polynomials $\Psi_{\alpha_k^i}, i = 1, \dots, N$ are orthonormal with respect to the marginal distributions $p_{X_i}(x_i),\ i = 1, \dots, N$. This orthonormality condition reads:

$$\langle \Psi_{\alpha_k^i}(X), \Psi_{\alpha_l^i}(X) \rangle_{\mathcal{L}^2} = \mathbb{E}\left[\Psi_{\alpha_k^i}(X).\Psi_{\alpha_l^i}(X)\right] = \delta_{k,l} \qquad \forall \alpha_k^i, \alpha_l^i \in \mathbb{N} \qquad (III.5)$$

where $\delta_{k,l}$ denotes the Kronecker symbol equal to 1 when $k = l$ and 0 otherwise.

In the original version of the PCE proposed by *(Weiner, 1983),* the polynomial chaos basis is made of Hermite polynomials to represent the random processes from a set of normal variables. The resulting metamodel, called Weiner-Hermite PCE, can be used to represent model responses that depend only on normal distributions. Fortunately, an extended release, referred to as generalized PCE, has been developed by *(Xiu and Karniadakis, 2002)* to deal with non-normal random variables based on the Askey family of hypergeometric polynomials. In table III.1 are listed the polynomial families associated to the most popular continuous and discrete distributions.

Table III. 1. Correspondence between distributions of random variables and orthogonal polynomials

Type	Distribution	Support	Polynomial
Continuous	Normal	$\mathbb{R}$	Hermite
	Uniform	$[-1,1]$	Legendre
	Gamma	$\mathbb{R}^+$	Laguerre
	Chebyshev	$[-1,1]$	Chebyshev
	Beta	$[-1,1]$	Jacobi
Discrete	Poisson	$\{0,1,2,\dots\}$	Charlier
	Binomial	$\{0,1,2,\dots,M\}$	Krawtchouk

In engineering problems, the components of the N-dimensional random variable $\boldsymbol{X} = \{X_1, \dots, X_N\}^T$ may have different distributions not belonging to the families given in table III.1, which can also be correlated with each other. This general case can be easily addressed by using isoprobabilistic transformations $\boldsymbol{X} = T(\boldsymbol{U})$ (see section 2.1 of Chapter II for more details). Then, the PCE-based metamodel represented by equation (III.1) can be naturally rewritten in the standard random space as follows:

$$Y = f(\boldsymbol{X}) = f \circ T(\boldsymbol{U}) = h(\boldsymbol{U}) \approx h^{PCE}(\boldsymbol{U}) = \sum_{k=0}^{P-1} a_k \boldsymbol{H}_{\boldsymbol{\alpha}_k}(\boldsymbol{U}) \qquad (III.6)$$

where $\boldsymbol{U} = \{U_1, \dots, U_N\}^T$ is an N-dimensional normal variable with independent components $U_i, i \in \{1, \dots, N\}$ following a standard normal distribution $\varphi_{U_i}(u_i), i \in \{1, \dots, N\}$ with zero mean and unit standard deviation,

and $\boldsymbol{H}_{\boldsymbol{\alpha}_k}(\boldsymbol{U}), k = 0, \dots, P-1$ are multivariate Hermite polynomials which can be built by a tensorization of a set of univariate Hermite polynomials $H_{\alpha_k^i}(U_i), i = 1, \dots, N$, with respective degrees $\alpha_k^i, i = 1, \dots, N$. For the sake of illustration, the seven first univariate (N=1) Hermite polynomials are plotted in figure III.1.

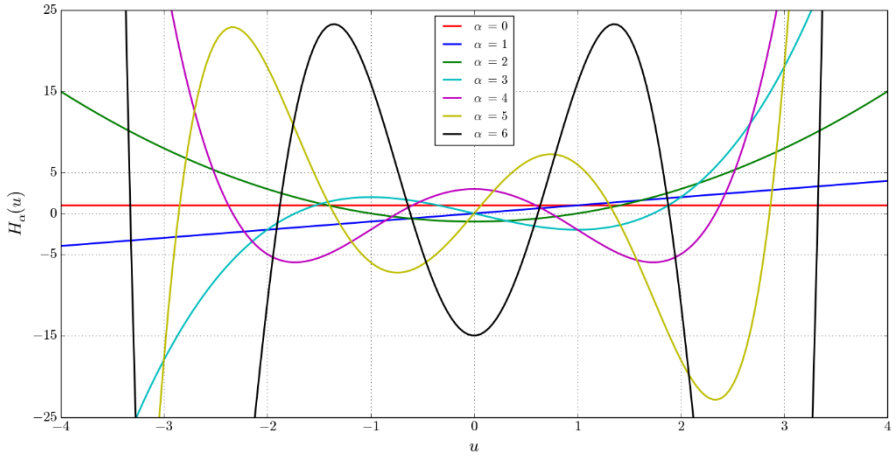

Figure III. 1. Univariate Hermite polynomials $H_\alpha(u), \alpha = 0, \dots, 6$

In the following, the mathematical formulation of the quantities of interest will be set up in the standard random space. Thus, the polynomial chaos basis used to construct the PCE-based metamodels will comprise multivariate Hermite polynomials obtained by tensor products of univariate orthonormal Hermite polynomials.

2.2. Computation of the PCE coefficients

Once the truncated polynomial chaos basis has been built up, the unknown coefficients $a_k, k = 0, \dots, P-1$ have to be determined to completely construct the PCE-based metamodel of interest. In the literature, two families of approaches can be distinguished to solve this issue. Intrusive approaches, introduced since the appearance of the PCE at the early of 1990's *(Ghanem and Spanos, 1991)*, aim at computing the PCE coefficients by minimizing the following residual under the constraint that it is orthogonal to the selected polynomial chaos basis:

$$\langle \sum_{k=0}^{P-1} a_k \, \boldsymbol{H}_{\boldsymbol{\alpha}_k}(\boldsymbol{U}), \boldsymbol{H}_{\boldsymbol{\alpha}_l} \rangle = 0, \forall \, l = 0, \dots, P-1 \qquad (III.7)$$

The solution of the above minimization problem is obtained by a Galerkin projection scheme, which requires adaptations of the governing equations related to the considered mechanical model, which explains why these approaches are called intrusive. Unfortunately, when these governing equations involve nonlinearities, performing these adaptations could be a challenging task. If in addition, the probabilistic dimension is high, the Galerkin projection scheme often leads to a large system of coupled equations which require a considerable computational cost. To face this problem of inefficiency of intrusive approaches, some alternatives methods have been developed in the few last decades, called non-intrusive approaches. In these approaches, the mechanical model is considered as a black box and the coefficients of the PCE are simply computed by a finite set of evaluations of the mechanical model on an appropriate finite set of

realizations of the uncertain parameters in the random space, without any need for adaptation of the governing equations related to the mechanical model. Non-intrusive approaches are themselves composed of two categories, namely projection and regression methods which will be detailed in the next subsections.

2.2.1. Projection methods

a) Principle

Since the PCE-metamodel is built in an N-dimensional standard random space, thus the polynomial chaos basis consists of N-variate Hermite polynomials. The orthonormality condition between the components of the polynomial chaos basis reads:

$$\langle \boldsymbol{H}_{\boldsymbol{\alpha}_k}(\boldsymbol{U}), \boldsymbol{H}_{\boldsymbol{\alpha}_l} \rangle_{\mathcal{L}^2} = \mathbb{E}\left[\boldsymbol{H}_{\boldsymbol{\alpha}_k}(\boldsymbol{U}).\boldsymbol{H}_{\boldsymbol{\alpha}_l}(\boldsymbol{U})\right] = \delta_{\boldsymbol{\alpha}_k,\boldsymbol{\alpha}_l} \qquad \forall \boldsymbol{\alpha}_k, \boldsymbol{\alpha}_l \in \mathbb{N}^N \tag{III.8}$$

where $\delta_{\boldsymbol{\alpha}_k,\boldsymbol{\alpha}_l}$ denotes the Kronecker symbol equal to 1 when $\boldsymbol{\alpha}_k = \boldsymbol{\alpha}_l$ and 0 otherwise.

The projection methods take advantage of the orthonormality of the truncated polynomial chaos basis $\boldsymbol{H}_{\boldsymbol{\alpha}_k}(\boldsymbol{U}), k = 0, \dots, P-1$, to compute the unknown coefficients $a_k, k = 0, \dots, P-1$. Indeed, referring to the orthonormality condition above, the projection of the PCE-based metamodel $h^{PCE}(\boldsymbol{U})$ given by equation (III.6) onto the polynomial chaos basis $\boldsymbol{H}_{\boldsymbol{\alpha}_k}(\boldsymbol{U}), k = 0, \dots, P-1$, allows us to compute the unknown coefficients $a_k, k = 0, \dots, P-1$ using the following expression:

$$\langle \boldsymbol{H}_{\boldsymbol{\alpha}_l}(\boldsymbol{U}), h^{PCE}(\boldsymbol{U}) \rangle_{\mathcal{L}^2} = \mathbb{E}\left[\boldsymbol{H}_{\boldsymbol{\alpha}_l}(\boldsymbol{U}).\sum_{k=0}^{P-1} a_k\, \boldsymbol{H}_{\boldsymbol{\alpha}_k}(\boldsymbol{U})\right] = \sum_{k=0}^{P-1} a_k\, \overbrace{\mathbb{E}\left[\boldsymbol{H}_{\boldsymbol{\alpha}_l}(\boldsymbol{U}).\boldsymbol{H}_{\boldsymbol{\alpha}_k}(\boldsymbol{U})\right]}^{=\delta_{\boldsymbol{\alpha}_k,\boldsymbol{\alpha}_l}\,(since\ III.8)} = a_l \tag{III.9}$$

It is clear from equation (III.9) that the coefficient $\boldsymbol{\alpha}_l$ associated to the N-variate Hermite polynomial $\boldsymbol{H}_{\boldsymbol{\alpha}_l}(\boldsymbol{U})$, is equal to the expected value of the weighted polynomial expansion $\boldsymbol{H}_{\boldsymbol{\alpha}_l}(\boldsymbol{U}).h^{PCE}(\boldsymbol{U})$ of the approximation $h^{PCE}(\boldsymbol{U})$ of the random model response Y. Mathematically speaking, the expected value of a continuous random N-variate function is defined as an N-dimensional integral, so equation (III.9) can be reformulated as follows:

$$a_l = \mathbb{E}\left[\boldsymbol{H}_{\boldsymbol{\alpha}_l}(\boldsymbol{U}).h^{PCE}(\boldsymbol{U})\right] = \int_{\mathbb{R}^N} \boldsymbol{H}_{\boldsymbol{\alpha}_l}(\boldsymbol{u}).h^{PCE}(\boldsymbol{u})\, \varphi_{\boldsymbol{U}}(\boldsymbol{u})\, d\boldsymbol{u} \tag{III.10}$$

Thanks to the above equation, where $\varphi_U(\boldsymbol{u})$ denotes the PDF of the N-dimensional normal variable $\boldsymbol{U}$, the computation of the PCE coefficients is nothing else than the evaluation of a set of N-dimensional integrals, which can be ensured by means of numerical integration schemes, such as those studied in Chapter II, whose key ingredient consists in approximating an integral by a weighted sum. For more details on the mathematical framework related to these integration schemes, the reader can refer to Chapter II of the thesis manuscript.

b) Monte-Carlo Simulation and variants

The simplest way to compute the N-dimensional integral defined by equation (III.10) is the use of simulation methods such as MCS and its variants. The basic idea is to generate a set of N-dimensional

integration points $\boldsymbol{u}^j = \left(u_1^j, \dots, u_N^j\right), j = 1, \dots, M$, following a random sampling scheme, namely pseudo-random number generator with respect to the distributions of the uncertain parameters. Since the mathematical formulations of the quantities of interest (i.e., here the quantity of interest is the N-dimensional integral representing the coefficients of the PCE) are derived in the standard random space, the integration points are sampled with respect to an N-dimensional normal distribution $\varphi_{\boldsymbol{U}}(\boldsymbol{u})$. Furthermore, since all points belonging the random space have the same probability to be sampled, $w^j = 1/M\,, j = 1, \dots, M$, thus the coefficient a_l related to the N-variate Hermite polynomial $\boldsymbol{H}_{\boldsymbol{\alpha}_l}(\boldsymbol{U})$ can be estimated by the following weighted sum:

$$a_l = \int_{\mathbb{R}^N} \boldsymbol{H}_{\boldsymbol{\alpha}_l}(\boldsymbol{u}).\, h^{PCE}(\boldsymbol{u})\; \varphi_{\boldsymbol{U}}(\boldsymbol{u})\; d\boldsymbol{u} \;\approx \sum_{j=1}^{M} w^j\; \boldsymbol{H}_{\boldsymbol{\alpha}_l}(\boldsymbol{u}^j).\, f \circ T(\boldsymbol{u}^j) = \frac{1}{M}\sum_{j=1}^{M} \boldsymbol{H}_{\boldsymbol{\alpha}_l}(\boldsymbol{u}^j).\, f \circ T(\boldsymbol{u}^j) \qquad (III.11)$$

where $w^j, j = 1, \dots, M$ are the respective weights of the integration points $\boldsymbol{u}^j, j = 1, \dots, M$, T is the isoprobabilistic transformation allowing to transform the integration points, firstly sampled in the standard random space, into a set of points $\boldsymbol{x}^j = T(\boldsymbol{u}^j), j = 1, \dots, M$ belonging to the original physical random space, and f is the mathematical mapping representing the mechanical model. MCS are robust and converge for any $\mathcal{L}^2$-function.

The associated error ϵ_{MCS} used to assess the accuracy of the estimates provided by MCS, reads:

$$\epsilon_{MCS} = \sqrt{\frac{\mathbb{V}\left[\boldsymbol{H}_{\boldsymbol{\alpha}_l}(\boldsymbol{u}).\, f \circ T(\boldsymbol{u})\right]}{M}} \qquad (III.12)$$

where $\mathbb{V}[.]$ denotes the variance operator. Although the convergence of MCS is less affected by the dimensionality and the mathematical rank (i.e., in statistical moments analysis for instance, the mean and the central variance are respectively represented by 1st and 2nd order ranked integrals) of the integral to be estimated, it is clear from equation (III.12) that the error ϵ_{MCS} decreases with $1/\sqrt{M}$, which reveals the major drawback of MCS, that is its slow convergence that makes impossible its application when the evaluation of the integrand is computational time-demanding.

To enhance the convergence of MCS advanced sampling schemes such as Latin hypercube sampling *(Mckay and al, 1979)* and quasi-random numbers *(Niederreiter, 1992)* can be used, which provide integration points with a better filling of the random space than pseudo-random number generators. Unfortunately, this enhancement is not yet sufficient to allow the use of MCS to handle over greedy mechanical models, such as those dealing with fatigue fracture problems.

c) Full tensor-product cubature

An alternative to MCS for the computation of the PCE coefficients is the use of full tensor-product integration schemes. Accordingly, the coefficient a_l can be estimated by the following M^{th} order isotropic Gauss-Hermite full tensor-product integration formula, since we work in the standard random space:

$$a_l = \int_{\mathbb{R}^N} \boldsymbol{H}_{\boldsymbol{\alpha}_l}(\boldsymbol{u}).\, h^{PCE}(\boldsymbol{u})\, \varphi_{\boldsymbol{U}}(\boldsymbol{u})\, d\boldsymbol{u} \approx \sum_{j_1=1}^{M} \dots \sum_{j_N=1}^{M} w_1^{j_1} \dots w_N^{j_N}\, \boldsymbol{H}_{\boldsymbol{\alpha}_l}\left(u_1^{j_1} \dots u_N^{j_N}\right).\, f \circ T(u_1^{j_1} \dots u_N^{j_N}) \qquad (III.13)$$

where $u_i^{j_i}, j_i = 1, \dots, M$ are the selected integration points in the i^{th} direction of the standard random space, defined as the roots of an univariate Hermite polynomial $H_M(u)$ of degree M, and $w_i^{j_i}, j_i = 1, \dots, M$ are the corresponding weights.

When a PCE-based metamodel h^{PCE} of degree p is used to approximate the random model response of interest, the integrand $\boldsymbol{H}_{\boldsymbol{\alpha}_l}(\boldsymbol{u}).\, h^{PCE}(\boldsymbol{u})$ in equation (III.10) is consequently a polynomial of degree $p + |\boldsymbol{\alpha}_l| \leq 2p$ (with $|\boldsymbol{\alpha}_l| = \alpha_l^1 + \cdots + \alpha_l^N$). It follows that an N-dimensional isotropic Gauss-Hermite formula of degree $M = p + 1$ will be able to provide the exact value of the coefficient a_l, which requires $(p+1)^N$ evaluations of the integrand. Thus, we can immediately see the main limit of full tensor-product integration schemes to handle high dimensional integrals especially when the integrand itself is obtained by a heavy numerical procedure.

d) Sparse grids cubature

To reduce the computational effort required by full tensor-product integration schemes, Smolyak method *(Smolyak, 1963)* based on sparse integration grids is an interesting alternative. The basic idea is also to perform a tensor product to build the integration formula but having the particularity that this tensor product is defined as a linear combination of one-dimensional cubature formulae having high degrees in some directions and much lower degrees in the remaining dimensions.

Let us consider one-dimensional cubature formulae of degree $l \geq 1$, each one based on M_l integration points and weights able to compute the exact value of the integral of a one-dimensional polynomial of degree equal or less than $2M_l - 1$. Now by performing linear combination of products of the latter one-dimensional cubature formulae, the estimate of the coefficient a_l according to the Smolyak integration scheme of degree $l \leq N$, reads:

$$a_l \approx \sum_{|\boldsymbol{k}|=l}^{l+N-1} (-1)^{l+N-1-|\boldsymbol{k}|}\, C_{N-1}^{|\boldsymbol{k}|-l} \sum_{j_1=1}^{k_1} \dots \sum_{j_N=1}^{k_N} w_1^{j_1} \dots w_N^{j_N}\, \boldsymbol{H}_{\boldsymbol{\alpha}_l}\left(u_1^{j_1} \dots u_N^{j_N}\right).\, f \circ T(u_1^{j_1} \dots u_N^{j_N}) \qquad (III.14)$$

where $|\boldsymbol{k}| = k_1 + \cdots + k_N$ is the sum of the components of the multi-index $\boldsymbol{k} = (k_1, \dots, k_N) \in \mathbb{N}^N$, $k_j, j = 1, \dots, N$, is the degree of the one-dimensional cubature formula used in the j^{th} direction of the standard random space and C denotes the combination operator.

With a Smolyak cubature formula of degree $l + p$, we can estimate the exact value of the integral of a polynomial of degree $2p + 1$ *(Novak and Ritter, 1999)*. Thus, the same formula allows us to obtain the exact value of the coefficient a_l since the degree of the polynomial integrand $\boldsymbol{H}_{\boldsymbol{\alpha}_l}(\boldsymbol{u}).\, h^{PCE}(\boldsymbol{u})$ in equation (III.10) does not exceeds $2p$. The corresponding computational cost tends asymptotically to $(2^p/p!)N^p$ integrand evaluations for integrals of high dimensionality, clearly demonstrating the efficiency of the Smolyak

integration scheme over full tensor-product integration schemes. Indeed, the computational cost increases polynomially with the dimension of the integral, which is far less than the exponential increase $(p+1)^N$ of full tensor-product integration schemes. Despite the efficiency of sparse grid-based integration schemes for high dimensions, the number of integrand evaluations remains too large to be applied to computationally demanding mechanical models, especially when a high level of accuracy is required for the construction of the PCE-based metamodels, i.e., for a high truncation degree p.

e) Efficient cubature formulae

Instead of using integration schemes constructed from either a full tensorization or a linear combination of unidimensional cubature formulae, a serious alternative to deal with the curse of dimensionality problem is the use of the efficient cubature formulae studied in Chapter II. One can remind that these fifth-degree cubature formulae can compute efficiency the expected value of a random quantity. This has been well established through the first application example dealing with the integration of an explicit purely N-dimensional mathematical function studied in section 5.1.1 of Chapter II. Since the PCE coefficients are defined as expected values of polynomial functions, as can be seen in equation (III.10), their computation can be efficiently conducted by one of the cubature formulae I-VI. Accordingly, the estimation of the coefficient a_l reads:

$$a_l = \int_{\mathbb{R}^N} \boldsymbol{H}_{\boldsymbol{\alpha}_l}(\boldsymbol{u}).\, h^{PCE}(\boldsymbol{u})\; \varphi_{\boldsymbol{U}}(\boldsymbol{u})\; d\boldsymbol{u} \;\approx \sum_{j=1}^{M_K} w_K^j\, \boldsymbol{H}_{\boldsymbol{\alpha}_l}\left(\boldsymbol{u}_K^j\right).\, f \circ T\left(\boldsymbol{u}_K^j\right) \qquad (III.15)$$

where the capital index $K = I, II, \dots, VI$, denotes the type of the cubature formula to be used and M_K is the number of integration points related to cubature formula K.

It is clear from the above expression that the estimate provided by cubature formulae I-VI is similar to that given by MCS since only one summand is required, but a much smaller number of integration points are needed to ensure a good level of accuracy. Indeed, instead of using pseudo-random number generators as in the case of MCS, the integration points are selected in a smart way to guarantee a better filling of the random space. Since the cubature formulae are all fifth-degree integration schemes as recalled previously, they can estimate efficiently the expected value of a PCE-based metamodel with moderate polynomial degree, more than sufficient to provide an accurate approximation of the random model response of interest.

Figure III.2 compares the number of integrand evaluations required by full tensor-product integration schemes for various truncation degree p and that required by cubature formulae I-IV as a function of the dimension N of the integral to be computed. As can be seen, using the cubature formulae I-VI to compute the PCE coefficients provides significant computational cost savings. In addition, the number of integrand evaluations and, consequently, the corresponding number of mechanical model evaluations, does not depend on the truncation degree p of the PCE as for the full tensor-product and Smolyak integration schemes. This first attempt based on PCE-based metamodels and efficient cubature formulae I-V,

developed to tackle, on one hand, the problem of the curse of dimensionality and on the other hand the problem of the additional computation cost observed in Chapter II when switching from one type of uncertainty propagation analysis to another and when using in a *crude* (i.e., directly on the primary mechanical model) manner the cubature formulae I-V to compute the quantities of interest, will be called in the following, *full-PCE* approach. This is also a first response to the question which closed the previous chapter of the thesis. Note that, the denotation *full* is used since *all* the PCE coefficients are retained to build the metamodel of the model response of interest. The flowchart displayed in figure III.3 summarizes the steps of the full-PCE approach.

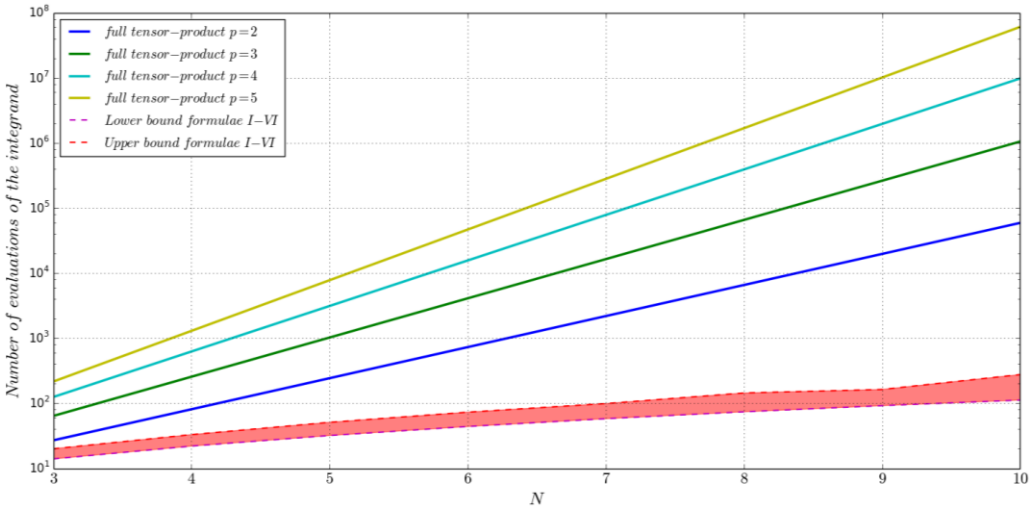

Figure III. 2. Computational cost of full tensor-product integration schemes and cubature and formulae I-IV with respect to the dimension N

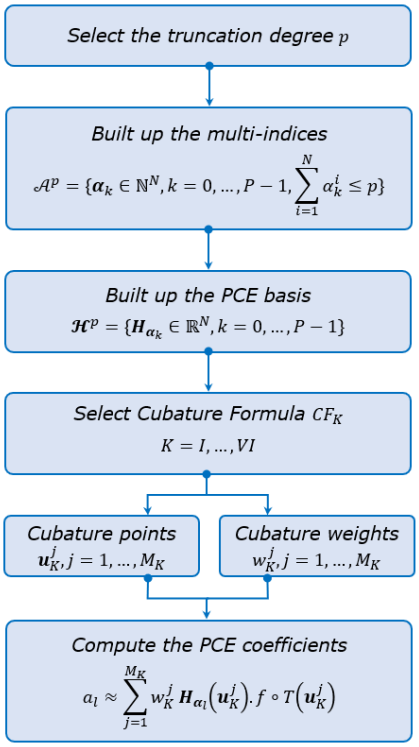

Figure III. 3. Computational flowchart of the full-PCE approach

2.2.2. Regression methods

a) Principle

Regression methods have been used first by *(Isukapalli, 1999)* and later by *(Berveiller, 2005)*, to compute the unknown coefficients of the PCE. Unlike projection methods, where the PCE coefficients are computed one by one by evaluating multidimensional integrals, regression methods estimate all the coefficients at the same time by solving a minimization problem in the least-squares sense, which could considerably reduce the computation effort. Indeed, the number of evaluations of the primary mechanical model varies in the range $[2P, 3P]$, which is much lower, for instance, than that associated with the Smolyak integration scheme, asymptotically equal to $2^p P$, where P denotes the number of coefficients to be computed for a given truncation degree p.

Let $\boldsymbol{a} = \{a_{\alpha_0}, a_{\alpha_1}, \dots, a_{\alpha_{P-1}}\}^T$ and $\boldsymbol{\mathcal{H}}(\boldsymbol{U}) = \{\boldsymbol{H}_{\alpha_0}(\boldsymbol{U}), \boldsymbol{H}_{\alpha_1}(\boldsymbol{U}), \dots, \boldsymbol{H}_{\alpha_{P-1}}(\boldsymbol{U})\}^T$ two vectors denoting respectively the unknown coefficients of the PCE and the polynomial chaos basis made of multivariate Hermite polynomials. The regression technique consists in finding the vector of coefficients $\boldsymbol{a}$ that minimizes the mean square error $\mathbb{E}[(\boldsymbol{a}^T\, \boldsymbol{\mathcal{H}}(\boldsymbol{U}) - f \circ T(\boldsymbol{U}))^2]$, that is:

$$\hat{\boldsymbol{a}} = \underset{\boldsymbol{a}\in\mathbb{R}^{\boldsymbol{P}}}{\operatorname{argmin}}\{A(\boldsymbol{a}) \equiv \mathbb{E}[(\boldsymbol{a}^T\, \boldsymbol{\mathcal{H}}(\boldsymbol{U}) - f \circ T(\boldsymbol{U}))^2]\} \qquad (III.16)$$

The optimality condition $\frac{dA}{da}(\hat{\boldsymbol{a}}) = 0$ related to the above optimization problem allows us to write the following equality:

$$\mathbb{E}[\boldsymbol{\mathcal{H}}(\boldsymbol{U})\boldsymbol{\mathcal{H}}(\boldsymbol{U})^T]\hat{\boldsymbol{a}} = \mathbb{E}[\boldsymbol{\mathcal{H}}(\boldsymbol{U}) f \circ T(\boldsymbol{U})] \qquad (III.17)$$

The quantity $\boldsymbol{\mathcal{H}}(\boldsymbol{U})\boldsymbol{\mathcal{H}}(\boldsymbol{U})^T$ represents the covariance matrix of the P-dimensional random vector $\boldsymbol{\mathcal{H}}(\boldsymbol{U})$, with P statistically independent components since the PCE-based metamodel is built in the standard random space whose directions are represented by independent standard normal variables.

Consequently, the mathematical expectation of the $\mathbb{E}[\boldsymbol{\mathcal{H}}(\boldsymbol{u})\boldsymbol{\mathcal{H}}(\boldsymbol{u})^T]$ of the covariance matrix $\boldsymbol{\mathcal{H}}(\boldsymbol{U})\boldsymbol{\mathcal{H}}(\boldsymbol{U})^T$ is reduced to the $P \times P$ unit matrix $\mathbb{I}_{P\times P}$, and equation (III.17) can be rewritten as follows:

$$\hat{\boldsymbol{a}} = \mathbb{E}[\boldsymbol{\mathcal{H}}(\boldsymbol{U}) f \circ T(\boldsymbol{U})] \qquad (III.18)$$

In practice, the minimization problem defined by equation (III.16) is discretized on the basis of a set of sample points $\boldsymbol{\mathcal{U}} = \{\boldsymbol{u}^j = (u_1^j, \dots, u_N^j), j = 1, \dots, M\}$, also called experimental design, to replace the expectation operator $\mathbb{E}[.]$ by its empirical estimate. Thus, the minimization problem reads:

$$\hat{\boldsymbol{a}} = \underset{\boldsymbol{a}\in\mathbb{R}^{\boldsymbol{P}}}{\operatorname{argmin}} \left\{ \frac{1}{M} \sum_{j=1}^{M} (h^{PCE}(\boldsymbol{u}^j) - f \circ T(\boldsymbol{u}^j))^2 \right\} = \underset{\boldsymbol{a}\in\mathbb{R}^{\boldsymbol{P}}}{\operatorname{argmin}} \left\{ \frac{1}{M} \sum_{j=1}^{M} \left(\sum_{k=0}^{P-1} a_k\, \boldsymbol{H}_{\boldsymbol{\alpha_k}}(\boldsymbol{u}^j) - f \circ T(\boldsymbol{u}^j) \right)^2 \right\} \qquad (III.19)$$

where $h^{PCE}(\boldsymbol{u}^j)$ and $f \circ T(\boldsymbol{u}^j)$ are respectively the responses of the PCE-based metamodel and the primary mechanical model at the point $\boldsymbol{u}^j$.

Now, by performing some algebra, the least-square estimates of the PCE coefficients $\hat{\boldsymbol{a}}$ are obtained as follows:

$$\hat{\boldsymbol{a}} = (\boldsymbol{\mathcal{H}}^T\boldsymbol{\mathcal{H}})^{-1}\boldsymbol{\mathcal{H}}^T\boldsymbol{\mathcal{Y}} \qquad (III.20)$$

where $\boldsymbol{\mathcal{Y}} = \{y^j = f \circ T(\boldsymbol{u}^j), j = 1, \dots, M\}$ is a sample set of points representing the respective responses of the mechanical model at the points $\boldsymbol{\mathcal{U}} = \{\boldsymbol{u}^j = \left(u_1^j, \dots, u_N^j\right), j = 1, \dots, M\}$ of the experimental design and $\boldsymbol{\mathcal{H}}$ is an $M \times P$ matrix called information matrix where its $(j,k)^{th}$ entry $\mathcal{H}_{jk}, j = 1, \dots, M, k = 1, \dots, P$ is defined as the response of the k^{th} N-variate Hermite polynomial $\boldsymbol{H}_{\boldsymbol{\alpha}_k}$ of total degree $\boldsymbol{\alpha}_k$ at the sampling point $\boldsymbol{u}^j$.

The choice of a suitable experimental design $\boldsymbol{\mathcal{U}} = \{\boldsymbol{u}^j = \left(u_1^j, \dots, u_N^j\right), j = 1, \dots, M\}$ is of great importance, especially its size M, to obtain a well-conditioned regression problem and consequently accurate estimates of the PCE coefficients. Indeed, if M is just slightly greater than the number P of unknown coefficients to be computed, this may lead to an ill-conditioned information matrix $\boldsymbol{\mathcal{H}}$ and consequently to an intractable regression problem. On the other hand, that is, if M is very high, this may induce an unaffordable computational cost in case the mechanical model itself is computational time-demanding, since the corresponding number of evaluations of the mechanical model will be high. In the literature, the value of M is commonly chosen in the range $[2P, 3P]$ to ensure a better balance between the computational cost and the accuracy of the estimates. The simplest way to build the experimental design is to use sample points obtained from pseudo-random number generators such as in the case of MCS. In such a case, *(Owen, 1998)* has shown that the variance $\mathbb{V}[\hat{\boldsymbol{a}}]$ of the estimates of the PCE coefficients tends asymptotically to $\frac{1}{M}\mathbb{E}[\boldsymbol{H}(\boldsymbol{U})^2(h^{PCE}(\boldsymbol{U}) - f \circ T(\boldsymbol{U}))^2]$ when M is very high. The efficiency of solving the regression problem can be enhanced by using experimental designs built from advanced sampling techniques such as Latin hypercube or quasi-random numbers, which ensure a better filling of the domain of variation of the uncertain parameters. For a given level of accuracy, it has been shown *(Riahi and al., 2012)* that MCS based on Halton quasi-random numbers converges faster than those based on Latin hypercube samples or pseudo-random numbers.

Another way to the reduce the computational effort required to estimate the PCE coefficients using regression methods is to build experimental designs from a set of unevenly weighted point samples as suggested by *(Isukapalli, 1999)* instead of a sample set of equally weighted point samples like those obtained by classical sampling techniques. Based on this idea, experimental designs built from suitable combinations of Gauss-Hermite integration points have been introduced by (*Berveiller, 2005)*. The key ingredients to build such an experimental design consist of first generating a sample set of N-tuples representing all possible combinations of $p + 1$ one-dimensional Gauss-Hermite integration points, and then the experimental design is built from the first $2P + 1$ combinations after sorting them in ascending order based on the distance of each point from the origin. Note that sparse grids related to Smolyak integration scheme and integration points of cubature formulae I-VI can also be used to build experimental designs. The latter alternative will be investigated in the following to improve the efficiency of regression methods for the estimation of the PCE coefficients. The key idea is to find a smart truncation scheme able to reduce

the number of unknown PCE coefficients to be computed by discarding those that have insignificant contribution on the quantities of interest, and, of course, without any loss on the accuracy of the obtained PCE-based metamodels. Thus, the computational effort can be significantly reduced since only a small experimental design is required to solve the regression problem.

b) Truncation scheme based on low-order interactions

With reference to the previous developments, the PCE-based metamodel is built using a complete polynomial chaos basis, that is the terms corresponding to all multivariate polynomials whose respective total degrees do not exceed a given degree p are retained. For problems with high dimensionality N, a major part of the PCE coefficients represents interactions between uncertain parameters, even for moderate truncation degree p. Fortunately, for engineering problems experience has shown that high order interactions have often insignificant effect, which means that the corresponding PCE coefficients are close to 0. Thus, the size of the polynomial chaos basis can be reduced by retaining only the terms representing main and low-order interactions effects.

Let $\boldsymbol{\mathcal{H}}^{p} = \left\{\boldsymbol{H}_{\boldsymbol{\alpha}_k}, \boldsymbol{\alpha}_k \in \mathbb{N}^N \; such \; that \sum_{i=1}^{N} \alpha_k^i \leq p\right\}$ a complete polynomial chaos basis for a given truncation degree p, and $\boldsymbol{\mathcal{H}}^{p,q} = \left\{\boldsymbol{H}_{\boldsymbol{\alpha}_k}, \boldsymbol{\alpha}_k \in \mathbb{N}^N \; such \; that \; \sum_{i=1}^{N} \alpha_k^i \leq p \; and \; \sum_{i=1}^{N} \mathbb{1}_{\{\alpha_k^i \neq 0\}} \leq q\right\}$ an incomplete, called also sparse, polynomial chaos basis for a given truncation degree p and interaction order $q < p$, i.e., only q-variate polynomials whose respective total degrees do not exceed a given degree p are retained. If the allowed maximum interaction order q is not high, the cardinality of the sparse polynomial chaos basis $\boldsymbol{\mathcal{H}}^{p,q}$ will be much lower than that of the complete polynomial chaos basis $\boldsymbol{\mathcal{H}}^{p}$.

The efficiency of the truncation scheme based on sparse polynomial basis can be assessed by the *economy* $\mathcal{E}^{p,q}$ defined by the following ratio:

$$\mathcal{E}^{p,q} = \frac{\mathrm{card}(\boldsymbol{\mathcal{H}}^{p}) - \mathrm{card}(\boldsymbol{\mathcal{H}}^{p,q})}{\mathrm{card}(\boldsymbol{\mathcal{H}}^{p})} \times 100 \qquad (III.21)$$

where $\mathrm{card}(\boldsymbol{\mathcal{H}}^{p})$ and $\mathrm{card}(\boldsymbol{\mathcal{H}}^{p,q})$ are the cardinalities of the complete $\boldsymbol{\mathcal{H}}^{p}$ and sparse $\boldsymbol{\mathcal{H}}^{p,q}$ polynomial chaos bases respectively.

As can be seen in figure III.4, for a PCE-based metamodel of degree $p = 5$, which is sufficient to represent the response of interest of the primary mechanical model, a truncation scheme based on sparse polynomial chaos basis for a maximum interaction order $q = 3$, is far more efficient than that based on a complete polynomial chaos basis, especially for high dimensionality. For instance, when $N = 10$ the economy $\mathcal{E}^{5,3}$ is around 43%, which allows to reduce the size of the experimental design used in the computation of the PCE coefficients and consequently the computational effort required to carry out the uncertainty propagation analysis of interest. The maximum interaction order q can be chosen either by following a step-by-step scheme where the value of q is increased gradually to achieve a target level of accuracy on the estimates of the PCE coefficients, or by performing a preliminary screening analysis *(Morris, 1991)*

which allows, based on local sensitivity indices, to split the uncertain parameters into three categories, those with weak main effect, those with linear and additive effects and those with nonlinear or interaction effect. Note that screening analysis are not computational time-demanding, thus the loss of efficiency on the whole computational process is very limited.

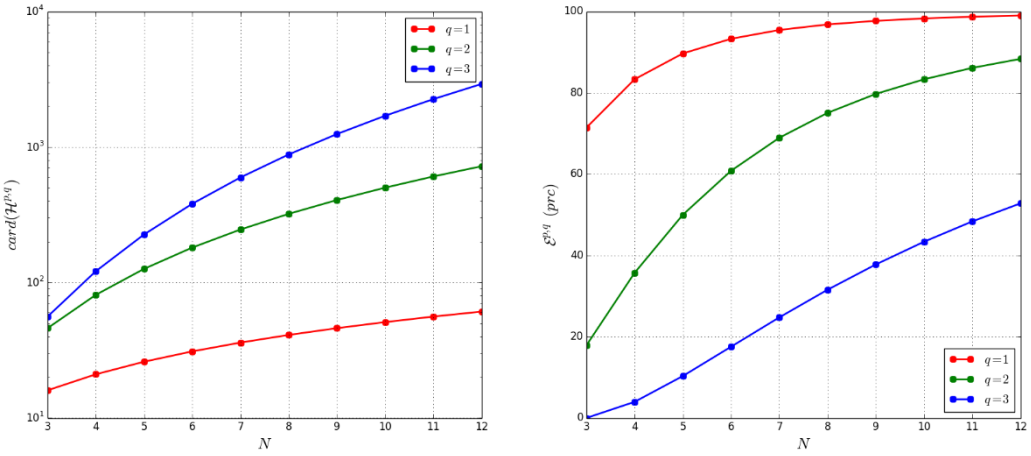

Figure III. 4. The cardinality $card(\mathcal{H}^{p,q})$ (left) and the economy $\mathcal{E}^{p,q}(\%)$ (right) of a sparse polynomial chaos basis $\mathcal{H}^{p,q}$ of degree $p = 5$, for various allowed maximum interaction order q with respect to the dimensionality N

c) Truncation scheme based on second moment information

Commonly, the convergence criteria are established based on the variance of the quantities of interest. Thus, if a prior information about the estimate of the second order statistical moments is already available, the latter could be a useful tool to identify the most significant terms on the quantities of interest, when a step-by-step algorithm is used to build the polynomial chaos basis. Indeed, at each iteration k of this algorithm, the polynomial chaos basis - denoted here by $\mathcal{H}^{p,q,\sigma^2}$ (i.e., σ^2 in $\mathcal{H}^{p,q,\sigma^2}$ refers to the target variance of the quantity of interest) - is enriched by a new candidate polynomial $\boldsymbol{H}_{\boldsymbol{\alpha}_k}$. If the related PCE term induces a significant change on the estimate of the variance $\sigma^2_{PCE,k}$, thus getting closer to the target variance σ^2, the candidate $\boldsymbol{H}_{\boldsymbol{\alpha}_k}$ is retained. Otherwise, i.e. the relative error $\left|\sigma^2_{PCE,k} - \sigma^2_{PCE,k-1}/\sigma^2_{PCE,k-1}\right|$ is smaller than ε_1, the candidate $\boldsymbol{H}_{\boldsymbol{\alpha}_k}$ is discarded from the polynomial chaos basis and another candidate is tested in the next iteration until a given level of accuracy ε_2 is achieved for the whole iterative procedure.

Note that the values of ε_1 used in the criterion of enrichment of the polynomial chaos basis and ε_2 used in the stopping condition of the step-by-step algorithm, are set respectively to 10^{-6} and 10^{-3}, which allow us, on the one hand, to avoid ill-conditioned information matrix, thus an intractable regression problem, and, on the other hand, to ensure a good accuracy on the estimates of the quantities of interest. Of course, other values can be chosen depending on the complexity of the problem of interest and the accuracy to be achieved.

The main steps of this truncation scheme based on second moment information are summarized on the flowchart depicted in figure III.5. As can be seen, the proposed truncation scheme based on second moment prior information can be combined with the truncation scheme based on low-order interactions

presented in the previous section, in order to enhance the sparsity of the polynomial chaos basis $\mathcal{H}^{p,q,\sigma^2}$ and thus achieve greater efficiency in computing the PCE coefficients. This approach to build efficient PCE-based metamodels is denoted in the following by sparse-PCE, which is our second response to the question which closed Chapter II of the thesis.

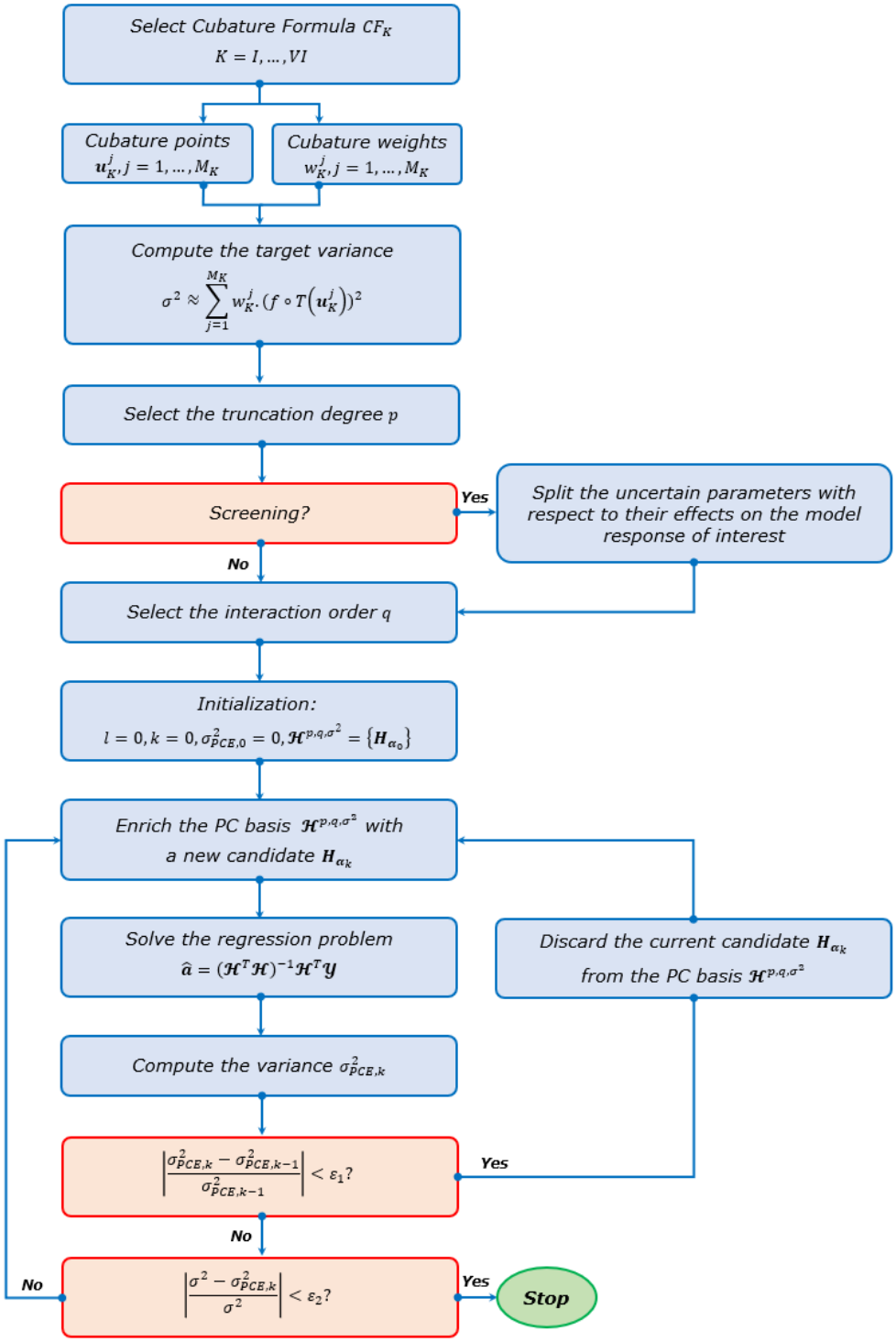

Figure III. 5. Computational flowchart of the sparse-PCE approach

It is important to recall here that the idea behind the implementation of the two approaches called full-PCE and sparse-PCE is to avoid the additional computational efforts observed when cubature formulae I-VI are

directly used on the mechanical model, and when one wishes to change the type of uncertainty propagation analysis. For instance, a statistical moments analysis can be carried out, first, by the crude cubature formulae I-VI, which provides a target estimate of the variance of the model response, and then the sparse-PCE approach is used to construct a metamodel that can be used to perform either a sensitivity or a reliability analysis. The accuracy of the sparse-PCE approach can be improved when the stopping criteria of the stepwise algorithm is established based on higher-order statistical moments such as skewness and kurtosis, instead of variance, provided that the mechanical model evaluations already available are sufficient to obtain a well-conditioned regression problem.

2.3. Post-processing of the PCE-based metamodels

Once the PCE-based metamodel for the model response of interest is built either by full-PCE or sparse-PCE approach, any kind of uncertainty propagation analysis can be carried out with efficiency. Two alternatives are available either by performing MCS on the PCE-based metamodel or by post-processing its coefficients. The latter alternative is addressed in the following.

2.3.1. Computation of the statistical moments

The statistical moments of the random variable Y representing the uncertainty of the model response y of interest can be easily derived from the coefficients $a_k, k = 0, \dots, P-1$. Thanks to the orthonormality of the polynomial chaos basis, the estimates of the first four statistical moments for a given degree p, read:

$$\hat{\mu}_{Y,p} = \hat{a}_0 \tag{III.22}$$

$$\hat{\sigma}^2_{Y,p} = \sum_{k=1}^{P-1} \hat{a}_k^2 \tag{III.23}$$

$$\hat{\delta}_{Y,p} = \frac{1}{\hat{\sigma}^3_{Y,p}} \sum_{k_1=1}^{P-1} \sum_{k_2=1}^{P-1} \sum_{k_3=1}^{P-1} \mathbb{E}[\boldsymbol{H}_{\boldsymbol{\alpha}_{k_1}}(\boldsymbol{U})\, \boldsymbol{H}_{\boldsymbol{\alpha}_2}(\boldsymbol{U})\, \boldsymbol{H}_{\boldsymbol{\alpha}_{k_3}}(\boldsymbol{U})]\ \hat{a}^2_{k_1}\, \hat{a}^2_{k_2} \hat{a}^2_{k_3} \tag{III.24}$$

$$\hat{\kappa}_{Y,p} = \frac{1}{\hat{\sigma}^4_{Y,p}} \sum_{k_1=1}^{P-1} \sum_{k_2=1}^{P-1} \sum_{k_3=1}^{P-1} \sum_{k_4=1}^{P-1} \mathbb{E}\left[\boldsymbol{H}_{\boldsymbol{\alpha}_{k_1}}(\boldsymbol{U})\, \boldsymbol{H}_{\boldsymbol{\alpha}_2}(\boldsymbol{U})\, \boldsymbol{H}_{\boldsymbol{\alpha}_{k_3}}(\boldsymbol{U})\, \boldsymbol{H}_{\boldsymbol{\alpha}_{k_4}}(\boldsymbol{U})\right] \hat{a}^2_{k_1} \hat{a}^2_{k_2} \hat{a}^2_{k_3}\, \hat{a}^2_{k_4} \tag{III.25}$$

Since the PCE-based metamodel is written in the standard random space and the polynomial chaos basis is built up using multivariate Hermite polynomials, the expectations in equations (III.24) and (III.25) can be computed analytically. Once these estimates of the mean $\hat{\mu}_{Y,p}$, the variance $\hat{\sigma}^2_{Y,p}$, the skewness $\hat{\delta}_{Y,p}$ and the kurtosis $\hat{\kappa}_{Y,p}$ are obtained a moment-based technique can be used to construct the PDF $\hat{f}_{Y,p}(y)$.

2.3.2. Computation of Sobol sensitivity indices

In addition to the statistical moments, Sobol sensitivity indices can be derived from appropriate combinations of the PCE coefficients. We only focus on first order $\hat{S}^1_{i,p}$ and total $\hat{S}^T_{i,p}$ Sobol sensitivity indices, measuring respectively the main and the total effects of an uncertain parameter $X_i, i = 1, \dots, N$ on the randomness of the model response of interest.

The estimates of these quantities based on the coefficients of the PCE-based metamodel are obtained by the following expressions:

$$\hat{S}^1_{i,p} = \frac{1}{\hat{\sigma}^2_{Y,p}} \sum_{k=1,\boldsymbol{\alpha}_k \in \mathcal{A}^1_i}^{P-1} \hat{a}^2_k \qquad (III.26)$$

$$\hat{S}^T_{i,p} = \frac{1}{\hat{\sigma}^2_{Y,p}} \sum_{k=1,\boldsymbol{\alpha}_k \in \mathcal{A}^T_i}^{P-1} \hat{a}^2_k \qquad (III.27)$$

where $\mathcal{A}^1_i = \{\boldsymbol{\alpha}_k \in \mathbb{N}^N \; such \; that \; \alpha^i_k \neq 0, \alpha^{j\neq i}_k = 0\}$ is the set of multi-indices with zeros components except the i^{th} one, and $\mathcal{A}^T_i = \{\boldsymbol{\alpha}_k \in \mathbb{N}^N \; such \; that, \alpha^i_k \neq 0\}$ is the set of multi-indices with non zeros i^{th} component.

Note that the higher order Sobol sensitivity indices $S_{i_1,\dots,i_s}, s = 2,\dots,N$, which measure the effect of the interaction between the uncertain parameters $(x_{i_1},\dots,x_{i_s})$, can also be obtained in the same way as the first and total indices. For more details on this issue, the reader can refer to *(Sudret, 2008)*.

2.3.3. Computation of the failure probability

As already stated in section 2.4 of Chapter II, reliability analysis aims to compute the probability of failure of an engineering system with respect to a prescribed serviceability criterion. From a mathematical point of view, the serviceability criterion is defined by the so-called limit state or performance function, often denoted by $G(\boldsymbol{x})$ or $H(\boldsymbol{u}) = G \circ T(\boldsymbol{u})$, respectively into the physical and the standard random spaces.

Typically, in engineering problems, the serviceability criterion can be defined by the fact that the model response of interest $y(\boldsymbol{x})$, which is a random quantity with a probabilistic model Y, since it depends on some uncertain parameters $\boldsymbol{x}$ having a probabilistic model $\boldsymbol{X}$, remains below an admissible threshold $y_{threshold}$ which can be a deterministic or random quantity.

Consequently, the performance function reads:

$$G(\boldsymbol{x}) = y_{threshold} - y(\boldsymbol{x}) = y_{threshold} - y \circ T(\boldsymbol{u}) = H(\boldsymbol{u}) \qquad (III.28)$$

In the case where the response of interest $y \circ T(\boldsymbol{u})$ is provided by an implicit computational model, it can be replaced by its PCE-based metamodel $h^{PCE}(\boldsymbol{u})$ to obtain an analytical formulation of the performance function, given by:

$$H(\boldsymbol{u}) = y_{threshold} - y \circ T(\boldsymbol{u}) \approx y_{threshold} - h^{PCE}(\boldsymbol{u}) \qquad (III.29)$$

The probability of failure P_f, related to the performance function $H(\boldsymbol{u})$, can be easily computed by either by performing MCS on equation (III.29) or by evaluating the following unidimensional integral, since the PDF $\hat{f}_{Y,p}(y)$ of the random variable Y, representing the variability of the model response y, is already known (see section 2.3.3).

$$P_f = \text{Prob}[H(\boldsymbol{u}) \leq 0] \approx \hat{P}_{f,p} = \text{Prob}[y_{threshold} - h^{PCE}(\boldsymbol{u}) \leq 0] = \int_{-\infty}^{+\infty} \hat{f}_{Y,p}(y) \, F_{y_{threshold}}(y) \; dy \qquad (III.30)$$

where $F_{y_{threshold}}(y)$ denotes the CDF of the random variable representing the uncertainty on the admissible threshold $y_{threshold}$. The above integral can be evaluated analytically if a suitable formulation is available for the integrand $\hat{f}_{Y,p}(y)\, F_{y_{threshold}}(y)$ or numerically otherwise, without any additional runs of the primary implicit mechanical model.

3. Application to fatigue fracture problems

In this section, four fatigue crack growth problems are addressed to investigate the approaches proposed above. Various kinds of uncertainty propagation analysis, namely statistical moments and distributions analysis, reliability analysis and sensitivity analysis, are carried out.

The first problem deals with crack growth in a CCP specimen subjected to a constant amplitude fatigue loading, problem for which, fortunately, testing data are available in the literature. They are used to identify the probabilistic models of the uncertain parameters. In addition to assessing the efficiency of the proposed approaches, this first example is used to also study the effect of the distributions of the uncertain parameters and of their statistical characteristics on the results of the probabilistic computations.

The second example considers a nonlinear cracked pipe where the fracture driving force, defined as the Rice's integral, is computed through a greedy computational time FEM. The structural integrity of the cracked pipe, defined as the risk that the fracture driving force will exceed the fracture toughness of the constitutive materials, is evaluated based on the statistical moments results given by the proposed PCE-based methods and a *Demand-Capacity* reliability approach (see section 2.4 of Chapter II).

The third example deals with a mixed mode crack growth problem. The studied structure represents a rectangular plate containing an inclined crack at the edge. The effect of the spatially varying uncertainty of the Young's modulus of the constitutive materials, on the variability of the mechanical responses defined as the opening fracture mode SIF K_I, on the in-plane shear fracture mode SIF K_{II} and on the bifurcation angle θ, is studied.

3.1. Crack growth in CCP specimen

3.1.1. Problem statement

The first example deals with the crack growth in a CCP specimen which was previously studied in section 2.4 of Chapter I of the thesis, but only from a deterministic point of view. Now, we want to push our analysis much further and we are interested in assessing the effect of the uncertainty of some material properties on fatigue lifetime. First, a statistical analysis is carried out on the fatigue crack growth data provided by the experimental tests performed on CCP specimens *(Hudson, 1969)*, on the one hand to point out the probabilistic character of the fatigue crack growth process, and, on the other hand to identify the probabilistic models capable of accurately representing the variability of the uncertain parameters. Figure III.6 depicts the histogram of the logarithm $\log_{10}$ of the Fatigue Crack Growth Rate (FCGR) denoted by

da/dN. As can be observed, a normal distribution with a mean -9.5149 and a standard deviation 2.0275, fits the histogram derived from Hudson's experimental data very well. This leads to a coefficient of variation of about 21.3% on the value of the FCGR, which clearly demonstrates the uncertain character of this parameter. The suitability of the normal distribution to represent the FCGR uncertainty is also confirmed by the Q-Q plot in figure III.6, where the green line represents the reference line plotted from two samples drawn from the same distribution. Indeed, as can be seen, most of the $\log_{10}(da/dN)$ points lie on the reference line especially those in the vicinity of the mean value. However, the points at both the left and right ends of the Q-Q plot, which represent the lower and upper tails of the normal distribution, respectively, deviate from the reference line. The deviation at the left end is due to the non-linearity of the FCGR approaching the threshold ΔK_{th}, while the deviation at the right end is attributed to the non-linearity of the FCGR when approaching the fracture toughness K_{Ic} of the constitutive material of the CCP specimen. The value of the indicator R^2 assessing the goodness of fit of the FCGR to the reference line of the Q-Q plot is close to 1, again confirming the ability of the normal distribution to accurately fit the FCGR derived from Hudson's experimental data.

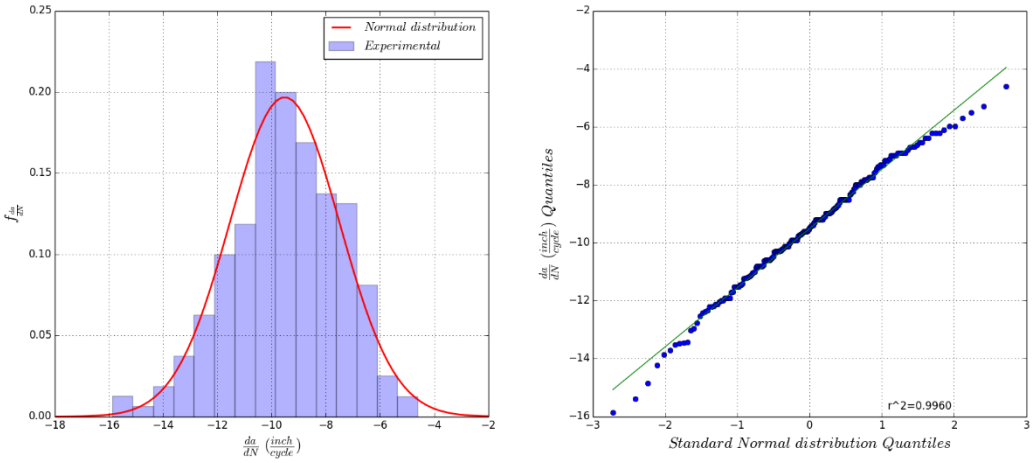

Figure III. 6. Histogram of $log_{10}(da/dN)$ from Hudson's data (left), Q-Q plot of $log_{10}(da/dN)$ from Hudson's data with standard normal PDF (right)

In the following, it is assumed that the FCGR is well represented by the Walker model (see equation I.24 in Chapter I), whose parameters C_1, m_1 and γ follow a normal distribution in the log-log space where they are fitted. The statistical characteristics of these parameters are obtained by performing a least-squares multiple linear regression on the experimental data and using the following log-log transformed release of Walker model:

$$y = B + A_1 x_1 + A_2 x_2 \qquad (III.31)$$

where $y = \log_{10}(da/dN)$, $B = \log(C_1)$, $A_1 = m_1$, $A_2 = -m_1(1-\gamma)$, $x_1 = \log_{10}(\Delta K)$, and $x_2 = \log_{10}(1-R)$.

The statistical moments (i.e., the mean value μ and the variance σ^2), and the correlation matrix $[\boldsymbol{\rho}]$ of the parameters A_1, A_2 and B are listed in table III.2.

Table III. 2. Crack growth in CCP specimen: statistical characteristics of the transformed Walker model

	μ	σ^2	$[\boldsymbol{\rho}]$
A_1	3.8681	2.2911 10^{-3}	$[\boldsymbol{\rho}] = \begin{bmatrix} 1 & -0.7305 & -0.9756 \\ -0.7305 & 1 & 0.8315 \\ -0.9756 & 0.8315 & 1 \end{bmatrix}$
A_2	-1.7052	3.5716 10^{-3}	
B	-21.0737	26.4442 10^{-3}	

A strong statistical dependence between the parameters is observed since the off-diagonal components $|\rho_{ij}|$, $\{i \neq j\}$ of the correlation matrix $[\boldsymbol{\rho}]$ are relatively close to 1. This find is in line with the observations made earlier by several researchers based on statistical analysis performed on Virkler's fatigue crack growth data *(Virkler and al, 1979)*, as pointed out in Chapter I of the thesis. Note that, positive values of the coefficient of correlation ρ_{ij}, $\{i \neq j\}$ indicate variances (i.e., the variances corresponding to the uncertain parameters x_i and x_j) change in a similar direction, while negative values imply variances change in inverse directions. As can be seen, strong negative correlation is observed between A_1 and A_2 and between A_1 and B, which can induce some computational instability when dealing with uncertainty propagation analysis. Fortunately, this problem is anticipated since, as said in Chapter II of the thesis, the quantities of interest (i.e., statistical moments, probability of failure or sensitivity indices) required by the uncertainty propagation analysis are written in the normal standard random space, which allows us to mitigate the effect of strong negative correlations.

3.1.2. Statistical moments and distributions analysis

Next, we assess the effect of the uncertain parameters on the variability of the model response, taken here as the fatigue crack growth life. The latter, denoted by N_f, is computed through the integration of Walker model based on Simpson's rule (see section 2.3 of Chapter I), and assuming that the crack propagates from an initial length a_0 to a critical length a_c:

$$N_f = \int_{a_0}^{a_c} \frac{(1-R)^{m_1(1-\gamma)}}{C_1\,\Delta K_I(a)^{m_1}}\,da \qquad (III.32)$$

where R is the stress ratio, ΔK_I is the SIF range computed by a FEM, C_1, m_1 and γ are uncertain parameters representing the constitutive material of the CCP specimen, whose statistical characteristics can be easily derived from the results given in table III.2.

Of interest are the first four statistical moments of the model response. The estimates are computed by crude MCS involving 10^5 runs of the FEM representing the CCP specimen. Note that, due to the high number of runs of the FEM required by MCS to reach the convergence of the estimates, only the loading condition corresponding to a stress ratio $R = 0.2$, mean stress $\sigma_m = 15\,ksi$ and alternating stress $\sigma_a = 10\,ksi$, is analyzed.

As can be seen in figure III.7 the convergence of the first four statistical moments is reached after 10^5 MCS. The obtained estimates of the mean and standard deviation are, respectively, $\hat{\mu} = 8447$ cycles and $\hat{\sigma} = 265$ cycles, indicating a relatively small effect of the uncertain parameters on the variability of the fatigue crack growth life N_f since the corresponding coefficient of variation is about 3.14%. It is important to

remind that these results represent only one loading condition and the uncertain parameters may have a significant effect on the model response for other loading conditions.

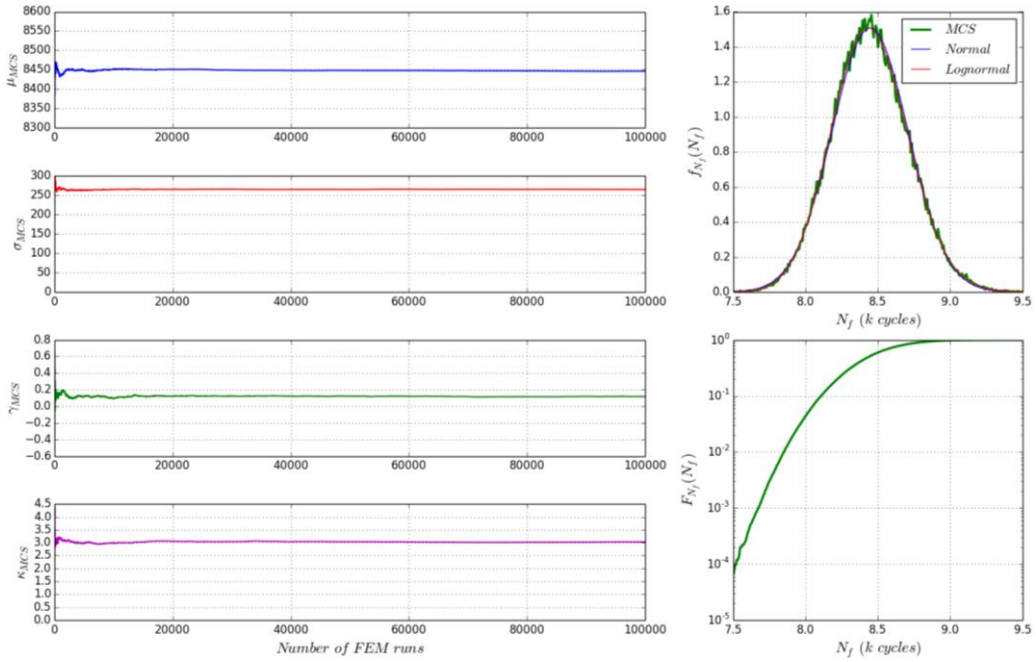

Figure III. 7. Crack growth in CCP specimen: convergence of crude MCS

The PDF and the corresponding CDF of the fatigue crack growth life are also built. In addition, the PDF is compared to some standard distributions with known mathematical formulation. As can be observed, the normal distribution is in full agreement with the PDF built from MCS. This result is also confirmed by the Q-Q plot in figure III.8, comparing samples drawn from the fatigue crack growth life distribution obtained by MCS and those drawn from standard normal distribution, where a major part of the points is in the vicinity of the reference line.

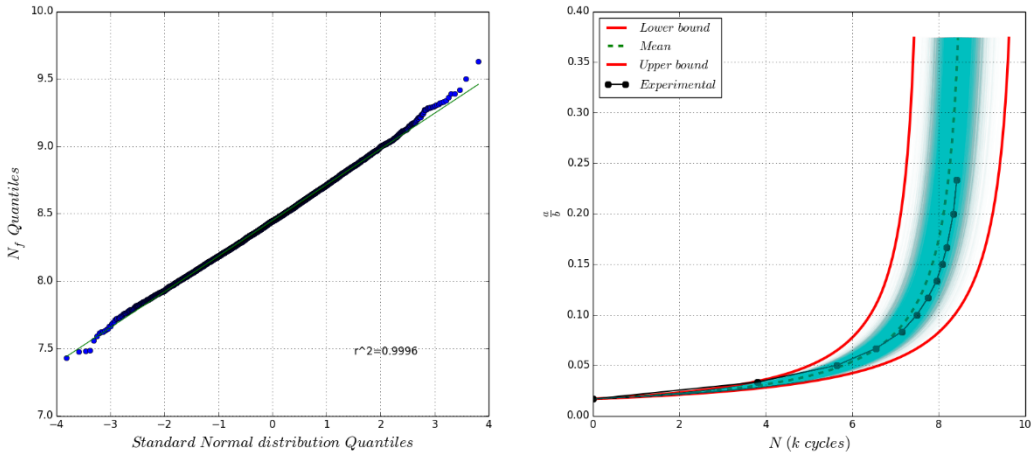

Figure III. 8. Crack growth in CCP specimen: Q-Q plot of the model response N_f with standard Normal PDF (left), probabilistic crack growth curves (right)

Based on MCS samples, crack growth curves, representing the evolution of the effective crack length a/b (i.e., the real crack length divided by the half-width of the CCP specimen) versus the number of loading cycles N are also plotted in figure III.8. To obtain smooth curves the fatigue crack growth life is computed at several crack lengths by integrating Walker model from the initial crack length a_0 to a given incremental

crack length a_i. For each crack increment the mean $\hat{\mu}$ and the standard deviation $\hat{\sigma}$ of the fatigue crack growth life are computed, which allow us to obtain the mean crack growth curve in addition to the lower and upper bounds defined as the crack growth curves at $\hat{\mu} - 3\hat{\sigma}$ and $\hat{\mu} + 3\hat{\sigma}$, respectively. These curves further demonstrate the variability of both the loading cycles and the crack length. The crack growth curve corresponding to Hudson's experimental data for the same loading condition, falls within three standard deviations of the mean and is very close to the mean curve.

To investigate the effect of the correlation between the uncertain parameters on the variability of the fatigue crack growth lifetime, another MCS is performed by considering the Walker model parameters C_1, m_1 and γ as statistically independent, i.e., the off-diagonal coefficients of correlation ρ_{ij}, $\{i \neq j\}$ are set to 0.

The estimates of the mean and the standard deviation of the model response are, respectively, $\hat{\mu} = 8633\ \text{cycles}$ and $\hat{\sigma} = 1854\ \text{cycles}$, which implies a coefficient of variation around 21.5%, much larger than that obtained previously for the case of correlated uncertain parameters and which indicates a significant variability of the fatigue crack growth lifetime, which is not the case in reality. This result calls into question the hypothesis, often made when performing probabilistic analysis on fatigue crack growth problems, that the uncertain parameters, especially those related to the crack growth model, are considered as statistically independent parameters. Thus, we clearly emphasize the importance of properly selecting the probabilistic model (i.e., the type of distribution), used to represent the uncertain parameters, as well as its statistical characteristics (i.e., statistical moments and correlation coefficients) when carrying out uncertainty propagation analysis.

Figure III.9 illustrates the PDF of the fatigue crack growth life N_f in the case of uncorrelated uncertain parameters. It appears that this PDF can no longer be described by a normal distribution and agrees rather with a lognormal distribution. This behavior is clearly confirmed by the Q-Q plot depicted next to the plot of the PDF.

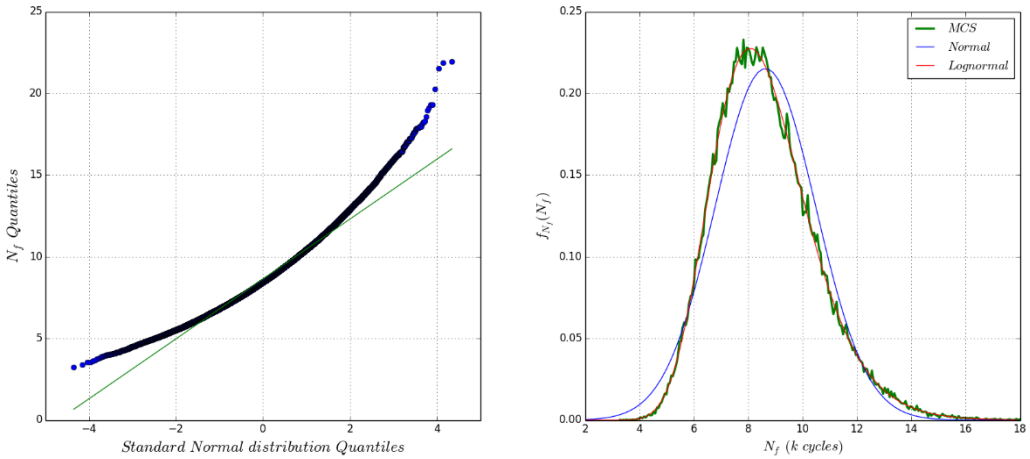

Figure III. 9. Crack growth in CCP specimen: Q-Q plot (left), PDF (right) of the model response N_f for the case of uncorrelated uncertain parameters

In the following, we use PCE-based metamodels as alternatives to MCS to perform uncertainty propagation through the crack growth model of the CCP specimen. The first approach named full-PCE aims to build a metamodel of the model response where cubature formulae I-VI, previously studied in Chapter II, are used to handle the multidimensional integrals involved in the computation of the unknown coefficients of the PCE.

Then, the first four statistical moments of the fatigue crack growth life can be obtained, either directly from the coefficients of the PCE or by performing MCS on the metamodel. In table III.3 are listed the estimates of the first four statistical moments of the fatigue crack growth life, derived from the coefficients of a PCE of degree $p = 2$. The ratio between these estimates and those given by 10^5 crude MCS, is taken here as an accuracy indicator and plotted in figure III.10.

Table III. 3. Crack growth in CCP specimen: statistical moments of the fatigue crack growth life

Statistical moments	Full-PCE (2nd order PCE and cubature formula *i*, *i={I,II,…,VI}*)						MCS
	I	II	III	IV	V	VI	
μ	8446.392	8446.392	8446.392	8446.392	8446.392	8446.392	8446.602
σ	265.490	265.490	265.490	265.490	265.490	265.490	264.649
γ	0.09872	0.09871	0.09870	0.09871	0.09884	0.09875	0.11725
κ	3.01314	3.01314	3.01314	3.01314	3.01318	3.01315	3.02850
Number of FEM runs	14	21	19	19	14	19	10^5

As can be seen from the results depicted in table III.3, independently from the cubature formulae used in the computation of the unknown PCE coefficients, the proposed method works well for the prediction of the statistical moments of the model response since the corresponding estimates are in good agreement with the reference solution, especially for the mean and the standard deviation where the accuracy indicators $\hat{\mu}/\mu_{MCS}$ and $\hat{\sigma}/\sigma_{MCS}$ are close to 1. This high accuracy is achieved with a low computational cost, since in the worst case only 21 evaluations of the FEM are required.

For higher order statistical moments, more particularly for the skewness, the ratio $\hat{\gamma}/\gamma_{MCS}$ is around 0.85 which could be interpreted as a lack of accuracy of the proposed method. Fortunately, this is not really the case, since this *poor* value of the indicator of accuracy $\hat{\gamma}/\gamma_{MCS}$ is not fully due to a significant discrepancy between the estimate given by the proposed method and the reference solution but is also due to the magnitude of the skewness which tends to increase the relative error. However, for the kurtosis where its accuracy is much more difficult to achieve than for the skewness, since having a higher statistical order, the ratio $\hat{\kappa}/\kappa_{MCS}$ is too close to 1.

Note that the accuracy of the proposed method can be enhanced by increasing the truncation order of the PCE. In figure III.10 we compare the accuracy of the statistical moments estimates derived from the PCE coefficients and those obtained from 10^5 MCS applied on the corresponding PCE-metamodel. As can be observed, the latter approach can be viewed as an alternative to enhance the accuracy of the proposed method. Indeed, for the skewness the ratio $\hat{\kappa}/\kappa_{MCS}$ is now around 0.97 which is achieved when cubature formula VI is used to compute the unknown PCE coefficients.

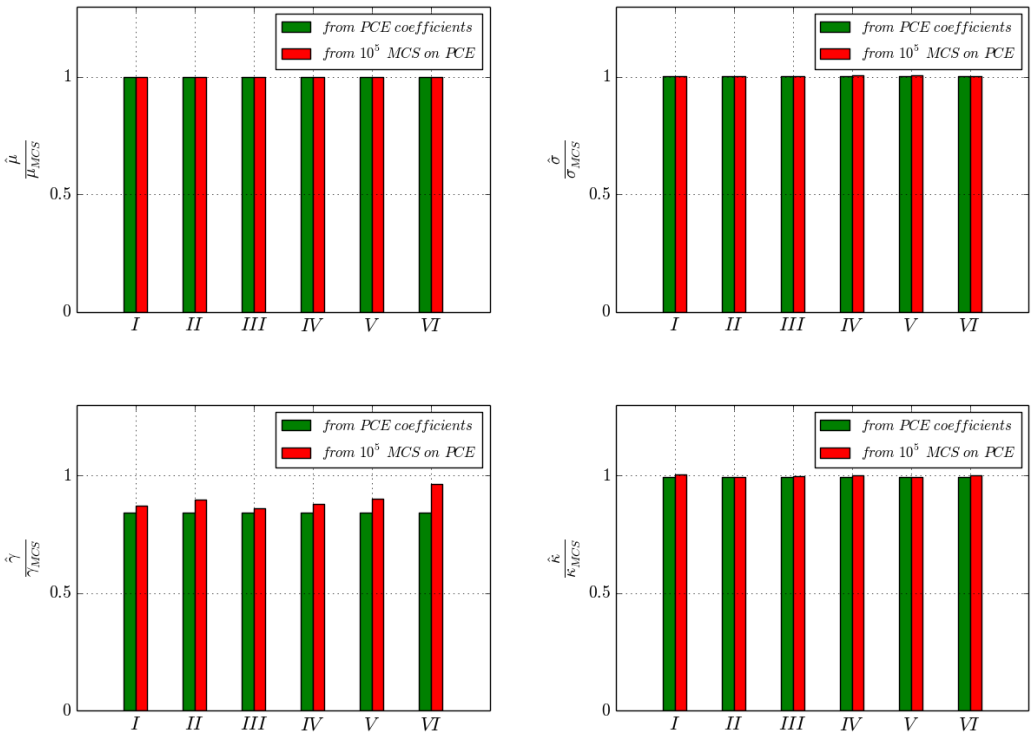

Figure III. 10. Crack growth in CCP specimen: convergence analysis of the statistical moments

We are also interested in the convergence of the metamodel corresponding to the PCE. To avoid redundancy, and since all cubature formulae give fairly the same results, only the metamodel built from PCE coefficients obtained from cubature formula VI is plotted in figure III.11. The fatigue crack growth lifetime N_f obtained from the metamodel given by the PCE is plotted with respect to each uncertain parameter $x_i, i \in \{1,2,3\}$, in the range $[\mu_i \pm 3\sigma_i]$.

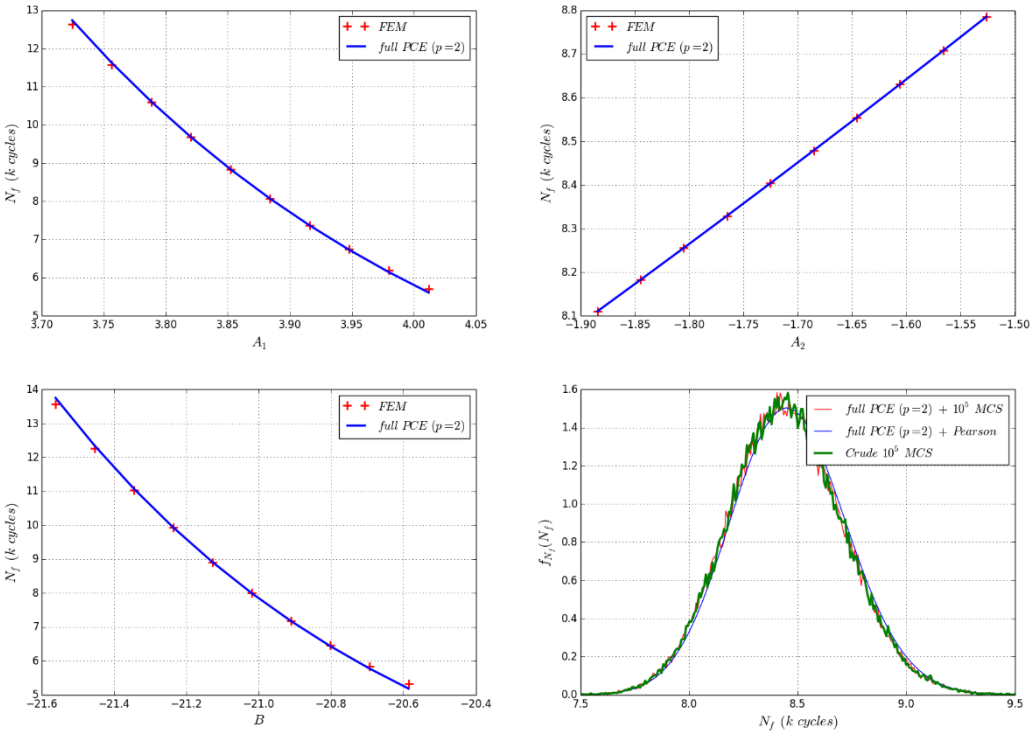

Figure III. 11. Crack growth in CCP specimen: convergence of the metamodel relative to a PCE of degree $p = 2$

As can be seen, the metamodel relative to a PCE of degree $p = 2$ is sufficient to reproduce accurately the real behavior of the FEM representing the CCP specimen. Indeed, the metamodel fits very well the response of the FEM evaluated at a new set of points different from the integration points used previously in the computation of the unknown coefficients of the PCE. We can observe that the fatigue crack growth lifetime exhibits a nonlinear behavior with respect to the uncertain parameters $B = \log(C_1)$ and $A_1 = m_1$, and varies linearly with $A_2 = -m_1(1-\gamma)$. In figure III.11 we also compare the PDFs of the fatigue crack growth life, constructed either by using moments technique based on the estimates of the first four statistical moment derived from the PCE coefficients, or by performing MCS on the metamodel relative to the PCE. As can be seen, the PDFs are in good agreement with that built from 10^5 crude MCS.

3.1.3. Sensitivity analysis

In the following, we conduct a sensitivity analysis to evaluate the contribution of each uncertain parameters on the variability of the model response. Hence, the first-order and total Sobol sensitivity indices, respectively, denoted by S_1 and S_T, are the quantities of interest, whose estimates are directly derived from the PCE coefficients of degree $p = 2$ used previously in the statistical moments analysis. Thus, no additional evaluations of the FEM are needed.

Table III. 4. Crack growth in CCP specimen: first-order and total Sobol indices obtained by PCE of degree $p = 2$

	A_1	A_2	B
$\hat{S_1}$	0.15126	0.37210	0.47633
$\hat{S_T}$	0.15138	0.37233	0.47658

The results are listed in table III.4. It appears that the parameter $A_1 = m_1$ has a moderate effect on the variability of the model response, whereas the parameters $B = \log(C_1)$ and $A_2 = -m_1(1-\gamma)$ have a significant effect. This means that the variability of the fatigue crack growth lifetime of the CCP specimen is driven by the uncertainty in the parameters C_1 and γ of the Walker model, with the parameter C_1 having the dominant contribution. Furthermore, the total indices are nearly equal to the first-order indices, indicating that the interaction effects between the uncertain parameters are negligible.

It is important to note that although the uncertain parameters are statistically dependent, the Sobol indices are still computable, but their interpretation becomes a difficult task. Indeed, referring to the total variance decomposition given by equation (2.16) presented in section 2.3 of Chapter II, it is difficult to know if the contribution of a given uncertain parameters on the variability of the model response is due to its importance in the model structure or to its correlation with other influent parameters. To overcome this problem, the Sobol sensitivity indices must be derived from partial variances related to an ANCOVA (ANalysis of COVAriance) decomposition *(Li and Rabitz, 2010; Chastaing and al., 2012)*, instead of partial variances associated to an ANOVA decomposition (see section 2.3 of Chapter II).

The genuine idea behind the ANCOVA decomposition is to decompose the partial variances into a variance part, which measures the contribution of an uncertain parameter due to its importance in the model structure, and a covariance part, which measures the contribution of an uncertain parameters due to a possible correlation with other parameters. Hence, these two contributions are no longer merged as in the

ANOVA decomposition. We recall here that the main purpose of the present sensitivity analysis is not to separate the sources of contribution but to identify important and unimportant parameters on the variability of the model response. Global sensitivity analysis based on ANCOVA decomposition has gained increasing popularity in the last few years and will be obviously a priority area of research for us.

For the sake of validation, first-order and total Sobol indices are computed by post-processing PCE coefficients of degrees $p = \{1,3\}$. The results obtained, when using cubature formula VI to compute the unknown coefficients of the PCE, are plotted in figure III.12, together with those derived previously from a PCE of degree $p = 2$. As can be seen, the convergence of the first-order and total Sobol indices is well achieved by a full PCE of degree $p = 2$. Moreover, the Sobol indices provided by a PCE of degree $p = 1$ are slightly different from those achieved at the convergence point, which indicates once again that the effects of interaction between uncertain parameters are weak and the major part of the variability of the fatigue crack growth lifetime is due to the main effects.

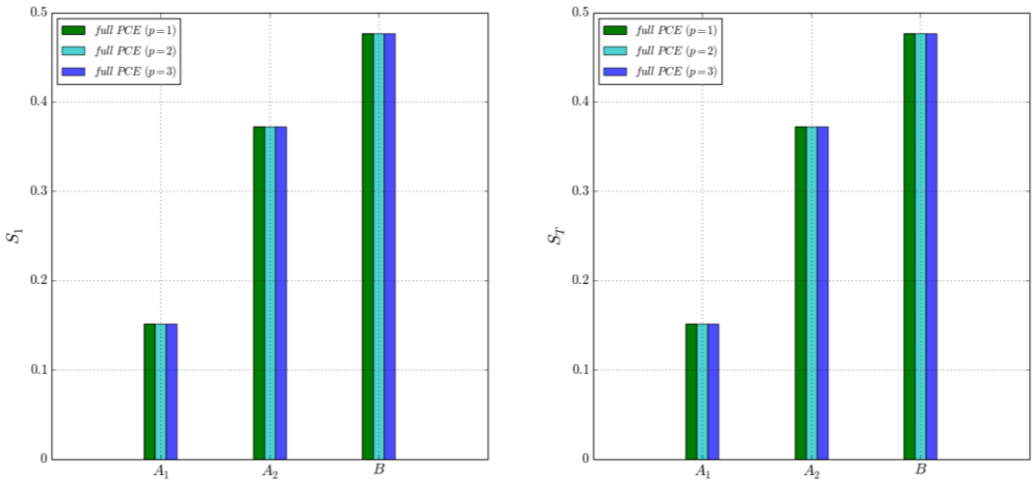

Figure III. 12. Crack growth in CCP specimen: convergence of the first-order and total Sobol indices

3.1.4. Discussion

It can be noted from this example that the proposed full-PCE approach is able to perform moments and sensitivity analysis at a very low computational cost. Indeed, depending on the cubature formula used to handle the multidimensional integrals defining the unknown coefficients of the PCE, the required number of evaluations of the FEM is in the range [14, 21] for a PCE of degree $p = 2$ where the convergence of the quantities of interest is achieved. In addition, although a full PCE is used to represent the model response, which means that all coefficients related to a PCE of a given degree p are retained, the computational cost slightly increases with the probabilistic dimension, and it is independent from the chosen degree of the PCE.

Furthermore, when passing from a moments analysis to a sensitivity analysis or the opposite, no additional computational cost is required, since the evaluations of the FEM are only needed to build the PCE, then any kind of probabilistic analysis could be performed, either by post-processing the PCE coefficients or by performing MCS on the metamodel of the mechanical response. This clearly allows us to overcome the inefficiency of crude cubature formulae pointed out in Chapter II, where the required set of evaluations of

the mechanical model depends not only on the integration points related to the chosen cubature formula but also on the type of the probabilistic analysis to be addressed. Indeed, the comparison of equations (II.3) and (II.23) (see sections 2.2 and 2.3 of Chapter II) shows that the integrands to be evaluated for the computation of statistical moments and partial variances are not the same. It appears that performing MCS on the metamodel could enhance the estimates of statistical moments, especially the higher order one such as the skewness and the kurtosis, when a lack of accuracy is observed on the estimates provided by the post-processing of the PCE coefficients.

Finally, thanks to the present example, we have shown how it is important to identify the right probabilistic models and their statistical characteristics when performing uncertainty propagation analysis, especially through mechanical models dealing with crack growth under fatigue loading where some uncertain parameters exhibit a statistical dependency. Indeed, when the correlation between the constants of the Walker law, which is proven by statistical analysis on experimental data, is not considered, the uncertainty propagation analysis provides erroneous results on the variability of the fatigue crack growth lifetime of the CCP specimen. Consequently, wrong decisions could be taken by the decision-makers, in the design stage for instance or in the maintenance scheduling when dealing with existent structures.

3.2. Nonlinear cracked pipe

3.2.1. Problem statement

The present problem deals with an axysymmetrically cracked pipe as depicted in figure III.13. Such a component is extensively used in nuclear plants where it is often subjected to large variations of thermal and mechanical loads which can lead to crack initiation and growth toward a critical length inducing its failure. This problem has been introduced first by *(Pendola and al., 2000)* to assess the reliability of the cracked pipe with respect to accidental loads, using an original approach in that time, based on combination of finite elements computations and quadratic response surface. Later, this same problem has been used by *(Riahi and al., 2012)* as a benchmark example to compare the efficiency of pseudo-random numbers, Latin hypercube samples and quasi-random numbers when MCS is used to compute the unknown coefficients of a PCE-based metamodel. The cracked pipe with internal radius $R_i = 393.5\,mm$ and thickness $t = 62.5\,mm$, contains a symmetrically centered circumferential internal crack with length $a = 15\,mm$, and is subjected to an internal pressure $P = 15.5\,MPa$ and an axial tension $\sigma_t = 140\,MPa$. Due to the boundary conditions at the ends of the cracked pipe, the internal pressure P induces a longitudinal tension pressure, in addition to the axial tension σ_t. Thus, the stress σ_0 due the end effects, reads:

$$\sigma_0 = P\frac{R_i^2}{(R_i + t)^2 - R_i^2} \qquad (III.33)$$

We are interested in ductile fracture which concerns materials where crack growth involves plasticity. Thus, we must take into account the effect of this plasticity on the crack driving forces. The elastoplastic behavior of the constitutive material of the cracked pipe is described by the well-known Ramberg-Osgood *(Anderson, 1995)* stress-strain relationship given by:

$$\epsilon = \frac{\sigma}{E} + \alpha \frac{\sigma_y}{E} \left(\frac{\sigma}{\sigma_y}\right)^n \qquad (III.34)$$

where σ is the stress, ϵ the strain, E the Young's modulus, σ_y the yield strength, α a dimensionless material parameter and n the strain hardening exponent.

The stress-strain curve representing the Ramberg-Osgood behavior law, which will be used later in the computation of the fracture parameters of interest, is shown in figure III.13.

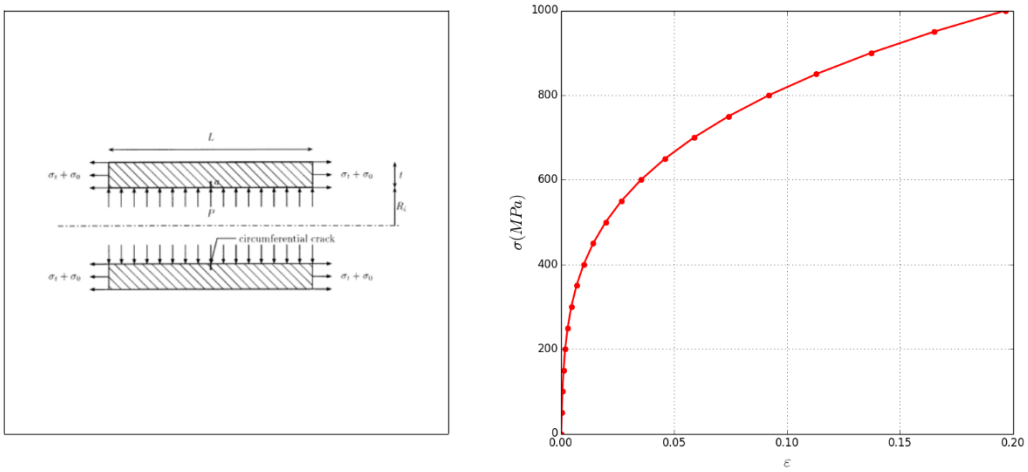

Figure III. 13. Geometry and applied loads of the cracked pipe (left, after Pendola and *al., 2000), stress-strain curve associated to the Ramberg-Osgood behavior law (right)*

There are several ways to characterize the mechanical fields in the region where the crack appears and grows. When the constitutive material exhibits an elastic behavior the Stress Intensity Factors (SIF) are often used to describe the stress singularity observed at the vicinity of the crack tip. However, for elastoplastic materials, the SIF are not sufficient to adequately describe ductile fracture. For this reason, the J-integral, also called Rice's integral *(Rice, 1968)*, whose formulation is based on energy considerations, is used as the driving force when crack growth goes with plasticity (see section 2.1.1 in Chapter 1). The initiation of crack growth is observed when the value of the Rice's integral exceeds the fracture toughness J_{Ic} of the constitutive material. For mechanical and civil engineering problems, where the components or structures considered often have a complex geometry, the computation of the Rice's integral is only possible through a numerical procedure. Therefore, a FEM is developed under the finite element software *(cast3m, 2021)* to predict the ductile fracture of the cracked pipe. Due to the symmetry of the problem, we model only half of the pipe. The corresponding finite element mesh is made of 709 6-noded triangular elements and 1553 nodes, as shown in figure III.14. As can be seen, the mesh is extremely refined around the crack tip to ensure good accuracy on the estimate of the Rice's integral. Since the constitutive material of the cracked pipe exhibits nonlinear behavior, the estimate of the Rice's integral, denoted by J_{Rice}, is obtained by an incremental Finite Element Analysis (FEA), as shown in figure III.14. It is important to note that the size of the mesh elements, especially those around the crack tip, as well as the number of increments in the FEA are chosen very carefully based on a parametric study on the accuracy of the estimate of the Rice's integral J_{Rice}. For the sake of illustration, a single run of the FEM requires about 10 seconds with an Intel® Core™ i7-10850H CPU processor.

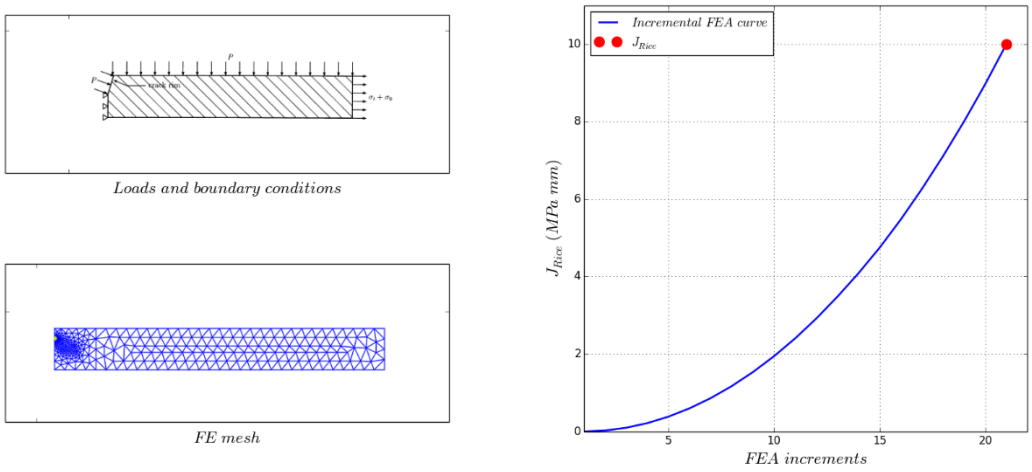

Figure III. 14. Nonlinear cracked pipe: applied loads and boundary conditions (upper left, after Pendola and al., 2000), finite element mesh (lower left), evolution of J_{Rice} with respect to the FEA increments (right)

The uncertain inputs include the four parameters of the Ramberg-Osgood behavior law, namely the Young's modulus E, the yield strength σ_y, the coefficient α and the strain hardening exponent n, whose distributions and asociated statistical characteristics are listed in table III.5.

Table III. 5. Nonlinear cracked pipe: probability distributions and statistical characteristics of the random variables

Parameter	Distribution	μ	σ
$E\ (MPa)$	Lognormal	175500	10000
$\sigma_y\ (MPa)$	Lognormal	259.5	10
n	Normal	3.5	0.1
α	Normal	1.15	0.15

3.2.2. Statistical moments and distributions analysis

First, statistical moments analysis is performed to assess the effect of the uncertain parameters on the variability of the model response defined as the Rice's integral J_{Rice}. Since all cubature formulae I-VI provide correct results, only cubature formula VI is used here, on the one hand to avoid redundancy in the presentation of the obtained results, on the other hand this cubature formula has a free parameter Δ (see section 4.6 of Chapter II) which seems to be very useful for constructing suitable experimental designs when the sparse-PCE approach is used to carry out uncertainty propagation analysis. For comparison purposes, the first four statistical moments of the model response of interest J_{Rice} are computed using the two proposed approaches, namely the full-PCE and the sparse-PCE, where the polynomial degree p is set to 2. For the full-PCE approach, the unknown coefficients are computed either by the full tensor-product Gauss-Hermite scheme (see equation III.13) or by the cubature formula VI (see equation III.15). For the sparse-PCE approach, the target variance of the model response of interest is computed by the crude cubature formulae VI, and then the unknown coefficients are computed by regression based on experimental design built from the integration points of the cubature formula IV and the corresponding FEM responses.

The results obtained are listed in Table III.6 and compared to the estimates provided by crude MCS, taken as reference solutions. As can be seen, the estimates of the first four statistical moments obtained by the proposed methods are overall in good agreement with the reference ones, since the maximum relative

error is equal to 0.01%, 0.19%, 3.67% and 1.84%, respectively for the mean, standard deviation, skewness and kurtosis. This good accuracy is achieved with low computational cost since only 33 runs of the FEM are required for both the proposed full-PCE and sparse-PCE approaches when the cubature formula VI is used. Due to the proposed truncation scheme based on the second moment information, the polynomial chaos basis $\mathcal{H}^{p,q,\sigma^2}$ used in the sparse-PCE approach contains only 10 components, instead of 15 as for a full polynomial chaos basis $\mathcal{H}^{p}$, which means that 5 components have insignificant effect on the model response and can be discarded from the PCE-based metamodel. As a result, the *economy* $\mathcal{E}^{p,q,\sigma^2} = 100 \times (\mathrm{card}(\mathcal{H}^{p}) - \mathrm{card}(\mathcal{H}^{p,q,\sigma^2})/\mathrm{card}(\mathcal{H}^{p}))$ (i.e., defined in the same way as in equation III.21) of the sparse polynomial chaos basis $\mathcal{H}^{p,q,\sigma^2}$ is around 33%, showing a significant decrease in the computational effort required to estimate the PCE coefficients by regression.

Table III. 6. Nonlinear cracked pipe: statistical moments of the Rice's integral J_{Rice}

Statistical moments	Full-PCE		Sparse-PCE	Crude formula VI	MCS
	GH*	Formula VI			
μ	16.7348	16.7347	16.7347	16.7347	16.7322
σ	0.98589	0.98639	0.98620	0.98643	0.98779
γ	0.18773	0.19806	0.19606	0.19781	0.19104
κ	3.04983	3.05487	3.05322	3.00158	3.05801
Number of FEM runs	81	33	33	33	10^5

* *GH: Gauss-Hermite*

Figure III.15 compares the PDFs and CDFs obtained by a moment-based technique using the estimates of the first four statistical moments given by the different proposed approaches. As can be seen, the PDFs and CDFs corresponding to the full-PCE and sparse-PCE approaches are in good agreement with the reference ones given by 10^5 crude MCS, throughout the range of variation of the model response J_{Rice}. As can be observed from the CDFs plot, where a logarithmic scale is used on the vertical axis to highlight the behavior at the tails of the distribution, high accuracy is obtained in these regions of great interest when performing reliability analysis. Clearly, the full-PCE and sparse-PCE approaches yield superior estimates of the PDF and the CDF of the model response, compared to the approach based on crude cubature formula VI. Indeed, a slight discrepancy between the corresponding CDF and the reference one is observed at the left tail of the distribution.

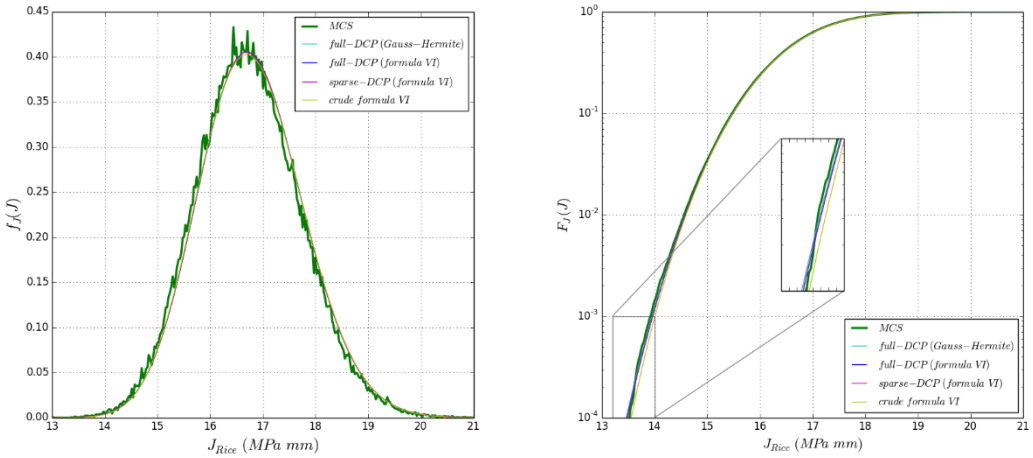

Figure III. 15. Nonlinear cracked pipe: comparison of the PDFs and CDFs of the model response J_{Rice}

As an illustration, figure III.16 shows the convergence of the statistical moments obtained by crude MCS, directly applied on the FEM. As can be seen, convergence is well achieved with a sample size of 10^5, but with a huge computational cost since, as stated previously, the FEM is itself time consuming due to the incremental FEA required to solve the nonlinear fracture problem. The PDF of the Rice's integral J_{Rice} is also constructed and compared to conventional distributions, showing that the lognormal distribution gives the best fit. In addition, the CDF is obtained by direct integration of the PDF and can be used to perform a reliability analysis if necessary.

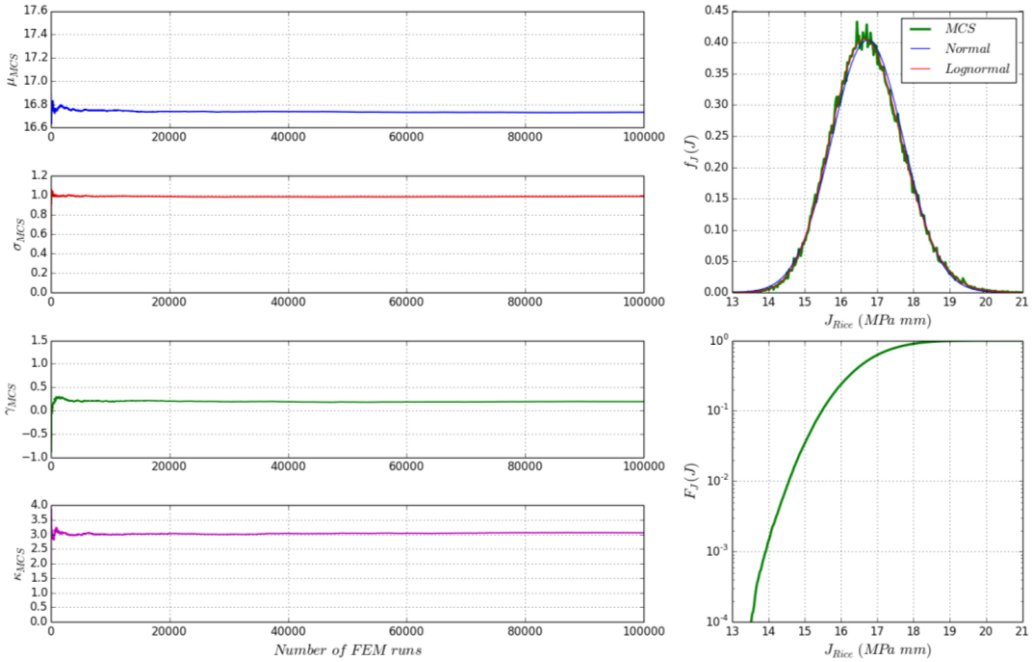

Figure III. 16. Nonlinear cracked pipe: convergence of crude MCS

3.2.3. Sensitivity analysis

Next, we conduct a sensitivity analysis to assess the contribution of each uncertain parameters on the variability of the crack driving force J_{Rice}. The first-order and total Sobol indices are computed by the proposed approaches by post-processing the coefficients of the corresponding PCE-based metamodels and using equations III.26 and III.27, respectively. The obtained results are reported in figure III.17. As can be seen, the estimates given by the full-PCE and sparse-PCE approaches are almost identical. Since MCS is not practical in this problem to compute the Sobol sensitivity indices due to the relatively expensive cost of a single run of the incremental FEA required to compute the Rice's integral, the full-PCE approach where the coefficients are obtained by a full tensor-product Gauss-Hermite integration scheme is used as the reference method. Referring to the first-order or the total Sobol indices, it appears that the variability of the model response J_{Rice} is mainly due to the uncertainty of the Young's modulus E, while the coefficient α and the strain hardening exponent n of the Ramberg-Osgood behavior law, have insignificant effects and can be considered as deterministic quantities, thus set to their respective mean values. The effect of interaction between uncertain parameters is also negligible since the total indices have roughly the same values as the first-order indices.

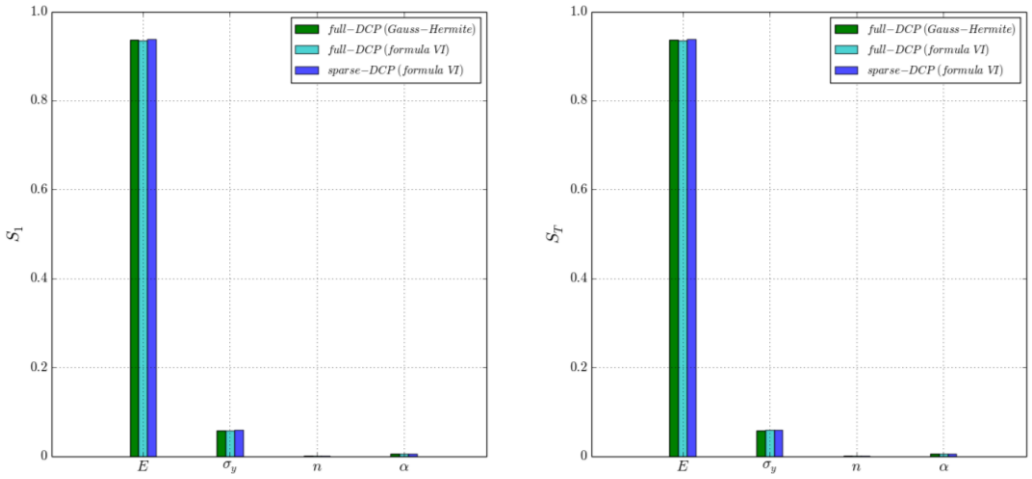

Figure III. 17. Nonlinear cracked pipe: convergence of the first-order and total Sobol indices

3.2.4. Reliability analysis

In the following, a reliability analysis is performed to study the effect of the axial tension magnitude σ_t on the integrity of the cracked pipe. Pipe failure is observed when the Rice's integral J_{Rice} exceeds the fracture toughness J_{Ic} of the constitutive material. Therefore, the performance function is as follows:

$$G(\boldsymbol{x}) = J_{Ic} - J_{Rice}(\boldsymbol{x}) \qquad (III.35)$$

The fracture toughness J_{Ic} is taken here as uncertain parameter, in addition to the uncertain parameters gathered in the vector $\boldsymbol{x} = \{E, \sigma_y, n, \alpha\}$, considered in the statistical moments and sensitivity analyses conducted previously. It is assumed to follow a lognormal distribution with a mean $52\,MPa\,mm$ and a standard deviation $9.5\,MPa\,mm$. The axial tension σ_t is taken as a deterministic parameter ranging from $140\,MPa$ up to $200\,MPa$. It represents the effect of an accidental increase in load, whose nominal value is about $140\,MPa$, that could occur during the pipe lifetime. The main issue of the reliability analysis is to obtain the probability of failure as a function of the magnitude of the axial tension, in order to be able to make the right decision as to whether or not to perform repair operations on the pipe. Indeed, by knowing the cumulated damage, i.e. the crack length, and the corresponding failure probability, we can decide if the repair of the pipe must be done urgently, or if we can still wait. Conversely, if a threshold level of reliability must be guaranteed, for instance by referring to design codes recommendations, the curve representing the evolution of the probability of failure with respect to the magnitude of the axial tension, gives us the allowable load that the pipe should support. To build this curve, the probability of failure is computed for some values of the axial tension varying in the range $[140\,MPa,\ 200\,MPa]$, based on the computational method presented in section 2.3.3 of this chapter. For more computational cost savings, the results obtained at each step of the incremental FEA, required to compute the Rice's integral, are stored in a database where a step size of $5\,MPa$ is taken to cover the entire range of variation of the axial tension σ_t. For a given value of the axial tension σ_t, a PCE-based metamodel $h_{\sigma_t}^{PCE}(\boldsymbol{u})$ is built in the standard random space, either by the full-PCE or the sparse-PCE approach. Thus, the performance function $G(\boldsymbol{x})$ defined by equation III.35 can be approximated as follows:

$$H(\boldsymbol{u}) = J_{Ic} - J_{Rice} \circ T(\boldsymbol{u}) \approx J_{Ic} - h^{PCE}_{\sigma_t}(\boldsymbol{u}) \qquad (III.36)$$

Knowing the PDF of the fracture toughness J_{Ic}, and the PDF of the Rice's integral J_{Rice} which can be easily built either by performing MCS on the metamodel $h^{PCE}_{\sigma_t}(\boldsymbol{u})$, or by a moment-based technique using the statistical moments estimates obtained by post-processing the coefficients of the metamodel $h^{PCE}_{\sigma_t}(\boldsymbol{u})$, an approximation of the failure probability P_f, for a given value of σ_t and PCE degree p, can be provided by assessing the following unidimensional integral:

$$P_f = \text{Prob}[H(\boldsymbol{u}) \leq 0] \approx \hat{P}_{f,p,\sigma_t} = \text{Prob}\left[J_{Ic} - h^{PCE}_{\sigma_t}(\boldsymbol{u}) \leq 0\right] = \int_0^{+\infty} \hat{f}_{J_{Rice},p,\sigma_t}(J)\, F_{J_{Ic}}(J)\; dJ \qquad (III.37)$$

where $\hat{f}_{J_{Rice},p,\sigma_t}(J)$ is the approximation of the PDF of Rice's integral J_{Rice} and $F_{J_{Ic}}(J)$ is the CDF of the fracture toughness J_{Ic}, which are already available under analytical forms.

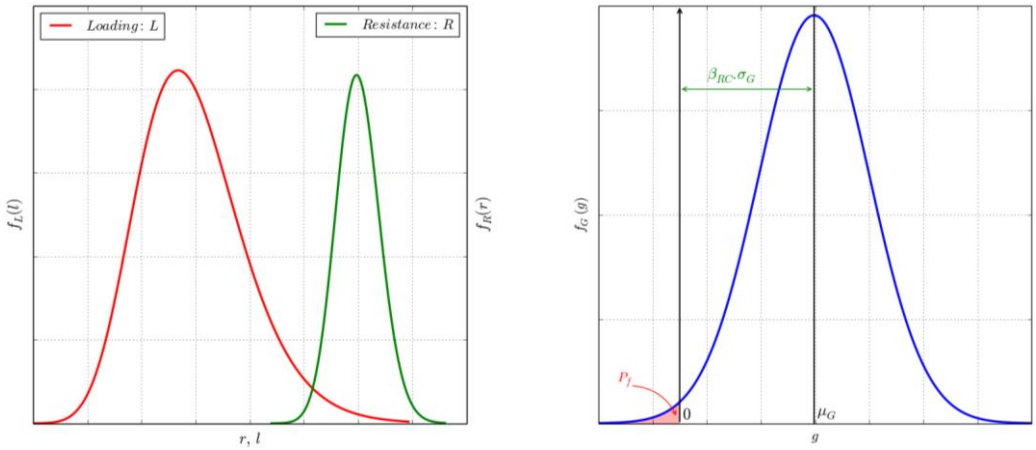

Figure III. 18. Nonlinear cracked pipe: Resistance-Loading reliability problem (left), PDF of the performance function and definition of the reliability index of Rjanitzyne-Cornell

If we look at equations III.35, III.36 and III.37, we clearly find the well-known elementary reliability problem, referred to in the literature as either by the *Capacity-Demand (C-D)* or the *Resistance-Loading (R-L)* problem, the basic principle of which is illustrated in figure III.18 (see also section 2.4 of Chapter II for more details on this issue).By analogy, the fracture toughness J_{Ic} represents the *Resistance* part, whereas the Rice's integral J_{Rice} represents the *Loading* part. Since the fracture toughness J_{Ic} follows a lognormal distribution, and the Rice's integral also tends to follow a lognormal distribution as shown in the statistical moments analysis conducted previously, the evaluation of the integral III.37 can be avoided, and the failure probability can be approximated as follows:

$$\hat{P}_{f,p,\sigma_t} = \int_0^{+\infty} \hat{f}_{J_{Rice},p,\sigma_t}(J)\, F_{J_{Ic}}(J)\; dJ = \Phi(-\beta_{RC}) \qquad (III.38)$$

In the above equation, Φ denotes the CDF of a standard normal variable and β_{RC} denotes the reliability index of Rjanitzyne-Cornell, defined as the weighted distance $\beta_{RC}.\sigma_G$ between the failure domain and the mean of the performance function. In the case of lognormal distributions, the reliability index of Rjanitzyne-Cornell reads:

$$\beta_{RC} = \frac{\mu_G}{\sigma_G} = \frac{\mu_{\ln(J_{Ic})} - \mu_{\ln(J_{Rice})}}{\sqrt{\sigma^2_{\ln(J_{Ic})} - \sigma^2_{\ln(J_{Rice})}}} \qquad (III.39)$$

where μ_G and σ_G are, respectively, the mean and the standard deviation of the performance function G, $\mu_{\ln(J_{Ic})}$ and $\sigma_{\ln(J_{Ic})}$ are, respectively, the mean and the standard deviation of the normal distribution $\ln(J_{Ic})$, $\mu_{LN(J_{Rice})}$ and $\sigma_{\ln(J_{Rice})}$ are, respectively, the mean and the standard deviation of the normal distribution $\ln(J_{Rice})$, and $\ln$ denotes the Neperian logarithm function.

It is important to note that the estimation of the failure probability by evaluating the integral III.37 is not a difficult task since the integrand is now available in an analytical form. But, having in mind the idea to provide simple computational tools to engineers to assess the reliability of their designs, the use of equations III.38 and III.39 for this purpose seems to be the best solution, since it does not require extensive knowledge of mathematics and probability theory. The estimates of the reliability indices and the corresponding failure probabilities obtained by the proposed approaches are listed in Table III.7. The same results are also shown in figure III.19. As can be seen, the proposed approaches are in good agreement overall with the reference solutions provided by FORM, since the relative error on the estimate of the reliability index varies in the range [0.01%, 1.97%]. The magnitude of the failure probability, which is related to the magnitude of the axial tension σ_t, has a weak effect on the accuracy of the estimates given by either the full-PCE or the Sparse-PCE approaches. For the highest magnitude of the axial tension σ_t, which is $200\ MPa$, we obtain the largest relative error on the estimate of the reliability index, but it remains at an acceptable level. This increase of the relative error is probably due to the high nonlinearity observed in the mechanical behavior of the constitutive material, especially around the crack tip, when $\sigma_t = 200\ MPa$. Indeed, such a magnitude of the axial tension induces high stresses in the cracked pipe close to the yield stress of the constitutive material. For such a situation, the relative error can be reduced by using more steps on the incremental FEA required to compute the Rice's integral.

Table III. 7. Nonlinear cracked pipe: comparison of the reliability analysis results given by the proposed methods and FORM

σ_t (MPa)	FORM		Full-PCE						Sparse-PCE		
			GH			Formula VI					
	$\hat{P}_f$	$\hat{\beta}$	$\hat{P}_f$	$\hat{\beta}$	$\epsilon_\beta(\%)$	$\hat{P}_f$	$\hat{\beta}$	$\epsilon_\beta(\%)$	$\hat{P}_f$	$\hat{\beta}$	$\epsilon_\beta(\%)$
140	2.139 10^{-9}	5.873	2.129 10^{-9}	5.874	0.014	2.132 10^{-9}	5.874	0.010	2.130 10^{-9}	5.874	0.011
160	2.942 10^{-6}	4.531	2.959 10^{-6}	4.529	0.028	2.985 10^{-6}	4.527	0.068	2.982 10^{-6}	4.527	0.064
180	2.139 10^{-3}	3.039	1.261 10^{-3}	3.021	0.608	1.261 10^{-3}	3.021	0.610	1.261 10^{-3}	3.021	0.608
200	1.186 10^{-1}	1.198	1.200 10^{-1}	1.175	1.970	1.201 10^{-1}	1.175	1.992	1.198 10^{-1}	1.175	1.862

As an illustration, figure III.19 shows the PDFs of the Rice's integral J_{Rice} and fracture toughness J_{Ic} for $\sigma_t = 180\ MPa$. As can be observed, the lognormal distribution fits both PDFs very well. Thus, the previously method presented, which consists in solving an elementary *R-L* reliability problem, can be unambiguously applied to provide a suitable estimate of the failure probability.

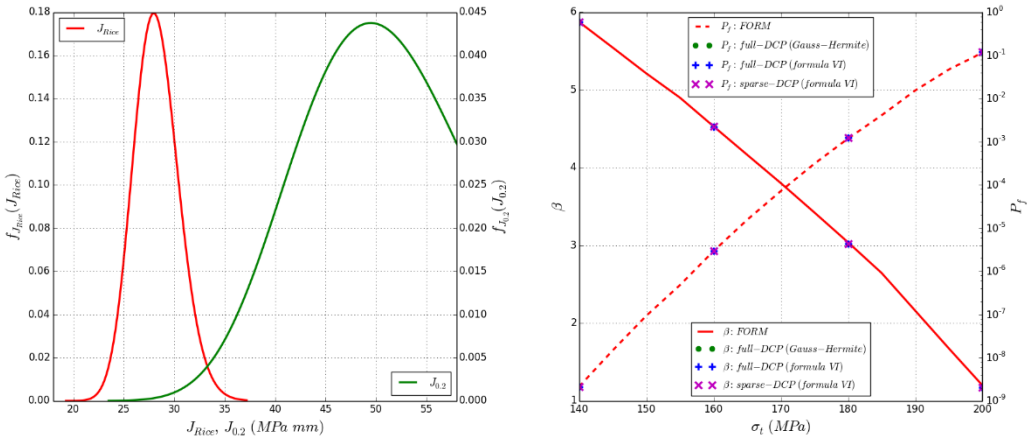

Figure III. 19. Nonlinear cracked pipe: Resistance-Loading reliability problem for $\sigma_t = 180\,MPa$ (left), comparison of the reliability analysis results given by the proposed methods and FORM (right)

Before closing discussion on this application example, an interesting, even obvious question that we should ask ourselves is: is there is any changes in the importance order of contributions of the uncertain parameters on the variability of the Rice's integral due to the increase of the axial tension σ_t? To find a clear response, let us plot the total Sobol sensitivity indices with respect to the magnitude of the axial tension when varying in the range $[140\,MPa, 200\,MPa]$ as depicted in figure III.20. As expected, the picture does not the same for all values of the axial tension, which has a physical meaning. Indeed, when the axial increases the constitutive material exhibits a high plastic behavior, especially in the vicinity of the crack, and thus whey the yield strength σ_y becomes the most contributor uncertain parameter on the variability of Rice's integral for the highest value of the axial tension, that is $\sigma_t = 200\,MPa$. However, no significant change in the contributions of the coefficient α and the strain hardening exponent n of the Ramberg-Osgood behavior law, which remain the uncertain parameters with the weakest effects.

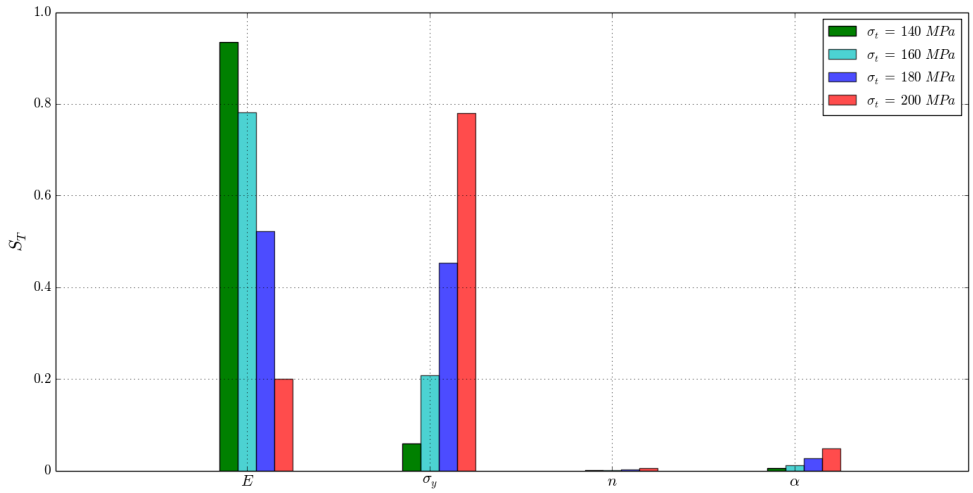

Figure III. 20. Nonlinear cracked pipe: evolution of the total Sobol indices with respect to the magnitude of the axial tension σ_t

3.2.5. Discussion

Through this example, we have demonstrated that the proposed approaches, named full-PCE and sparse-PCE, are able to carry out statistical moments, sensitivity, and reliability analysis at very low computational cost, since only 33 runs of the FEM are required to obtain a good accuracy on the corresponding quantities

of interest. Furthermore, the same set of evaluations of the FEM is used to address all three kinds of analysis, with no additional computational cost when changing from one kind of analysis to another, as observed in Chapter II when the crude cubature formulae I-VI are used to compute the multidimensional integrals representing the quantities of interest corresponding to the uncertainty propagation analysis to be conducted. In this case, the computational cost gain factor is equal to 3 (i.e., 33 evaluations of the FEM instead of 99 required by the crude cubature formula VI). In particular, the truncation scheme based on second moment information used to build up the polynomial chaos basis $\mathcal{H}^{p,q,\sigma^2}$ in the sparse-PCE approach, reduces the computational efforts when the unknown PCE coefficients are the solution of a least-square regression problem. Indeed, the sparsity compared to a full polynomial chaos basis $\mathcal{H}^{p}$ is about 33%, which means that about one-third of the components of the PCE-based metamodel have an insignificant effect on the model response, defined as the Rice's integral of the cracked pipe. Finally, the reliability analysis has shown that the proposed approaches are in overall good agreement with each other and with the estimates of the reliability indices and corresponding failure probabilities obtained by FORM, which was taken as the reference method. Since a closed-form representation is obtained for the PDF of the Rice's integral J_{Rice}, which fits a lognormal distribution, the failure probability is computed by solving a simple R-L reliability problem, which allows us to avoid handling integrals quantities and provides a suitable tool for engineering practices. Through parametric reliability analysis carried out in function of the axial tension σ_t, we have shown that the accuracy of the proposed approaches is weakly affected by the magnitude of the failure probability to be computed.

3.3. Spatially varying uncertainty in inclined edge-cracked plate

3.3.1. Problem statement

Consider the rectangular plate of height $2L = 2\,units$ and width $W = 1\,unit$ visualized in figure III.21. It is subjected to tensile load $\sigma = 1\,unit$ on its bottom and top edges and has an open inclined crack with dimensions $a = z = 0.5\,unit$. This problem has been first introduced by *(Long and al, 2016)* to perform a local sensitivity analysis on the fracture driving forces, using the stochastic scaled boundary finite element method. Later, this problem was addressed in *(Chahine and al, 2021)* to assess the reliability of the inclined cracked plate considering the two-dimensional spatial variability of the mechanical properties of the constitutive material.

Due to the orientation of the initial crack with respect to the applied load, this later naturally tends to propagate in a mixed fracture mode, instead of a simple opening fracture mode. Thus, a FEM is developed in the software *(cast3m, 2021)* to compute the fracture driving forces, namely the opening fracture mode SIF K_I, the in-plane shear fracture mode SIF K_{II} and the bifurcation angle θ. The finite element mesh, consisting of 976 6-node triangular elements and 2155 nodes, is extremely refined around the crack tip, as shown in figure III.21, to ensure good accuracy of the fracture driving forces estimates. However, a coarse mesh is used in vicinity of the outer plate edges, to reduce the number of Degrees Of Freedom

(DOF) in the overall finite element mesh, and therefore optimize the computational cost required by a single FEM run.

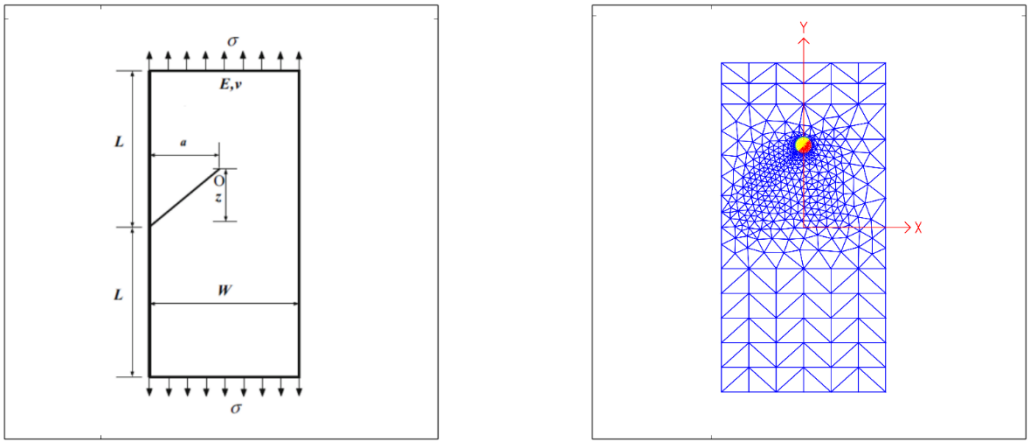

Figure III. 21. Inclined edge-cracked plate: geometry and applied loads (left), finite element mesh (left)

The Young's modulus $E(\boldsymbol{z},\omega)$ of the constitutive material of the cracked plate is considered as an uncertain parameter whose variability varies along both the horizontal and the vertical directions denoted by x and y, respectively, and gathered in the vector $\boldsymbol{z} = (x, y)$. It is modeled by a two-dimensional lognormal random field, with mean value $\mu_E = 20.7\,10^6\,units$ and standard deviation $\sigma_E = 2.07\,10^6\,units$, which can be defined simply as the exponential of a normal random field $v(\boldsymbol{z},\omega) = \mathrm{Ln}(E(\boldsymbol{z},\omega))$ with mean $\mu_v = \ln(\mu_E) - \frac{1}{2}\ln(1+\sigma_E^2/\mu_E^2)$ and standard deviation $\sigma_v = \sqrt{\ln(1+\sigma_E^2/\mu_E^2)}$:

$$E(\boldsymbol{z},\omega) = \exp[v(\boldsymbol{z},\omega)] = \exp[\mu_v + \sigma_v.u(\boldsymbol{z},\omega)] \qquad (III.40)$$

where ω is a parameter to underline the randomness of $E(\boldsymbol{z},\omega)$ and $u(\boldsymbol{z},\omega)$ is a standard normal random field of zero mean and unit standard deviation, governed by the following exponential autocorrelation function:

$$\rho(\boldsymbol{z}_1,\boldsymbol{z}_2) = \exp\left[-\left(\frac{|x_1-x_2|}{l_{cx}} + \frac{|y_1-y_2|}{l_{cy}}\right)\right] \qquad (III.41)$$

In the above equation, $\boldsymbol{z}_1 = (x_1, y_1)$ and $\boldsymbol{z}_2 = (x_2, y_2)$ are two points in the spatial domain representing the cracked plate, $l_{cx} = 0.5\,unit$ and $l_{cy} = 1.5\,units$ are the correlation lengths in the horizontal and the vertical directions, respectively, and $|.|$ denotes the absolute value.

The standard normal random field $u(\boldsymbol{z},\omega)$ is discretized using the Karhunen-Loève (KL) method *(Ghanem and Spanos, 1991)*, instead of the EOLE method used in section 5.2.2 of Chapter II. Indeed, as first shown by *(Li and Der Kiureghian, 1993)*, and later confirmed by *(Sudret and Der Kiureghian, 2000)* through a benchmark study, for a given truncation order M, the KL method is more accurate than the EOLE method in the case of an exponential autocorrelation function, since it provides the lowest variance error, especially within the variation domain Ω of the random field to be represented. However, special attention must be taken at the boundaries of Ω where the EOLE may exhibit more accurate results than the KL method. These facts are clearly illustrated in figure III.22, which shows a comparison of the variance error provided by the EOLE and KL methods of degree $M = 10$, used for the representation of a standard normal random field

governed by an exponential autocorrelation function with correlation length $l_c = 5$ in the one-dimensional domain $\Omega = [0, 10]$.

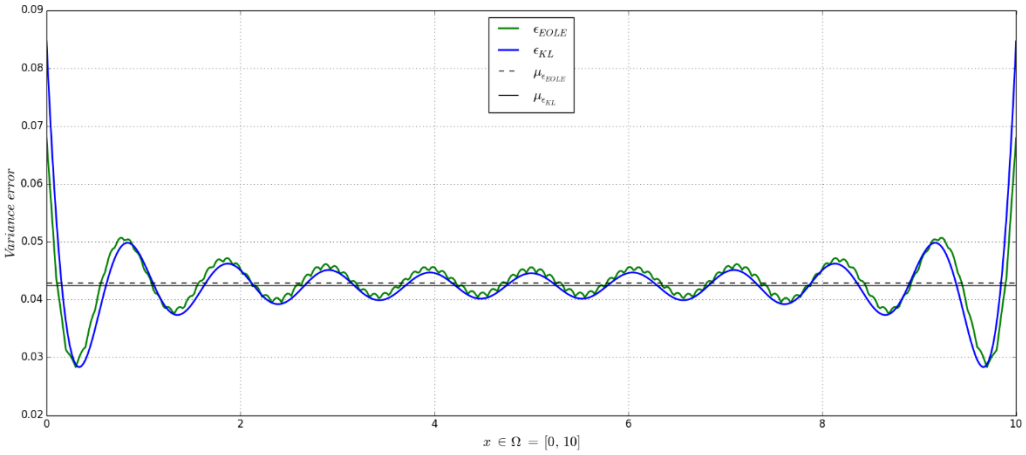

Figure III. 22. Inclined edge-cracked plate: comparison of the variance error provided by the EOLE and KL methods

Referring to the KL method, the M^{th} order approximation of the lognormal random field $E(\mathbf{z}, \omega)$ reads:

$$\hat{E}(\mathbf{z}, \omega) = \exp[\mu_v + \sigma_v . \sum_{i=1}^{M} \sqrt{\lambda_i}\, \varphi_i(\mathbf{z})\, u_i(\omega)] \qquad (III.42)$$

where $u_i(\omega), i \in \{1, \dots, M\}$ are independent standard normal variables, λ_i and $\varphi_i(\mathbf{z})$ are respectively eigenvalues and eigenfunctions obtained by solving the following Fredholm integral equation corresponding to the autocorrelation function $\rho(\mathbf{z}, \mathbf{z}')$:

$$\int_{\Omega} \rho(\mathbf{z}, \mathbf{z}')\, \varphi_i(\mathbf{z}') = \lambda_i\, \varphi_i(\mathbf{z}) \qquad (III.43)$$

Fortunately, for our problem where the two-dimensional spatial domain $\Omega = [-0.5, 0{,}5] \times [-1, 1]$ has a rectangular geometry and the random field $E(\mathbf{z}, \omega)$ follows an exponential autocorrelation function, the Fredholm integral equation can be solved analytically and a closed from solutions of the eigenvalues λ_i and the eigenfunctions $\varphi_i(\mathbf{z})$ can be obtained. Interested readers can find, detailed information about the mathematical derivation of these quantities in *(Ghanem and Spanos, 1991)*, and some advice about the practical implementation for one-dimensional and two-dimensional random fields in *(Sudret and Der Kiureghian, 2000)*.

In the following, a 24th order truncated KL expansion is used to model the spatial variability of the Young's modulus of the constitutive material of the cracked plate following a lognormal random field. This means that only the first 24 largest eigenvalues λ_i, already sorted in ascending order, and the corresponding eigenfunctions $\varphi_i(\mathbf{z})$ are retained in equation III.42. These KL terms account for 90% of the variability of the Young's modulus random field. Thus, the uncertainty propagation problem is recast as a function of 24 independent standard normal variables $u_i(\omega), i \in \{1, \dots, 24\}$. Hence, for a given realization of these random variables, a realization $\hat{E}(\mathbf{z}, \omega)$ of the random field representing the Young's modulus of the cracked plate is obtained from equation III.42. Figures III.23 shows a sample of 10 realizations of $\hat{E}(\mathbf{z}, \omega)$.

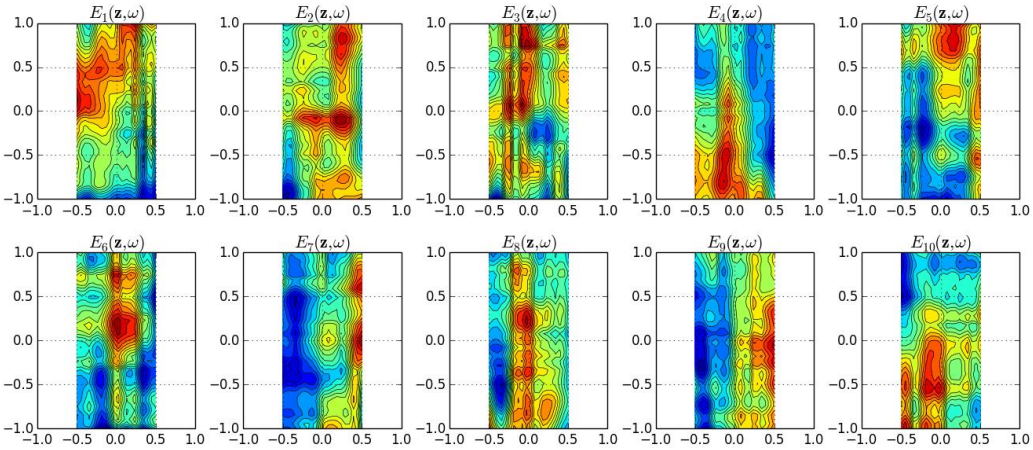

Figure III. 23. Inclined edge-cracked plate: example of 10 realizations of the Young's modulus field $E(\mathbf{z},\omega)$ with mean $\mu_E = 20.7\ 10^6\ units$ and standard deviation $\sigma_E = 2.07\ 10^6\ units$

Due to the spatial variability of the Young's modulus, the components of the displacement field induced by the load applied to the cracked plate are also spatially varying uncertain parameters that can be conveniently represented by random fields. Of interest are the horizontal and the vertical displacements given by the FEM at the 2155 nodes of the finite element mesh depicted in figure III.21. The corresponding random fields are denoted by $d_x(\mathbf{z},\omega)$ and $d_y(\mathbf{z},\omega)$, respectively. Figure III.24 shows 10 realizations of the random field of the equivalent displacement $d(\mathbf{z},\omega) = \sqrt{d_x^2(\mathbf{z},\omega) + d_y^2(\mathbf{z},\omega)}$, associated respectively with the realizations of the Young's modulus random field presented in figure III.23.

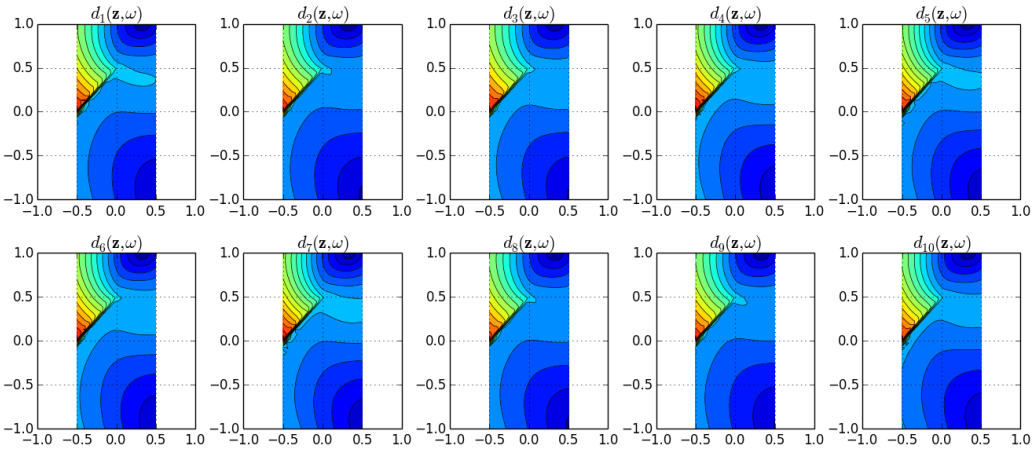

Figure III. 24. Inclined edge-cracked plate: example of 10 realizations of the equivalent displacement field $d(\mathbf{z},\omega)$

As can be seen, the equivalent displacement $d(\mathbf{z},\omega)$ is indeed a spatially varying quantity, which means that at each node of coordinate $\mathbf{z}_k = (x_k, y_k), k = 1,\dots,2155$ in the cracked plate, the variability of the corresponding equivalent displacement $d(\mathbf{z}_k,\omega)$ can be simply represented by a random variable where the related statistical characteristics are to be determined by statistical analysis on an available sample of realizations. Figure III.25 shows the spatial variation of the mean $\mu_d(\mathbf{z},\omega)$ and standard deviation $\sigma_d(\mathbf{z},\omega)$ of the equivalent displacement with respect to the coordinates $\mathbf{z}_k = (x_k, y_k), k = 1,\dots,2155$ of the nodes of the finite element mesh, computed based on 10^5 crude MCS. As can be observed, these statistical parameters $\mu_d(\mathbf{z},\omega)$ and $\sigma_d(\mathbf{z},\omega)$ are also random fields. The PDFs of the equivalent displacement recorded

at the nodes of coordinates $\boldsymbol{z}_1 = (0, 0.49)$ and $\boldsymbol{z}_2 = (-0.29, -0.05)$ are also plotted. The comparison with standard distributions shows that the lognormal distribution is the best candidate to fit both PDFs.

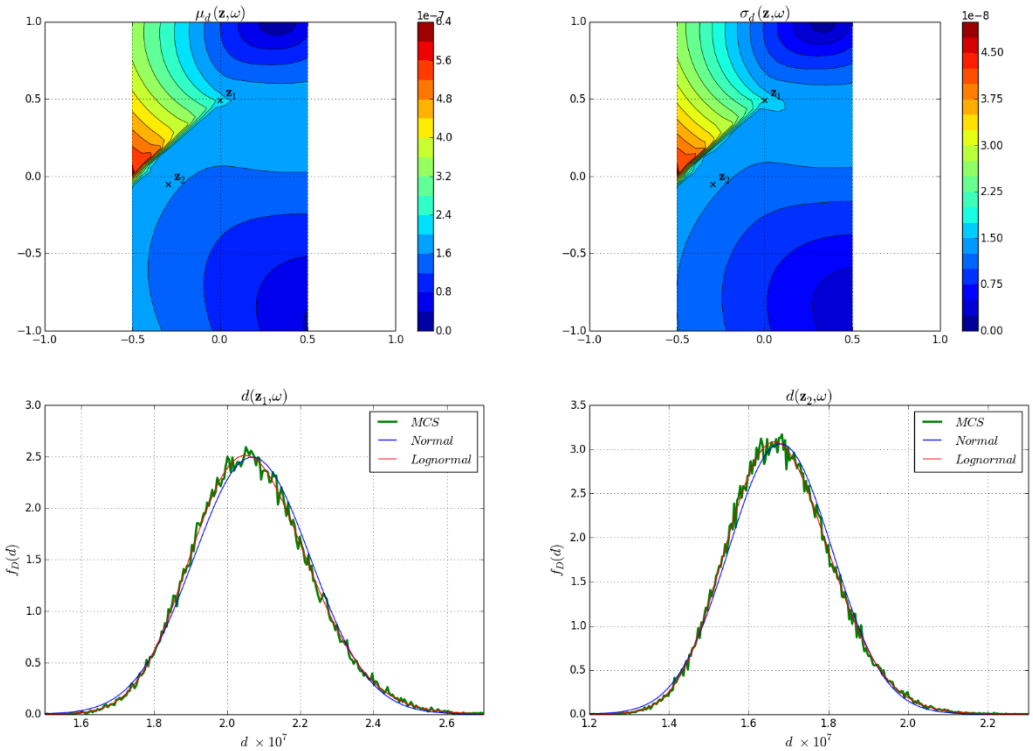

Figure III. 25. Inclined edge-cracked plate: equivalent displacement mean (upper left), standard deviation (upper right), PDF at node of coordinate $\boldsymbol{z}_1 = (0, 0.49)$ (lower left) and PDF at node of coordinate $\boldsymbol{z}_2 = (-0.29, -0.05)$ (lower right)

3.3.2. Statistical moments and distributions analysis

The fracture driving forces of interest are the opening fracture mode SIF K_I, the in-plane shear fracture mode SIF K_{II}, the bifurcation angle θ and the effective SIF K_{eff}, gathered in the model responses vector $y = \{K_I, K_{II}, \theta, K_{eff}\}^T$.

As a first step, a statistical moments and distribution analysis is performed to assess the effect of the spatial randomness of the Young's modulus on the variability of these fracture driving forces. The statistical moments of each model response are computed by the full-PCE and sparse-PCE approaches based on cubature formula II, which ensure a better efficiency than the other cubature formulae studied in Chapter II, especially for the present problem with relatively high probabilistic dimensionality. The results obtained for the first two first statistical moments, i.e., the mean and the standard deviation, with a PCE of degree $p = 2$, are listed in Table III.8 and compared to the estimates given by crude cubature formula II and 10^5 crude MCS. As can be seen, the results given by the all the proposed approaches are in complete agreement. The discrepancy with respect to the reference estimates given by 10^5 MCS is insignificant for all the mechanical responses of interest. It appears that the uncertainty on the Young's modulus, i.e., 10% deviation from its mean value, has a moderate effect on the variability of the crack driving forces, since the coefficients of variation corresponding to the opening fracture mode SIF K_I, the in-plane shear fracture mode SIF K_{II}, the bifurcation angle θ and the effective SIF K_{eff}, are equal to 2.75%, 3.97%, 1.55% and

2.93%, respectively. It is important to notice that the PCE-based metamodels corresponding to the four mechanical responses of interest, are built from the same set of 651 evaluations of the FEM. Thus, handling non-scalar random responses does not affect the efficiency of the full-PCE and sparse-PCE approaches in any way. The truncation of the polynomial chaos basis based on second moment information significantly reduces the computational effort devoted to solving the least-square regression problem used in the sparce-PCE approach to estimate the PCE coefficients. Indeed, only 25 of the 325 components of the full polynomial chaos basis $\mathcal{H}^p$ have significant contributions on the model responses. The corresponding *economy* index $\mathcal{E}^{p,q,\sigma^2} = 100 \times (\mathrm{card}(\mathcal{H}^p) - \mathrm{card}(\mathcal{H}^{p,q,\sigma^2})/\mathrm{card}(\mathcal{H}^p))$ is about 92%, which shows high sparsity in the truncated polynomial chaos basis $\mathcal{H}^{p,q,\sigma^2}$.

Table III. 8. Inclined edge-cracked plate: statistical moments of the crack driving forces K_I, K_{II}, θ and K_{eff}

	Statistical moments	Full-PCE	Sparse-PCE	Crude formula II	MCS
K_I	μ	2.8253	2.8253	2.8253	2.8255
	σ	0.0779	0.0781	0.0781	0.0778
K_{II}	μ	1.2061	1.2061	1.2061	1.2061
	σ	0.0460	0.0460	0.0460	0.0479
θ	μ	36.776	36.776	36.776	36.774
	σ	0.5570	0.5570	0.5570	0.5713
K_{eff}	μ	6.8846	6.8846	6.8846	6.8849
	σ	0.1992	0.1992	0.1992	0.2022
Number of FEM runs		651	651	651	10^5

Let us now turn our attention to the respective distributions of the mechanical responses. The PDFs of the four crack driving forces are built by a moment-based technique using only the statistical moments estimates given by the full-PCE approach in order to avoid redundancy, since as stated previously, a small discrepancy is observed between the results given by the full-PCE and the sparse-PCE approaches.

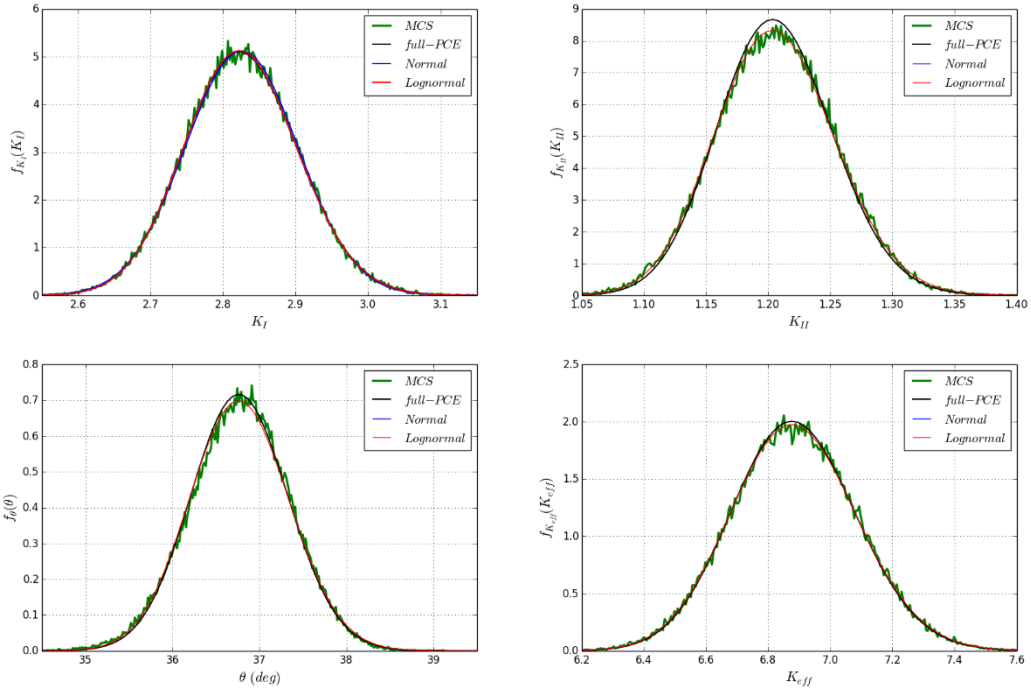

Figure III. 26. Inclined edge-cracked plate: comparison of the PDFs of the crack driving forces K_I, K_{II}, θ and K_{eff}

As can be observed in figure III.26 the obtained PDFs are in good agreement with those of the reference constructed from 10^5 crude MCS. Furthermore, it appears that the lognormal distribution is the best candidate for fitting the PDFs of the four crack driving forces of interest. This finding is of great interest since closed-form solutions are now available for the PDFs, which are more appropriate for designers. In addition, as demonstrated in previous application example, having an analytical representation of the PDFs avoids the evaluation of multidimensional integrals, since the estimation of the failure probability can be performed by solving a simple R-L reliability problem.

3.3.3. Sensitivity analysis

Next, a sensitivity analysis is conducted to assess the contribution of the uncertain parameters $u_i(\omega), i \in \{1, \dots, 24\}$, resulting from the representation of the random field $E(\mathbf{z}, \omega)$ by a 24$^{\text{th}}$ order KL expansion, on the variability of the effective SIF K_{eff}. It is important to remind that this effective crack driving force, which is derived from the opening fracture mode SIF K_I, the in-plane shear fracture mode SIF K_{II} and the bifurcation angle θ, can be considered from a physical point of view as an opening fracture mode SIF in the direction along the bifurcation angle θ. This parameter is of a great importance when dealing with mixed-mode fracture problems since it is used in the computation of the fatigue crack growth life instead of K_I and K_{II}. Moreover, when a reliability analysis is to be performed with respect to a serviceability criterion function of the fracture toughness of the constitutive material, the effective SIF K_{eff} should also be used.

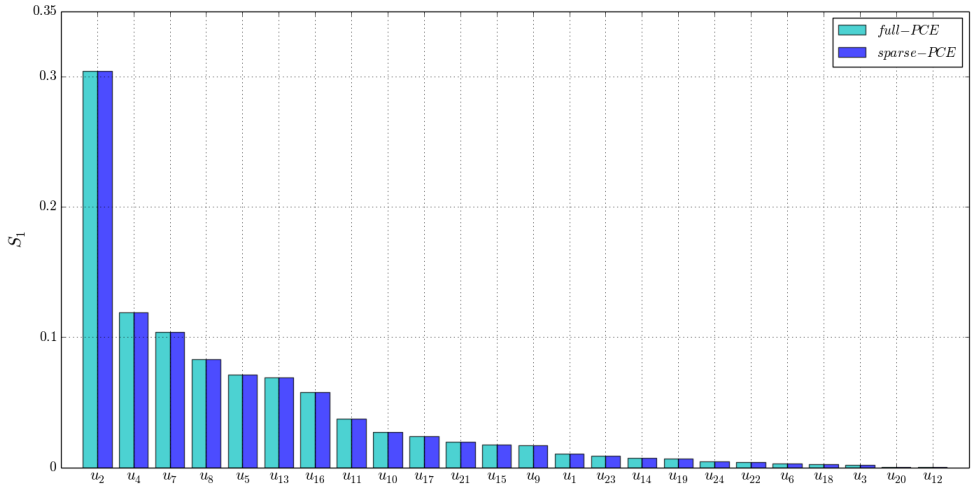

Figure III. 27. Inclined edge-cracked plate: comparison of the estimates of the first-order Sobol indices

Due to the high probabilistic dimension of the problem, the evaluation of Sobol indices by MCS or crude cubature formula II is impractical. Therefore, the following sensitivity analysis relies only on the full-PCE and sparse-PCE approaches. Figure III.27 compares the estimates of the first-order Sobol indices obtained by post-processing the PCE coefficients of the metamodels given by the full-PCE and sparse-PCE approaches. As can be seen, the first-order sensitivity indices given by both the full-PCE and sparse-PCE approaches are practically identical. This fact can be considered as an indicator of convergence for the obtained estimates and they can therefore represent the reference solution. A very fast decay of the main

effect of the uncertain parameters is observed. Moreover, the uncertain parameter $u_2(\omega)$, corresponding to 2nd eigenmode of the KL expansion, is by far the most significant effect among all the uncertain parameters, whereas $u_{20}(\omega)$ and $u_{12}(\omega)$ have almost no effect on the variability of the effective SIF K_{eff}. In figure III.28 are depicted the total Sobol indices. As previously stated for the first-order indices, the estimates provided by the full-PCE and sparse-PCE approach are quite similar. We observe that the order of importance of the uncertain parameters is the same as for the first-order indices. The sum of the total indices $\sum_{i=1}^{24} S_{Ti}$ is approximately equal to 1, which means that the interactions between the uncertain parameters have weak effects on the model response of interest. Indeed, if we compare the total indices with the respective first-order ones, it appears that the differences are negligible, again demonstrating the insignificance of the contributions of the interaction effects. As pointed out in Figure III.28, a very fast decay of the importance of the uncertain parameters is observed, with the 10 first uncertain parameters $u_i(\omega), i \in \{2, 4, 7, 8, 5, 13, 16, 11, 10, 17\}$ explaining roughly 90% of the total variance of the effective SIF K_{eff}. This demonstrates a moderate effective probabilistic dimensionality of the mechanical response of interest despite the large nominal probabilistic dimension, 24, corresponding to the number of eigenmodes required by the KL expansion to accurately represent the spatially varying uncertainty in the Young's modulus of the constitutive material of the cracked plate. Although we do not have a true reference solution for the Sobol sensitivity indices, the obtained estimates are in good agreement with the results of the local sensitivity analysis conducted by *(Long and al, 2016)*, since it has been shown that the uncertain parameters $u_2(\omega)$ and $u_4(\omega)$, corresponding to the 2nd and 4th eigenmodes of the KL expansion, respectively, are the most important on the variability of the SIFs of K_I and K_{II}. Indeed, the local sensitivity indices obtained by the central difference method with respect to the uncertain parameters $u_2(\omega)$ and $u_4(\omega)$, are respectively $\partial K_I/\partial u_2 = -0.0292$ and $\partial K_I/\partial u_4 = 0.0270$ for the opening fracture mode SIF K_I, and $\partial K_{II}/\partial u_2 = -0.0254$ and $\partial K_{II}/\partial u_4 = 0.0105$ for the in-plane shear fracture mode SIF K_{II}.

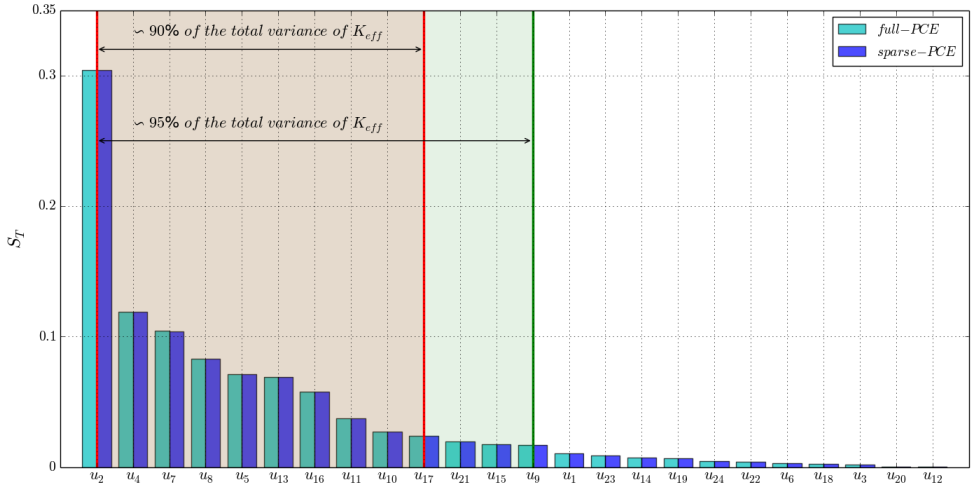

Figure III. 28. Inclined edge-cracked plate: comparison of the estimates of the total Sobol indices

It is important to notice that the sensitivity analysis conducted here did not require any additional runs of the FEM, since the Sobol sensitivity indices are derived from the coefficients of the metamodels already built in the statistical moments and distribution analysis conducted earlier.

3.3.4. Discussion

We clearly demonstrate the efficiency of the full-PCE and sparse-PCE approaches for conducting different types of uncertainty propagation analysis through a computationally demanding implicit mechanical model. Indeed, assuming that the crude cubature formula II is used to conduct the same sensitivity analysis, we would have to perform at least 651 evaluations of the FEM to obtain the estimates the Sobol sensitivity indices, in addition to the 651 evaluations already required by the statistical moments analysis. Thus, both proposed approaches reduce the computational effort by at least a factor of two, and possibly a factor of three if a reliability analysis is carried out later. It is worth noting that the computational cost required by the sparse-PCE approach is due to the derivation of second moment information needed to build the sparse chaos polynomial basis, rather than the estimation of the PCE coefficients. If prior second moment information are already available, the computational cost gain should be more noticeable. As demonstrated previously, the effective probabilistic dimension, defined as the number of eigenmodes required in the KL expansion to explain a given percentile of the total variance of the model response of interest, is lower than the nominal probabilistic dimension. For instance, the first 10 and 15 eigenmodes explain 90% and 95% of the total variance of the effective SIF K_{eff}, respectively. Consequently, many components of the full polynomial chaos basis should vanish, since they have zeros sensitivity indices, implying fewer PCE coefficients to be computed and a better sparsity of the polynomial chaos basis.

4. Conclusion

Response surface methods rely on the construction of suitable approximations, called metamodels, of the uncertain responses of an implicit mechanical model. In this chapter, we have focused on the well-known PCE method which provides metamodels obtained by expanding the model responses of interest on a multivariate orthonormal polynomial basis. The mathematical formalism related to the construction of the PCE method is recalled. The standard random space has been preferred for the construction of PCE-based metamodels to provide a generalized representation capable of handling statistically independent, as well as dependent, uncertain parameters. The computation of the unknown coefficients of the PCE-based metamodels, can be performed either by projection or regression techniques. For high-dimensional uncertainty propagation problems, it has been shown that the projection technique can lead to high computational cost, when classical integration schemes, such as the Gauss-Hermite full tensor-product scheme, are used to evaluate the multidimensional integrals involved in the computation of the PCE coefficients. The regression technique is also inefficient in such a situation, especially when a full polynomial chaos basis is used to build up the metamodels. Two alternative approaches have been developed to circumvent this inefficiency.

The first approach, called full-PCE, is derived from projection techniques, where the efficient cubature formulae I-VI studied in Chapter II are used instead of the classical integration schemes to compute the PCE coefficients. It has been shown that these fifth-degree cubature formulae require a limited number of evaluations of the integrand of the multidimensional integrals representing the PCE coefficients. Unlike the

Gauss-Hermite full tensor-product integration scheme, their efficiency is less affected by the degree of the polynomial chaos basis chosen to construct the PCE-based metamodels. The second approach, called sparce-PCE, is derived from regression techniques, where an efficient truncation scheme uses prior available second statistical moment information to identify the most important components of the polynomial chaos basis on the model responses of interest. In this way, the PCE coefficients corresponding to the components with weak effects are discarded, and the computational efforts devoted to solving the regression problem is significantly reduced. In this context, an economy index has been introduced in the form of a ratio between the respective cardinalities of the sparse and the full chaos polynomial basis, which allows us to objectively assess the computational cost saving obtained by the proposed truncation scheme based on the second moment information. Regardless of the use of the full PCE approach or the sparse PCE approach, two methods have been proposed to carry out the uncertainty propagation analysis, either by post-processing the PCE coefficients or by performing MCS on the obtained PCE-based metamodels.

The accuracy and efficiency of the so-called full-PCE and sparse-PCE approaches have been carefully investigated in this chapter through three mechanical problems dealing with fatigue fracture. These three application examples have validated the ability of the proposed approaches to perform different types of uncertainty propagation analysis through time-consuming implicit mechanical models with high probabilistic dimensionality. Through the first example dealing with crack growth in CCP specimen that involves correlated uncertain parameters, it has been shown that the full-PCE approach is able to efficiently conduct statistical moments and sensitivity analysis, since the number of FEM runs required to achieve the target accuracy on the estimates of the quantities of interest, varies between 14 to 21, depending on the cubature formula used in the computation of the PCE coefficients. It appears that the accuracy of the statistical moments estimates obtained by MCS on the PCE-based metamodel of the fatigue crack growth life is slightly better than that given by the post-processing of the PCE coefficients, especially for skewness and kurtosis. It has been pointed out that we should be very careful when choosing the probabilistic model used to model the variability of the uncertain parameters. Indeed, as it has been shown, the omission of the statistical dependence between the parameters of the fatigue crack growth Walker law, induces erroneous results in the uncertainty propagation analysis, since in such a case the coefficient of variation of the fatigue crack growth life is equal 21.5%, while it should be about 3.14%.

The second example involves a greedy computational time mechanical model, since an incremental FEA is required to assess the Rice's integral used as the fracture driving force when dealing with ductile fracture problems. In this application, it has been shown that both the full-PCE and sparse-PCE approaches can perform statistical moments and distributions, sensitivity, and reliability analysis with a high efficiency. Unlike the crude cubature formulae studied in Chapter II, where additional evaluations of the primary implicit mechanical model are required each time, one switches from one type of uncertainty propagation analysis to another, the two proposed approaches allow all three types of uncertainty propagation analysis to be addressed at the same time based on the same set of evaluations of the FEM needed to compute the Rice's integral. It is found from the statistical moments analysis that the proposed approaches give more

accurate estimates of the statistical moments than crude cubature formula VI, since the maximum relative error with respect to the reference solutions given by 10^5 crude MCS, does not exceed 3.7%. This high accuracy allows the PDF of the mechanical response to be constructed directly using a simple moment-based technique. It has been shown that the full-PCE and the sparse-PCE approaches based on the cubature formula VI require the same computational cost, i.e., 33 FEM runs, and more efficient than the classical PCE approach based on the Gauss-Hermite full product-tensor integration scheme, which requires 81 FEM evaluations. Compared to the crude cubature formula VI, a noticeable lower bound computational gain factor of 3 is obtained. Moreover, the use of prior second moment information reduced the computational effort spent on solving the least-square problem when the sparse-PCE approach is used. Indeed, it appears that only 10 of the 15 components of a full polynomial chaos basis have a significant effect on the model response, resulting in an economy of 33% on the computation of the PCE coefficients by regression. Through the sensitivity analysis, it has been shown that interactions between the uncertain parameters have an insignificant effect on the variability of the Rice's integral, since the total Sobol indices have the same values as the respective first-order indices. In addition, physically meaningful sensitivity indices have been obtained. For low values of the axial tension applied to the cracked pipe, the Young's modulus appears to be the most important uncertain parameter for the variability of the Rice's integral. However, for high values of the axial tension, where the fracture of the constitutive material goes with important plastic strains in vicinity of the crack tip, the yield strength becomes the most significant uncertain parameter. It can be retained that the coefficient α and the strain hardening exponent n of the Ramberg-Osgood behavior law have a weak contribution on the variability of the Rice's integral. Therefore, they can be considered as deterministic parameters and set of their respective mean values, thus reducing the probabilistic dimension of the problem. Since accurate PDFs are available for the Rice's integral and the lognormal distribution is in good agreement with them, we have been able to estimate the failure probability by solving a simple R-L reliability problem. Through a parametric study as a function of the axial tension applied to the cracked pipe, it has been shown that the proposed approaches give an accurate estimate of the reliability index since the relative error with respect to the estimates given by FORM is less than 2%.

Example 3 has a high probabilistic dimensionality since a 24^{th} order KL representation is used to model the spatial randomness of the Young's modulus of a plate containing an inclined crack. It has been shown that the full-PCE and sparse-PCE approaches are capable of efficiently conducting different kinds of uncertainty propagation analysis through a mechanical model with high probabilistic dimension. It appears that considering vector-valued model responses does not affect the efficiency of the proposed approaches. From the statistical and distributional analysis, it can be retained that the spatial variability of Young's modulus has a moderate effect on the variability of the crack driving forces of interest since the corresponding coefficients of variation vary in the range [1.55%, 3.97%]. In addition, it has been observed that the lognormal distribution fits the PDFs of all the four crack driving forces very well. Through the sensitivity analysis, it has been shown that the uncertain parameters related to the eigenmodes of the KL expansion act separately on the variability of the effective SIF K_{eff}, since the contributions of the interaction effects is small compared to those of the main effects. It appears that the effective probabilistic dimension is low

compared to the nominal one, which allows us to discard the PCE coefficients that have an insignificant effect on the model responses, and thus improves the efficiency of the proposed approaches.

The various analysis carried out in this chapter have allowed us to demonstrate the good accuracy and efficiency of the two proposed approaches, called full-PCE and sparse-PCE. By using the well-established polynomial chaos expansion method, analytical representations, often called metamodels in the literature of uncertainty propagation analysis, have been built for a scalar as well as for a vector-valued model responses, initially provided by a time consuming implicit mechanical model. Thus, it is no longer necessary to run additional cycles of the primary implicit mechanical model when one wishes to switch from one type of uncertainty propagation analysis to another, as was the case when using crude cubature formulae, I-VI. Clearly, we find in this chapter a consistent response to the question asked earlier at the end of Chapter II.

Conclusion

The work we have done in this thesis was intended to develop *unified* approaches able to perform efficiently the three possible kinds of uncertainty propagation analysis, i.e., statistical moments and distributions, sensitivity, and reliability analysis, through a greedy computational time mechanical models. A particular interest was given to fatigue fracture problems. The challenge was to merge different well-established mathematical methods to propose robust probabilistic computational strategies whose efficiency is less affected by the probabilistic dimension and the complexity (i.e., the order of the statistical moment, the order of the sensitivity index and the magnitude of the failure probability) of the quantities of interest corresponding to the uncertainty propagation analysis to be performed. This purpose seems to be achieved through the development carried out in Chapters II and III, where good results are obtained for a large panel of application examples.

After a reminder of the general framework of mechanical fatigue and particularly of the fatigue crack growth phenomenon, several existing probabilistic models allowing the evaluation of the effect of uncertainties on fracture driving forces were reviewed. Two main categories of probabilistic models were distinguished. The models belonging to the first category are based on Markov chains theory to take into account the sources of uncertainty in the fatigue crack growth process. These purely statistical models, as considered in the literature, have been criticized for their inconsistency with the physics of the fatigue crack growth phenomenon, although they can handle mixed-mode fracture problems. The second category contains models that are more consistent with the physics, obtained by randomizing traditional deterministic crack growth laws, such as the well-known Paris-Erdogan law, by introducing random variables or processes. Most of these probabilistic models suffer from inefficiency when the fracture driving forces of interest (i.e., stress intensity factors, fatigue lifetime…) are derived from time-consuming mechanical models. This inefficiency is even more visible when the probabilistic dimensionality is high. Moreover, only scalar-type variabilities are treated by these models. The spatial randomness of the material properties, which requires the use of advanced probabilistic models called random fields, which most lead to a significant increase of the probabilistic dimensionality, is omitted in the probabilistic studies of fatigue fracture. This is why three original approaches to uncertainty propagation were developed in this work.

The first approach developed in Chapter II uses six distinct cubature formulae, taken from an broad literature review, to compute multidimensional integrals representing the quantities of interest related to type of uncertainty propagation analysis to be performed. As with the well-known MCS, these cubature formulae approximate a multidimensional integral by one summand of integrand evaluations over a set of smartly sampled integration points in the standard random space. Thus, the

computational cost savings are significant compared to full tensor-product integration schemes where one summand in each direction of the random space is required to compute a multidimensional integral. After taking a general look at the principle of propagation through models representing physical phenomena at the beginning of Chapter II, the mathematical formulations of the quantities of interest, i.e., the first four statistical moments, the sensitivity indices and the failure probability, were established. It was shown that a common issue is the handling of multidimensional integrals. Through a benchmark study conducted on various application examples ranging from a simple mathematical equation to an implicit model requiring computation time and involving spatially varying uncertain parameters, we have demonstrated that with the exception of cubature formula IV where the computational cost grows exponentially with the probabilistic dimension, all remaining cubature formulae are able to perform efficiently any kind of uncertainty propagation analysis. For high probabilistic dimensions, it appears that cubature formula II provides the best balance between efficiency and accuracy. It has been shown that problems involving a higher heterogonous mixture of random variables should be handled with great care, since a loss of accuracy was observed on the results given by some cubature formulae. Despite the various advantages offered by cubature formulae I-VI over classical integration schemes, the associated computational cost can explode for high probabilistic dimensions, especially when one wishes to switch from one kind of uncertainty propagation analysis to another. Indeed, additional evaluations of the primary mechanical model are required, since the multidimensional integrals representing the quantities of interest corresponding to statistical moments, sensitivity or reliability analysis involve different integrands.

Remedies to overcome the problem of inefficiency of the crude cubature formulae I-VI, i.e., when applied directly to the primary mechanical model, were proposed in Chapter III. Two approaches, called full-PCE and sparse-PCE, were devised based on the well-known chaos polynomial expansion. The key ingredient was to build approximations, called metamodels, by projecting the responses of interest of the model onto a suitable multivariate orthonormal polynomial basis. Once these metamodels are obtained any type of uncertainty propagation analysis can be addressed, either by performing MCS or by post-processing the PCE coefficients. The standard random space was preferred to build the PCE-based metamodels, on the one hand to take advantage of the suitable mathematical properties of the Hermite polynomial basis that simplify the derivation of some quantities of interest such as the statistical moments, on the other hand to obtain a generalized representation of the metamodels able to consider uncorrelated as well as correlated uncertain parameters. In the full-PCE approach, a full polynomial chaos basis was used to construct the metamodels where the PCE coefficients were computed by projection based on the efficient cubature formulae I-VI. It appears that the computational effort devoted to PCE coefficients estimation is less affected by the

probabilistic dimensionality and the polynomial degree chosen to build the metamodels, in contrast to the Gauss-Hermite full tensor-product integration scheme where the number of the mechanical model evaluations grows exponentially in such a situation. In the sparse-PCE approach, an incomplete polynomial chaos basis is used to build the metamodels, where the PCE coefficients were obtained by solving a least-square regression problem. The sparse polynomial chaos basis was obtained by an original truncation scheme based on prior available second moment information, where the important components are automatically identifier if significant change is observed on the variance of the model responses of interest. The Full-PCE and sparse-PCE approaches were applied to three typical fatigue fracture problems. The first one deals with crack growth in a CCP specimen where the considered uncertain parameters are statistically dependent. The second example deals with the ductile fracture of a cracked pipe where the mechanical response of interest represents the Rice's integral available through an incremental FEA requiring a high computational cost demanding . The third problem, with a high probabilistic dimension, is additionally interested in the effect of the spatial variability of the Young's modulus on the mixed-mode fracture driving forces. Both approaches were found to be efficient in deriving, based on the same set of evaluations of the primary implicit mechanical model, statistical moments and distributions, sensitivity indices and failure probabilities of failure. Indeed, accurate estimates of all these quantities are obtained using only 651 FEM runs for the problem with the highest probabilistic dimensionality, which is equal to 24. It was pointed out that the accuracy of higher order statistical moments, such as the skewness and the kurtosis, was better when the estimates were obtained by performing MCS on the metamodels rather than by post-processing the PCE coefficients. Due to the high accuracy of the obtained mechanical responses PDFs, it was shown that the failure probability can be computed by solving a simple R-L reliability problem, instead of computing a multidimensional integral. Furthermore, the accuracy of the estimates, which are in good agreement with those provided by the first order reliability method, is less affected by the magnitude of the target failure probability. Although, both proposed approaches require the same number of mechanical model evaluations, the sparse-PCE reduces the computational effort devoted to the post-processing of the PCE coefficients. It appeared that the higher is the sparsity of the polynomial chaos basis, which was measured by introducing a sparsity index called economy, the lower the computational cost. Furthermore, it was shown that a major part of the computational cost of the sparse-PCE approach is due to the computation of the variance of the model response of interest required by the truncation scheme used to identify the important components of the polynomial chaos basis. Thus, if prior information on the variance is available, the sparse-PCE approach should be noticeably more efficient than the full-PCE approach. In the first application example, the importance of choosing the right probabilistic model to represent the true variability of the uncertain parameters was emphasized. Omitting the correlation between the parameters of the fatigue crack growth law,

which is a bad practice yet often observed in probabilistic studies, leads to erroneous results since the variability of the fatigue crack growth lifetime is abnormally high compared to the real situation where these parameters are naturally correlated. In the second application example, sensitivity analysis provided physically meaningful results. It was shown that the relative contributions of the uncertain parameters depend on the magnitude of the plastic strains surrounding the crack tip. When the axial tension applied to the cracked pipe is at its nominal magnitude, the plastic strains are confined in the crack tip, resulting in brittle fracture, and it was shown that the Young's modulus had the largest contribution on the variability of the Rice's integral. For accidentally high magnitudes of the axial tension, it was observed that the yield strength was the most significant uncertain parameter since the constitutive material exhibits a high plastic behavior. Statistical moments and distributions analysis performed in the third application example showed a moderate effect of the spatial randomness of the Young's modulus on the variability of the mixed-mode fracture driving forces. It was noticed that the effective probabilistic dimension is small compared to the nominal one. Referring to the total Sobol indices, only 10 out of 24 random variables, corresponding to the 10 most important eigenmodes of the KL expansion, explain 90% of the total variance of the effective SIF. Finally, it was shown that the full-PCE and sparse-PCE remain efficient even when vector-valued model responses were considered.

The three approaches that have been developed, namely crude cubature formulae, full-PCE and sparse-PCE, fulfill the objectives that motivated this thesis. In addition to the interesting results obtained either concerning the computational enhancement of the uncertainty propagation approaches or the understanding of the close relationship between uncertainties and fatigue fracture, the undertaken work allowed us to identify various tracks to further improvements at different levels.

The first level concerns the enhancement of deterministic mechanical models by integrating complex physical phenomena observed during the fatigue crack growth to provide more realistic crack driving forces. One such phenomenon is the crack retardation due to overloads, which can occur either accidently during constant amplitude loading or naturally during variable amplitude loading. It is well-known that a single overload induces a decrease of the crack growth rate, leading to an increase of the fatigue lifetime. Such a free increase of the fatigue lifetime is of great interest to managers of mechanical components and civil engineering structures as it can be a way to optimize the maintenance operations and, consequently, reduce the overall cost spent during the service life. Many well-established models are available in the literature to consider the retardation due to overloads based on plasticity theory. The key ingredient consists in weighting the classical crack growth laws by a correction function whose parameters are derived from experimental data. These retardation models can be straightforwardly integrated into explicit or implicit mechanical models. The efficiency

of the overloads, which can be measured by the induced increase in fatigue lifetime, depends on many parameters such as their amplitudes, the time interval between them as well as their periodicity. Thus, it seems very interesting to investigate if there is an optimal combination of these parameters to maximize the increase of fatigue lifetime.

The second level concerns the improvement of the efficiency of the proposed uncertainty propagation approaches to deal with problems with higher probabilistic dimensionality. A first track for such an improvement is to use more efficient cubature formulae. In Chapter II of the thesis, it has been shown that cubature formula V is a very promising candidate. The issue is to find a straightforward way to build orthogonal arrays for high dimensions. In this context, it will be relevant to investigate the well-established mathematical tools called Galois fields which are extensively used in information coding and computers cryptography. As shown in the third application example, the effective probabilistic dimension is much smaller than the nominal dimension for problems with random fields. Thus, finding a way to compute the effective probabilistic dimension before performing the uncertainty propagation analysis should mitigate the effect of the probabilistic dimension on the computational cost. For this purpose, screening approaches, such as the Morris method, which is very efficient since the corresponding sensitivity indices can be computed either for separated or gathered uncertain parameters, may be used. Finally, the investigation of suitable metamodeling techniques, including High Dimensional Model Representation (HDMR) will be of great interest.

References

(Ahmadzadeh and al, 2019) *G. Ahmadzaded and A. Varvani-Farahani, Energy-based damage descriptions to assess fatigue life of steel samples undergoing various multiaxial loading spectra, Int J Damage Mech, 28, pp. 35-57, 2019.*

(Ai and al, 2019) *Y. Ai, S.P. Zhu, D. Liao, J.A.F.O. Correia, C. Souto, A.M.P. De Jesus, B. Keshtegar, Probabilistic modeling of fatigue life distribution and size effect of components with random defects, Int. J. Fatigue 126, pp; 165 -173, 2019.*

(Alabd Alhafez, 2018) *I. Alabd Alhafez, C. J. Ruestes, H. M. Urbassek,Size of the Plastic Zone Produced by Nanoscratching , Tribol Lett 66, 2018.*

(Baldeweck, 1999) *H. Baldeweck. Méthodes des éléments finis stochastiques – Application à la géotechnique et à la mécanique de la rupture. Thèse de doctorat, Université d'Evry-Val d'Essonne, France, 1999.*

(Basquin, 1910) *O.H. Basquin, The exponential law of endurance tests. In: Proceedings of the American Society for Testing and Materials. 625-623, 1910.*

(Bathias and al, 1997) *C. Bathias, J. Bailon, La fatigue des matériaux et des structures, édition revue et argumentée. Éditions HERMES, Paris, 1997.*

(Bea and al, 1999) *J.A. Bea, M. Doblaré, L. Gracia, Evaluation of the probability distribution of crack propagation life in metal fatigue by means of probabilistic finite element method and B models. Engng Fract Mech; 63 6:675-711, 1999.*

(Beden and al, 2009) *S. Beden, S. Abdullah, A.K. Ariffin, Review of Fatigue Crack Propagation Models for Metallic Components. European Journal of Scientific Research, vol. 28, no 3, 2009.*

(Bernardo, 2015) *Performance of cubature formulae in probabilistic model analysis and optimization, J. Comput. Appl. Math., 280 110-124, 2015.*

(Berveiller, 2005) *M. Berveiller, Eléments finis stochastiques : approches intrusive et non intrusive pour des analyses de fiabilité, Ph. D. thesis, Université Blaise Pascal, Clermont-Ferrand, 2005.*

(Blatman, 2009) *G. Blatman, Adaptive sparse polynomial chaos expansions for uncertainty propagation and sensitivity analysis. Ph. D. thesis, Université Blaise Pascal - Clermont II, 2009.*

(Blatman and Sudret, 2011) *G. Blatman, B. Sudret, Adaptive sparse polynomial chaos expansions based on least angle regression. J Comput Phys, 230 (6), 2345–67, 2011.*

(Bogdanoff and al, 1985) *J.L. Bogdanoff, F. Kozin, Probabilistic models of cumulative damage. New York: Wiley, 1985.*

(Breitung, 1984) *K. Breitung, Asymptotic approximation for multinormal integrals, J. Eng. Mech, ASCE. 110, (3), 357-366, 1984.*

(Brezin and Zhidkov, 1965) *I. Berezin, N. Zhidkov, Computing Methods. Addison-Wesley, Reading, MA, 1965.*

(Bush and al, 1988) *M.L. Bush, J.L. Lebrun, X-Ray diffraction study of stress distributions following a single overload, Fatigue Crack under variable amplitude loading, Edited by J. Petit, D.L. Davidson, S. Suresh, P. Rabbe, Elsevier Applied Science, pp. 76-86, 1988.*

(Casciati and al, 2007) *F. Casciati, P. Colombi, L. Faravelli, Inherent variability of an experimental crack growth curve. Struct Saf, 29:66-76, 2007.*

(Cast3m, 2021) *Castem. http://www-cast3m.cea.fr, 2021.*

(Castillo and al, 2008) *E. Castillo, A. Fernandez-Canteli, H. Pinto, M.L. Ruiz-Ripoll, A statistical model for crack growth based on tension and compression Wöhler fields. Engng Fract Mech, 75:4439- 4449, 2008.*

(Castillo and al, 2005) *E. Castillo, A. Iglesias, R. Ruiz-Cobo, Functional equations in applied sciences Mathematical in Science Engineering, vol 199, Amesterdam: Elsevier B.V, 2005.*

(Chahine and al, 2021) *S. Chahine, H. Riahi, D. Bigaud. Propagation d'incertitudes par combinaison de chaos polynômial creux et quadrature efficace: application à la fissuration par fatigue. JFMS 2020, 11ème Journées Fiabilité des Matériaux et des Structures, Clermont-Ferrand, France, Mar 2020.*

(Chambers and al, 1991) *A. Chambers, T.Hyde, Mixed mode fatigue crack growth at 550 degrees c under plane stress conditions in jethete m152. Engineering Fracture Mechanics, 39(3), 1991.*

(Chang and al, 2006) *J. Chang, JQ. Xu, J. Mutoh, A general mixed-mode brittle fracture criterion for cracked materials. Engng Fract Mech. 73, 1249-1263, 2006.*

(Chastaing and al., 2012) *Chastaing, G., F. Gamboa, and C. Prieur, Generalized Hoeffding-Sobol decomposition for dependent variables - application to sensitivity analysis. Technical Report hal-00649404, GdR MASCOT-NUM (Méthodes d'Analyse Stochastique des Codes et Traitements Numériques), 2012.*

(Chiquet and al, 2009) *J. Chiquet, N. Limnios, M. Eid, Piecewise deterministic Markov processes applied to fatigue crack growth modelling. Journal of Statistical Planning and Inference; 139(5):1657 – 1667, 2009.*

(Choi and al, 2012) *S.K. Choi, R.V. Grandhi, R.A. Canfield, C.L. Pettit Polynomial chaos expansion with latin hypercube sampling for estimating response variability. AIAA J, 42 (6), 1191–8, 2012.*

(Ciavarella and al, 2018) *M. Ciavarella and A. Papangelo, On the distribution and scatter of fatigue lives obtained by integration of crack growth curves: Does initial crack size distribution matter?, Eng Fract Mech, 191, pp.111 - 124, 2018.*

(Coffin, 1954) *LF. Coffin, A study of the effects of cyclic thermal stresses on a ductile metal. Transaction of the American Society of Mechanical Engineers.76; 931-950, 1954.*

(Cools, 2002) *R. Cools, Advances in multidimensional integration, J. Comput. Appl. Math., 149, 1-12, 2002.*

(Cools, 2003) *R. Cools, An encyclopaedia of cubature formulas, J. Complexity, 19, (3),445-453, http://www.cs.kuleuven.ac.be/~nines/research/ecf/ecf.html, 2003.*

(Cools and Rabinowitz, 1993) *R. Cools, P. Rabinowitz, Monomial cubature rules since Stroud: a compilation, J. Comput. Appl. Math., 48, 309-326, 1993.*

(Cukier and al, 1978) *H. Cukier, R. Levine, K. Shuler, Nonlinear sensitivity analysis of multiparameter model systems. J. Comput. Phys, 26, 1-42, 1978.*

(Daneshpour and al, 2012) *S. Daneshpour, J. Dyck, V. Ventzke, and N. Huber, Crack retardation mechanism due to overload in base material and laser welds of Al alloys, International Journal of Fatigue, vol. 42, pp. 95–103, 2012.*

(Ding and Xu, 2021) *C. Ding, J. Xu, An improved adaptive bivariate dimension-reduction method for efficient statistical moment and reliability evaluations, Mech. Syst. Signal Process., 149, 2021.*

(Dirik and al, 2018) *H. Dirik and T. Yalçinkaya, Crack path and life prediction under mixed mode cyclic variable amplitude loading through XFEM, 2018.*

(Dowling, 2013) *E.N. Dowling, Mechanical behavior of materials. 2013.*

(Dowling, 2007) *E.N. Dowling, Mechanical Behavior of Materials: Engineering Methods for Deformation, Fracture, and Fatigue, 3rd ed. Pearson Education, Inc., Upper Saddle River, NJ, 2007.*

(Dubourg, 2011) *V. Dubourg, Adaptive surrogate models for reliability analysis and reliabilitybased design optimization. Ph. D. thesis, Université Blaise Pascal - Clermont II, 2011.*

(Dugdale, 1960) *D.S. Dugdale, J. Mech. and Physi. Solids, vol. 8, pp.100-104, 1960.*

(Elber, 1971) *W. Elber, The significance of fatigue crack closure. ASTM Special Technical Publication, vol. 486, 1971.*

(Erdogan and al, 1963) *F. Erdogan, G. Sih, On the crack extension in plates under plane loading and transverse shear. Journal of Basic Engineering, 85:519 -525, 1963.*

(Eurocode 3, 1996) *Norme ENV 1993-1-9. Eurocode 3 : Calcul des structures en acier – Partie 1-9 : Règles générales – Règles supplémentaires pour la résistance à la fatigue des structures en acier. Paris: AFNOR; 1996.*

(Faure, 1982) *H. Faure, Discrépance de suite associées à un système de numeration (en dimension s), Acta Artithmetica, 41, 337-351, 1982.*

(Fei and al, 2020) *C.W. Fei, H. Li, H.T. Liu, C. Lu, B. Keshtegar, L.Q. An, Multilevel nested reliability-based design optimization with hybrid intelligent regression for operating assembly relationship, Aerosp. Sci. Technol. 103, 2020.*

(Fichtl and Prinja, 2011) *E.D. Fichtl, A.K. Prinja. The stochastic collocation method for radiation transport in random media, J Quant Spect Rad Trans, 112, 646-659, 2011.*

(Forman and al, 1967) *R.G. Forman, V.E. Kearney, R.M. Engle, Numerical analysis of crack propagation in cyclic-loaded structures. J Basic Eng; 89:459-464, 1967.*

(Frondelius and al, 2022) *T. Frondelius, T. Kaarakka, R. Kouhia, J. Makinen, H. Orelma and J. Vaara, Stochastic continuum approach to high-cycle fatigue: Modelling stress history as a stochastic process, 2022.*

(Fuhring and al, 1979) *H. Fuhring, T. Seeger: Dugdale crack closure analysis of fatigue cracks under constant amplitude loading. Engng. Fract. Mech., vol. 11, pp. 99-122, 1979.*

(Ganapathysubramanian and Zabaras, 2007) *B. Ganapathysubramanian, N. Zabaras. Sparse grid collocation schemes for stochastic natural convection problems. J. Comput. Phys. 225, 652-685, 2007.*

(Gao and al, 2020) *H.F. Gao, E. Zio, J.J. Guo, G.C. Bai and C.W. Fei, Dynamic probabilistic-based LCF damage assessment of turbine blades regarding time-varying multi-physical field loads, Eng. Fail. Anal., 108, Article 107193, 2020.*

(Gdoutos, 1984) *E. Gdoutos, Problems of mixed mode crack propagation. Martinus Nijho, 1984.*

(Genz, 1986) *A. Genz, Fully symmetric interpolatory rules for multiple integrals. SIAM J Numer Anal 23, 1273–1283, 1986.*

(Genz and Keister, 1996) *A. Genz, B. Keister, Fully symmetric interpolatory rules for multiple integrals over infinite regions with Gaussian weight. J Comput Appl Math, 71, 299–309, 1996.*

(Gerstner and Griebel, 2003) *T. Gerstner, M. Griebel. Dimension-adaptive tensor-product quadrature. Computing, 71, 65-87, 2003.*

(Gerstner and Griebel, 1998) *T. Gerstner, M. Griebel, Numerical integration using sparse grids, Numer. Algorithms., 18, 209-232, 1998.*

(Ghanem, 1999) *R. Ghanem, Ingredients for a general purpose stochastic finite elements implementation, Comput. Methods Appl. Mech. Engrg. 168, 19-34, 1999.*

(Ghanem and Spanos, 1991) *R.G. Ghanem, S.D. Spanos. Stochastic finite elements: a spectral approach. Berlin: Springer; 1991.*

(Ghonem and al, 1987) *H. Ghonem, S. Dore, Experimental study of the constant probability crack growth curves under constant amplitude loading. Engng Fract Mech; 27:1-25, 1987.*

(Griffith, 1921) *A.A. Griffith, The phenomena of rupture and flow in solids. Philosophical transactions of the royal society of london. Series A, containing papers of a mathematical or physical character, vol. 221, 1921.*

(Halton, 1960) *J.H. Halton. On the efficiency of certain quasi-random sequences of points in evaluating multi-dimensional integrals. Numer. Math, 2, 84-90, 1960.*

(Hammersley and Handscomb, 1964) *J.M. Hammersley and D.C. Handscomb, Monte Carlo methods, Wiley, 1964.*

(Hasofer and Lind, 1974) *A.M. Hasofer, N.C. Lind, Exact and invariant second moment code format. J. Eng. Mech, ASCE, 100, (1), 111-121, 1974.*

(He and al, 2020) *J.C. He, S.P. Zhu, D. Liao, X.P. Niu, Probabilistic fatigue assessment of notched components under size effect using critical distance theory, Eng. Fract. Mech. 235, 2020.*

(He and al, 2015) *W. He, J. Liu, D. Xie, Probabilistic life assessment on fatigue crack growth in mixed-mode by coupling of Kriging model and finite element analysis, Eng. Fract. Mech. 139, 2015.*

(Hemnesi and al, 2022) *K. Hemnesi, F. Ellmer, M. Farajian, I. Varfolomeev and M. Luke, On the evaluation of overload effects on the fatigue strength of metallic materials, published by Elsevier B.V., 2021.*

(Hong and Lind, 1996) *H.P. Hong, N.C. Lind, Approximate reliability analysis using normal polynomial and simulation results, Struct. Saf., 18, 329-339, 1996.*

(Hourlier and al, 1978) *F.Hourlier, D.McLean and A. Pineau, Fatigue crack growth behaviour of ti-5al-2· 5sn alloy under complex stress (mode I+ steady mode III). Metals Technology, 5(1):154-158, 1978.*

(Hudson, 1969) *C. M. Hudson, Effect of Stress Ratio on Fatigue-Crack Growth in 7075-T6 and 2024-T3 Aluminum-Alloy Specimens. NASA Technical Note NASA TN D-5390, Langley Research Center, Langley Station, Hampton, VA, August, 1969.*

(Hussain and al, 1974) *M.Hussain, S.PU, J.Underwood, Strain energy release rate for a crack under combined mode I and mode II. Fracture Analysis: Proceedings of the 1973 National Symposium on Fracture Mechanics, Part II ASTM International, 1974.*

(Irwin, 1960) *G.R. Irwin, Plastic zone near a crack and fracture toughness, in Proceedings of the 7th Sagabore research conference on mechanics & metals behavior of sheet material, vol. 4, New York, pp. 463–78, 1960.*

(Irwin, 1957) *G.R. Irwin, Analysis of stresses and strains near the end of a crack traversing a plate, Journal of Applied Mechanics, 24. , 1957.*

(Ishikawa and al, 1984) *H. Ishikawa, A. Tsurui and A. Utsumi, Proc. Fatigue 84 I, 511, 1984.*

(Isukapalli, 1999) *S.S. Isukapalli. Uncertainty analysis of transport-transformation models. PhD thesis, The State University of New Jersey, 1999.*

(Kamal and al, 2018) *M. Kamal and M. Rahman, Advances in fatigue life modeling; a review, Renew Sustain Energy Rev, 82, pp. 940-949, 2018.*

(Konakli and Sudret, 2016) *K. Konakli, B. Sudret Global sensitivity analysis using low-rank tensor approximations, Reliab Eng Syst Saf, 156, 64-83, 2016.*

(Krige, 1951) *D. Krige, A statistical approach to some basic mine valuation problems on the Witwatersrand. J. of the Chem., Metal. and Mining Soc. of South Africa, 52(6), 119–139, 1951.*

(Kuperberg, 2006) *G. Kuperberg Numerical cubature using error-correcting codes SIAM J. Numer. Anal., 44 (3), 897-907, 2006.*

(Laird, 1967) *Laird, C. The influence of metallurgical structure on the mechanisms of fatigue crack propagation. In Fatigue crack propagation. ASTM International, 1967.*

(Landgraf, 1970) *R. W. Landgraf, The Resistance of Metals to Cyclic Deformation, Achievement of High Fatigue Resistance in Metals and Alloys, ASTM STP 467, Am. Soc. for Testing and Materials,West Conshohocken, PA, pp. 3–36, 1970.*

(Lang and al, 1999) *M. Lang, G. Marci, The influence of single and multiple overloads on fatigue crack propagation, Fatigue and Fracture of Engineering Materials and Structures, 22, pp. 257-271, 1999.*

(Lassen and al, 2002) *T. Lassen, JD. Sorensen, A probabilistic damage tolerance concept for welded joints. Part 1: data base and stochastic modeling. Marine Structures; 15:599-613, 2002.*

(Lee and Kwak, 2006) *S. Lee, B. Kwak, Response surface augmented moment method for efficient reliability analysis. Structural safety 28, 261-272, 2006.*

(Li and al, 2021) *X.Y. Li, Z. Tao, J.P. Wu, W. Zhang, Uncertainty theory based reliability modeling gor fatigue, Eng. Fail. Anal., 119, Article 104931, 2021.*

(Li and al, 2020) *Y.Z. Li, S.P. Zhu, D. Liao and X.P. Niu, Probabilistic modeling of fatigue crack growth and experimental verification, Eng. Failure Analysis 118, Article 104862, 2020.*

(Li and al, 2019) *N.P. Li, G. Nagi, Y.G. Lei, L.K. Bian, X.S. Si, Remaining usefel life prediction of machinery under time-varying operating conditions based on a two-factor state-space model, Reliab. Eng. Syst. Saf;, 186, pp. 88-100, 2019.*

(Li and al, 2018) *H. Li, H.Z. Huang, Y.F. Li, J. Zhou and J. Mi, Physics of failure-based reliability prediction of turbine blades using multi-source information fusion, Appl. Soft Comput., 72, pp. 624- 635, 2018.*

(Li and al, 2002) *G. Li, S.W. Wang, H. Rabitz. Practical approaches to construct RS-HDMR component functions. Journal of Physical Chemistry. 106: 8722-8733, 2002*

(Li and Der Kiureghian, 1993) *C.C. Li, A. Der Kiureghian, Optimal discretization of random fields, J Eng Mech, 119 (6), 1136-1154, 1993.*

(Li and Rabitz, 2010) *G. Li, H. Rabitz, Global Sensitivity Analysis for Systems with Independent and/or Correlated Inputs. J. Phys. Chem., 114, 6022–6032, 2010.*

(Liao and al (1), 2020) *D. Liao, S.P. Zhu, J.A.F.O. Correia, A.M.P. De Jesus and F. Berto, Recent advances on notch effects in metal fatigue: A review, Fatigue Fract. Eng. Mater. Struct. 43, pp. 637 – 659, 2020.*

(Liao and al (2), 2020) *D. Liao, S.P. Zhu, B. Keshtegar, G. Qian, Q. Wang, Probabilistic framework for fatigue life assessment of notched components under size effects, Int. J. Mech. Sci. 181, 2020.*

(Lieurade, 1988) *H.P. Lieurade, Effet des contraintes résiduelles sur le comportement à la fatigue des pièces et des structures industrielles, Revue Traitement Thermique -218-, pp.15-28, 1988.*

(Lin and al, 2017) *L. Zhu, M.P. Jia, A new approach for the influence of residual stress on fatigue crack propagation, Elsevier, Results in Physics, Vol. 7, pp. 2204-2212, 2017.*

(Lin and al, 2016) *Y.C. Lin, C.Y. Zhao, M.S. Chen, D.D. Chen, A novel constitutive model for hot deformation behaviors of Ti–6Al–4V alloy based on probabilistic method, Appl. Phys. A Mater. Sci. Process. 122 (8), 2016.*

(Liu and al, 2022) *X. Liu, J. Liu, H. Wang and X. Yang, Prediction and evaluation of fatigue life considering material parameters distribution characteristic, Int J Struct Integr, 13(2), pp. 309 – 326, 2022.*

(Liu and al, 2020) *X.T. Liu, F.C. Kan, H.J. Wang, X.F. Xin, Z.Q. Wand and H. Huang, Fatigue life prediction of clutch sleeve based on abrasion mathematical model in service period, Fatigue Fract. Eng. Mater. Struct., 43, p.p. 488 – 501, 2020.*

(Liu and al, 2011) *M. Liu, Z. Gao, J.S. Hesthaven. Adaptive sparse grid algorithms with applications to electromagnetic scattering under uncertainty, Appl Num Math, 61, 24-37, 2011.*

(Long and al, 2019) *X.Y. Long, K. Liu, C. Jiang, Y. Xiao and S.C. Wu, Uncertainty propagation method for probabilistic fatigue crack growth life prediction, Theor. Appl. Fract. Mech. 103, Article 102268, 2019.*

(Long and al, 2016) *X.Y. Long, C. Jiang, C. Yang, X. Han, W. Gao, J. Liu, A stochastic scaled boundary finite element method, Comput Methods Appl Mech Eng, 308. 23-46, 2016.*

(Low, 2013) *Y.M. Low, A new distribution for fitting four moments and its applications to reliability analysis, Structural Safety, 42, 12-25, 2013.*

(Lu and al (1), 2020) *C. Lu, Y.W. Feng, C.W. Fei, S.Q. Bu, Improved decomposed-coordinated kriging modeling strategy for dynamic probabilistic analysis of multicomponent structures, IEEE Trans. Reliab. 69 (2), 2020.*

(Lu and al (2), 2020) *C. Lu, and al., Moving extremum surrogate modeling strategy for dynamic reliability estimation of turbine blisk with multi-physics fields, Aerosp. Sci. Technol. 106, 2020.*

(Lu and al, 2004) *J. Lu, D. Darmofal, Higher-dimensional integration with Gaussian weight for applications in probabilistic design. Soc Ind Appl Math 26, 613–624, 2004.*

(Lu and Darmofal, 2004) *J. Lu, D.L. Darmofal, Higher-dimensional integration with Gaussian weight for applications in probabilistic design, SIAM J. Sci. Comput., 26, 613-624, 2004.*

(Madsen and al, 1986) *H.O. Madsen, S. Krenk, N.C. Lind. Methods of structural safety. Prentice-Hall, Englewood Cliffs: New Jersey; 1986.*

(Manjunatha and al, 2004) *C. M. Manjunatha and B. K. Parida, Prediction of fatigue crack growth after single overload in an aluminum alloy, AIAA Journal, vol. 42, no. 8, pp. 1536–1542, 2004.*

(Manson, 1954) *S.S. Manson, Behaviour of Materials under conditions of thermal stress. National Advisory Commission on Aeronautics: Report 1170 Cleveland: Lewis Flight Propulsion Laboratory, 1954.*

(Mareau and al, 2019) *C. Mareau and F. Morel, A continuum damage mechanics-based approach for the high cycle fatigue behavior of metallic polycrystals, Int J Damage Mech, 28 (2019), pp. 838-856, 2019.*

(Matherson, 1962) *G, Matheron, Traité de géostatistique appliquée. Editions Technip, 1962.*

(Matsuoka and al, 1976) *S. Matsuoka, K. Tanaka, M. Kawahara, The retardation phenomenon of fatigue crack growth in HT80 steel, Engng. Fract. Mech., vol. 8, pp.507-523, 1976.*

(Mckay and al, 1979) *M.R. Mckay, R.J. Beckman, W.K. Conover, A comparison of three methods for selecting values of input variables in the analysis of output from a computer code, Technometrics, 2, 239-245, 1979.*

(McNamee and Stenger, 1967) *J. McNamee, F. Stenger, Construction of fully symmetric numerical integration formulas, Numer. Math., 10, 327–344, 1967.*

(Melchers and Ahammad, 2004) *R.E. Melchers, M. Ahammed, A fast approximate method for parameter sensitivity estimation in Monte Carlo structural reliability, Comput Struct, 82 (1), 55-61, 2004.*

(Metropolis and Ulam, 1949) *N. Metropolis, S. Ulam, The Monte Carlo method, J. Am. Stat. Assoc, 44, 335-341, 1949.*

(Morris, 1991) *M.D. Morris. Factorial sampling plans for preliminary computational experiments, Technometrics, 33: 161-174, 1991.*

(Mysovskikh, 1980) *I. P. Mysovskikh, The approximation of multiple integrals by using interpolatory cubature formulae, in Quantitative Approximation, R. A. DeVore and K. Scherer, eds., Academic Press, New York, 217–243, 1980.*

(Nataf, 1962) *A. Nataf, Détermination des distributions dont les marges sont données, Comptes Rendus de l'Académie des Sciences, 225:42-43, 1962.*

(Niederreiter, 1992) *H. Niederreite, Random number generation and quasi-Monte Carlo methods, SIMA, Philadelphia, PA, USA, 1992.*

(Niu and al, 2020) *X.P. Niu, and al., Probabilistic modeling of uncertainties in fatigue reliability analysis of turbine bladed disks, Int. J. Fatigue, 2020.*

(Ni, 2002) *C.C. Ni, Study of stochastic fatigue crack growth models and their experimental verification. PhD thesis, National Taiwan University, 2002.*

(Niederreiter, 1992) *H. Niederreiter. Random number generation and quasi-Monte Carlo methods. SIAM, Philadelphia, PA, USA, 1992.*

(Nobile and al, 2006) *F. Nobile, R. Tempone, C. Webster. A sparse grid stochastic collocation method for elliptic partial differential equations with random input data. Technical Report MOX Report 85, Politecnico di Milano, 2006.*

(Nouy, 2010) *A. Nouy, Proper generalized decompositions and separated representations for the numerical solution of high dimensional stochastic problems, Arch Comput Methods Eng, 17, 403-434, 2010.*

(Novak and Ritter, 1999) *E. Novak, K. Ritter. Simple cubature formulas with high polynomial exactness. Constructive approximation. 15: 499-522, 1999.*

(Oden and al, 2003) *J.T. Oden, T. Belytschko, V. Babuska, T.J.R. Hughes, Research directions in computational mechanics, Compt. Method. Appl. Mech. Eng. 192, 913-922, 2003.*

(Owen, 1998) *A. Owen. Detecting near linearity in high dimensions. Technical report, Stanford University, Department of Statistics, 1998.*

(Owen, 1992) *A. Owen, A central limit theorem for Latin hypercube sampling, J. Royal. Stat. Soc, Series B54, 541-551, 1992.*

(Panmetsa and Grandhi, 2003) *R.C. Penmetsa, R.V. Grandhi, Adaptation of fast Fourier transformations to estimate structural failure probability, Finite Elem Anal Des, 39 (5–6), 473-485, 2003.*

(Paris and al, 1963) *P. Paris,F. Erdogan, A critical analysis of crack propagation laws. J Basic Eng; 85:528-534, 1963.*

(Pearson and Tukey, 1965) *E.S. Pearso, M. Tukey, Distributions whose first four moments are known. Biomerika, 6, 126-132, 1965.*

(Pelloux, 1969) *R. M. N. Pelloux, Mechanisms of formation of ductile fatigue striations. ASM Transactions Quarterly, 62(1), 1969.*

(Pendola and al., 2000) *Pendola M, Mohamed A, Lemaire M, Hornet P. Combination of finite element and reliability methods in nonlinear fracture mechanics. Reliability Engineering & System Safety. 70, 15-27, 2000.*

(Phillips, 1980) *G. M. Phillips, A survey of one-dimensional and multidimensional numerical integration, Comput. Phys. Comm., 20, 17–27, 1980.*

(Rabitz and Aliş, 1999) *H. Rabitz, Ö.F. Aliş. General foundations of high-dimensional model representations, Journal of Mathematical Chemistry. 25: 197-233, 1999*

(Rahman, 2008) *S. Rahman. A polynomial dimensional decomposition for stochastic computing. International Journal for Numerical Methods in Engineering. 76: 2091-2116, 2008.*

(Ralph and al, 2001) *I.S. Ralph, A. Fatemi, R.R. Stephens, and O.H. Fuchs, Metal fatigue in engineering, 2001.*

(Rasmussen and Williams, 2006) *C. Rasmussen, C. Williams. Gaussian processes for machine learning. Adaptive computation and machine learning. MIT Press, Cambridge, Massachusetts, Internet edition, 2006.*

(Ray and al, 1997) *A. Ray, S. Tangirala, A nonlinear stochastic model of fatigue crack dynamics. Probabilistic Engineering Mechanics 12 (1), 33-40, 1997.*

(Riahi, 2013) *H. Riahi, Analyse de structures à dimension stochastique élevée: application aux toitures bois sous sollicitation sismique. Ph. D. thesis, Université Blaise Pascal - Clermont II, 2013.*

(Riahi and al., 2012) *H. Riahi, Ph. Bressolette, A. Chateauneuf. Reliability assessment using combination of polynomial chaos and simulations: application to nonlinear fracture mechanics. 10th world congress on computational mechanics, Sâo Paulo-Brazil, 8-13 July 2012.*

(Rice, 1968) *JR. Rice, A path independent integral and the approximate analysis of strain concentration by notches and cracks. Journal of Applied Mechanics. 35: 379–386, 1968.*

(Rice, 1967) *J.C. Rice, Mechanics of crack tip deformation and extension by fatigue, ASTM STP 415, pp.247-308, 1967.*

(Righiniotis and al, 2003) *T.D. Righiniotis, M.K. Chryssanthopoulos, Probabilistic fatigue analysis under constant amplitude loading. Journal of Constructional Steel Research; 59(7):867 – 886, 2003.*

(Romano and al, 2018) *S. Romano, A. Bruckner-Foit, A. Brandao, J. Gumpinger, T. Ghidini and S. Beretta, Fatigue properties of AlSi10Mg obtained by additive manufacturing: Defect-based modelling and prediction of fatigue strength, Eng Fract Mech, 187, pp.165 -189, 2018.*

(Rosenblatt, 1952) *M. Rosenblatt, Remarks on a multivarite transformation, Ann Math Statist, 23, 470-472, 1952.*

(Royer, 1986) *J.Royer, A specimen geometry for plane mixed modes. Engineering Fracture Mechanics, 23(4):763-775, 1986.*

(Sankararaman and al, 2011) *S. Sankararaman, Y. Ling, S. Mahadevan, Uncertainty quantification and model validation of fatigue crack growth prediction. Engineering Fracture Mechanics; 78(7):1487 – 1504, 2011.*

(Saltelli and al, 2000) *A. Saltelli, K. Chan, E.Scott, Sensitivity analysis. J. Wiley & Sons, 2000.*

(Saltelli and Sobol 1995) *A. Saltelli, I. Sobol, About the use of rank transformation in sensitivity of model output. Reliab. Eng. Sys. Safety, 50, 225-239.*

(Santner and al, 2003) *T. Santner, B. Williams, W. Notz, The design and analysis of computer experiments. Springer series in Statistics. Springer, 2003.*

(Saxena and al, 1996) *A. Saxena, C.L. Muhlstein, Fatigue Crack Growth Testing; ASM International, Member/Customer Service Center: Materials Park, OH, USA, Volume 19, pp. 410–412, 1996.*

(Schütz, 1996) *Schütz W. A history of fatigue. Eng Fract Mech.; 54:263-300, 1996.*

(Schijve, 2009) *J. Schijve Fatigue of structures and materials. Second edition: Springer; 2009.*

(Schijve and al, 2004) *J. Schijve, M. Skorupa, A. Skorupa, T. Machniewicz, and P. Gruszczynski, Fatigue crack growth in the aluminium alloy D16 under constant and variable amplitude loading, International Journal of Fatigue, vol. 26, no. 1, pp. 1–15, 2004.*

(Schijve, 1979) *J.Schijve, eng.fract. mech., vol 11, pp. 167-221, 1979.*

(Schijve, 1962) *J.Schijve, Fatigue crack propagation in light alloy sheet material and structure, Advances in Aeronautical Sciences, Oxford: Pergamon press, 3, pp; 387-408, 1962.*

(Schlier, 2004) *C. Schilier, Error trends in Quasi-Monte Carlo integration, Computer Physics Communications, 159, (2), 93-105, 2004.*

(Schürer, 2003) *R. Schürer, A comparison between (quasi-)Monte Carlo and cubature rule-based methods for solving high-dimensional integration problems, Mathematics and Computers in Simulation, 62, (3-6), 509-517.*

(Sih, 1991) *G. Sih, Mechanics of fracture initiation and propagation: surface and volume energy density applied as failure criterion, 1991.*

(Sih, 1974) *G. Sih, Strain energy density factor applied to mixed mode crack problems. International Journal of Fracture, 10(3):305-321, 1974.*

(Smith and al, 1985) *E. Smith, K. Pascoe, Fatigue crack initiation and growth in a high strength ductile steel subject to in phase biaxial loading. American Society for Testing and Materials STP 853, pages 111-134, 1985.*

(Smola and Schölkopf, 2006) *A. Smola, B. Scholkopf. A tutorial on support vector regression. Stat. Comput. 14, 199-222, 2006.*

(Smolyak, 1963) *S. Smolyak, Quadrature and interpolation formulas for tensor products of certain classes of functions. Soviet. Math. Dokl. 4, 240-243, 1963.*

(Sobczyk and al, 1995) *K. Sobczyk, J. Trebicki, Spencer BF. Modeling of curvilinear random fatigue crack growth. Engng Fract Mech; 52 (4):703-715, 1995.*

(Sobczyk and al, 1992) *K. Sobczyk, B.F. Spencer, Random fatigue: from data to theory. Boston: Academy Press; 1992.*

(Sobczyk and al, 1991) *K. Sobczyk, J. Trebicki, Cumulative jump-correlated model for random fatigue. Engng Fract Mech; 40:201-210, 1991.*

(Sobczyk and al, 1989) *K. Sobczyk, J. Trebicki, Modeling of random fatigue by cumulative jump process. Engng Fract Mech; 34 (2):477-493, 1989.*

(Sobol, 1998) *I. Sobol. On quasi-Monte Carlo integrations, Mathematics and Computers in Simulation, 47, 103-112, 1998.*

(Sobol, 1993) *I. Sobol, Sensitivity estimates for nonlinear mathematical models, Math. Modeling & Comp. Exp, 1, 407-414, 1993.*

(Soize and Ghanem, 2004) *Soize, C. and R. Ghanem, Physical systems with random uncertainties: chaos representations with arbitrary probability measure. SIAM J. Sci. Comput. 26 (2), 395-410, 2004.*

(Song and al, 2020) *L.K. Song, G.C. Bai and X.Q. Li, A novel metamodeling approach for probabilistic LCF estimation of turbine disk, Eng. Fail. Anal., 120, Article 105074, 2020.*

(Song and al, 2019) *L.K. Song, G.C. Bai and C.W. Fei, Probabilistic LCF life assessment for turbine discs with DC strategy-based wavelet neural network regression, Int. J. Fatigue 119, p.p. 204, 2019.*

(Stroud, 1971) *A.H. Stroud, Approximate Calculation of Multiple Integrals, Prentice-Hall, Englewood Cliffs, NJ, USA, 1971.*

(Stroud, 1967) *A.H. Stroud, Some fifth degree integration formulas for symmetric regions II, Numer Math, 9, 460-468, 1967.*

(Stroud and Secrest, 1963) *A. H. Stroud and D. Secrest, Approximate integration formulas for certain spherically symmetric regions, Math. Comput., 17, 105–135, 1963.*

(Sudret, 2008) *B. Sudret. Global sensitivity analysis using polynomial chaos expansions. Reliab. Eng. Syst. Saf, 93: 964-979, 2008.*

(Sudret and Der Kiureghian, 2000) *Sudret B, Der Kiureghian A. Stochastic finite element methods and reliability: a state-of-the-art report. Department of Civil and Environmental Engineering, University of California; 2000.*

(Tada and al, 1973) *H. Tada, P. Paris, and G.R. Irwin, The Stress Analysis of Cracks Hand- book, 3rd ed. Del Research Corp., Hellertown, Pa, ch. 2, pp. 101_305, 1973.*

(Taira and al, 1979) *S.Taira, K. Tanaka, Local residual stress near fatigue crack tip, Transactions ISIJ, vol. 19, pp. 41 1-418, 1979.*

(Taleba and al, 2016) *W. Taleba, C. Gardina , C. Sarrazin-Baudoux, Plasticity induced crack closure during fatigue crack propagation: numerical prediction of the crack front shape in 304L stainless steel, 2016.*

(Tanaka, 1974) *K. Tanaka, Fatigue crack propagation from a crack inclined to the cyclic tensile axis. Engineering Fracture Mechanics, 6(3):493-507, 1974.*

(Tang and al, 2016) *K. Tang, P.M. Congedo, R. Abgrall, Adaptive surrogate modeling by ANOVA and sparse polynomial dimensional decomposition for global sensitivity analysis in fluid simulation, J. Comput. Phys., 314, 557-589, 2016.*

(Tsurui and al, 1986) *A. Tsurui and H. Ishikawa, Structural Safely 4, 15, 1986.*

(Vapnik and al, 1997) *Vapnik, V., S. Golowich, and A. Smola, Advances in Neural Information Processing Systems 9, Chapter Support vector method for function approximation, regression estimation, and signal processing. MIT Press, 1997.*

(Vasudevan and al, 1995) *A.K. Vasudevan, K. Sadananda, Classification of fatigue crack growth behaviour, Metallurgical and Materials Transaction A, 26A, pp. 1221-1234, 1995.*

(Victoir, 2004) *N. Victoir, Asymmetric cubature formulae with few points in high dimension for symmetric measures, SIAM J. Numer. Anal., 42, 209-227, 2004.*

(Virkler and al, 1979) *D.A. Virkler, B.M. Hillberry, P.K. Goel, The statistical nature of fatigue crack propagation. Jou Eng Mat Tech, ASME; 101:148-153, 1979.*

(Walker, 1970) *E.K.Walker, The Effect of Stress Ratio During Crack Propagation and Fatigue fot 2024-T3 and 7075-T6 Aluminium, ASTM STP 462, American Society for Testing and Materials, Philadelphia 1970.*

(Wand and Jones, 1995) *M. Wand, M. Jones, Kernel smoothing, Chapman and Hall, 1995.*

(Wang and al, 2021) *B.W. Wang, L.Y. Xie, J.X. Song, B.F. Zhao, C. li and Z.Q. Zhao, Curved fatigue crack growth prediction under variable amplitude loading by artificial neural network, Int. J. Fatigue, 142, Article 105886, 2021.*

(Wang and al, 2004) *R. Wang, U. Diwekar, C.E.G. Padró, Efficient sampling techniques for uncertainties in risk analysis, Environ. Prog., 23, (2) (2004), pp. 141-157.*

(Wei and al, 2008) *D. L. Wei, Z. S. Cui, and J. Chen, Uncertainty quantification using polynomial chaos expansion with points of monomial cubature rules, Comput. Struct.* ***86,*** *2008.*

(Weiner, 1983) *N. Weiner. The homogeneous chaos. American Journal of Mathematics. 60 (4): 897-936, 1983.*

(Wessel and al, 1972) *E. T. Wessel, W. G. Clark, Pryle Fracture mechanics technology, Applied to heavy section steel fracture 2nd international conference on fracture Brighton, p. 72, 13-18 April 1972.*

(Westergaard, 1939) *H. Westergaard, Bearing pressures and cracks. Journal of Applied Mechanics, 61:49 -53, 1939.*

(Wheatley and al, 1999) *G. Wheatley, X.Z. Hu, Y. Estrin, Effects of a single tensile overload on fatigue crack growth in a 316L steel, Fatigue and fracture of engineering materials and structures, 22, pp. 1041-1051, 1999.*

(Wu and al, 2004) *W.F. Wu, C.C. Ni, Probailistic models of fatigue crack propagation and their experimental verification. Probab Engng Mech; 19:247-257, 2004.*

(Wu and al, 2003) *W.F. Wu, C.C. Ni, A study of stochastic fatigue crack growth modeling through experimental data. Probabilistic Engineering Mechanics; 18:107 – 118, 2003.*

(Xiang and al, 2011) *Y. Xiang, Y. Liu, Application of inverse first-order reliability method for probabilistic fatigue life prediction. Probabilistic Engineering Mechanics; 26(2):148 – 156, 2011.*

(Xiao and Lu, 2018) *S. Xiao, Z. Lu, Reliability Analysis by Combining Higher-Order Unscented Transformation and Fourth-Moment Method, ASCE-ASME J. Risk Uncertainty in Eng. Syst, Part A: Civ. Eng, 4 (1), 2018.*

(Xiu and Karniadakis, 2002) *D. Xiu, GE Karniadakis. The Weiner-Askey polynomial chaos for stochastic differential equations. SIAM J Sci Comput. 24(2): 619-644, 2002.*

(Xu and Lu, 2017) *J. Xu , Z.H Lu, Evaluation of moments of performance functions based on efficient cubature formulation, J. Eng. Mech., 143, 2017.*

(Xu and al, 2012) *J. Xu, J.B. Chen and J. Li, Probability density evolution analysis of engineering structures via cubature points, Computational Mechanics, 2012, 50, (1), 135–156, 2012.*

(Xu and Dang, 2019) *J. Xu, C. Dang, A new bivariate dimension reduction method for efficient structural reliability analysis, Mech. Syst. Signal Process., 115, 281-300, 2019.*

(Xu and Kong, 2018) *J. Xu, F. Kong, A cubature collocation based sparse polynomial chaos expansion for efficient structural reliability analysis, Struct Saf, 74, 24-31, 2018.*

(Xu and Rahman, 2004) *H. Xu, S. Rahman. A generalized dimension-reduction method for multidimensional integration in stochastic mechanics. International Journal for Numerical Methods in Engineering. 61: 1992-2019, 2004*

(Yang and al, 1996) *J.N. Yang, S.D. Manning, A simple second order approximation for stochastic crack growth analysis, Eng. Fract. Mech. 53 (5), 677–686, 1996.*

(Yang and al, 1990) *J.N. Yang, S.D. Manning, Stochastic crack growth analysis methodologies for metallic structures. Engng Fract Mech; 37:1105-1124, 1990.*

(Yuan and al (1), 2019) *R. Yuan, and al., Simulation-based design and optimization and fatigue characteristics for high-speed backplane connector, Adv. Mech. Eng. 11 (6) 1–10, 2019.*

(Yuan and al (2), 2019) *R. Yuan, and al., A Reliability Analysis Method of Accelerated Performance Degradation Based on Bayesian Strategy, IEEE Access 7, 2019.*

(Zhang, 2019) *J.J. Zhang, Chapter 4 - Basic rock fracture mechanics, Applied Petroleum Geomechanics, Pages 133-161, 2019.*

(Zhang, 1992) *X.B. Zhang, Etude numérique de la propagation de fissures par la mécanique de la rupture. Thèse de l'université Blaise Pascal, France 139, 1992.*

(Zhang and al, 2019) *C.Y. Zhang, J.S. Wei, H.Z. Jing, C.W. Fei and W.Z. Tang, Reliability-based low fatigue life analysis of turbine blisk with generalized regression extreme neural network methods, Materials 12, 2019.*

(Zhang and al, 2014) *Y.G. Zhang, Y.L. Huang, Z.M. Wu, N. Li, A high order unscented kalman filtering method, Acta Automatica Sinica, 40 (5), 838-848, 2014.*

(Zheng and al, 2020) *D.F. Zeng, T. Xu, J. Wang, L.T. Lu, W; Meng, B. Jiang and Q. Zou, Investigation of the crack initiation of subsurface rolling contact fatigue in railway wheels, Int. J; Fatigue, 130, Article 105281, 2020.*

(Zhu and al, 2020) *S.P. Zhu, Y.Z. Hao, D. Liao, Probabilistic modeling and simulation of multiple surface crack propagation and coalescence, Appl. Math. Model. 78, 2020.*

(Zhu and al (1), 2018) *S.P. Zhu, Q. Liu, W. Peng, X.C. Zhang, Computational-experimental approaches for fatigue reliability assessment of turbine bladed disks, Int. J. Mech. Sci. 142–143, 2018.*

(Zhu and al (2), 2018) *S.P. Zhu, Q. Liu, Q. Lei, Q. Wang, Probabilistic fatigue life prediction and reliability assessment of a high-pressure turbine disc considering load variations, Int. J. Damage Mech. 27 (10), 2018.*

RÉSUMÉ

Ce travail présente une approche hybride permettant d'effectuer des calculs de propagation d'incertitudes. Elle est basée sur des Surfaces de Réponses Stochastiques (SRS) pour la construction de représentations analytiques des réponses de modèles mécaniques implicites. Les coefficients des SRS, définis par des intégrales multidimensionnelles sont calculés par des schémas de quadrature efficaces permettant de réduire le nombre d'évaluations du modèle mécanique implicite, particulièrement dans le cas où le nombre de paramètres incertains est élevé. La précision et l'efficacité de l'approche ont été démontrées via le traitement d'une large variété de problèmes de fissuration par fatigue.
Les niveaux de complexité auxquels les ingénieurs devront faire face résident dans la difficulté de comprendre le phénomène de fatigue et le caractère très aléatoire de ce phénomène. Ainsi le problème est de proposer une approche qui permette de garantir le meilleur compromis entre la représentation du comportement réel de la fissure par fatigue et la prise en compte des différentes sources d'incertitude. Les principaux objectifs de ce travail sont de calculer des intégrales multidimensionnelles avec une approche qui équilibre entre l'efficacité et la précision et de développer une approche unifiée capable d'effectuer efficacement les trois types d'incertitude : (1) Évaluer les moments statistiques et construire la densité de probabilité ; (2) une analyse de sensibilité basée sur une décomposition de la variance ; (3) Évaluer la probabilité de défaillance par une analyse de fiabilité.

mots-clés : Propagation d'incertitudes, variabilité spatiale, quadrature efficace, chaos polynômial creux, fissuration par fatigue

ABSTRACT

This work presents a hybrid approach to perform uncertainty propagation. It is based on Stochastic Response Surfaces (SRS) for the construction of analytical representations of implicit mechanical model responses. The coefficients of the SRS, defined by multidimensional integrals, are calculated by effective quadrature schemes allowing to reduce the number of evaluations of the implicit mechanical model, particularly in the case where the number of uncertain parameters is high. The accuracy and effectiveness of this approach have been demonstrated through the treatment of a wide variety of fatigue cracking problems.
The levels of complexity that engineers will have to deal with lies in the difficulty of understanding fatigue phenomena and the very random nature of the fatigue phenomenon. Thus the problem is to propose an approach that allows to guarantee the best compromise between the representation of the real behavior of the fatigue crack and the consideration of the different sources of uncertainty. The main to objectives of this work is computing multidimensional integrals with an approach that balance between the efficiency and the accuracy and to develop a unified approaches able to perform efficiently the three kinds of uncertainty: (1) Evaluate the statistical moments and constructing the probability density; (2) a sensitivity analysis based on a variance decomposition; (3) Evaluate the probability of failure by a reliability analysis.

keywords : Uncertainty propagation, spatial variability, efficient cubature, sparse polynomial chaos, fatigue crack

université angers

Présidence de l'université
40 rue de rennes – BP 73532
49035 Angers cedex
Tél. 02 41 96 23 23 | Fax 02 41 96 23 00